Influence of chemical structure on molecular interactions and microstructure of organic photovoltaic materials

Submitted in fulfilment of the requirements of the degree of Doctor of Philosophy

Anne Antoinette Yvette Guilbert
Department of Physics, Imperial College London

May 2013

Declaration of originality:

Except in the places where specific reference is made, the results presented in this thesis are the product of my own work.

To clarify, all steady-state UV-vis absorption and most of the photoluminescence spectroscopy (at the only exception of the results presented in Figure 4.8) and differential scanning calorimetry measurements as well as modelling results are the product of my own work. The rest of the results are either the product of the work of one of my collaborator (the reference "Data from" is mentioned) or the product of my work and one of my collaborator (the reference "in collaboration with" is mentioned).

Copyright declaration:

The copyright of this thesis rests with the author and is made available under a Creative Commons Attribution Non-Commercial No Derivatives licence. Researchers are free to copy, distribute or transmit the thesis on the condition that they attribute it, that they do not use it for commercial purposes and that they do not alter, transform or build upon it. For any reuse or redistribution, researchers must make clear to others the licence terms of this work.

Acknowledgements

I would like to thank:

- my supervisor Prof. Jenny Nelson for her support during these last three years. I would like to thank her for make the thesis submission happens almost on time. Jenny, we did it!
- Dr. Natalie Stingelin for her kindness, help and availability.
- all my collaborators: Tiziano Agostinelli, Annalisa Bruno, Luke X. Reynold, Simon King, Andrew MacLachlan, Mark A. Faist, Jizhong Yao, Thomas Kirchartz, Ellis Pires, Samuele Lilliu, J. Emyr Macdonald, Malte Schmidt, Mariano Campoy-Quiles and Antonio Urbina.
- all my colleagues from Jenny's, Natalie's, Joao Cabral's group and also the PhD students from H724 for both the interesting scientific discussions and all the fun we had.
- the EXSS office (Carolyn, Bhavna and Juraci) and Loli
- the IC high performance computing centre, especially Simon A. Burbidge.
- Mark Owen and Charlotte for their friendship
- Jean-Michel for having pushed me to apply at Imperial, his support and for having this special place in my life.
- Nikolay for having supported me during the writing up and making my life everyday sunnier.

Finalement, j'aimerais remercier ma famille (maman, papa, Francois et Lucile, Claire et la petite derniere Laura) pour leur soutien et le fait qu'il soit toujours present pour moi.

Abstract

The performance of organic solar cells based on blend films of a conjugated polymer and a fullerene derivative is strongly related to the blend microstructure. Therefore, in selecting new materials for improved light harvesting or higher photovoltage, it is essential to understand the effect of chemical structure on molecular interactions in order to find ways to control the final blend microstructure.

In this thesis, we first address the influence of the number of side chains attached to the fullerene on the microstructure of a regioregular poly(3-hexylthiophene)(P3HT): fullerene blend using transmission electron microscopy, steady-state and ultra-fast photoluminescence spectroscopy and grazing incidence X-Ray diffraction (GIXRD). We investigate the influence of fullerene side chains on the P3HT:fullerene binary phase behaviour using differential scanning calorimetry (DSC). We relate our findings to the observed optoelectronic properties of the same binary systems. This study highlights the importance of miscibility and crystallisation in microstructure development.

Secondly, we seek a spectroscopic probe of the onset of aggregation (or solubility limit) of fullerenes in polymer. We study regiorandom P3HT:fullerene blend films as a function of fullerene type and content using steady-state and ultra-fast photoluminescence spectroscopy. We relate the onset of fullerene aggregation with the appearance of charge transfer (CT) state emission. We correlate the CT state emission energy with fullerene crystallisation, probed by DSC.

Thirdly, we address the influence on polymer packing of the bridging atom between the backbone and the side chains in poly[2,1,3-benzothiadiazole-4,7-diyl[4,4-bis(2-ethylhexyl)-4H-cyclopenta[2,1-b:3,4-b']dithiophene-2,6-diyl]] (PCPDTBT) using GIXRD and molecular modelling. We find that chemical substitution of the carbon bridging atom by silicon increases side chain flexibility, leading to different crystal structures. Finally, we use quasi-elastic neutron scattering and molecular dynamics to probe the side chain dynamics of polythiophenes with different side chain lengths.

Contents

1 Introduction: Organic Photovoltaic and Blend Microstructure 17

1.1 General Context of Organic Photovoltaics . . . 18

1.1.1 Energy demand, climate change and sustainability . . . 19

1.1.2 Cost: Levelised Cost of Electricity . . . 20

1.1.3 Environmental Impact: Life Cycle Analysis and Energy Payback Time . . . 22

1.1.4 Commercialisation: Efficiency, Lifetime, Material Availability and Outlook . . . 23

1.2 Organic solar cell - general concept . . . 25

1.2.1 Semiconductor properties of organic molecular solids . . . 26

1.2.2 Organic solar cell working principle . . . 33

1.2.3 Band gap engineering for highly efficient organic solar cells: the microstructure bottleneck . . . 38

1.3 Microstructure development . . . 41

1.3.1 Soft matter states . . . 41

1.3.2 Miscibility . . . 46

1.3.3 Phase separation . . . 49

1.4 Influence of microstructure on organic solar cell performances . . . 55

1.4.1 Microstructure of bulk heterojunction . . . 55

1.4.2 Miscibility effect on solar cell performances . . . 56

1.4.3 Vertical phase separation . . . 58

1.4.4 Crystallisation effect on solar cell performances . . . 58

1.4.5 Thermodynamic coarsening influence on organic solar cell lifetime . . . 59

1.4.6 Modelling techniques: bridging the gap between chemical structure and microscopic phenomena . . . 59

1.5 Motivations and outline . . . 62

2 Methods 73

2.1 Photophysical methods . . . 75

2.1.1 Steady state UV-vis absorption and photoluminescence spectroscopy . . . 75
2.1.2 Experimental . . . 75
2.1.3 Time resolved photoluminescence spectroscopy: ultrafast fluorescent upconversion . . . 76
2.1.4 Experimental . . . 77
2.1.5 Variable angle spectroscopic ellipsometry . . . 77
2.2 Thermoanalytical method: differential scanning calorimetry . . . 80
2.2.1 Principle . . . 80
2.2.2 Experimental . . . 81
2.3 Structural characterisation . . . 83
2.3.1 Transmission electron microscopy . . . 83
2.3.2 Grazing Incidence X-Ray Diffraction . . . 84
2.3.3 Quasi-elastic incoherent neutron scattering . . . 87
2.4 Sample preparation . . . 90
2.4.1 Materials . . . 90
2.4.2 Photophysical methods . . . 91
2.4.3 Differential scanning calorimetry . . . 91
2.4.4 Structural characterisation . . . 92
2.5 Molecular Dynamics . . . 93
2.5.1 Principle . . . 93
2.5.2 Force field . . . 94
2.5.3 Molecular dynamics parameters . . . 98

3 Probing the miscibility and phase behaviour of blends of poly(3-hexylthiophene) and fullerene multi-adducts using photoluminescence spectroscopy and differential scanning calorimetry 103
3.1 Motivations . . . 105
3.2 Background: fullerene multi-adducts blended with P3HT - a decrease in electrochemical loss that does not translate into an improvement of power conversion efficiency . . . 107
3.3 Characterisation of the microstructure of P3HT:fullerene multi-adduct blend films . . . 109
3.3.1 Structural characterisation . . . 109
3.3.2 Photophysical characterisation . . . 112
3.4 Discussion: different mechanisms of microstructure development . . . 117
3.5 Characterisation of the phase behaviour of P3HT:fullerene blend films . 120
3.6 Conclusion . . . 124

4 Probing the PCBM multi-adduct solubility in regiorandom poly(3-hexylthiophene) 131
4.1 Motivation . . . 133

4.2 Probing the onset of fullerene aggregation . . . 134
4.2.1 Photophysical characterisation . . . 134
4.2.2 Discussion: solubility limit . . . 139
4.2.3 Evidence of PCBM crystallisation . . . 141
4.3 Energetics . . . 143
4.3.1 Probing changes in electronic structure by spectroscopic ellipsometry . . . 143
4.3.2 CT emission . . . 144
4.4 Conclusion . . . 146

5 Influence of bridging atom type and side chains on the crystallisation of cyclopentadithiophene-benzothiadiazole polymer derivatives 149
5.1 Motivation . . . 151
5.2 Background: improvement of the power conversion efficiency by substituting the sp3 carbon bridging atom in cyclopentadithiophene-benzothiadiazole polymer derivatives . . . 152
5.3 Characterisation of polymer packing using GIXRD . . . 155
5.4 Force field development . . . 160
5.5 Crystal structure, Gibbs free energy and potential energy surface . . . 168
5.5.1 Effect of the backbones on the intermolecular potential energy . 169
5.5.2 Effect of the side chains on the intermolecular potential energy 172
5.5.3 Discussion . . . 175
5.6 Influence of the chemical structure on the crystalline order . . . 177
5.6.1 Influence of the chemical structure of the backbones on the intermolecular potentials . . . 177
5.6.2 Influence of the chemical structure of the side chains on the intermolecular potentials . . . 182
5.7 Conclusion . . . 186

6 Quasi-Elastic Incoherent Neutron Scattering and Molecular Dynamics Study on the Dynamics of Poly-alkyl-thiophenes 191
6.1 Motivation . . . 193
6.2 Quasi-Elastic Incoherent Neutron Scattering Study on the Dynamics of Poly-alkyl-thiophenes . . . 194
6.3 Molecular Dynamics on the Dynamics of Poly-alkyl-thiophenes . . . 198
6.3.1 Force Field and Molecular Dynamics Parameters . . . 198
6.3.2 Molecular dynamics results . . . 199
6.3.3 Activation energies of motions . . . 205
6.4 Conclusion . . . 207

7 Conclusion 209
7.0.1 Influence of the chemical structure of the fullerene . . . 210

7.0.2 Influence of the chemical structure of the polymer 211

A Quantum Chemistry **213**

A.1 Hartree-Fock method 213

A.2 Møller-Plesset method 214

A.3 Density Functional Theory 215

A.4 Basis sets 217

B C-PCPDTBT and Si-PCPDTBT force fields **219**

C C-APFO3 and Si-APFO3 force fields **223**

List of Figures

1.1 Picture of an organic solar module 18
1.2 World energy consumption between 1965 and 2011. 19
1.3 Levelised costs of electricity (LCE) (a) in the USA and (b) in the UK for different energy source. 21
1.4 Comparison of energy payback times and global warning potentials over 100 years of different PV technologies (a) with glass substrates and (b) with flexible substrates. 22
1.5 Scheme of an organic solar cell. 25
1.6 Bonds between two sp^2 hybridised carbon atoms. 26
1.7 Scheme of the electronic ground state and an excited state of a diatomic molecule. 28
1.8 Theoretical absorption spectrum with Franck-Condon progressions. . . 29
1.9 Measured absorbance of regioregular (RR) P3HT, regiorandom (RRa) P3HT, PCBM and blend of P3HT:PCBM (1:1 ratio in weight) 30
1.10 Jablonski energy diagram illustrating the different possible transition between the electronic states of a single molecule. 31
1.11 Theoretical absorption and photoluminescence spectra with Franck-Condon progressions. 32
1.12 Photoluminescence spectra of regioregular (RR) P3HT, regiorandom (RRa) P3HT and blends of P3HT:PCBM. 32
1.13 Band diagram of an organic solar cell depicting the different steps involved in the light conversion to electricity. 33
1.14 State diagram illustrating the key processes of exciton dissociation into polarons. 35
1.15 Theoretical heat capacity as a function of temperature of semi-crystalline materials. 42
1.16 Free energy difference as a function of the nucleus radius. 43
1.17 Schematic of a liquid drop showing the contact angle θ. 44
1.18 Nucleation and crystal growth rates as a function of the temperature. . 45
1.19 Scheme of a polymer lamella and of a spherulite. 46

1.20 A random walk chain on an incompressible lattice. 47
1.21 Free energy of mixing ΔG_{mix} as a function of composition ϕ_2 at different temperatures T.Phase diagram (temperature as a function of composition ϕ_2) for a binary system in the solid state extracted from ΔG_{mix} 51
1.22 Eutectic phase diagram. 52
1.23 Scheme showing the microstructure of a bulk heterojunction 55

2.1 Scheme illustrating the principle of ellipsometry measurements. 77
2.2 Scheme illustrating differential scanning calorimetry. 80
2.3 DSC scans of P3HT, PCBM and P3HT:PCBM (1:3). 81
2.4 Bright-field TEM micrograph of as-spun P3HT:PCBM (1:1). 84
2.5 Scattering geometry of a GIXRD experiment. 85
2.6 GIXRD pattern and out-of-plane line profile of as-spun P3HT:PCBM. . 86
2.7 Quasi-elastic intensity $I_{exp}(Q = 1\text{Å}^{-1}, \omega)_{T=165K}$ in the energy domain and the corresponding intermediate scattering function $S_{inc}(Q = 1\text{Å}^{-1}, t)_{T=165K}$ in the time domain. 89
2.8 (a) $PC_{61}BM$, $PC_{61}BM$ (b) bis- and (c) tris-adducts, (d) $PC_{71}BM$, (e) P3HT and (f) C6- and Si-PCPDTBT. 90
2.9 Flow chart of a Molecular Dynamics algorithm. 94
2.10 Representation of the different distances and angles in atomistic models. 96

3.1 TEM micrographs of as-spun (a-c) and annealed (d-f) ∼85 mol% P3HT blend films of P3HT:PCBM (a,d),P3HT:bis-PCBM (b,e), and P3HT:tris-PCBM (c,f). 109
3.2 (a) Proposed monoclinic unit cell for P3HT. GIXRD patterns of as-spun films: (b) P3HT:PCBM, (c) P3HT:bis-PCBM, and (d) P3HT:tris-PCBM (1:1). 110
3.3 GIXRD out-of-plane profiles of as-spun films of P3HT:PCBM, P3HT:bis-PCBM and P3HT:tris-PCBM (1:1) 111
3.4 Absorption (a-c) and steady-state PL (d-f) profiles for as-spun P3HT:PCBM (a,d), P3HT:bis-PCBM (b,e), and P3HT:tris-PCBM (c,f) blends. 112
3.5 Normalised quantum yield of as-spun P3HT:fullerene films of different compositions. 113
3.6 Ultra-fast time-resolved emission decay traces of as-spun blends of (a) P3HT:PCBM, (b) P3HT:bis-PCBM, and (c) P3HT:tris-PCBM. . . . 115
3.7 Time components of the bi-exponential decay fits to the ultrafast fluorescence up-conversion decays for as-spun and annealed films. 116
3.8 Schematics depicting the proposed microstructure of as-spun and annealed films of P3HT:PCBM, P3HT:bis-PCBM, and P3HT:tris-PCBM. 119

3.9 DSC scans of (a) P3HT:PCBM, (b) P3HT:bis-PCBM and (c) P3HT:tris-PCBM films of different compositions at a heating rate of 10 °C/min. . 121
3.10 DSC scans of (a) P3HT:bis-PCBM and (b) P3HT:tris-PCBM films of different compositions at a heating rate of 2°C/min. 122
3.11 P3HT:PCBM, P3HT:bis- and tris-PCBM non-equilibrium phase diagrams. 122
3.12 Open circuit voltage V_{oc} (a), short circuit current J_{sc} (b), fill factor FF (c) and power conversion efficiency PCE (d) as a function of P3HT content (mol %) averaged on five ITO/PEDOT:PSS/P3HT:bis-PCBM/Al devices. 123

4.1 Absorption (a,b) and steady-state PL (c,d) profiles for as-spun blends of RRa-P3HT:PCBM (a,c), and RRa-P3HT:bis-PCBM (b,d). (e) Normalised quantum yield of as-spun RRa-P3HT:fullerene films of different compositions. 135
4.2 Normalised quantum yield of as-spun RRa-P3HT:fullerene films of different compositions. 136
4.3 Normalised ultrafast time-resolved emission decay traces of as-spun blends of (a) RRa-P3HT:PCBM, and (b) RRa-P3HT:bis-PCBM.(c) Normalised initial fluorescence intensity of as-spun blends of RRa-P3HT:PCBM and RRa-P3HT:bis-PCBM. (d) Time components of the mono-exponential decay fits to the ultrafast fluorescence up-conversion decays for as-spun blends of RRa-P3HT:PCBM and RRa-P3HT:bis-PCBM. 137
4.4 Normalised ultrafast time-resolved emission decay traces of regio-regular (RR) P3HT, regio-random (RRa) P3HT and blends of RR-P3HT:PCBM and RRa-P3HT:PCBM. 138
4.5 Schemes representing the average distance from an exciton generation site to a quenching site for (a) a non-homogeneously and (b) a homogeneously dispersed system. 140
4.6 DSC scans of RRa-P3HT:PCBM blends of different compositions. . . . 141
4.7 Absorption coefficients of PCBM into RRa-P3HT extracted from VASE measurements for different PCBM content. 143
4.8 (a) Normalised PL spectra of RRa-P3HT:PCBM blends at different concentrations. (b) CT emission energy of RRa-P3HT:PCBM blends as a function of PCBM content. 145

5.1 Chemical structure of PCPDTBT. 152
5.2 Proposed monoclinic crystal structure for (a) C-PCPDTBT and (b) Si-PCPDTBT. 155

5.3 GIXRD patterns of (a) C-PCPDTBT, (b) Si-PCPDTBT, blends of (c) C-PCPDTBT and (d) Si-PCPDTBT with $PC_{70}BM$. 156
5.4 GIXRD (a) out-of-plane and (b) in-plane profiles of C-PCPDTBT, Si-PCPDTBT, C-PCPDTBT:$PC_{70}BM$ and Si-PCPDTBT:$PC_{70}BM$ films. . 157
5.5 Azimuthal scan profile obtained at $q_{(100)}$ peak positions for Si-PCPDTBT film. 157
5.6 GIXRD patterns of (a) C-PCPDTBT:$PC_{70}BM$ and (b) $PC_{70}BM$. 159
5.7 Atom class definitions for C-PCPDTBT and Si-PCPDTBT. 160
5.8 Energies calculated using first principle methods and potential that we include in the force field for the CA-CW!-C!-CA dihedral of C-PCPDTBT.161
5.9 Partial charges for (a) C-PCPDTBT and (b) Si-PCPDTBT derived from quantum chemical calculations. 163
5.10 (a) CT-X-CT angle, (b) CA-X-CT-CH, (c) X-CT-CH-CT and (d) CT-CT-CH-CT dihedrals. 164
5.11 Energies calculated using first principles methods and potential that we include in the force field (denoted as "intrinsic") for (a) the angle CT-X-CT, the dihedrals (b) CA-X-CT-CH, (c) X-CT-CH-CT for both C-PCPDTBT and Si-PCPDTBT and (d) CT-CT-CH-CT. 165
5.12 (a) Isolated monomer in a box of chloroform.(b) 3D spatial distribution function of side chains.(c,d) 2D slices perpendicular to the backbone of the spatial distribution of side chains of isolated (c) C-PCPDTBT and (d)Si-PCPDTBT monomers. 166
5.13 Alternating cyclopentadithiophene and benzothiadiazole units pointing in the opposite directions 168
5.14 Backbones of C-PCPDTBT and Si-PCPDTBT quantum chemically relaxed using B3LYP/6-311g(d,p). 169
5.15 Geometry of the initial structure representative of a crystal. 170
5.16 (a,b) Potential energy surfaces and (c,d) Lennard-Jones potential energy surfaces for (a,c) C-PCPDTBT and (b,d) Si-PCPDTBT. 171
5.17 (a) Potential energy surface and (b) Lennard-Jones potential energy surface for C-PCPDTBT. 173
5.18 Contributions of the (a) backbones-backbones and (b) side chains-side chains interactions to the Lennard-Jones potential energy surface for C-PCPDTBT. 174
5.19 Chemical structures of pFTBTT and pSiF-DBT 177
5.20 GIXRD (a) out-of-plane and (b) in-plane profiles of C-APFO3, Si-APFO3, C-APFO3:$PC_{60}BM$ and Si-APFO3:$PC_{60}BM$. 178
5.21 Potential energy surfaces of (a) C-PCPDTBT and (b) C-APFO3. 179
5.22 Contributions of the side chain-side chain interactions to the Lennard-Jones potential energy surface for (a) C-PCPDTBT and (b) C-APFO3. 181
5.23 Chemical structure of (a) C8-PCPDTBT and (b) C16-PCPDTBT. 182

5.24 Potential energy surfaces of (a) C6-PCPDTBT, (b) C8-PCPDTBT and (c) C16-PCPDTBT. 184
5.25 Contributions of the side chains-side chains interactions to the Lennard-Jones potential energy surfaces of (a) C6-PCPDTBT, (b) C8-PCPDTBT and (c) C16-PCPDTBT. 185

6.1 Mean square displacement as a function of time for different temperatures for (a) P3HT and (b) P3OT. 195
6.2 Temperature dependence of the exponent χ determining the sublinear dependence of the mean square displacement for P3HT and P3OT from the experiments performed with OSIRIS (18-90 ps). 196
6.3 Definition of the different hydrogen groups C1-C7, methyl and backbones for (a) P3HT and (b) P3OT. 198
6.4 Mean-square displacement as a function of time for different temperatures between 0 K and 500 K for (a) P3HT and (b) P3OT. 201
6.5 Temperature dependence of the mean square displacement at 1 ps for (a) P3HT and (b) P3OT for different group of hydrogens.(c) Comparison between P3HT and P3OT mean square displacement obtained by MD simulations on all the hydrogens of the system and the mean square displacement extracted from measurements. 202
6.6 Density of P3HT calculating from simulations as a function of the temperature. 203
6.7 Temperature dependence of the mean square displacement at 1 ps for P3HT as calculated in NPT and NVT ensembles. 203
6.8 Temperature dependence of the exponent χ determining the sublinear dependence of the mean square displacement for (a) P3HT and (b) P3OT from molecular dynamics in time windows corresponding to the time window of OSIRIS (18-90 ps). 204
6.9 Dihedral angular distribution of (a) the methyl end group and (b) the dihedral describing the torsion of the backbones as a function of the temperature. 205
6.10 Potential energy for each dihedral angles as a function of the inverse of the temperature. 206

A.1 Flow chart of the Hartree-Fock algorithm 214
A.2 Flow chart of Kohn-Sham algorithm 215

C.1 Atom class definitions for C-APFO3 and Si-APFO3. 223
C.2 Partial charges for (a) C-APFO3 and (b) Si-APFO3 derived from quantum chemical calculations. 224

List of Figures

List of Tables

1.1 Influence of increasing efficiency on environmental loads of organic photovoltaic systems. 23

3.1 Fit parameters of GIXRD line profiles and estimated P3HT domain sizes of as-spun P3HT:PCBM, P3HT:bis-PCBM and P3HT:tris-PCBM (1:1). 111
3.2 Ratio of initial fluorescence intensity of as-spun P3HT:fullerene blends with respect to neat P3HT films from fluorescence up-conversion measurements. 113

5.1 Characteristics of solar cells based on C- and Si-PCPDTBT. 153
5.2 Indexes, positions q, corresponding spacing distances d, $FWHM$, and coherence length ξ of the OOP GIXRD peaks of C-PCPDTBT, Si-PCPDTBT, C-PCPDTBT:$PC_{70}BM$ and Si-PCPDTBT:$PC_{70}BM$. 158
5.3 Indexes, positions q, corresponding spacing distances d, $FWHM$, and coherence length ξ of the IP GIXRD peaks of C-PCPDTBT, Si-PCPDTBT, C-PCPDTBT:$PC_{70}BM$ and Si-PCPDTBT:$PC_{70}BM$. 158

6.1 Temperature of activation for the different motions in (a) P3HT and (b) P3OT. 206

B.1 Mass and Lennard-Jones parameters. 219
B.2 Equilibrium bond lengths and bond force constants. 220
B.3 Equilibrium angles and angle force constants. 221
B.4 Equilibrium dihedral angles and dihedral angle force constants. 222
B.5 Improper dihedral force constants. 222

C.1 Equilibrium bond lengths and bond force constants. 223
C.2 Equilibrium angles and angle force constants. 223
C.3 Equilibrium dihedral angles and dihedral angle force constants. 224
C.4 Improper dihedral force constants. 224

List of Tables

CHAPTER 1

Introduction: Organic Photovoltaic and Blend Microstructure

Section 1.1

General Context of Organic Photovoltaics



Figure 1.1: Picture of an organic solar module [1].

The active layer of organic solar cells is composed of organic semiconductors: polymers, oligomers or small molecules. The whole cell is not organic, the electrodes are nowadays usually composed of Indium Tin Oxide (ITO) and Aluminium or Calcium. However, the ultimate target would be to produce all-organic or at least all-solution processable solar cells. In this section, we highlight the potential of organic photovoltaics as a sustainable product to meet the increasing energy demand.

1.1.1 Energy demand, climate change and sustainability

The energy demand has not ceased to grow for a century and will continue to grow in all probability since emerging countries such as China have not finished their development yet. This energy demand has been mainly sustained so far by fossil energy sources: oil, coal and natural gas (see Figure 1.2). However, based on the current proved exploitable reserves and daily production, the resources in fossil energy will be consumed within the next 200 years [2]. This creates an insecurity of energy supplies.

Furthermore, this growing consumption of fossil resources has been proven to be linked with an increase in gas emissions, especially carbon dioxide associated with global warming (see Figure 1.2). Thus, either exploiting existing fossil resources (that could not be exploited because of either technology issues or commercial reasons) or exploiting newly discovered fossil resources can no longer be regarded as sustainable possibilities. Therefore, to address this challenge of energy sustainability, the development of sustainable low-carbon energy technologies is a pressing need.

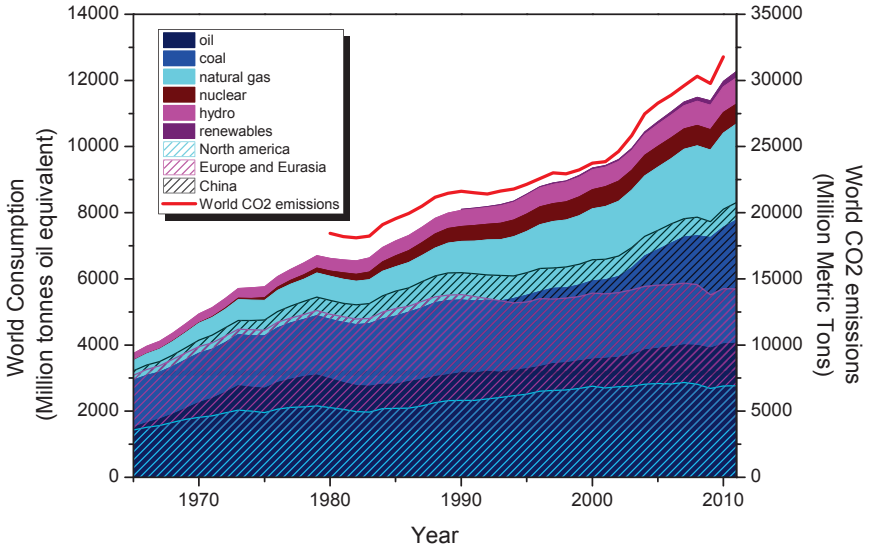


Figure 1.2: World energy consumption between 1965 and 2011 [3, 4].

So far we have been talking about primary energy [1]. In the following, we will speak about energy carrier, mainly electricity. Alternative energy sources are already used such as nuclear electricity, hydroelectricity, biomass, wind and solar energy but they are fulfilling only a very small portion of this energy demand (see Figure 1.2). More-

[1] energy form found in nature that has not been subjected to any conversion or transformation process

over, these alternative resources do not fulfil all the requirements to replace fossil energy sources as a main source of energy.

Because solar energy is the most abundant resource of energy on earth, photovoltaic (PV) power appears as a high potential low-carbon energy source. Since the Kyoto protocol in 1998, the photovoltaic market has experienced a fast growth with average annual growth rate of 40 % [5]. The last decade fast growth has been largely stimulated by very encouraging policy. However, following the economic crisis of 2007, in most of the countries the policy incentives have been cut.

If in some countries such as Italy and Spain the grid parity have been reached for PV, the remaining high investment costs of actual PV systems are expected to be the most important barrier to further PV development in the other countries. Therefore, cheaper PV technologies could enable at least to sustain this very fast growth.

Most of current PV systems are crystalline Silicon (c-Si)[2] modules (85 to 90% of the global annual market). Current cheaper PV module alternatives are based on inorganic thin films technologies (amorphous Silicon(a-Si), micro-morph Silicon (mc-Si), Cadmium-Telluride (CdTe), Copper-Indium-diselenide (CIS) and Copper-Indium-Galium-Diselenide (CIGS)). Thin film technologies represent already 10 to 15% of the global annual market and are expected to gain market shares [5].

A non-commercial candidate is organic solar cell technology which still suffers from low efficiencies and poor lifetimes in comparison with inorganic PV technologies. However, organic technology presents also numerous advantages such as light weight, flexibility, low-cost, roll-to-roll manufacturability, low environmental impact and large availability of materials.

1.1.2 Cost: Levelised Cost of Electricity

A correct quantity to compare the cost of electricity produced by different sources of energy is the levelised cost of electricity (LCE). Under the estimation of 5% efficiency and of 5-year lifetime, the levelised cost of electricity produced by organic solar cells is estimated to range between 490 to 850 US$/MWh [6] that is to say 304 to 528 GBP/MWh while the levelised cost of electricity produced by other source of energy

[2] Crystalline Silicon encompasses single crystalline Silicon (sc-Si) and multi-crystalline Silicon (mc-Si).

ranges from 57.8 to 400.7 US$/MWh, of which solar PV ranges from 122.2 to 400.7 US$/MWh, according to the Energy Information Administration [7] or from 51 to 378 GBP/MWh, of which solar PV ranges from 343 to 378 GBP/MWh, according to the UK Department of Energy and Climate Change [8] (see Figure 1.3). Organic solar cells are far from being competitive.

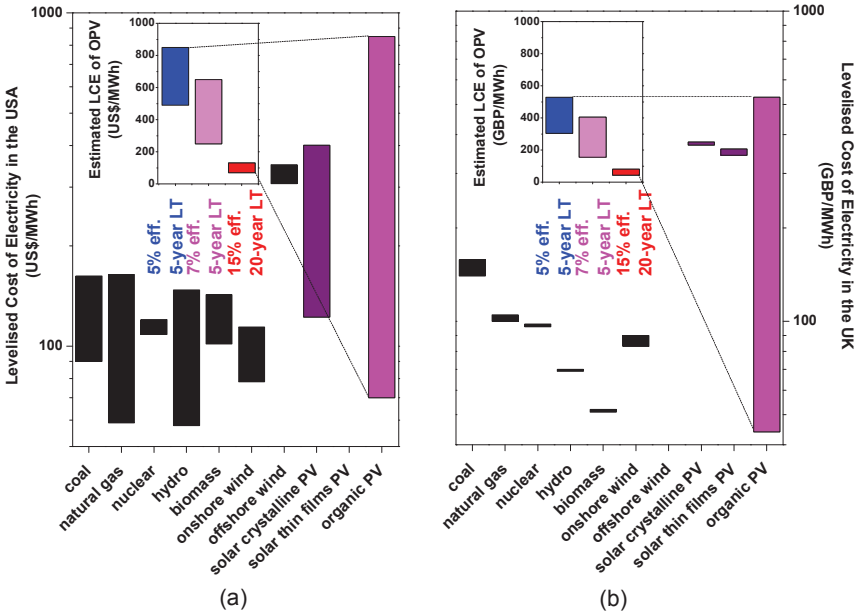


Figure 1.3: Levelised costs of electricity (LCE) (a) in the USA and (b) in the UK for different energy source and that of organic solar cell based on estimations for different efficiencies (eff.) and lifetime (LT).The height of bars represents the range of estimates[7, 8, 6].

The levelised cost of electricity is impacted by different PV module dependent factors, namely efficiency, lifetime, module cost and investment. Based on actual estimated manufacturing costs, an increase in efficiency up to 7% would already lead to a levelised cost of electricity ranging from 250 to 650 US$/MWh [6] - that is to say 155 to 404 GBP/MWh - which will make organic solar cells competitive on the solar market. Obviously, further improvement in efficiency and lifetime should lead to lower costs and may make organic solar cells a competitive energy source (based on an 15% efficiency and a 20 year-lifetime, the levelised cost of electricity drops to 70-130 US$/MWh [6] or 44-81 GBP/MWh).

1.1.3 Environmental Impact: Life Cycle Analysis and Energy Payback Time

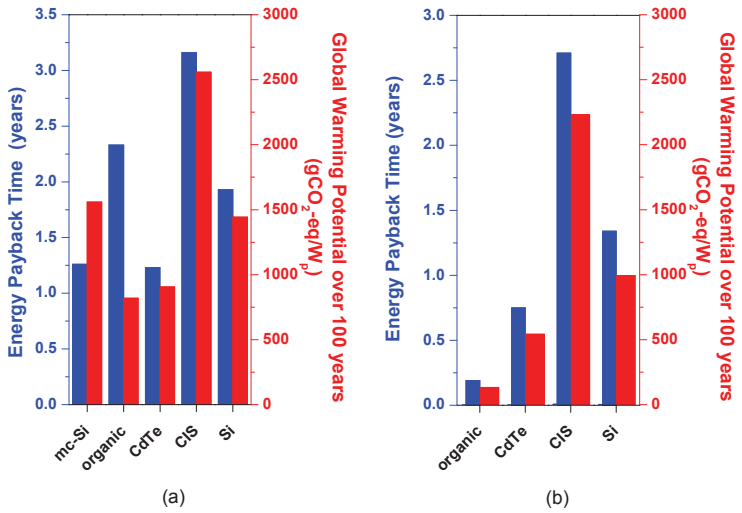


Figure 1.4: Comparison of energy payback times and global warning potentials over 100 years of different PV technologies (a) with glass substrates (all framed and with balance of system) and (b) with flexible substrates (all unframed and without balance of system)[9].

The energy payback time for organic PV systems is very low in comparison with inorganic based PV systems and, on a watt-peak basis, the environmental impacts of polymer PV systems are lower than for inorganic based PV systems. Especially for flexible modules, the environmental impacts are substantially lower (see Figure 1.4). However, since organic PV exhibits poor lifetimes (of the order of 3 years at the moment), more than one module is needed to generate power over the lifetime of an inorganic module, typically around 20 years. Improving organic PV system lifetime is thus mandatory. Obviously, increasing the efficiency of the polymer PV systems - which is assumed to be 5% in Figure 1.4 - will decrease the global warming potential for one module and thus will decrease the minimum required lifetime for polymer PV systems to retain the advantages of their low-environmental impact production (see Table 1.1).

Table 1.1: Influence of increasing efficiency on environmental loads of organic photovoltaic systems[9].

	organic photovoltaic system efficiency					
	glass substrate			flexible substrate		
	5%	8%	11%	5%	8%	11%
minimum required lifetime (years)	13	8	6	2.4	1.5	1.1

1.1.4 Commercialisation: Efficiency, Lifetime, Material Availability and Outlook

As seen in Section 1.1.2 and Section 1.1.3, to decrease both cost and environmental impact, it is crucial to increase the efficiency and lifetime of organic PV systems. This should increase their competitiveness firstly with their inorganic counterparts and secondly with the other sources of electricity. However, there is an uncertainty in the price of organic PV systems because the price does not depend only on the balance of module cost but also on the balance of system cost. As the first one decreases, the second one becomes the limiting factor unless organic PV systems may be integrated at lower cost than other PV technologies.

Assessing efficiency for organic solar cells is not easy. Firstly, organic solar cells are tested using the standard measurements for conventional solar cells (direct sunlight). However, the sensitivity of the power conversion efficiency of organic solar cells to conditions such as intensity, diffuse light, temperature, ... differs from other PV technologies [10]. Secondly, the new high efficiency polymers that lead to an increase of solar cell efficiencies up to 10% [11] require more processing steps to be synthesised leading to higher environmental impacts. Furthermore, that may lead to difficulties to mass produce, that is to say to higher material costs [12]. Therefore, there will be probably a trade-off between efficiency and complexity of the materials used in the active layer.

Those high efficiency polymers still require light chemistry in comparison with the purification of metallurgical silicon for PV use. This highly energy intensive and time-consuming step has recently limited the availability of electronic grade Silicon feedstock for Silicon PV manufacturing. This problem of resource availability is also

encountered with the other thin film PV technologies CdTe and CIGS. Energy is also a political issue and states wish to reach autonomy. However, at the moment, most of the purification of metallurgical silicon is processed in China and most of the rare earth needed for PV is now held by China.

This problem of resources exist also with organic PV system due to the use of an ITO transparent electrode. However, alternatives exist such as conductive polymers. If good efficiencies can be achieved with such electrodes, this will not only solve the problem of material availability but will decrease the cost of the module (the ITO electrode is one of the most expensive element of the module), the energy pay back time (it is also by far the most energy consuming step in the module production) [13] and will probably increase the lifetime, especially for flexible substrate.

To summarise, by raising the efficiency and lifetime of organic solar cells, organic PV can become competitive for different applications, indoor and outdoor, in-grid and off-grid providing that the balance of system does not limit organic PV cost. Their energy pay back times are very short making them extremely environmentally friendly if a decent lifetime is reached and a solution is found to recycle the waste. Because of their flexibility, possible transparency and roll-to-roll processability on different scale, they can be easily integrated. The fact that all the materials can be synthesised make them a sustainable solution. However, there is still the inherent problem linked with photovoltaics, the fact that they cannot produce electricity during night. Therefore, the grid has to be improved e.g. through use of smart grids and efficient and sustainable ways to store electricity have to be achieved.

Section 1.2

Organic solar cell - general concept

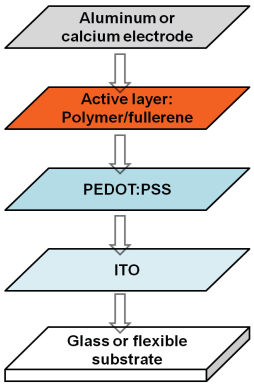


Figure 1.5: Scheme of an organic solar cell.

In the previous section, we have shown the potential of organic photovoltaics as a sustainable product to meet the increasing energy demand. However, to achieve a sustainable product, a number of issues have to be addressed among them increasing the efficiency and the lifetime. In this section, we will present the general concept of organic solar cells.

The conversion of light into electricity requires the generation of both negative and positive charges as well as a driving force that can push these charges through an external electric circuit. State-of-the-art organic solar cells consist of an active layer composed of a blend of a conjugated polymer (the most widely used polymers are poly(3-hexylthiophene-2,5-diyl) (P3HT), poly[N-9'-heptadecanyl-2,7-carbazole-alt-5,5-(4',7'-di-2-thienyl-2',1',3'-benzothiadiazole)] (PCDTBT) and a fullerene derivative (often phenyl-C61-butyric acid methyl ester ($PC_{61}BM$) or phenyl-C71-butyric acid methyl ester ($PC_{71}BM$) deposited from solution on a glass or a flexible substrate, which has been beforehand coated with ITO and poly(3,4-ethylenedioxythiophene) poly(styrenesulfonate) (PEDOT:PSS). Then, an aluminium or calcium electrode is evaporated on top of the active layer (see Figure 1.5). In this section, we first review the semiconducting properties of some organic materials; then, the working principle of organic solar cell is presented and finally, we highlight the importance of the active layer microstructure.

1.2.1 Semiconductor properties of organic molecular solids

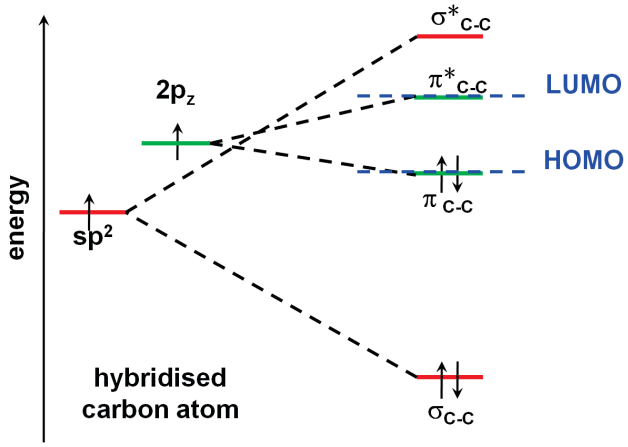


Figure 1.6: In the ground state, a carbon atom has four valence electrons, two in the 2s subshell and two in the 2p subshell. An excited state can be formed by promoting one of its 2s electrons into the empty 2p orbital. The s orbital and two of the p orbitals will reorganise into three sp^2 hybrid orbitals. Two sp^2 hybrid orbitals from two carbon atoms can merge to give σ molecular orbitals and two pure p_z orbitals can merge to form π molecular orbitals. Since sp^2 orbitals highly overlap in comparison with the p_z orbitals, the splitting between bonding and anti-bonding orbitals will be smaller for π-orbitals and thus the π-orbital forms the HOMO and a π^*-orbital the LUMO of the formed molecule.

If most organic materials are insulators, some exhibit semiconducting properties due to a more or less extended π-electron system of the molecules. This is due to sp^2-hybridization, which may occur with carbon atoms. Usually, sp^2 hybrid orbitals highly overlap to form σ-bonds while the remaining p_z-orbitals weakly overlap to form π-bonds. This leads to a weaker splitting between the bonding and anti-bonding π- and π^*-orbitals than between the bonding and anti-bonding σ- and σ^*-orbitals. Therefore, in typical organic materials with π- and σ-bonds, a π-orbital forms the Highest Occupied Molecular Orbital (HOMO) and a π^*-orbital the Lowest Unoccupied Molecular Orbital (LUMO) (see Figure1.6).

1.2.1.1 Exciton photogeneration

Unlike in conventional solar cells where the absorption of photons leads directly to the formation of free charge carriers, in organic semiconductors, absorption of photons leads rather to electrically neutral excited states of the organic semiconductor, often regarded as intramolecular coulombically bound electron-hole pairs, called Frenkel excitons. Frenkel excitons are usually localised on one molecule or a polymer chain segment, in other words, confined within a volume of few nm^3. This spatial confinement combined with the low dielectric permittivity of organic semiconductors ($\epsilon \approx 3-4$) results in a large Coulomb binding energy (around 1 eV) in comparison with the thermal energy [14]. Consequently, singlet excitons in an organic semiconductor tend not to dissociate into free polarons [1] but rather decay to the ground state within few nanoseconds, with fluorescence (singlet-singlet transition) as a possible radiative decay path [15]. Intersystem crossing can also occur and the resulting triplet excitons exhibit longer lifetime up to milliseconds, with phosphorescence as a possible radiative decay path [16].

1.2.1.2 Absorption

Because the quantum states of molecules have not only an electronic contributions but also vibrational contributions, molecular spectra are closely spaced band spectra in contrast to atomic line spectra. Each electronic state has a vibrational structure, characterised by vibrational quantum numbers v (see Figure 1.7). A range of different photon energies can excite a molecule from its ground state to its first excited state by exciting different vibrational states. These are referred to as vibronic transitions. The ground state normally occupies the lowest vibronic levels (vibronic levels with energies within k_BT of $v = 0$) [17].

The likeliness or intensity of a transition from an initial vibrational state (v) of the ground electronic level to some vibrational state (v') of an excited electronic state depending on the photon energies $\hbar\omega_{Ph}$ is given by:

$$I(\hbar\omega_{Ph}) = \sum_F | < \Psi_F|\mu|\Psi_I > |^2 \delta(E_F - E_I - \hbar\omega_{Ph}) \tag{1.1}$$

where Ψ_I and Ψ_F are the wavefunctions of the initial and final state respectively, E_I and E_F are the energy of the initial and final states respectively. μ is the molecular dipole operator and is determined by the charge $-e$ and locations r_i of the electrons

[1] Charges interact with their environment in organic solar cells. They can deform the whole molecule where they reside. Thus, the charge carriers are dressed in more or less extended polarisation clouds and are known as polarons.

as well as the charges $+eZ_j$ and locations R_j of the nuclei:

$$\begin{aligned} \mu &= \mu_e + \mu_N \\ &= -e\sum_i r_i + e\sum_j Z_j R_j \end{aligned} \tag{1.2}$$

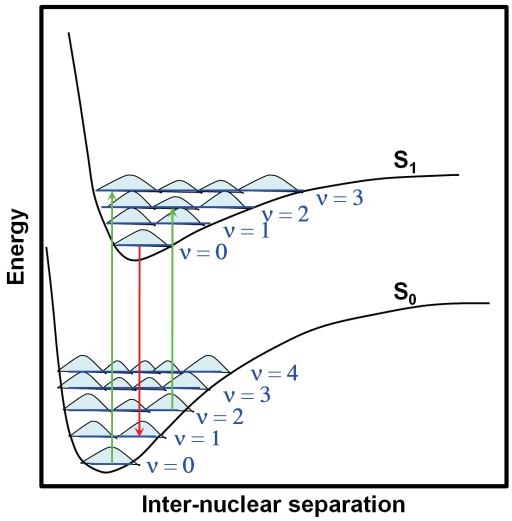


Figure 1.7: Scheme of the electronic ground state and an excited state of a diatomic molecule. Vibrational levels of both states are represented in blue. Franck-Condon principle is illustrated with the green and red arrows.

According to the Born-Oppenheimer approximation,

$$\Psi(r, R, S_z) = \phi(r, R)\chi_v(R)\phi_s(S_z) \tag{1.3}$$

where r and R are the set of electronic and nuclear coordinates respectively, S_z is the z-component of the spin. $\phi(r, R)$, $\chi_v(R)$ and $\phi_s(S_z)$ denote the electronic, the nuclear and the spin wavefunction respectively. Thus,

$$\begin{aligned} < \Psi_F|\mu|\Psi_I > &= \int \phi_F^*(r, R)\chi_{v'}^*(R)\phi_s'^*(S_z)\mu_e\phi_I(r, R)\chi_v(R)\phi_s(S_z)drdRdS_z \\ &+ \int \phi_F^*(r, R)\chi_{v'}^*(R)\phi_s'^*(S_z)\mu_N\phi_I(r, R)\chi_v(R)\phi_s(S_z)drdRdS_z \\ &= \int \chi_{v'}^*(R)[\phi_F^*(r, R)\mu_e\phi_I(r, R)dr]\chi_v(R)dR \int \phi_s'^*(S_z)\phi_s(S_z)dS_z \\ &+ \int \phi_F^*(r, R)\chi_{v'}^*(R)\mu_N\phi_I(r, R)\chi_v(R)drdR \int \phi_s'^*(S_z)\phi_s(S_z)dS_z \end{aligned} \tag{1.4}$$

Since the electronic transitions are likely to happen so quickly that the nuclei do not

have time to rearrange to their new equilibrium positions (Condon approximation), $\phi(r,R) \simeq \phi(r,R=R_0) = \phi(r)$ [17]. Thus the equation 1.4 can be simplified to:

$$\begin{aligned} < \Psi_F|\mu|\Psi_I > = & \int \chi^*_{v'}(R)\chi_v(R)dR \int \phi^*_F(r)\mu_e\phi_I(r)dr \int \phi'^*_s(S_z)\phi_s(S_z)dS_z \\ & + \int \phi^*_F(r)\phi_I(r)dr \int \chi^*_{v'}(R)\mu_N\chi_v(R)dR \int \phi'^*_s(S_z)\phi_s(S_z)dS_z \end{aligned} \quad (1.5)$$

Because the electronic wavefunctions of different states are orthogonal, the second part of the equation is null. Finally, the intensity of a vibronic transition is given by:

$$I(\hbar\omega_{Ph}) = \sum_F | < \chi_{v'}|\chi_v > |^2 | < \phi_F|\mu_e|\phi_I > |^2 | < \phi'_s|\phi_s > |^2 \delta(E_F - E_I - \hbar\omega_{Ph}) \quad (1.6)$$

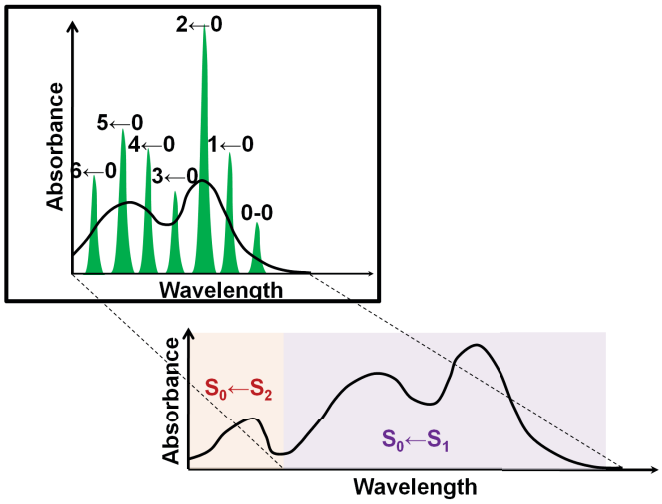


Figure 1.8: Theoretical absorption spectrum with Franck-Condon progressions (green peaks). The black curves represent the broadening of the transitions in liquid and solid states.

The intensity of each vibronic transition depends on the degree of overlapping of the vibrational wavefunctions of both the ground and excited states ($< \chi_{v'}|\chi_v >$). $| < \chi_{v'}|\chi_v > |^2$ (Franck-Condon factor) modulates the intensity of the vibronic transitions that are highly dependent on spin ($| < \phi'_s|\phi_s > |^2$) and electronic ($| < \phi_F|\mu_e|\phi_I > |^2$) selection rules. For example, singlet-triplet transitions are much less likely than singlet-singlet transitions. This gives rise to multi-peaks absorption spectra with Franck-Condon progressions [18, 19, 20] such as depicted in Figure 1.8. Incident photons of varying wavelength may have sufficient energy to populate higher excited states than the first excited state.

Those closely spaced vibrational energy levels as well as the thermal motion allow a broad range of photon energies to match a particular electronic transition, leading to continuum absorption and emission spectra. The black curves in Figure 1.8 represent the broadening of the transitions in liquid and solid states.

Combination of monomers into a conjugated macromolecule such as a conjugated polymer leads to changes in both absorption and emission, mainly shift of the spectra bands. Packing of different molecules into closely packed structures where electronic states are affected by the neighbouring molecules leads likewise to shift of the spectra band. For example, in the case of strong-coupling when the exciton transfer time is much shorter than the vibrational relaxation (delocalisation of the wavefunction along the backbone of the polymer), the polymer absorption peak is shifted from the monomer absorption peak, which is, thus, manifested only as a shoulder [17].

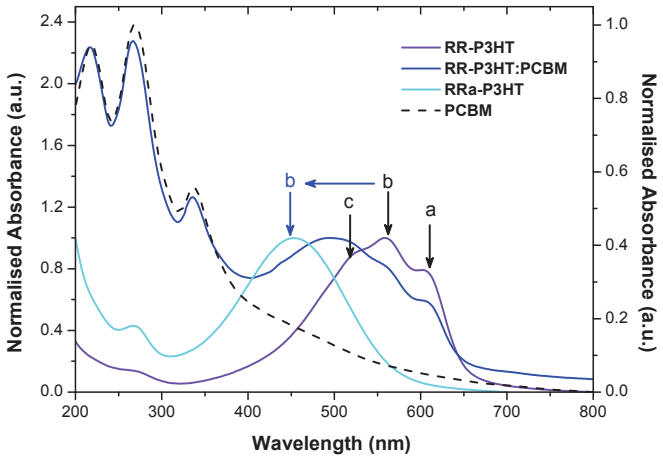


Figure 1.9: Measured absorbance of regioregular (RR) P3HT, regiorandom (RRa) P3HT, PCBM and blend of P3HT:PCBM (1:1 ratio in weight)

Typical absorption spectra for P3HT, PCBM and P3HT:PCBM films are plotted in Figure 1.9. The absorption spectrum of regioregular (RR) P3HT is well structured with pronounced 0-0, 0-1 and 0-2 vibronic progressions at 610, 560 and 520 nm (a, b and c in Figure 1.9 respectively). The regiorandom (RRa) P3HT is broader, less structured and is blue-shifted with respect to the RR-P3HT spectrum. This blue-shift is usually attributed to the localisation of the exciton wavefunction, due to the breaking of the conjugation length by the defects of RRa-P3HT, that leads to an increase in the exciton energy. The distribution of the conjugation lengths is not only centred around a lower value but also broader in RRa-P3HT. That leads to a larger number of possible electronic transitions and thus, to a broader spectrum. The increase in intensity of the 610 nm feature is usually attributed to more ordering of P3HT, or in other words linked with P3HT crystallisation.

1.2.1.3 Emission and competing processes

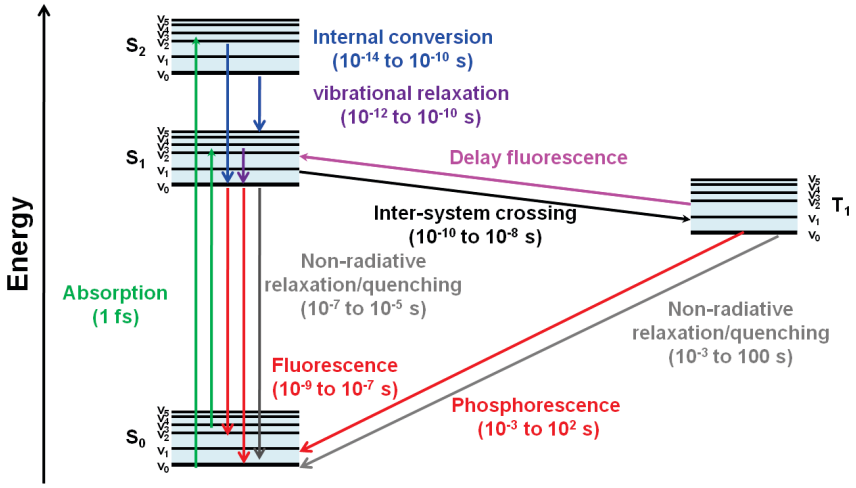


Figure 1.10: Jablonski energy diagram illustrating the different possible transition between the electronic states of a single molecule (the timescale of each process is given in brackets). S_0 is the electronic ground state of the molecule. S_1 and S_2 are two excited singlet states of the molecule. T_1 is one triplet excited states of the molecule. V_0 to V_5 are the vibrational levels of both ground and excited states [17].

After the absorption of a photon, several processes will occur with varying probabilities and time-scales (see Figure 1.10). The most likely will be the relaxation to the lowest vibrational energy level of the first excited state: vibrational relaxation that can be preceded by internal conversion[3]. These processes occur within a picosecond. An excited molecule exists in that lowest excited singlet state for periods of the order of a nanosecond before finally relaxing to the ground state either radiatively (fluorescence) or non-radiatively [17].

Due to the rapid decay to the lowest vibrational energy level of the first excited state and the fact that transitions to higher vibrational energy levels of the ground state are allowed, the energies associated with fluorescence transitions are typically lower than those associated with absorption. Thus, emission spectra are usually shifted to longer wavelengths, Stokes shift (see Figure 1.11)[17].

Several other relaxation pathways compete with fluorescence. The excited state energy can decay non-radiatively, the excited molecule can transfer its energy to excite a neighbouring similar molecule (exciton transport) or transfer a charge to an acceptor

[3]Vibronic transition from a high energy state to a lower energy state without emission of photons. The difference in energy is absorbed into the vibrational modes of the molecule and results in heat generation.

molecule, or intersystem crossing to the lowest excited triplet state can occur. Intersystem crossing can result either in emission of a photon through phosphorescence or a transition back to the excited singlet state that yields delayed fluorescence (see Figures 1.10). Note that these processes are not necessarily first order processes [17].

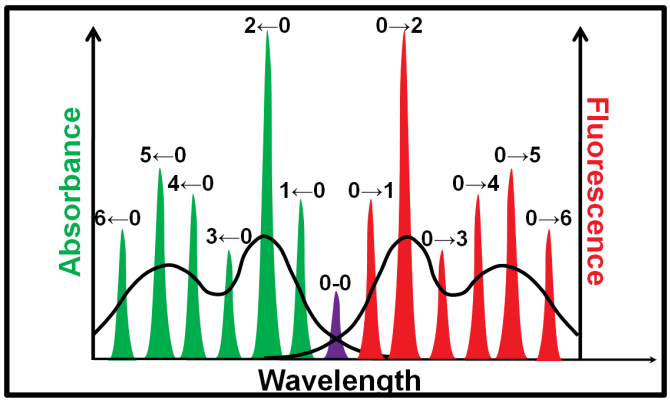


Figure 1.11: Theoretical absorption and photoluminescence spectra with Franck-Condon progressions (green and red peaks). The black curves represent the broadening of the transitions that occurs in liquid and solid states.

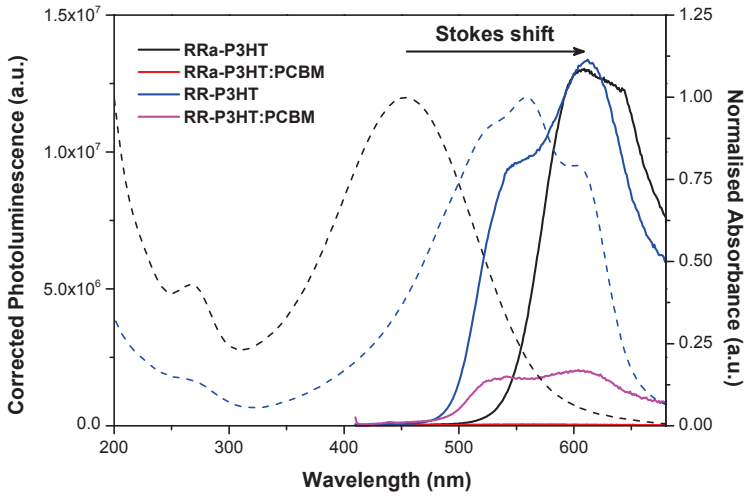


Figure 1.12: Photoluminescence spectra of regioregular (RR) P3HT, regiorandom (RRa) P3HT and blends of P3HT:PCBM (1:1 ratio in weight). The spectra have been corrected by the absorbance of the sample at the excited wavelength: 450 nm for the samples with RRa-P3HT and 510 nm for the samples with RR-P3HT. The dotted curves are the absorption spectra of RRa-P3HT (black) and RR-P3HT (blue).

In Figure 1.12, emission spectra of RRa- and RR-P3HT and blends of these materials with PCBM are plotted. As for the absorption spectra, the emission spectrum of RR-P3HT is red-shifted and more structured in comparison with the one of RRa-P3HT. The addition of PCBM quenches significantly the polymer emission in both cases.

1.2.2 Organic solar cell working principle

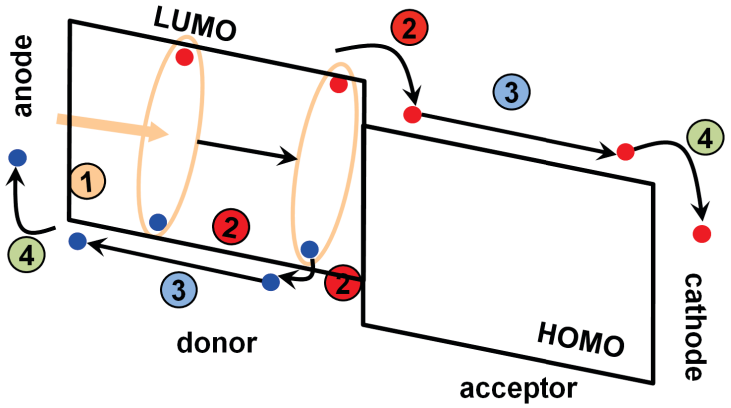


Figure 1.13: Band diagram of an organic solar cell depicting the different steps involved in the light conversion to electricity: (1) exciton photogeneration, (2) exciton diffusion and dissociation, (3) charge transport and (4) charge collection.

1.2.2.1 Exciton dissociation

Excitons carry energy but no net charges. Therefore, they need to be dissociated. Dissociation of excitons is known to occur when introducing a second material that has a higher affinity for electrons the electron acceptor, typically a fullerene derivative (heterojunction concept) [21, 22]. The conjugated polymer is then referred to as the donor material. Before dissociation can take place, a singlet exciton needs to diffuse to such heterojunctions. Exciton diffusion is known to occur via Förster resonant energy transfer (FRET) [23]. The exciton diffusion length, typically around 10 nm, is significantly shorter than the absorption length of usual conjugated polymers (around 100 nm). This reduces the photoactive region of a bilayer solar cell to a

thin layer of about 10 nm around the heterojunction and thus limits drastically the external quantum efficiency [4]. To overcome this issue, the bulk heterojunction concept was introduced [24, 25, 26] where the acceptor is more or less dispersed in the donor matrix. If the length scale of such blend is smaller than the exciton diffusion length, almost no singlet exciton recombination is expected.

When an exciton reaches an heterojunction (or is photogenerated next to such heterojunction), the exciton feels a different environment than in the bulk material. This interfacial influence leads in favourable case to a partial transfer of the excitation to the other type of molecule and the exciton is referred to as an exciplex [27, 28].

Since most of the light is absorbed by the conjugated polymer, the singlet excitons are more likely to be photogenerated within the donor phase. Therefore, the bound electron of such singlet exciton can be transferred from the donor conjugated polymer segment to the fullerene molecule or the exciton can be transferred to the acceptor, this step being followed by a subsequent hole transfer to the donor. Some light is still absorbed by the fullerene and the opposite process can also occur [29, 30, 129, 32]. This charge transfer is reported to be extremely fast, on the order of tens of femtoseconds. The result of this charge transfer is a negative polaron on the acceptor and a positive polaron on the donor. The partly separated charges are still held by Coulombic forces, but the binding energy is lower than the one involved in Frenkel exciton, by an amount equal to the gain in free energy. This polaron pair is called charge transfer (CT) complex[5] and is the intermediate step from an exciton into a pair of free polarons [34].

CT complex emissions have been observed by photothermal deflection spectroscopy [35], photoluminescence spectroscopy [35, 36, 37, 163], Fourier-transform photocurrent spectroscopy [39] and electroluminescence spectroscopy [163, 40] in different polymer:fullerene blends such as polyfluorene:PCBM blends [35, 36], PPVs:PCBM [37, 39] and P3HT:PCBM [39]. Benson *et al.* [35] found a correlation between efficient photocurrent generation and emission of the CT state, suggesting that the CT state may be involved in the charge separation process. Moreover, Hallermann *et al.* [37] found a binding energy of about 130 meV for the CT state in MDMO-PPV:PCBM blends, which is four times smaller than the exciton binding energy in pristine MDMO-PPV further supporting the idea that the CT state is involved in the charge separation process. Moreover, Hallermann *et al.* [37] showed that the CT state can be directly excited below the bandgap of the polymer, suggesting that the

[4] Ratio of the number of charge carriers collected to the number of photons of a given energy shining on the solar cell

[5] An exciplex can generally be regarded as a hybrid state with partly CT character and a certain fraction of a local excitation on one (or both) molecules of the donor-acceptor system [33].

formation of a CT state results from a ground-state interaction between the polymer and the fullerene molecules. Panda *et al.* [41] showed that the energy of the CT absorption bands observed in solution correlates with the electrochemical oxidation potential of the π-conjugated donor and the reduction potential of the acceptor.

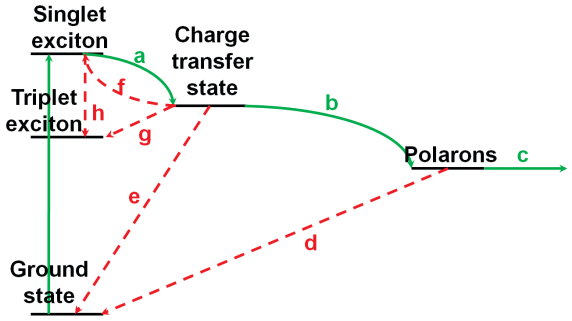


Figure 1.14: State diagram illustrating the key processes of exciton dissociation into polarons: a) singlet exciton dissociation into CT state, b) CT state dissociation into polarons, c) charge transport, d) bimolecular recombination of polarons, e) geminate recombination to ground state, f) regeneration of singlet exciton, g) electron back transfer to triplet exciton and h) inter-system crossing [42].

Excitons dissociate into CT complexes only at energetically favourable donor-acceptor interface, providing that the free energy difference is large enough. This difference in free energy is usually described as the energy offset between the lower unoccupied molecular orbital (LUMO) of the donor and the LUMO of the acceptor for an electron transfer and between the higher occupied molecular orbitals (HOMOs) of the acceptor and donor for an hole transfer. However, LUMOs and HOMOs represent energy levels of uncharged molecules and thus do not describe charged molecules and cannot be related directly to optical transitions. Therefore, a more correct way to describe this free energy difference is to describe it by the energetic difference between the exciplex state and the CT state (this is even more realistic due to the energetic disorder of organic semiconductors and the different possible nature of interfaces in a polymer-fullerene blend) (see Figure 1.14). An additional driving force is still required to separate this CT state into free polarons.

1.2.2.2 Charge transfer complex dissociation

A commonly used model for considering the separation of CT complexes into two free polarons is the Braun-Onsager model [43, 44]. This is used to calculate the escape yield of a coulombically bound pair of polarons of opposite charge. Within the framework of that model, the CT complex can either geminately recombine (monomolecular process) or being dissociated to free polarons with a rate depending on the free po-

laron mobilities, the initial CT complex radius, the Coulomb binding energy of the CT complex, the thermal energy and the built-in electric field of the solar cell. The geminate recombination of the CT complex may result in exciplex emission [45]. The possibility that free polarons can meet to generate bound polaron pairs is also taken into account. This means that CT complexes are also an intermediate step in free polaron recombinations.

If the Braun-Onsager model takes into account the geminate recombination of the CT complex, undesirable CT complex recombinations can also occur by regeneration of the singlet exciton and give delayed photoluminescence or by an electron back transfer from the acceptor to a triplet exciton state [46, 47, 48, 42] (see Figure 1.14).

1.2.2.3 Alternative exciton dissociation model: long-distance exciton dissociation

A new approach involving long-distance exciton dissociation has been recently proposed. It assumes that photoexcitation leads directly to relatively delocalised coulombically bound charges. The proposed mechanism involved in such long-distance exciton dissociation is the tunnelling of the bound electron from the donor to the acceptor. The rate of tunnelling is determined by the electronic coupling, which depends on the involved electronic states of the donor and acceptor and their spatial separation R_{DA}. According to quantum mechanics, the rate of tunnelling of an electron k_T through a rectangular barrier with a height ΔE and a width R is given by:

$$k_T \propto exp(-\frac{2}{\hbar}\sqrt{2m_e\Delta E}R) \tag{1.7}$$

where m_e is the mass of an electron and $\hbar$ the reduced Planck constant. By analogy, the rate of exciton dissociation k_{ED} by electron tunnelling from the donor to the acceptor can be expressed as following:

$$k_{ED} \propto exp(-\beta R_{DA}) \tag{1.8}$$

where β is an attenuation factor that depends on the energy difference between the initial state of the donor and the final state of the acceptor. Caruso *et al.* calculated this rate k_{ED} as a function of R_{DA} for values of β ranging from 0.2 $Å^{-1}$ to 0.6 $Å^{-1}$ [49]. This range of β values was selected in agreement with experimental work on donor-bridge-acceptor molecules. The calculated exciton dissociation rates are

varying from $\sim 10^2$ s^{-1} and $\sim 10^9$ s^{-1} at $R_{DA} = 60$Å for $\beta = 0.6$ Å^{-1} and $\beta = 0.2$ Å^{-1} respectively to $\sim 10^{12}$ s^{-1} at R_{DA}= 3.5 Å. Then, they calculated the exciton dissociation probability density as a function of R_{DA} for the different β values using a kinetic model where the exciton can either dissociate with the rate k_{ED}, hope to the neighbouring lattice site with the rate k_{HO} or decay to the ground state with the rate k_R. k_{OH} was taken equal to $\sim 10^{11} - 10^{12}$ s^{-1} since the exciton diffusion coefficient in P3HT has been previously estimated to be $\sim 10^{-8} - 10^{-7}$ $m^2.s^{-1}$ [6]. k_R has been set to $2.5 * 10^9$ s^{-1}, as determined from the exciton lifetime measured in P3HT. They found according to this model that exciton dissociation tens of angstroms (from $\sim$ 10Å to $\sim$ 30Å for β values between 0.6 and 0.2 Å^{-1}) away from the heterojunction is kinetically favoured. The efficiency of such mechanism depends on the activation energy for tunnelling and the wavefunction extent, which are highly affected by the energy levels of both materials. Within the framework of that theory, CT states are not any longer an intermediate step for charge separation but only for charge recombination [49].

1.2.2.4 Charge carrier transport

Finally, when the free polarons are generated by either short-range or long-range exciton dissociation, they still need to travel to the respective electrodes where they will be available for injection into an external circuit. Due to the weak electronic interaction between conjugated segments or molecules, the electrical transport mostly takes place by hopping along conjugated segments or between molecules. Moreover, the disorder in molecular packing and in site energies results in a distribution of HOMOs and LUMOs, with lowest lying LUMO energy or highest lying HOMO energy states acting potentially as charge traps. As a result of both the weak electronic interaction and the charge traps, the resulting polaron mobilities are in the range of 10^{-6} to 1 $cm^2.V^{-1}.s^{-1}$. In donor-acceptor solar cells, the donor is mostly hole conducting, whereas the acceptor transport electrons. Although, conjugated polymers are known to exhibit ambipolar charge transport [50]. During the transport of the separated polarons to their respective contacts, charge carrier can recombine non-geminately (a bimolecular or second order process) via formation of a coulombically bound polaron pair [30].

[6] $D_E = k_{HO} * L^2$ where D_E is the exciton diffusion coefficient and L is the lattice site, which is 4 Å in this case.

1.2.3 Band gap engineering for highly efficient organic solar cells: the microstructure bottleneck

1.2.3.1 Band gap engineering

Only photons which have higher energies than the bandgap of a semiconductor can lead to exciton formation. Because most organic semiconductors exhibit bandgaps higher than 2.0 eV, the possible absorption in an organic solar cell is limited to about 30% of solar radiation. Fortunately, the absorption coefficient of organic materials is generally high (higher than $10^7\ m^{-1}$) so that only about 100 nm are necessary to absorb around 60% of the possible absorbed light [51]. Thus, because most of the light is absorbed by the polymer, it should be possible to enhance light harvesting and thus the photocurrent by engineering the band-gap of the conjugated polymer. This can be achieved by designing so-called low-bandgap polymers (polymer with bandgap lower than 1.5 eV) [52]. However, the energy levels of the donor-acceptor couple should remain sufficiently adjusted to maximise the generation of free charges. Designing new fullerene derivatives [53] or in general new acceptors such as: oligothiophene-S,S-dioxide based acceptors, cyano-based acceptors, 2-vinyl-4,5-dicyanoimidazole based acceptors, diketopyrrolopyrole-based acceptors, coploymers consisting of fluorene and bis-(thienyl)benzothidiazole [54], ... to decrease the energy losses during exciton dissociation is another option.

1.2.3.2 The microstructure bottleneck

However, electronic interactions between donor and acceptor are not sufficient to explain every aspect of organic solar cells. For example, arguments based only on electronic interactions fail to explain the influence of donor-acceptor ratios on device performance. As an illustration, the optimal weight ratio for P3HT:PCBM solar cell is 1.25:1 when it is 1:4 for solar cells based on poly(2-methoxy-5-(3',7'-dimethyloctyloxy))-p-pheylene vinylene (MDMO-PPV) blended with PCBM [129]. Due to P3HT broader absorption spectrum and above all the larger polymer content at the optimal ratio for P3HT:PCBM, P3HT:PCBM solar cells exhibit a nearly two times higher short circuit current than MDMO-PPV:PCBM solar cells [129]. This difference in optimal ratio, which has a huge impact on the solar cell performance as seen, is believed to be linked rather with the physical interaction than with the electronic interaction of the donor and acceptor components.

Characterisation techniques such as Transmission Electron Microscopy (TEM) in com-

bination with Selected Area Electron Diffraction (SAED) [55, 56], Scanning Electron Microscopy (SEM), electron tomography [57], Atomic Force Microscopy (AFM), Kelvin probe force microscopy [58], Nuclear Magnetic Resonance (NMR) [59] and Scanning Near Field Optical Microscopy (SNOM) [60] have been used to characterise the microstructure created by taking advantage of polymer and fullerene tendency to demix or, in other words, the tendency of the phases to separate. This phase separation seems at first to be a very attractive feature of polymer-fullerene blends. However, during this phase separation process, either domains that are too large for efficient exciton dissociation or insufficient percolation of electron and hole conducting phases is usually observed.

In fact, as mentioned earlier the length scale of the blend should be of similar magnitude to the exciton diffusion length to get efficient charge generation. However, the charge carrier transport in bulk heterojunction can be less efficient than in bilayer solar cells because of: firstly, a lack of donor and/or acceptor phase continuity that can lead to an increase in polaron recombination due to bipolar transport; secondly, the acceptor presence in the donor matrix that can in some cases hamper the donor crystallisation, which leads often to reduced charge mobilities and finally, the unselective contacts between the donor/acceptor with the cathode/anode that can lead to charge piling up at the metal-organic interface increasing the charge recombination rate.

As a conclusion, understanding the crystallisation and phase separation of such blend is important in order to control the degree of phase separation and connectivity of the different phases; thus, optimising the exciton dissociation and charge transport.

In the previous section, we first reviewed the semiconductor properties of organic conjugated materials. Their semiconductor properties originate from the sp^2 hybridisation of carbon atoms. The sp^2 hybrid orbitals highly overlap to form σ-bonds while the remaining pure p_z orbitals weakly overlap to form π-bonds. A π-orbital forms the highest occupied molecular orbital (HOMO) and a π^*-orbital forms the lowest unoccupied molecular orbital (LUMO). In such materials, absorption of light leads to the formation of Frenkel singlet excitons. Because the energy level of the molecules are defined by electronic and vibrational quantum numbers, absorption and fluorescence spectra are multi-peaks spectra with vibronic Frank-Condon progressions. Fluorescence spectra are shifted to lower energy in comparison to absorption spectra (Stokes shift). Additional broadening processes results in more featureless spectra than predicted by Frank-Condon principle. Several processes (not necessarily first order processes) compete with fluorescence with different probabilities and time-scales.

Then, we presented the working principle of organic solar cells. Since Frenkel excitons carry energy but not net charges, they need to be dissociated. Exciton dissociation is known to occur at donor (conjugated polymer) - acceptor (fullerene) interfaces. First, excitons need to diffuse to an heterojunction. The exciton diffusion length of about 10 nm limits the active part of the solar cell to layers of about 10 nm around an heterojunction. Taking advantage of the tendency of polymer and fullerene to demix, the bulk heterojunction concept has been introduced to maximise the interfacial surface between polymer and fullerene. When an exciton reaches an heterojunction, the bound electron in singlet exciton is transferred to the acceptor molecule providing the the free energy difference ($\simeq LUMO_D - HOMO_A$) is large enough. This electron transfer results in a negative polaron on the acceptor molecule and a positive polaron in the donor molecule coulombically bound in a charge transfer (CT) complex. The dissociation of the CT complex into free polarons depends on the polaron mobilities, the CT complex radius and Coulomb binding energy and the built-in electric field of the cell. Those exciton dissociation steps compete with the relaxation of either the exciton or the CT state to the ground state and electron-back transfers to the triplet exciton state. Finally, the transport of the free polarons to the electrode takes place through hopping from one molecule to another. Energetic disorder results in traps that may act as recombination centres for the free polarons.

Finally, we have highlighted the fact that some aspect of organic solar cells are rather linked to physical interactions of donor and acceptor than electronic interactions. Microstructure features such as length scale of the blend and continuity of the donor and acceptor phases are relevant to efficient charge generation and efficient charge transport respectively. In the next section, we will describe the microstructure development of polymer-fullerene blends.

Section 1.3

Microstructure development

As illustrated in the previous chapter, phase separation is a very attractive feature of polymer-fullerene blends but a stable controlled phase separation has to be achieved. Thus, a better understanding of the phase separation mechanism is required. In this section, the states of soft matter are described including the theory of crystallisation. Thus, the theory of miscibility and phase separation is reviewed. Finally, the implications of crystallisation, miscibility, phase separation and thermodynamic ageing on solar cell performances are highlighted.

1.3.1 Soft matter states

The σ- and the π-bonds of organic semiconducting materials are saturated, so that these molecules cannot form any additional covalent bonds to other molecules or atoms. Therefore, organic semiconducting materials can only be bound by intermolecular interactions. Intermolecular interactions or forces can be separated into four major contributions:

1. Repulsive interactions as a consequence of the Pauli exclusion principle
2. Attractive and repulsive electrostatic interactions between permanent multipoles
3. Polarisation: attractive interactions between a permanent dipole on one molecule and an induced dipole on another molecule
4. Dispersion: attractive interactions of instantaneous dipoles

Those intermolecular interaction energies, often referred to as van der Waals interactions are typically small and of the order of magnitude of the thermal energy. Thus, organic semiconducting materials tend to form weakly bonded, disordered solids.

In the solid state, some materials are amorphous glass. This glass is characterised by

configurational disorder and possibly entanglement [7] for polymers depending on their molecular weight and polydispersity. By increasing the temperature, such amorphous materials undergo a transition from a rigid solid, the glass to a more flexible rubbery material. The temperature at which this transition occurs is called the glass transition temperature (T_g) and it marks the onset of segmental motion (see Figure 1.15). The glass transition is not a first-order process since there is no associated entropic discontinuity [61, 62].

Most organic semiconductors are semi-crystalline, consisting of small crystalline regions embedded in a glassy phase. In such semi-crystalline materials, glass transition, crystallisation and melting can be observed since both amorphous and crystalline domains co-exist. The melting temperature (T_m) lies above the glass transition temperature (see Figure 1.15). Crystallisation occurs at a temperature (T_c) that lies between the glass transition and the melting temperatures (see Figure 1.15) [61, 62].

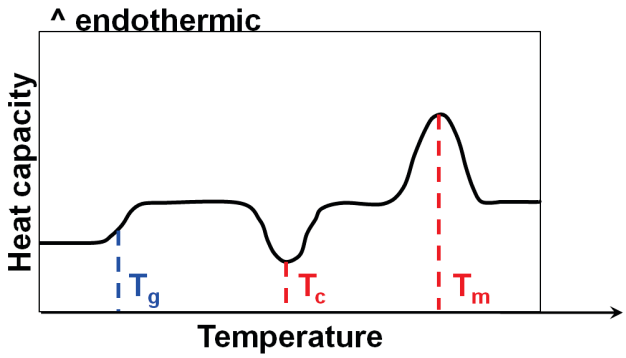


Figure 1.15: Theoretical heat capacity as a function of temperature of semi-crystalline materials featuring the glass transition temperature (T_g), the crystallisation temperature (T_c) and the melting temperature (T_m). Crystallisation and melting are second order transitons and thus, the heat capacity is discontinuous at the crystallisation and melting temperatures. Crystallisation is an exothermic process while melting is an endothermic process. The glass transition is a second order process. Thus, the heat capacity is continuous but its derivative is discontinuous.

1.3.1.1 Soft matter crystallisation

Nucleation Theoretically, nucleation of crystallites may occur homogeneously or heterogeneously. The creation of a nucleus implies the formation of an interface which costs energy due to surface tension σ. This energy cost can be counter-balanced by

[7] Entanglement is the topological restriction of molecular motion by other chains.

the energy gain of creating new volume in the case that supersaturation [8] is reached. For example, for a spherical cluster, the free energy difference can be expressed as in Equation 1.9 where ΔG_V is the change in free energy per unit volume. When the radius of such cluster becomes larger than $r^* = \frac{2\sigma}{|\Delta G_V|}$, nucleation becomes favoured and cluster growth is no longer limited by nucleation (see Figure 1.16) [61, 62].

$$\Delta G = -\frac{4}{3}\pi r^3 |\Delta G_V| + 4\pi r^2 \sigma \tag{1.9}$$

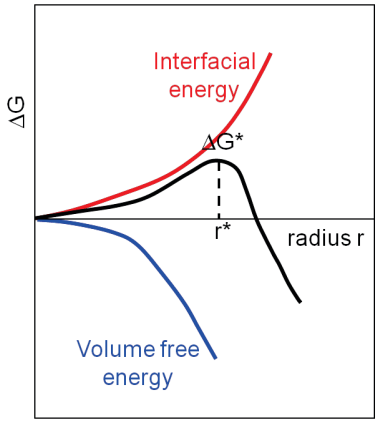


Figure 1.16: Free energy difference as a function of the nucleus radius.

Supersaturation can be reached by supercooling. At the melting temperature, ΔG_V is zero so $\Delta S_V = \frac{\Delta H_V}{T_m}$ (because $\Delta G_V = \Delta H_V - T\Delta S_V$). Thus, by defining the supercooling as $\Delta T = T_m - T$, the critical radius and the free energy required to reach this critical radius can be expressed as in Equations 1.10 and 1.11. Increasing the supercooling then lowers the energy barrier that needs to be overcome to favour nucleation and decreases as well the critical radius [61, 62].

$$r^* = \frac{2\sigma T_m}{|\Delta H_V|}\frac{1}{\Delta T} \tag{1.10}$$

$$\Delta G^* = \frac{16\pi\sigma^3 T_m^2}{3\Delta H_V^2}\frac{1}{\Delta T^2} \tag{1.11}$$

[8] An unstable system which has a greater concentration of a material in solution than would exist at equilibrium is said to be supersaturated

In most systems however, heterogeneous nucleation occurs preferentially. Nucleation in that case occurs at preferential sites such as phase boundaries, dust, defects ... Surfaces promote nucleation because of wetting and thus, the free energy needed for heterogeneous nucleation is given by Equation 1.12 where $f(\theta)$ is a function of the contact angle θ (see Figure 1.17) and is given by the Equation 1.13. The critical radius remains unchanged. However, the energy barrier is more or less reduced depending on the wetting ability of the preferential site [61].

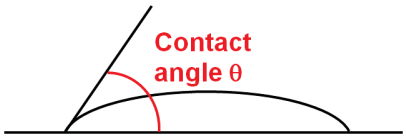


Figure 1.17: Schematic of a liquid drop showing the contact angle θ.

$$\Delta G_{heterogeneous} = \Delta G_{homogeneous} * f(\theta) \tag{1.12}$$

$$f(\theta) = \frac{1}{2} - \frac{3}{4}cos(\theta) + \frac{1}{4}cos^3(\theta) \tag{1.13}$$

Rate of nucleation The energy barrier defined in the previous subsection is the barrier that determines the kinetics of nucleation. Thus, the nucleation rate k_N is given by Equation 1.14 where ΔG^* is defined as above, k_B is the Boltzmann constant, T the temperature, T_m the melting temperature and $\Delta T = T_m - T$ the supercooling (see Figure 1.18) [61, 62].

$$\begin{aligned} k_N &\propto \exp\left(\frac{-\Delta G^*}{k_B T}\right) \\ &\propto \exp\left(-A\frac{1}{k_B T}\frac{T_m^2}{\Delta T^2}\right) \\ &\propto \exp\left(-A\frac{1}{k_B T}\frac{T_m^2}{(T_m - T)^2}\right) \end{aligned} \tag{1.14}$$

Rate of crystal growth The crystal growth rate, k_G is governed by two factors; (i) the formation rate of primary and secondary nuclei or nucleation rate k_N and (ii) the diffusion of molecules to the cluster d. The diffusion of molecules can be expressed as in Equation 1.15 where E_a^t is the activation energy for transport of molecules (it depends on the glass transition T_g) and thus, the crystallisation rate may be described by the Equation 1.16. As a result, the crystal growth rate looks like a bell curve distribution with the maximum lying at a temperature between the

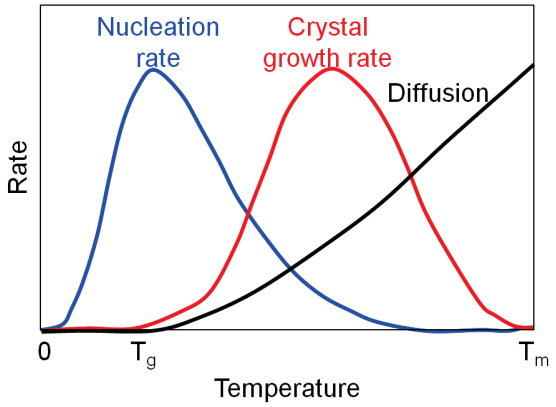


Figure 1.18: Nucleation and crystal growth rates as a function of the temperature.

melting and glass transition temperatures (see Figure 1.18) [61, 62].

$$d \propto \exp\left(\frac{-E_a^t}{k_B T}\right) \tag{1.15}$$

$$\begin{aligned} k_G &= k_N * d \\ &\propto \exp\left(-A\frac{1}{k_B T}\frac{T_m^2}{\Delta T^2}\right)\exp\left(\frac{-E_a^t}{k_B T}\right) \end{aligned} \tag{1.16}$$

1.3.1.2 Polymer Crystallisation

Under common crystallisation conditions, polymers crystallise in the form of lamellae (see Figure 1.19). Therefore, lamellae are commonly considered as the fundamental unit of a polymer crystal. Because the thickness of these lamellae is much smaller than the polymer chain length, individual chains may fold back into the same lamella or participate in close lamellae as well as be involved in the amorphous region (chain-folded lamella model). Once formed, chain-folded lamellae can be organised in larger structures known as spherulites. A spherulite consists of sheets of lamellae emerging from a central nucleus (see Figure 1.19). It can grow to millimetres in size [61, 62].

Even though the free energy is reduced by forming lamellae, lamellae cannot be the crystal equilibrium structure of polymer due to the disorder at the lamella surface. The ideal thermodynamic crystal structure would rather consist of fully extended chains packed together. This contrast between the observation and the theory can be explained by on the one hand, the irregularity of polymers and the weak intermolecular interactions and on the other hand, by the crystallisation of macromolecules being more likely determined by kinetics than by thermodynamics. In fact, due to their

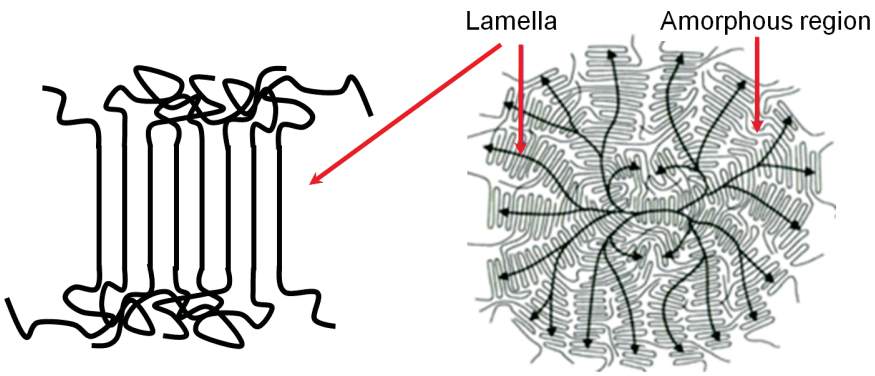


Figure 1.19: Scheme of a polymer lamella and of a spherulite [63].

length, polymers are very viscous (they can be entangled as well) and thus, suffer from low diffusion rates. The probability that a chain will fully extend is then very low, decreasing drastically the crystal growth rate. Therefore, the crystal growth is kinetically favoured for rather small lamella thickness. However, for small lamella thickness, the amount of interface increases thus reducing the gain in free energy. Consequently, the critical lamella thickness results from a compromise between thermodynamically stable and kinetically favoured [61].

However, since larger crystals are more thermodynamically favoured, the system will continue to evolve very slowly through coalescence and Ostwald ripening. This phenomenon is called thermodynamic coarsening [64].

1.3.2 Miscibility

Miscibility refers to the capability of a mixture to form a single phase [9] over certain ranges of temperature, pressure and composition [66].

[9] A phase is an entity of a material system which is uniform in chemical composition and physical state [65].

1.3.2.1 Thermodynamics: Gibbs free energy of mixing

A usual quantity used to describe the thermodynamics of a mixture is the *Gibbs free energy of mixing* ΔG_{mix}. It determines whether mixing at a given temperature T and given pressure is a spontaneous process. It depends on the enthalpy of mixing ΔH_{mix} and the entropy of mixing ΔS_{mix} (see Equation 1.17) [67, 68, 62].

$$\Delta G_{mix} = \Delta H_{mix} - T\Delta S_{mix} \tag{1.17}$$

1.3.2.2 Flory-Huggins formalism

Flory and Huggins derived mathematically the Gibbs free energy associated with mixing polymers - or random walk chains - and small molecules on an incompressible lattice (see Figure 1.20). To take into account the dis-symmetry in molecular sizes, they assumed that individual small molecules or individual polymer segments occupy sites on the lattice. Thus, the total number of sites N is given by equation 1.18 where N_1 is the number of small molecules and N_2 the number of polymer chains, each of which possesses x segments [10] [67, 62].

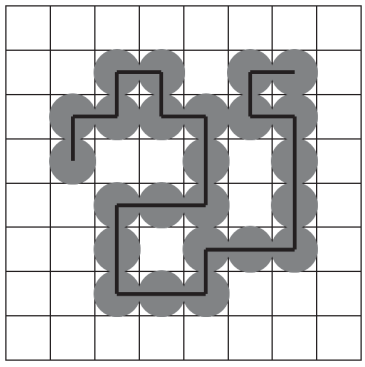


Figure 1.20: A random walk chain on an incompressible lattice.

$$N = N_1 + xN_2 \tag{1.18}$$

According to statistical mechanics, the entropy of mixing can be expressed following equation 1.19 where k_B is the Boltzmann constant and Ω is the number of possible molecular arrangements on the lattice and is given by equation 1.20. Giving the

[10] A segment can be smaller or larger than a monomer.

Stirling approximation, the entropy of mixing can be rewritten as in equation 1.21 where ϕ_1 and ϕ_2 are the lattice volume fractions of the small molecules and polymer chain segments respectively [67, 62].

$$\Delta S_{mix} = k_B ln\Omega \tag{1.19}$$

$$\Omega = \frac{N!}{N_1! x N_2!} \tag{1.20}$$

$$\begin{aligned} \Delta S_{mix} &= -k_B[N_1 ln(\frac{N_1}{N}) + xN_2 ln(\frac{xN_2}{N})] \\ &= -k_B(N_1 ln\phi_1 + xN_2 ln\phi_2) \end{aligned} \tag{1.21}$$

The enthalpy of mixing is a measure of the change in energy. Thus, it can be expressed by taking into account the molecular interactions at each lattice point. There are three possible molecular interactions: small molecule-small molecule, polymer segment-polymer segment and small molecule-polymer segment. Thus, the increase in energy per small molecule-polymer segment contact $\Delta\epsilon$ is given by equation 1.22, where ϵ_{ij} is the contact energy between segment i and segment j, and the enthalpy of mixing ΔH_{mix} can be expressed as the energy change per small molecule-polymer segment interactions (equation 1.23) where z is the coordination number [67, 62].

$$\Delta\epsilon = \epsilon_{12} - \frac{1}{2}(\epsilon_{11} + \epsilon_{22}) \tag{1.22}$$

$$\begin{aligned} \Delta H_{mix} &= xN_2 z\phi_1 \Delta\epsilon \\ &= N_1 z\phi_2 \Delta\epsilon \end{aligned} \tag{1.23}$$

Thus, a conjugated polymer-small molecule interaction parameter χ can be defined as in Equation 1.24 and the enthalpy of mixing ΔH_{mix} can be rewritten as in Equation 1.25. The Gibbs free energy of mixing is then given by Equation 1.26 where R is the gas constant and n the total number of moles of the system [67, 62].

$$\chi = \frac{z\Delta\epsilon}{k_B T} \tag{1.24}$$

$$\Delta H_{mix} = k_B T \chi x N_2 \phi_1 \tag{1.25}$$

$$\Delta G_{mix} = nRT[\chi \phi_1 \phi_2 + \phi_1 ln(\phi_1) + \phi_2 ln(\phi_2)] \tag{1.26}$$

At pressure constant, the Gibbs free energy of mixing depends mainly on the concentration ϕ, the temperature T and the interaction parameter χ. So far we have considered the mixing of components 1 and 2. In the next section, we will consider the coexistence of two phases a and b where a is a solid solution with 2 acting as the solute in a matrix of 1 and b is also a solid solution with 1 acting as the solute in a matrix of 2.

1.3.3 Phase separation

We have to consider open systems which are able to exchange matter with their surroundings. Taking a binary system for simplicity, the Gibbs free energy can be expressed as Equation 1.27 where n_i is the amount in moles of the component i and μ_i its chemical potential [67, 68, 62].

$$dG = -SdT + VdP + \mu_1 dn_1 + \mu_2 dn_2 \tag{1.27}$$

1.3.3.1 Phase equilibrium

If now we consider two different phases (denoted a and b), each containing the same two components and in direct contact with each other, each phase is still an open system although the two-phase system is closed so $dn_{ia} = -dn_{ib}$. We consider the transfer at constant T and P of dn_1 moles of the first component into phase a from phase b. Thus, the Gibbs free energy of the two-phase system can be written as Equation 1.28 [67, 68, 62].

$$\begin{aligned} dG &= dG_a + dG_b \\ &= \mu_{1a} dn_{1a} + \mu_{1b} dn_{1b} \\ &= (\mu_{1a} - \mu_{1b}) dn_{1a} \end{aligned} \tag{1.28}$$

The condition of equilibrium of two phases is $(dG)_{T,P} \leq 0$. Thus, the equilibrium condition should satisfy $\mu_{1a} = \mu_{1b}$. The Gibbs free energy per mole G_m of the total system at constant T and P is given by Equation 1.29 although in such binaries, $\phi_2 = 1 - \phi_1$. Therefore, we have Equation 1.30. Then, the equilibrium condition can be rewritten as in Equation 1.31 [67, 68, 62].

$$\begin{aligned} dG_m &= \mu_1 d\phi_1 + \mu_2 d\phi_2 \\ &= (\mu_1 - \mu_2) d\phi_1 \end{aligned} \tag{1.29}$$

$$(\frac{\partial G_m}{\partial \phi_1})_{T,P} = \mu_1 - \mu_2 \tag{1.30}$$

$$(\frac{\partial G_m(\phi_{1a})}{\partial \phi_1})_{T,P} = (\frac{\partial G_m(\phi_{1b})}{\partial \phi_1})_{T,P} \tag{1.31}$$

1.3.3.2 Phase behaviour

The theoretical phase diagram of a binary system is plotted in Figure 1.21. The black solid line (called the coexistence curve) corresponds to the solution of Equation 1.32. All homogeneous mixtures below the coexistence curve or in other words within the miscibility gap will separate into two mixed phases with compositions ϕ_{2a} and ϕ_{2b} respectively. However, the stability condition is given by Equation 1.33. The limit of stability is represented in Figure 1.21 by the black dashed line. Homogeneous mixtures lying between this curve and the coexistence curve are thermodynamically metastable and mixtures within the dashed curve are thermodynamically unstable. The upper critical solution temperature (UCST) is defined by Equation 1.34. Above that temperature, the components are miscible in all proportions. The UCST is highly dependent on molecular weight and χ [67, 68, 62].

$$(\frac{\partial \Delta G_{mix}(\phi_{1a})}{\partial \phi_1})_{T,P} = (\frac{\partial \Delta G_{mix}(\phi_{1b})}{\partial \phi_1})_{T,P} \tag{1.32}$$

$$(\frac{\partial^2 \Delta G_{mix}(\phi_{1a})}{\partial \phi_1^2})_{T,P} \geq 0 \tag{1.33}$$

$$(\frac{\partial^3 \Delta G_{mix}(\phi_{1a})}{\partial \phi_1^3})_{T,P} = 0 \tag{1.34}$$

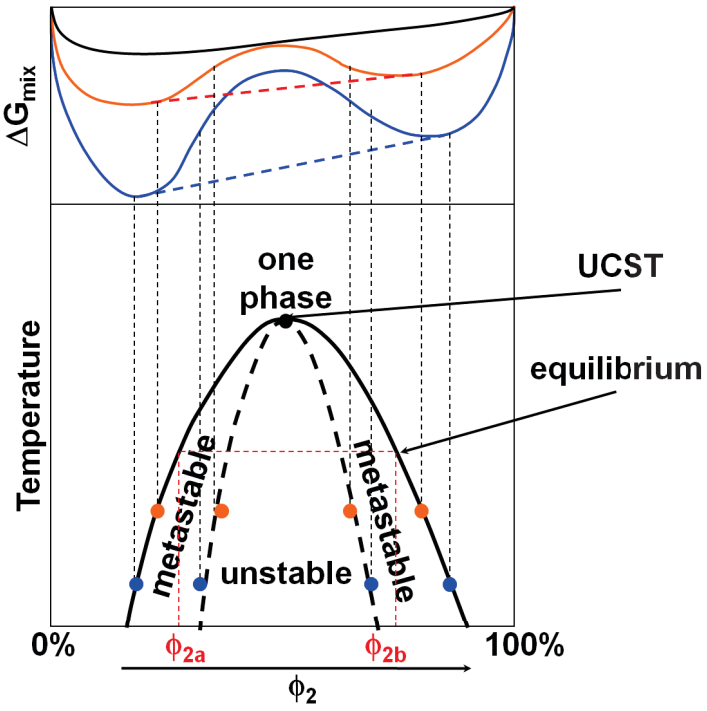


Figure 1.21: Free energy of mixing ΔG_{mix} as a function of composition ϕ_2 at different temperatures T ($T_{blue\ curve} < T_{red\ curve} < T_{black\ curve}$). Phase diagram (temperature as a function of composition ϕ_2) for a binary system in the solid state extracted from ΔG_{mix}. The phase diagram displays a miscibility gap (under the black solid line) separated in a metastable and an unstable region (black dashed line). Outside this miscibility gap, only one phase is present in the system.

To summarise, in the miscibility region, a polymer-fullerene system will form an homogeneous mixture. If the temperature of such mixture is lowered under the UCST, depending on the concentration, it may become either metastable or unstable [1].

[1] " Metastable miscibility refers to the capability of a mixture to exist for an indefinite period of time as a single phase that is separated by a small or zero energy barrier from a thermodynamically more stable multiphase system." [66].

In the case of an unstable blend, the phase separation occurs spontaneously and leads to a finely distributed bi-continuous two-phase microstructure, that coarsens over time driven by the minimisation of interfacial tension through a reduction of interfacial area. This process is known as spinodal decomposition.

If an homogeneous mixture is brought into the metastable region, it will tend to phase separate, but must first overcome a free energy barrier in order to nucleate a new phase. Therefore, the phase separation cannot proceed spontaneously but occurs via nucleation and growth, which is often associated with crystallisation from solution [69]. When the mixture is brought to the metastable region, small nuclei of a minority phase (e.g. of composition ϕ_{2a} in Figure 1.21) develop in time through diffusion from the surrounding homogeneous mixture. Once the surrounding mixture has reached the composition of the second phase (ϕ_{2b} in Figure 1.21), the nuclei will increase in size by firstly coalescing with each other and secondly by Ostwald ripening [70]. The second step occurs slowly in polymers because of their high viscosity. This phase separation process is known as binodal decomposition.

1.3.3.3 Eutectic phase behaviour

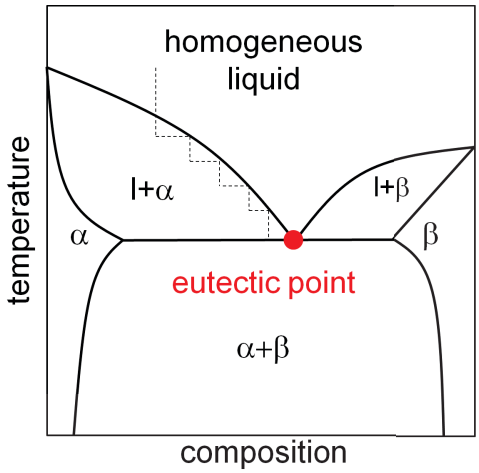


Figure 1.22: Eutectic phase diagram.

Partially immiscible components can exhibit eutectic phase behaviours (Figure 1.22). In such eutectic system, the melting temperatures of both components are depressed and intersect at the eutectic point. Consequently, at this eutectic point defined by a unique set of temperature and blending ratio, both components crystallise simultaneously from the melt leading to an intimately mixed fine-grained blend called the eutectic structure. At hypo- and hyper-eutectic composition, one component crys-

tallises from the melt before the other leading to the formation of primary crystals of this component. While continuing to cool down, the concentration of the melt in that component is decreased following the liquidus line (as shown by the doted lines in Figure 1.22) until at the eutectic temperature, it reaches the eutectic composition. Thus, the same decomposition as going from the melt through the eutectic will happen and the final structure will be composed of primary crystals of the excess component surrounding by an eutectic-like structure. Far from the eutectic composition, solid solutions may be formed [68].

The size of the miscibility gap plays a major role in that overlap. As mentioned previously, its existence and its extent depend on the free energy of mixing, which depends on polymer-fullerene interactions, temperature and composition. In fact, phase separation as seen through Flory-Huggins formalism is thermodynamically favoured if interactions between the fullerene and the polymer are smaller than between fullerenes on the one hand and polymers on the other hand. Favourable intermolecular interactions such as hydrogen bondings between donor and acceptor may restrain the miscibility gap and thus, limit the extent to which the phases separate [69]. In contrast, the tendency of either components to crystallise will enlarge the miscibility gap and thus, increase the tendency of the blend to phase separate.

To summarise, the most common solar organic semiconductor materials are weakly bonded by intermolecular interactions (commonly referred as to van der Waals forces) and tend to form semi-crystalline solids provided that they exhibit sufficient regular molecular structures. These semi-crystalline solids are defined by three transitions associated to transition temperatures: the glass transition (glass transition temperature T_g), melting (melting temperature T_m) and crystallisation (crystallisation temperature T_c). The crystallisation of organic semiconducting materials is highly determined by kinetics: nucleation and growth rates. The fundamental unit of polymer crystallisation is lamellae that can organise in larger structures such as spherulites.

Miscibility of polymer-fullerene blend is thermodynamically described by the Gibbs free energy of mixing ΔG_{mix}. According to Flory-Huggins theory, at pressure constant, the Gibbs free energy of mixing depends mainly on the blend concentration, the temperature and the interaction parameter χ. Phase separation can be favoured if the interactions between polymer and fullerene become smaller than the polymer-polymer and the fullerene-fullerene interactions. Phase separation can occur either spontaneously (spinodal decomposition) or via nucleation and growth (binodal decomposition) when an homogeneous mixture is brought to the miscibility gap. Partially miscible components can form eutectic systems that are characterised by intimately mixed fine-grained blend can form.

In the next section, we will highlight the influence of microstructure on the performances of organic solar cells.

Section 1.4

Influence of microstructure on organic solar cell performances

In the previous section, we reviewed the theory about soft matter crystallisation and phase separation. In this section, we will review the state of understanding of the conjugated polymer:fullerene blend microstructure and the influence of the microstructure on organic solar cell performances.

1.4.1 Microstructure of bulk heterojunction

Mixing [71] and demixing [138] experiments have been used to point out that the miscibility of polymer and fullerene is increasingly favoured as the temperature is increased, opposing on the one hand the belief that phase-pure domains form in bulk heterojuctions because of immiscibility of polymer and fullerene and suggesting on the other hand an upper critical solution temperature (UCST) for such binaries. Thus, the pure phase-discrete interface bulk heterojunction model is not valid and the partial immiscibility of the components leads rather to very complex microstructures with at least three phases: a neat polymer (possibly crystalline) phase, a neat fullerene (possibly crystalline) phase and an amorphous mixture of both (see Figure 1.23).

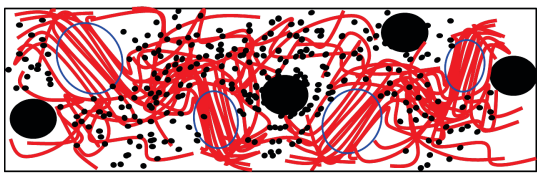


Figure 1.23: Scheme showing the microstructure of a bulk heterojunction . The blue circles show polymer crystallites. The large black spots represent fullerene aggregates or crystallites. The rest is an amorphous mixture of fullerene more or less well dispersed in the amorphous part of the polymer, which may feature liquid-liquid phase separation.

In most systems, the level of mixing within the amorphous part of the polymer is highly influenced by the polymer crystallisation. Because tie chains connect covalently the amorphous and crystalline regions, polymer crystallites become anchors that restrain the swelling of the amorphous part of the polymer due to the penetration of the fullerene within this part (the fullerenes diffuse only within the amorphous region because their enthalpy of mixing is not sufficient to overcome the heat of melting in the crystal) [73]. In some cases such as poly[2,5-bis(3-alkylthiophen-2-yl)thieno(3,2-b)thiophene] (PBTTT), the fullerenes can be accommodated between the side chains of the polymer, leading to co-crystallisation of fullerene and polymer [74].

Müller *et al.* [160] applied differential scanning calorimetry (DSC) on different polymer-fullerene blends to find the nature of the phase diagram of such binaries. They found that all the studied systems (poly(3-alkylthiophenes) (P3ATs) : PCBM blends) are of a simple eutectic nature but, the eutectic composition and temperature vary from one material to another.

Typical mixtures of 1:1 of P3HT:PCBM are below the spinodal derived from DSC [76] so the phase separation is not spontaneous. P3HT crystallisation leads to an increase in fullerene concentration within the amorphous part of P3HT. This bring the amorphous mixture within the spinodal region, resulting in nucleated PCBM crystals that rapidly grow to micrometer sizes from the supersaturated mixed amorphous phase [77]. It was shown by Campoy-Quiles *et al.* [78] that both polymer crystallisation and fullerene diffusion were essential to describe the evolution of the polymer:fullerene blend morphology.

1.4.2 Miscibility effect on solar cell performances

During this phase separation process that leads to the creation of at least three phases, either domains that are too large for efficient exciton dissociation or too small for sufficient percolation of electron and hole conducting phases are commonly observed.

For example, the study conducted by Hoppe *et al.* explains the poor efficiency of MDMO-PPV:PCBM bulk heterojunction solar cells cast from toluene [79] in terms of microstructure. They observed unconnected beads of PCBM hundred-nanometre large embedded in the MDMO-PPV matrix. By changing the solvent from toluene to chlorobenzene, it is possible to reduce drastically the size of the PCBM clusters and

improve the power conversion efficiency [80]. They concluded that, in solar cells cast from toluene, the negative polarons have to travel through a "polymer skin layer" to reach another PCBM cluster or the electrode. This insufficient percolation pathway for electrons was responsible for parasitic recombinations and poor efficiencies.

In the case of the P3HT:PCBM system, the as-cast film is quite homogeneous with little phase separation and solar cells based on P3HT:PCBM without post-production treatment exhibit poor efficiencies [59]. However, this initial morphology was found to be kinetically trapped and thermally unstable. Consequently, Padinger *et al.* [159] observed a significant increase in P3HT:PCBM solar cell efficiency by applying a thermal annealing post-production step. This increase in efficiency was correlated with an enhancement of the phase separation and with the polymer crystallisation.

More generally, it was shown by Kim *et al.* [82] that below the solubility limit, only hole transport was observed in transistor measurements while above the solubility limit, ambipolar transport begins to be observed due to the interconnection of larger electron-conducting PCBM domains. This can be probably linked with Müller *et al.* [160] observing a relationship between the eutectic composition and the maximum short circuit current: the optimum composition in term of short circuit current appeared to be slightly hypo-eutectic (shifted to higher fullerene content). This shift seems to depend on polymer crystallinity.

Recently, Treat *et al.* [161] tuned successfully the miscibility of fullerenes in poly(3-hexylselenophene) (P3HS) by varying the lengths of the fullerene derivative side chains since this should allow to trigger the fullerene-polymer interactions without significantly influencing the optical and electronic properties of the fullerenes. The goal was to improve the charge collection in solar cells. In fact, it has been previously reported that P3HS:PCBM solar cells suffer from low power conversion efficiency (PCE) due to low charge carrier collection. This has been attributed to insufficient percolation of the electron conducting phase due to high miscibility [136]. Treat *et al.* [161] show that decreasing the miscibility leads to an increase in the volume fraction of fullerene-rich domains and correlate this to an improvement of the fill factor due to an improvement in charge carrier collection. Interestingly, no significant variation in short circuit current was noticed. Decreasing too much the miscibility leads however to a bad short circuit current. This was attributed to the formation of large fullerene crystallites, reducing the interfacial area between polymer and fullerene, thus leading to poor charge generation.

1.4.3 Vertical phase separation

Campoy *et al.* [78] observed a vertical phase separation which is believed to arise from different interface properties: active layer/substrate and active layer/air during processing [85]. This vertical phase separation can have a major impact on phase connectivity to the electrode and thus on charge collection. Moreover, for thick cells, this vertical phase separation can have an impact on where within the layer the majority of charges are created and thus, may lead to more or fewer bimolecular recombinations due to shorter or longer distance to travel between the site of charge creation and charge collection.

1.4.4 Crystallisation effect on solar cell performances

Crystallisation induces a red-shift in the absorption onset by stabilising the HOMO and/or the LUMO of the material. This leads to a broadening of the absorption spectrum and is accompanied by an increase in the absorption coefficient at high wavelength (around 600 nm) [86, 87]. For example, regioregular P3HT which is a semi-crystalline polymer may absorb 60% more solar photons than regiorandom P3HT which is fully amorphous. Moreover, crystallisation leads often to higher charge mobility by easing the hopping of polarons between molecules and even allowing the tunnelling of charges if the orbital overlap becomes sufficient. Increasing absorption and charge mobility leads usually to higher photocurrent, thus to higher short circuit-current and better efficiencies [87].

Furthermore, close chain packing in crystalline polymers was suggested to lead to the delocalisation of polarons over several chains. Consequently, this larger polaron delocalisation may result in a larger distance between the charges bound in geminate pairs, lowering their binding energy and reducing geminate recombination [88]. Moreover, the improvement in charge carrier mobility may increase as well the probability of geminate pairs to escape their Coulomb radii and therefore, may lower again the geminate recombination [163, 89].

1.4.5 Thermodynamic coarsening influence on organic solar cell lifetime

As mentioned previously, the polymer-fullerene blend evolves from a highly metastable phase to increasingly stable phases. The best structure for device performance will in all probability not be the thermodynamically most stable. Since small organic molecules like the fullerene derivatives and even polymers may still have some freedom to diffuse slowly or recrystallize over time especially at temperature higher than the glass transition temperature, these gradual slow changes in the microstructure will lead to a degradation of the performance of the organic solar cells.

For example, the phase segregation of MDMO-PPV:PCBM mixtures has been studied by Yang *et al.* in detail [55]. It was found that the PCBM aggregates and forms microcrystallites that grow larger over time. Hoppe *et al.* showed that post-production thermal annealing leads to further phase separation of the favourable microstructure formed by changing the solvent from toluene to chlorobenzene [79]. The authors suggested that these morphology changes were due to low glass transition temperature of MDMO-PPV - around 45 °C - and that it would limit the long-term performance of solar cells based on these materials. Higher T_g materials are proposed to hamper the free diffusion of PCBM molecules by providing a stiffer donor matrix [90]. In the case of P3HT:PCBM, it is believed that the ability of P3HT to form rapidly a fibril network inhibits the fast diffusion of PCBM and thus, prevents the formation of too large fullerene crystallites and of a too large phase segregation [56].

1.4.6 Modelling techniques: bridging the gap between chemical structure and microscopic phenomena

A combination of modelling techniques have been used to understand the relationship between the chemical structure of the organic photovoltaic materials and their supramolecular organisation [91] and to study relevant phenomena to organic photovoltaics such as the charge transport in organics semiconductors [92, 93, 94]. Molecular dynamics is the technique of choice as it takes explicitly into account the intermolecular interactions driving the organisation of organic photovoltaic materials in solid. Several studies have investigated the structural arrangement of oligomers and

polymers in crystals [180, 96, 97], as well as amorphous structures [98, 99, 100]. For example, the influence of regioregularity [100] or the impact of interdigitation of alkyl side chains [101, 102] in thiophene based polymers on microstructure and transport properties have been reported.

To summarise, it has been shown that the partial immiscibility of polymer and fullerenes leads to very complex microstructure. Some systems such as P3HT:PCBM are of simple eutectic nature. Crystallisation and fullerene diffusion are two essential processes in the polymer:fullerene blend microstructure development.

Depending on the miscibility of the blend components, large unconnected beads of PCBM or homogeneous films with little phase separation have been observed. It has been shown that by slightly modifying the fullerene chemical structure, it is possible to tune the miscibility of the system. Moreover, changing the kinetics of the system using a different solvent or thermal treatment can modify the microstructure.

This phase separation does not occur only laterally but also vertically, with possible huge impact on the device performances. The obtained microstructures are not stable in time and leads to poor device lifetime.

Crystallisation leads to broader absorption spectra and higher charge mobilities. It is suggested to help the charge separation process through stabilisation of the energy levels.

A combination of modelling techniques can be useful to directly link the chemical structure of the blend components with the microstructure and relevant optoelectronic processes.

In the next section, we will highlight the motivations of the work presented in this thesis and give the outline structure of the thesis.

Section 1.5

Motivations and outline

In the previous section, we emphasised the fact that polymer-fullerene blend microstructures are rather complex microstructures exhibiting several phases such as a neat polymer (possibly crystalline) phase, co-crystals of polymer-fullerene, a neat fullerene (possibly crystalline) phase and an amorphous mixture of polymer and fullerene with possibly rich- and poor-fullerene phases. Such phase separation is required for organic photovoltaic devices but often either domains that are too large for efficient exciton dissociation or too small for sufficient percolation of electron and hole conducting phases are commonly observed leading to poor power conversion efficiencies. Furthermore, vertical phase separation can lead to detrimental lack of connectivity between conducting phases and electrodes, limiting the thickness of the cell active layer and thus leading to poor photocurrent.

In theory, the extent of phase separation highly depends on the polymer-fullerene interactions as described by the Flory-Huggins interaction parameters. This interaction parameter reflects the balance of interactions (polymer-fullerene, polymer-polymer and fullerene-fullerene) within the blends. These molecular interactions depend on the chemical structure of the organic photovoltaic materials but also on processing conditions. Thus, in this work, we focus on understanding the influence of the chemical structure of organic photovoltaic materials on the intermolecular interactions governing polymer-fullerene blend microstructures which are also influenced by processing conditions.

Firstly, we review the different methods used in this thesis. We first focus on understanding the influence of the number of side chains attached to the fullerene derivative on the microstructure of a regioregular poly(3-hexylthiophene)(P3HT):fullerene blend at a microscopic scale using transmission electron microscopy, steady-state and ultra-fast photoluminescence spectroscopy and grazing incidence X-Ray diffraction. We investigate the influence of the fullerene multiadducts on the phase behaviour of the P3HT:fullerene binary by differential scanning calorimetry (DSC) and relate our findings to observations of the effect of fullerene type on the optoelectronic properties of the same materials. This study highlights the importance of solubility and crystallisation that are the main topic of the rest of the thesis.

Secondly, we focus on finding a spectroscopic method to probe the onset of aggregation or in other words, solubility limit of fullerenes in amorphous polymer. We study the composition dependence of molecular organisation of fullerene multiadducts blended with regiorandom P3HT using steady-state and ultra-fast photoluminescence. We relate the onset of fullerene aggregation with the appearance of the charge transfer state feature in photoluminescence spectra. We correlate the shift in energy of the CT state emission with fullerene crystallisation probed by DSC and ellipsometry.

Thirdly, we focus on understanding the influence of the chemical substitution of the bridging atom between the backbone and the side chains on the crystallisation of poly [2,1,3-benzothiadiazole-4,7-diyl [4,4-bis(2-ethylhexyl)-4H-cyclopenta [2,1-b:3 ,4-b'] dithiophene -2,6- diyl] (PCPDTBT) by means of grazing X-ray diffraction and molecular modelling. We find that the main influence of the chemical substitution is an increase in flexibility of the side chains that leads to different crystal structures depending on the nature of the bridging atom.

Finally, we use quasi-elastic neutron scattering combined with molecular dynamics to probe the side chain dynamics of polythiophenes with different side chain lengths.

Bibliography

[1] Konarka, 2010.

[2] World Energy Council. 2010 survey of energy resources. 2010.

[3] BP statistical review of world energy. June 2012.

[4] U.S. Energy Information Administration. International Energy Statistics. 2012.

[5] International Energy Agency Renewable Energy Division. Technologie Roadmap - Solar Photovoltaic energy. 2010.

[6] J. Kalowekamo and E. Baker. Estimating the manufacturing cost of purely organic solar cells. *Solar Energy*, 83:1224–1231, 2009.

[7] Energy Infomation Administration. Annual Energy Outlook 2012. June 2012.

[8] Mott MacDonald. Costs of low-carbon generation technologies. Department of Energy and Climate Change, May 2011.

[9] A. L. Roes, E. A. Alsema, K. Blok, and M. K. Patel. Ex-ante environmental and economic evaluation of polymer photovoltaics. *Progress in Photovoltaics: Research and Applications*, 17:372–393, 2009.

[10] G. Marsh. PV: make way for the organic movement. *Renewable Energy Focus*, 9(4):34 – 40, 2008.

[11] Z. He, C. Zhong, S. Su, M. Xu, H. Wu, and Y. Cao. Enhanced power-conversion efficiency in polymer solar cells using an inverted device structure. *Nature Photonics*, 6(9):591 – 595, 2012.

[12] A. Anctil, C. Babbitt, B. Landi, and R.P. Raffaelle. Life-cycle assessment of organic solar cell technologies. In *Photovoltaic Specialists Conference (PVSC), 2010 35th IEEE*, pages 000742 –000747, june 2010.

[13] J.M. E. Christopher, A. Urbina, and J. Nelson. Environmental and economic assessment of ITO-free electrodes for organic solar cells. *Solar Energy Materials and Solar Cells*, 97(0):14 – 21, 2012.

[14] E. M. Conwell. *Organic Electronic Materials: Conjugated Polymers and Low Molecular Weight Organic Solids*, chapter Photophysics of Conducting Polymers, pages 127–180. Springer, 2001.

[15] R. Kersting, U. Lemmer, M. Deussen, H. J. Bakker, R. F. Mahrt, H. Kurz, V. I. Arkhipov, H. Bässler, and E. O. Göbel. Ultrafast field-induced dissociation of excitons in conjugated polymers. *Phys. Rev. Lett.*, 73:1440–1443, Sep 1994.

[16] A. Koehler and D. Beljonne. The singlet-triplet exchange energy in conjugated polymers. *Advanced Functional Materials*, 14(1):11–18, 2004.

[17] V. Bulovic, M. A. Baldo, and S. R. Forrest. *Organic Electronic Materials: Conjugated Polymers and Low Molecular Weight Organic Solids*, chapter Excitons and Energy Transfer in Doped Luminescent Molecular Organic Solids, pages 391–443. Springer, 2001.

[18] J. Franck and E. G. Dymond. Elementary processes of photochemical reactions. *Trans. Faraday Soc.*, 21:536–542, 1926.

[19] E. Condon. A theory of intensity distribution in band systems. *Phys. Rev.*, 28:1182–1201, Dec 1926.

[20] E. U. Condon. Nuclear motions associated with electron transitions in diatomic molecules. *Phys. Rev.*, 32:858–872, Dec 1928.

[21] C. W. Tang. Two-layer organic photovoltaic cells. *Applied Physics Letters*, 48:183–185, 1986.

[22] B. Miller, J. M. Rosamilia, G. Dabbagh, R. Tycko, R. C. Haddon, A. J. Muller, W. Wilson, D. W. Murphy, and A. F. Hebard. Photoelectrochemical behavior of C60 films. *Journal of the American Chemical Society*, 113(16):6291–6293, 1991.

[23] Th. Foerster. 10th spiers memorial lecture. Transfer mechanisms of electronic excitation. *Discussions of the Faraday Society*, 27:7–17, 1959.

[24] N. S. Sariciftci, L. Smilowitz, A. J. Heeger, and F. Wudl. Photoinduced electron transfer from a conducting polymer to buckminsterfullerene. *Science*, 258:1474–1476, 1992.

[25] J. J. M. Halls, C. A. Walsh, N. C. Greenham, E. A. Marseglia, R. H. Friend, S. C. Moratti, and A. B. Holmes. Efficient photodiodes from interpenetrating polymer networks. *Nature*, 376:498–500, 1995.

[26] G. Yu and A. J. Heeger. Charge separation and photovoltaic conversion in polymer composites with internal donor/acceptor heterojunctions. *Journal of Applied Physics*, 78:4510–4515, 1995.

[27] A. C. Morteani, R. H. Friend, and C. Silva. Exciton trapping at heterojunctions in polymer blends. *Journal of Chemical Physics*, 122:244906, 2005.

[28] C. Yin, T. Kietzke, D. Neher, and H. H. Hörhold. Photovoltaic properties and exciplex emission of polyphenylenevinylene-based blend solar cells. *Applied Physics Letters*, 90:092117, 2007.

[29] C. J. Brabec, G. Zerza, G. Cerrulo, S. De Silvestri, S. Luzzati, J. C. Hummelen,

and S. Sariciftci. Tracing photoinduced electron transfer process in conjugated polymer/fullerene bulk heterojunctions in real time. *Chemical Physics Letters*, 340:232–236, 2001.

[30] D. Hertel and H. Baessler. Photoconduction in amorphous organic solids. *ChemPhysChem*, 9(5):666–688, 2008.

[31] B. C. Thompson and J. M. J. Frechet. Polymer-fullerene composite solar cells. *Angewandte Chemie International Edition*, 47:58–77, 2008.

[32] J. Nelson. Polymer:fullerene bulk heterojunction solar cells. *Materials Today*, 14(10):462 – 470, 2011.

[33] C. Deibel and V. Dyakonov. Polymer-fullerene bulk heterojunction solar cells. *Reports on Progress in Physics*, 73:096401, 2010.

[34] E. L. Frankevich, A. A. Lymarev, I. Sokolik, F. E. Karasz, S. Blumstengel, R. H. Baughman, and H. H. Hörhold. Polaron-pair generation in poly(phenylene vinylenes). *Phys. Rev. B*, 46:9320–9324, Oct 1992.

[35] J. J. Benson-Smith, L. Goris, K. Vandewal, K. Haenen, J. V. Manca, D. Vanderzande, D. D. C. Bradley, and J. Nelson. Formation of a ground-state charge-transfer complex in polyfluorene//[6,6]-phenyl-C61 butyric acid methyl ester (PCBM) blend films and its role in the function of polymer/PCBM solar cells. *Advanced Functional Materials*, 17(3):451–457, 2007.

[36] M. A. Loi, S. Toffanin, M. Muccini, M. Forster, U. Scherf, and M. Scharber. Charge transfer excitons in bulk heterojunctions of a polyfluorene copolymer and a fullerene derivative. *Advanced Functional Materials*, 17(13):2111–2116, 2007.

[37] M. Hallermann, S. Haneder, and E. Da Como. Charge-transfer states in conjugated polymer/fullerene blends: below-gap weakly bound excitons for polymer photovoltaics. *Applied Physics Letters*, 93:053307, 2008.

[38] D. Veldman, O. Ipek, S. C. J. Meskers, J. Sweelssen, M. M. Koetse, S. C. Veenstra, J. M. Kroon, J.| van Bavel, S. S.and Loos, and R. A. J. Janssen. Compositional and electric field dependence of the dissociation of charge transfer excitons in alternating polyfluorene copolymer/fullerene blends. *Journal of the American Chemical Society*, 130:7721–7735, 2008.

[39] K. Vandewal, A. Gadisa, W. D. Oosterbaan, S. Bertho, F. Banishoeib, I. Van Severen, L. Lutsen, T. J. Cleij, D. Vanderzande, and J. V. Manca. The relation between open-circuit voltage and the onset of photocurrent generation by charge-transfer absorption in polymer-fullerene bulk heterojunction solar cells. *Advanced Functional Materials*, 18(14):2064–2070, 2008.

[40] K. Tvingstedt, K. Vandewal, A. Gadisa, F. Zhang, J. Manca, and O. Inganas. Electroluminescence from charge transfer states in polymer solar cells. *Journal of the American Chemical Society*, 131(33):11819–11824, 2009.

[41] P. Panda, D. Veldman, J. Sweelssen, J. J. A. M. Bastiaansen, B. M. W. Langeveld-Voss, and S. C. J. Meskers. Charge transfer absorption for pi-conjugated polymers and oligomers mixed with electron acceptors. *The Journal of Physical Chemistry B*, 111(19):5076–5081, 2007.

[42] C. Dyer-Smith, L. X. Reynolds, A. Bruno, D. D. C. Bradley, S. A. Haque, and J. Nelson. Triplet formation in fullerene multi-adduct blends for organic solar cells and its influence on device performance. *Advanced Functional Materials*, 20(16):2701–2708, 2010.

[43] L. Onsager. Deviations from Ohm's law in weak electrolytes. *Journal of Chemical Physics*, 2:599, 1934.

[44] C. L. Braun. Electric field assisted dissociation of charge transfer states as a mechanism of photocarrier production. *Journal of Chemical Physics*, 80:4157, 1984.

[45] J. J. Benson-Smith, J. Wilson, C. Dyer-Smith, K. Mouri, S. Yamaguchi, H. Murata, and J. Nelson. Long-lived exciplex formation and delayed exciton emission in bulk heterojunction blends of silole derivative and polyfluorene copolymer: the role of morphology on exciplex formation and charge separation. *The Journal of Physical Chemistry B*, 113(22):7794–7799, 2009.

[46] A. C. Morteani, R. H. Friend, and C. Silva. Endothermic exciplex-exciton energy-transfer in a blue-emitting polymeric heterojunction system. *Chemical Physics Letters*, 391(1-3):81 – 84, 2004.

[47] T. Offermans, P. A. van Hal, S. C. J. Meskers, M. M. Koetse, and R. A. J. Janssen. Exciplex dynamics in a blend of pi-conjugated polymers with electron donating and accepting properties: MDMO-PPV and PCNEPV. *Phys. Rev. B*, 72:045213, Jul 2005.

[48] S. Westenhoff, I. A. Howard, J. M. Hodgkiss, K. R. Kirov, H. A. Bronstein, C. K. Williams, N. C. Greenham, and R. H. Friend. Charge recombination in organic photovoltaic devices with high open-circuit voltages. *Journal of the American Chemical Society*, 130(41):13653–13658, 2008.

[49] D. Caruso and A. Trosi. Long-range exciton dissociation in organic solar cells. *Proceedings of the National Academy of Sciences of the United States of America*, 109:13498–13502, 2012.

[50] S. A. Choulis, Y. Kim, J. Nelson, D. D. C. Bradley, M. Giles, M. Shkunov, and

I. McCulloch. High ambipolar and balanced carrier mobility in regioregular poly(3-hexylthiophene). *Applied Physics Letters*, 85:3890, 2004.

[51] J.-M. Nunzi. Organic photovoltaic materials and devices. *Comptes Rendus Physique*, 3:523–542, 2002.

[52] H. A. M. van Mullekom, J. A. J. M. Vekemans, E. E. Havinga, and E. W. Meijer. Developments in the chemistry and band gap engineering of donor-acceptor substituted conjugated polymers. *Materials Science and Engineering: R: Reports*, 32:1–40, 2001.

[53] P. A. Troshin, H. Hoppe, J. Renz, M. Egginger, J. Y. Mayorova, A. E. Goryachev, A. S. Peregudov, R. N. Lyubovskaya, G. Gobsch, N. S. Sariciftci, and V. F. Razumov. Material solubility-photovoltaic performance relationship in the design of novel fullerene derivatives for bulk heterojunction solar cells. *Advanced Functional Materials*, 19:779–788, 2009.

[54] P. Sonar, J. P. F. Lim, and K. L. Chan. Organic non-fullerene acceptors for organic photovoltaics. *Energy and Environmental Science*, 4:1558, 2011.

[55] X. Yang, J. K. J. van Duren, R. A. J. Janssen, M. A. J. Michels, and J. Loos. Morphology and thermal stability of the active layer in poly(p-phenylenevinylene)/methanofullerene plastic photovoltaic devices. *Macromolecules*, 37:2151–2158, 2004.

[56] J. Yang, X. amd Loos, S. C. Veenstra, W. J. H. Verhees, M. M. Wienk, J. M. Kroon, M. A. J. Michels, and R. A. J. Janssen. Nanoscale morphology of high-performance polymer solar cells. *Nano Letters*, 5:579–583, 2005.

[57] S. S. van Bavel, E. Sourty, G. de With, and J. Loos. Three-dimensional nanoscale organization of bulk heterojunction polymer solar cells. *Nano Letters*, 9:507–513, 2009.

[58] H. Hoppe, T. Glatzel, M. Niggemann, A. Hinsch, M. Ch. Lux-Steiner, and N. S. Sariciftci. Kelvin probe force microscopy study on conjugated polymer/fullerene bulk heterojunction organic solar cells. *Nano Letters*, 5:269–274, 2005.

[59] C. Yang, J. G. Hu, and A. J. Heeger. Molecular structure and dynamics at the interfaces within bulk heterojunction materials for solar cells. *Journal of the American Chemical Society*, 128:12007–12013, 2006.

[60] Y.-C. Huang, Y.-C. Liao, S.-S. Li, M.-C. Wu, C.-W. Chen, and W.-F. Su. Study of the effect of annealing process on the performance of P3HT/PCBM photovoltaic devices using scanning-probe microscopy. *Solar Energy Materials and Solar Cells*, 93:888–892, 2009.

[61] B. Wunderlich. *Thermal Analysis of Polymeric Materials*. Springer, 2005.

[62] W. Hu. *Polymer Physics: A Molecular Approach*. Springer, 2013.

[63] Materialscientist. Schematic model of a spherulite. black arrows indicate direction of molecular alignment, May 2010.

[64] R. Koningsveld, K. Qolc, and W. J. MacKnightt. Thermodynamic aging of immiscible polymer blends. *Macromolecules*, 26:6676–6678, 1993.

[65] J. B. Clarke, J. W. Hastie, L. H. E. Kihlborg, R. Metselaar, and M. M. Thackeray. Definitions of terms relating to phase transitions of the solid state. *Pure and Applied Chemistry*, 66(3):577–594, 1994.

[66] W. J. Work, K. Horie, M. Hess, and R. F. T. Stepto. Definitions of terms related to polymer blends, composites, and multiphase polymeric materials (IUPAC recommendations 2004). *International Union of Pure and Applied Chemistry*, 76(11):1985–2007, 2004.

[67] U.W. Gedde. *Polymer Physics*. Kluwer Academic Publishers, 1995.

[68] R. Koningsveld, W. H. Stockmayer, and E. Nies. *Polymer phase diagrams: a textbook*. Oxford University Press, 2001.

[69] C. Vasile and A. K. Kulshreshtha. *Handbook of Polymer Blends and Composites*, volume 3A. Rapra Technology Limited, 2003.

[70] Jens Rieger. *Polymer Crystallization: Obervations, Concepts and Interpretations*, chapter Polymer Crystallization Viewed in the General Context of Particle Formation and Crystallization, page 2003. Springer, 2003.

[71] N. D. Treat, M. A. Brady, G. Smith, M. F. Toney, E. J. Kramer, C. J. Hawker, and M. L. Chabinyc. Interdiffusion of PCBM and P3HT reveals miscibility in a photovoltaically active blend. *Advanced Energy Materials*, 1(1):82–89, 2011.

[72] B. A. Collins, E. Gann, L. Guignard, X. He, C. R. McNeill, and H. Ade. Molecular miscibility of polymer-fullerene blends. *The Journal of Physical Chemistry Letters*, 1(21):3160–3166, 2010.

[73] H. W. Ro, B. Akgun, B. T. O'Connor, M. Hammond, R. J. Kline, C. R. Snyder, S. K. Satija, A. L. Ayzner, M. F. Toney, C. L. Soles, and D. M. DeLongchamp. Poly(3-hexylthiophene) and [6,6]-phenyl-C61-butyric acid methyl ester mixing in organic solar cells. *Macromolecules*, 45(16):6587–6599, 2012.

[74] A. C. Mayer, Michael F. Toney, Shawn R. Scully, Jonathan Rivnay, Christoph J. Brabec, Marcus Scharber, Marcus Koppe, Martin Heeney, Iain McCulloch, and Michael D. McGehee. Bimolecular crystals of fullerenes in conjugated polymers and the implications of molecular mixing for solar cells. *Advanced Functional Materials*, 19(8):1173–1179, 2009.

[75] C. Muller, T. A. M. Ferenczi, M. Campoy-Quiles, J. M. Frost, D. D. C. Bradley, P. Smith, N. Stingelin-Stutzmann, and J. Nelson. Binary organic photovoltaic blends: a simple rationale for optimum compositions. *Advanced Materials*, 20:3510–3515, 2008.

[76] D. R. Kozub, K. Vakhshouri, L. M. Orme, C. Wang, A. Hexemer, and E. D. Gomez. Polymer crystallization of partially miscible polythiophene/fullerene mixtures controls morphology. *Macromolecules*, 44(14):5722–5726, 2011.

[77] B. A. Collins, J. R. Tumbleston, and H. Ade. Miscibility, crystallinity, and phase development in P3HT/PCBM solar cells: toward an enlightened understanding of device morphology and stability. *The Journal of Physical Chemistry Letters*, 2(24):3135–3145, 2011.

[78] M. Campoy-Quiles, T. Ferenczi, T. Agostinelli, P. G. Etchegoin, Y. Kim, T. D. Anthopoulos, P. N. Stavrinou, D. D. C. Bradley, and J. Nelson. Morphology evolution via self-organization and lateral and vertical diffusion in polymer:fullerene solar cell blends. *Nature Materials*, 7:158–164, 2008.

[79] H. Hoppe, T. Glatzel, M. Niggemann, W. Schwinger, F. Schaeffler, A. Hinsch, M. Ch. Lux-Steiner, and N. S. Sariciftci. Efficiency limiting morphological factors of MDMO-PPV:PCBM plastic solar cells. *Thin Solid Films*, 511-512:587–592, 2006.

[80] S. E. Shaheen, C. J. Brabec, N. S. Sariciftci, F. Padinger, T. Fromherz, and J. C. Hummelen. 2.5% efficient organic plastic solar cells. *Applied Physics Letters*, 78:841, 2001.

[81] F. Padinger, R. S. Rittberger, and N. S. Sariciftci. Effects of postproduction treatment on plastic solar cells. *Advanced Functional Materials*, 13:85–88, 2003.

[82] J. Y. Kim and C. D. Frisbie. Correlation of phase behavior and charge transport in conjugated polymer/fullerene blends. *The Journal of Physical Chemistry C*, 112(45):17726–17736, 2008.

[83] N. D. Treat, A. Varotto, C. J. Takacs, N. Batara, M. Al-Hashimi, M. J. Heeney, A. J. Heeger, F. Wudl, C. J. Hawker, and M. L. Chabinyc. Polymer-fullerene miscibility: a metric for screening new materials for high-performance organic solar cells. *Journal of the American Chemical Society*, 134(38):15869–15879, 2012.

[84] A. M. Ballantyne, T. A. M. Ferenczi, M. Campoy-Quiles, T. M. Clarke, A. Maurano, K. H. Wong, W. Zhang, N. Stingelin-Stutzmann, J.-S. Kim, D. D. C. Bradley, J. R. Durrant, I. McCulloch, M. Heeney, J. Nelson, S. Tierney, W. Duffy, C. Mueller, and P. Smith. Understanding the influence of morphology on poly(3-

hexylselenothiophene):PCBM solar cells. *Macromolecules*, 43(3):1169–1174, 2010.

[85] D. S. Germack, C. K. Chan, R. J. Kline, D. A. Fischer, D. J. Gundlach, M. F. Toney, L. J. Richter, and D. M. DeLongchamp. Interfacial segregation in polymer/fullerene blend films for photovoltaic devices. *Macromolecules*, 43(8):3828–3836, 2010.

[86] T. Erb, U. Zhokhavets, G. Gobsch, S. Raleva, B. Stühn, P. Schilinsky, C. Waldauf, and C. J. Brabec. Correlation between structural and optical properties of composite polymer/fullerene films for organic solar cells. *Advanced Functional Materials*, 15:1193–1196, 2005.

[87] V. D. Mihailetchi, H. X. Xie, B. deBoer, L. J. A. Koster, and P. W. M. Blom. Charge transport and photocurrent generation in poly(3-hexylthiophene): methanofullerene bulk-heterojunction solar cells. *Advanced Functional Materials*, 16:699–708, 2006.

[88] J. G. Muller, J. M. Lupton, J. Feldmann, U. Lemmer, M. C. Scharber, N. S. Sariciftci, C. J. Brabec, and U. Scherf. Ultrafast dynamics of charge carrier photogeneration and geminate recombination in conjugated polymer:fullerene solar cells. *Physical Review B*, 72:195208, 2005.

[89] C. Dyer-Smith, J. J. Benson-Smith, D. D. C. Bradley, H. Murata, W. J. Mitchell, S. E. Shaheen, S. A. Haque, and J. Nelson. The effect of ionization potential and film morphology on exciplex formation and charge generation in blends of polyfluorene polymers and silole derivatives. *The Journal of Physical Chemistry C*, 113:14533, 2009.

[90] S. Bertho, I. Haeldermans, A. Swinnen, W. Moons, T. Martens, L. Lutsen, D. Vanderzande, J. Manca, A. Senes, and A. Bonfiglio. Influence of thermal ageing on the stability of polymer bulk heterojunction solar cells. *Solar Energy Materials & Solar Cells*, 91:385–389, 2007.

[91] O. A. Gus'kova, P. G. Khalatur, and A. R. Khokhlov. Self-assembled polythiophene-based nanostructures: Numerical studies. *Macromolecular Theory and Simulations*, 18:219–246, 2009.

[92] D. Andrienko, V. Marcon, and K. Kremer. Atomistic simulation of structure and dynamics of columnar phases of hexabenzocoronene derivatives. *The Journal of Chemical Physics*, 125:124902, 2006.

[93] J. Kirkpatrick, V. Marcon, J. Nelson, K. Kremer, and D. Andrienko. Charge mobility of discotic mesophases: a multiscale quantum and classical study. *Phys. Rev. Lett.*, 98:227402, May 2007.

[94] J. Nelson, J. J. Kwiatkowski, J. Kirkpatrick, and J. M. Frost. Modeling charge transport in organic photovoltaic materials. *Accounts of Chemical Research*, 42(11):1768–1778, 2009.

[95] M. Moreno, M. Casalegno, G. Raos, S. V. Meille, and R. Po. Molecular modeling of crystalline alkylthiophene oligomers and polymers. *The Journal of Physical Chemistry B*, 114(4):1591–1602, 2010.

[96] S. Dag and L.-W. Wang. Packing structure of poly(3-hexylthiophene) crystal: ab initio and molecular dynamics studies. *The Journal of Physical Chemistry B*, 114(18):5997–6000, 2010.

[97] C. Melis, L. Colombo, and A. Mattoni. Self-assembling of poly(3-hexylthiophene). *The Journal of Physical Chemistry C*, 115(2):576–581, 2011.

[98] N. Vukmirovic and L.-W. Wang. Charge carrier motion in disordered conjugated polymers: a multiscale ab initio study. *Nano Letters*, 9(12):3996–4000, 2009.

[99] Y.-K. Lan and C.-I Huang. Charge mobility and transport behavior in the ordered and disordered states of the regioregular poly(3-hexylthiophene). *The Journal of Physical Chemistry B*, 113(44):14555–14564, 2009.

[100] D. P. McMahon, D. L. Cheung, L. Goris, J. Dacuna, A. Salleo, and A. Troisi. Relation between microstructure and charge transport in polymers of different regioregularity. *The Journal of Physical Chemistry C*, 115(39):19386–19393, 2011.

[101] J. E. Northrup. Atomic and electronic structure of polymer organic semiconductors: P3HT, PQT, and PBTTT. *Phys. Rev. B*, 76:245202, Dec 2007.

[102] P. Brocorens, A. Van Vooren, M. L. Chabinyc, M. F. Toney, M. Shkunov, M. Heeney, I. McCulloch, J. Cornil, and R. Lazzaroni. Solid-state supramolecular organization of polythiophene chains containing thienothiophene units. *Advanced Materials*, 21(10-11):1193–1198, 2009.

CHAPTER 2

Methods

In this chapter, we first review the methods used to characterise the microstructure of blends of organic photovoltaic materials: photophysical methods (absorption, steady-state and ultrafast photoluminescence spectroscopy, variable angle spectroscopic ellipsometry), differential scanning calorimetry, structural characterisation methods (transmission electron microscopy, grazing incidence X-Ray diffraction and quasi-elastic incoherent neutron scattering). Then, we will review the sample preparation for each characterisation technique. Finally, molecular dynamics is introduced as a method to model organic photovoltaic materials.

Section 2.1

Photophysical methods

2.1.1 Steady state UV-vis absorption and photoluminescence spectroscopy

2.1.1.1 Principle

Ultraviolet-visible light spectrophotometer compares the intensity of light passing through a sample I to the intensity of light before it passes through the sample I_0. The ratio $\frac{I}{I_0}$ is called transmittance T and the absorbance A is related to the transmittance by $A = -log(T)$. A monochromator is used to separate the different wavelength of lights before the beam is split into two beams. One beam is used as reference (to measure $I_0(\lambda)$) while the other beam goes through the sample. The absorption process by conjugated molecules is discussed in section 1.2.1.2.

Photoluminescence spectrometer measures the intensity of light emitted by a sample as a function of the wavelength. The sample is excited by a monochrome light. The light emitted by the sample goes through a monochromator before reaching the detector. The emission process by conjugated molecules is discussed in section 1.2.1.3.

2.1.2 Experimental

UV-vis absorption and time-integrated PL spectroscopic data were measured using a Perkin-Elmer Lambda 25 spectrophotometer and a Horiba Jobin Yvon Fluorolog-2 PL spectrometer respectively. In some cases, photoluminescence spectroscopy has been performed using a laser at 448 nm and an InGaAs detector to probe lower

energies. Unless specifically stated in the figure caption, all photoluminescence data presented in this thesis are corrected using the absorption of the sample at the excited wavelength to account for small differences in the number of absorbed photons between samples due to different thicknesses or different amount of absorbing species. Quantum yields ϕ are calculating using the following equation:

$$\phi = \int \frac{I(\lambda)}{1 - 10^{-A(\lambda_0)}} d\lambda \tag{2.1}$$

where $I(\lambda)$ is the intensity of the emitted light at the wavelength λ and $A(\lambda_0)$ is the absorbance of the sample at the excitation wavelength λ_0.

2.1.3 Time resolved photoluminescence spectroscopy: ultrafast fluorescent upconversion

2.1.3.1 Principle

The sample is excited by a laser pulse and the intensity of the emitted light by the sample is recorded as a function of time. The decay of photoluminescence intensity as a function of time in a uniform population of molecules excited with a brief pulse of light could be described by an exponential function as in Equation 2.2 if excitons decay only radiatively or if all competing processes are first order processes. In Equation 2.2, $I(t)$ is the photoluminescence intensity measured at time t, I_0 is the initial intensity observed immediately after excitation within the time response of the set-up, and τ is the measured photoluminescence lifetime. However, the photoluminescence decay cannot often be fitted by a mono-exponential decay but by a double-exponential decay (Equation 2.3). The slower phase (usually >15 ps) is linked to intra-molecular exciton hopping. The fast energy transfer process (usually <15 ps) is related to torsional relaxation of the polymer chains [149].

$$I(t) = I_0 \exp\left(-\frac{t}{\tau}\right) \tag{2.2}$$

$$I(t) = I_0 \exp\left(-\frac{t}{\tau_{fast}}\right) \exp\left(-\frac{t}{\tau_{slow}}\right) \tag{2.3}$$

2.1.4 Experimental

Ultrafast time-resolved photoluminescence decays were measured using the femtosecond up-conversion technique. The samples were held in a nitrogen atmosphere and continuously translated through the excitation beam to eliminate photobleaching effects and local degradation of the films. Excitation was below the onset of intensity-dependent kinetics and was performed with the frequency-doubled output of a mode-locked Ti:sapphire laser supplying 70 fs pulses at 800 nm with a repetition rate of 80 MHz. The emission was upconverted in a beta-barium-borate crystal using the fundamental laser beam at 800 nm as the gate. Sum-frequency photons were dispersed in a monochromator and detected using a photomultiplier tube. The temporal resolution of the system was around 150 fs [162].

2.1.5 Variable angle spectroscopic ellipsometry

2.1.5.1 Principle

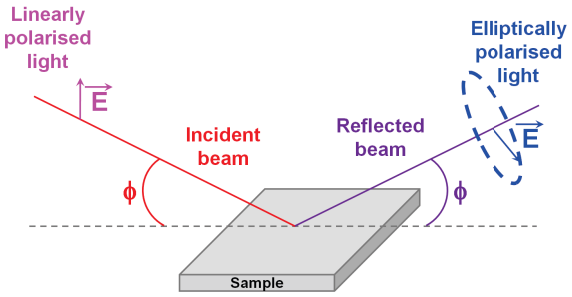


Figure 2.1: Scheme illustrating the principle of ellipsometry measurements.

Ellipsometry is a specular optical techniques that measures the change of polarisation state of light upon reflection on a sample at a non-normal incident angle. The incident

beam is linearly polarised. After reflection, the reflected beam is elliptically polarised (see Figure 2.1). The change in polarisation depends on the thickness and the complex refractive index of the multi-layered materials. Ellipsometry measures the complex reflectance ratio ρ, which is the ratio of p-polarised r_p on s-polarised r_s reflection coefficients:

$$\begin{aligned} \rho &= \frac{r_p}{r_s} \\ &= tan(\Psi)e^{i\Delta} \end{aligned} \tag{2.4}$$

where $tan(\Psi)$ is the amplitude ratio and Δ is the phase difference [105].

Variable angle spectroscopic ellipsometry (VASE) measures the complex ratio ρ as a function of wavelength λ and angle of incidence ϕ. Thus, in principle, the refractive index n and the extinction coefficient k can be extracted using the following equation:

$$\begin{aligned} < \epsilon > &=< \epsilon_1 > +i < \epsilon_2 > \\ &= (< n(\lambda) > +i < k(\lambda) >)^2 \\ &= sin(\phi)^2 \left[1 + tan(\phi)^2 \left(\frac{1 - \rho(\phi, \lambda)}{1 + \rho(\phi, \lambda)} \right) \right] \end{aligned} \tag{2.5}$$

where ϵ is the complex dielectric constant of the material and ϵ_1 and ϵ_2 its real and imaginary components respectively [105].

However, ellipsometry is sensitive to variations of the material optical properties through the samples. Thus, a model dependent analysis of the experimental data Ψ and Δ has to be performed. First, we construct a model of the optical structure of the sample consisting of layers of specified thicknesses and optical properties (refractive index and extinction coefficient as a function of wavelength). Then, we solve the Fresnel equations to calculate Ψ and Δ of the constructed model for the wavelength and angles of incidence used during the experiments. Afterwards, we compare the measured and predicted Ψ and Δ. Finally, we modify the model to get better fit of the measured Ψ and Δ and iterate until getting satisfying fits [105].

2.1.5.2 Experimental

VASE data were acquired at five angles between 55 and 75 using a SOPRALAB GES-5E rotating polarizer spectroscopic ellipsometer (SEMILAB) coupled with a CCD camera. The VASE data were modelled using the WinElli II piece of software. The Bruggeman effective medium approximation [105] is used to model the blends of amorphous polymer:fullerene. The fitting procedure is the following:

1. As a first approximation, the dielectric constant of both materials are assumed to be equal to the dielectric constant of the pure polymer and the pure fullerene.

The concentration is used as a free parameter.

2. We compare the fitted concentration with the experimental concentrations. In all cases, they appeared to be very close.

3. As a second approximation, we fix the concentrations to the fitted values. The dielectric constant of the polymer is assumed to be equal to the the dielectric constant of the pure polymer (the polymer being amorphous, its optical properties are less likely to change by blending with fullerenes). The dielectric constant of the fullerene is used as a free parameter.

Section 2.2

Thermoanalytical method: differential scanning calorimetry

2.2.1 Principle

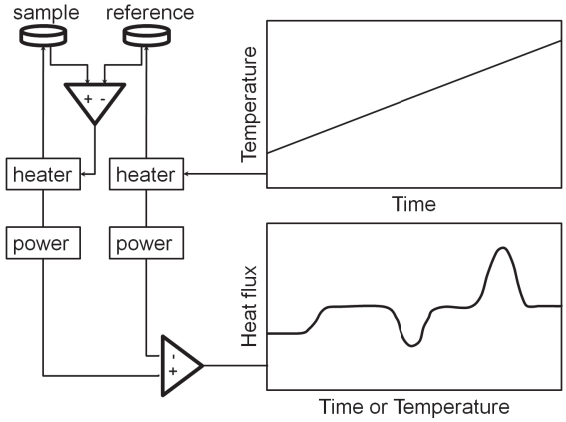


Figure 2.2: Scheme illustrating differential scanning calorimetry [106].

Differential Scanning Calorimetry (DSC) is a thermoanalytical technique in which the energy needed to establish a zero temperature difference between a sample and a reference during a controlled increase or decrease in temperature of the reference is measured. The reference is an inert material, in our experiment an empty aluminium pan. When the sample undergoes a physical transformation such as melting or crystallisation, the sample absorbs or releases heat leading to a difference in temperature between the sample and the reference. The resulting heat flow is recorded and plotted as a function of the temperature (see Figure 2.2). Since DSC is performed at constant pressure, the heat flow is equivalent to the enthalpy changes:

$$\left(\frac{dq}{dt}\right)_P = \frac{dH}{dt} \tag{2.6}$$

where q is heat, H is the enthalpy, t is the time and the subscript P refers to pressure. Thus, the integral of the peak (when the baseline has been removed) gives the total enthalpy change for the process.

2.2.2 Experimental

DSC was conducted under nitrogen using a Mettler Toledo DSC822 instrument.

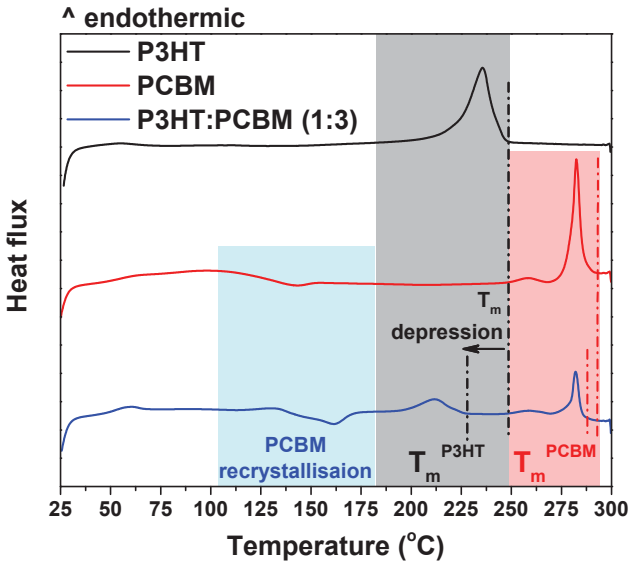


Figure 2.3: DSC scans of P3HT, PCBM and P3HT:PCBM (1:3)(heating rate: 10 °C/min).

Usual DSC scans for P3HT, PCBM and P3HT:PCBM (1:3) are plotted in Figure 2.3. The P3HT DSC heating scan is characterised by a broad endothermic peak around 230 °C. It is associated with the melting of P3HT. The DSC heating scan of PCBM presents more features: a small exothermic peak around 135 °C, a broad endothermic peak around 260 °C and a sharp endothermic peak around 280 °C. Both endothermic peaks are associated with the melting of PCBM. The presence of two melting peaks can be attributed to either the presence of polymorph crystals or to a melting-recrystallisation-melting process [107]. The exothermic peak is associated with recrystallisation of PCBM. The DSC scan of P3HT:PCBM presents all the features of both neat P3HT and neat PCBM.

The recrystallisation and the melting temperatures are considered to be the temperatures that correspond to the end of the peaks. So neat P3HT melting temperature is 240 °C, neat PCBM recrystallisation and melting temperatures are 160 and 290 °C respectively. When the materials are blended, the melting temperatures are depressed as can be seen in Figure 2.3: the melting of P3HT and PCBM occurs at 225 and 285 °C respectively.

Three scans are usually performed in order to detect possible degradations of the materials and experimental failures. The first scan is different from the second and the third ones since the first scan is sensitive to the processing.

Varying the heating and cooling rates does not modify the enthalpy change for a process or in other words, do not modify the integral of the peak associated with that process. However, when the rates are increased, less time is given to the material to experience a phase transition. Therefore, all the energy is released or absorbed during a smaller period of time leading to sharper and higher peaks. By contrast, when decreasing the heating and the cooling rates, more time is given to the material to experience a phase transition. Therefore, the energy is released or absorbed during a longer period of time. This lead to smaller and broadened peaks.

Section 2.3

Structural characterisation

Radiation interacts with matter, through scattering with electrons and nuclei. Depending on the wavelength and the nature of the radiation, different properties of the matter can be probed at different scale.

2.3.1 Transmission electron microscopy

2.3.1.1 Principle

When an electron interacts with the matter, it may be scattered either elastically or inelastically. Both mechanisms will change the angle the electron is moving at relative to the optical axis and leads, as well as absorption, to an electron density distribution at the exit of the sample. These variations are magnified and imaged on the fluorescent screen by the lens system. In a bright field image, the diffracted electrons are prevented from contributing to the image, so only the transmitted beam is allowed to form the image.

Mass-thickness contrast is due to incoherent elastic scattering of electrons. The cross section for elastic scattering depends on the atomic number Z. Thus, if the thickness is homogeneous, the region of higher Z elements will scatter more electrons and appear darker in the bright field image than the region of low Z elements (mass contrast). However, if the thickness is not homogeneous, more electrons will be scattered when the beam interacts with the thicker area. As a consequence, thicker area will appear darker in the bright field image (thickness contrast).

In order to reduce the number of scattering events, or in other words in order to maximise the number of detected electrons, the samples must be extremely thin: around 100 nanometres.

2.3.1.2 Experimental

TEM images were obtained using a JEOL 2000FX electron micrograph operated at 200 kV.

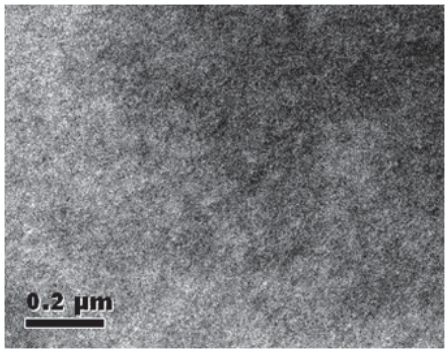


Figure 2.4: Bright-field TEM micrograph of as-spun P3HT:PCBM (1:1). Data from Simon P. King.

In Figure 2.4, the bright-field TEM micrograph of an as-spun P3HT:PCBM (1:1) film is displayed. The P3HT-rich areas appear bright and the PCBM -rich areas appear dark in this TEM micrograph because P3HT and PCBM have similar Z values but P3HT density (1.1 $g.cm^{-3}$) is lower than PCBM density (1.5 $g.cm^{-3}$) [148]. Images are 2D projections of the 3D thin film and that leads to difficulties in interpretation, especially because conjugated polymers and fullerenes are not very crystalline (usually a film is less than 20 % crystalline). If the films were crystalline enough, structural information could be extracted from the diffracted electrons. In the following, no quantitative information on either domain composition or size will be deduced from TEM data.

2.3.2 Grazing Incidence X-Ray Diffraction

2.3.2.1 Principle

X-ray radiations are not usually suited to probe thin films since the penetration depth is large leading to low diffracted intensities in comparison with the substrate and background. By using very low incident angles, Grazing Incidence X-Ray Diffraction (GIXRD) allows to overcome this problem. In fact, the very small incident angle with the sample surface leads to an increase in the path length of the X-ray beam through the film, increasing the diffracting volume. This larger diffracting volume

leads to an increase in the diffracted intensity, while at the same time, the diffracted intensity from the substrate has been reduced, resulting in an overall increase in the film signal-to-background ratio.

The incident X-Ray beam of wave vector $\vec{k_i}$ is kept at a grazing angle α_i close to the angle of total external reflection. The scattered beam of wave vector $\vec{k_f}$ makes an angle α_s with respect to the sample surface and an angle $2\theta_s$ with respect to the transmitted beam. The scattering vector $\vec{q}$ is defined as $\vec{q} = \vec{k_f} - \vec{k_i}$. The components q_{xy} and q_z of the scattering vector $\vec{q}$ are the components parallel and perpendicular to the surface of the sample respectively (see Figure 2.5). In the following, in-plane and out-of-plane line profile will refer to line profile along q_{xy} and q_z respectively.

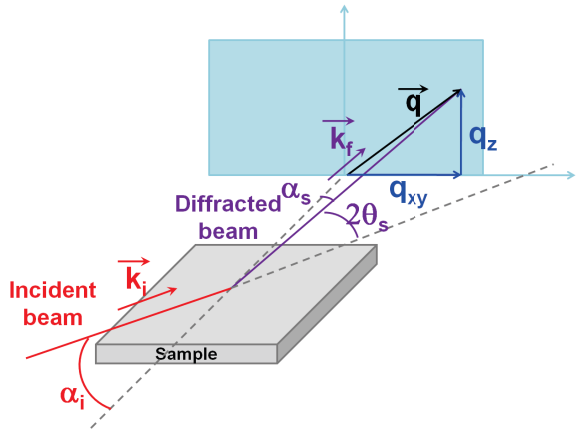


Figure 2.5: Scattering geometry of a GIXRD experiment.

2.3.2.2 Experimental

Some of the GIXRD measurements were performed at the I07 beamline (Diamond Light Source, UK). A chamber containing a hot plate, on which the samples were glued with conductive silver paint, and a system of motorized shields and slits to reduce the background noise, was mounted on a $2 + 3$ circle diffractometer with a hexapod sample stage. The chamber was filled with helium before the experiments started to avoid air scattering. A monochromatic radiation of 10 keV energy and resolution of $< 10^{-4}$ keV were used. Diffraction patterns were detected with a PILATUS 100K (Dectris) Si photodiode array detector. Single images were collected every 0.25 s, as a compromise between high signal-to-noise ratio and high sampling rate. After aligning the sample and detecting the critical angle, a standardized set of scans was performed for all of the samples.

Some of the GIXRD measurements were performed at the BM28 beamline at ESRF (European Synchrotron Radiation Facility) in Grenoble. A chamber and a system of motorized shields and slits to reduce the background noise were mounted on a 6-circle diffractometer with an Eulerian cradle. The chamber was slowly flushed with helium during the experiments to avoid air scattering. Diffraction patterns were detected with a MAR area detector.

In Figure 2.6, the GIXRD pattern of P3HT:PCBM (1:1) as well as the out-of-plane line profile extracted from that pattern are displayed. Three diffraction peaks can be assigned to P3HT while PCBM features only a broad ring. The P3HT peaks are commonly assigned as (100), (200) and (300) and correspond to spacing distance along the lamellar stacking direction.

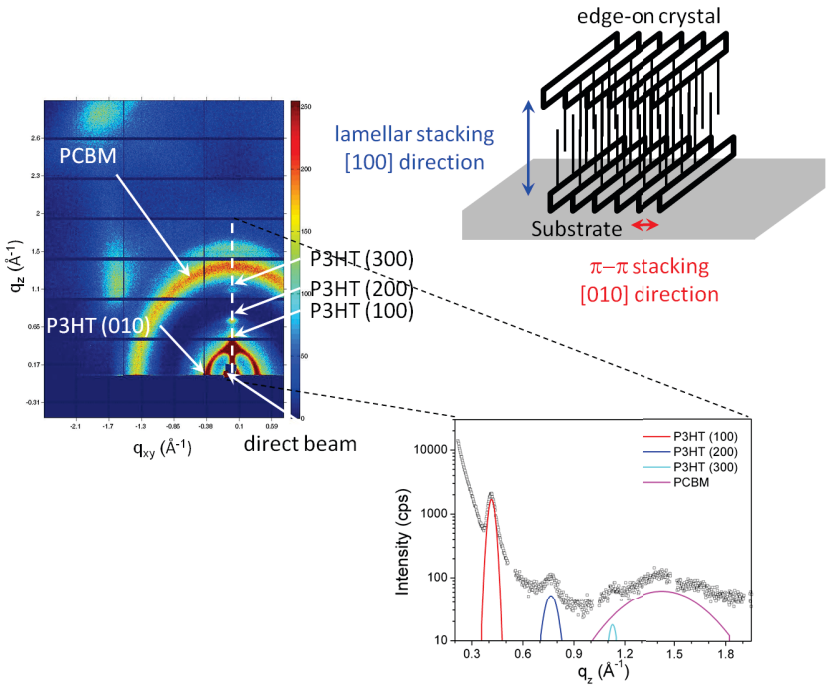


Figure 2.6: GIXRD pattern (scattering intensity as a function of q_z and q_{xy}) of as-spun P3HT:PCBM (1:1). The different peaks are indexed according to a monoclinic crystal structure as depicted in the inset. The [100] and [010] directions have been chosen to be the lamellar stacking direction and the $\pi - \pi$ stacking direction respectively. The crystal is edge on, the backbones or the [100] direction are perpendicular to the substrate. The second inset depicts the out-of-plane line profile (scattering intensity as a function of q_z) extracted from the GIXRD pattern. Measurements in collaboration with Tiziano Agostinelli, Ellis Pires and J. Emyr Macdonald.

2.3.3 Quasi-elastic incoherent neutron scattering

2.3.3.1 Principle

Incoherent scattering is related to scattering by individual atoms. Thus, incoherent scattering provides informations on individual motions, i.e. incoherent scattering is related to the self-correlation of a scattering centre. Hydrogen has a large incoherent scattering cross-section. As a consequence, the incoherent signals result mostly from the fluctuations in the position of hydrogen atoms within the sample.

Elastic incoherent neutron scattering (EINS) results from vibrational motions at low temperatures and large-amplitude stochastic fluctuations for temperatures higher than the glass transition on timescales of 0.1 femtosecond to 1 nanosecond. However, purely EINS occurs only at 0K. In fact, if the atoms are stochastically diffusing or the molecules undergo some stochastic motions, a scattering event will result in an energy transfer with the neutrons leading to the broadening of the elastic signal. This additional contribution is known as quasi-elastic neutron scattering (QENS). While elastic scattering provides information on structural properties, the detection of energy changes allow to study dynamics of macromolecules.

The incoherent scattering function $(S_{inc}(Q,\omega))_T$ in the elastic region at a given temperature has a purely elastic contribution: $(EISF(Q))_T\delta(\omega)$ where $(EISF(Q))_T$ is the elastic incoherent structure factor and $\delta(\omega)$ is the delta function. The incoherent scattering function $(S_{inc}(Q,\omega))_T$ has also a quasi-elastic contribution centred on $\hbar\omega = 0eV$: $(1-(EISF(Q))_T)\sum_n)(L_n(\omega))_T$, where $L_n(\omega)$ is a Lorentzian function. Each Lorentzian describes a different motion (either translational or rotational motion). All those motions are affected by vibrational motions that are described by the Debye-Waller factor $\exp(-\frac{w(T)}{3}Q^2)$ where $w(T)$ is a measure of the mean-square displacement of an atom. The incoherent scattering function $(S_{inc}(Q,\omega))_T$ is thus given by the equation:

$$(S_{inc}(Q,\omega))_T = \exp(-\frac{w(T)}{3}Q^2) * \left\{ (EISF(Q))_T\delta(\omega) + (1-(EISF(Q))_T)\sum_n (L_n(\omega))_T \right\} \quad (2.7)$$

$(I_{exp}(Q,\omega))_T$ is measured as a function of the momentum transfer Q and energy change $E = \hbar\omega$ in a quasi-elastic neutron scattering measurements. $(I_{exp}(Q,\omega))_T$

is practically fully determined by the incoherent scattering function of the hydrogens $(S_{inc}(Q,\omega))_T$.

As neutron scattering spectrometers offer a limited energy resolution, the measured functions are affected by the instrumental resolution function, $R(Q,\omega)$. The instrumental resolution function has been determined from the scattering of a vanadium sample, which is an incoherent elastic scatterer, at very low temperature 4 K (all the dynamical processes are supposed to be frozen): $R(Q,\omega) \simeq (I_{exp}^{vanadium}(Q,\omega))_{T=4K}$.

Thus, the double differential cross section is the convolution of the incoherent scattering function and the instrumental resolution:

$$(I_{exp}(Q,\omega))_T = (S_{inc}(Q,\omega))_T * R(Q,\omega) \tag{2.8}$$

The incoherent scattering function can be easily extracted in the time-domain using Fourier transforms:

$$S_{inc}(Q,t)_T = \frac{\int (I_{exp}(Q,\omega))_T e^{i\omega t} d\omega}{\int (R(Q,\omega))_T e^{i\omega t} d\omega} \tag{2.9}$$

In Figure 2.7, the quasi-elastic peak measured for P3HT is plotted in the energy domain. The corresponding intermediate scattering function calculated using Equation 2.9 is also plotted in the time domain.

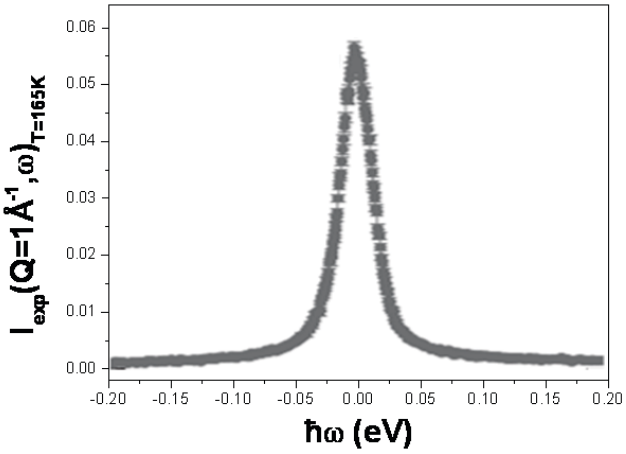
Each instrument has a maximum change in energy that can be detected. This maximum change in energy determines the energy window of the instrument and thus, the time window of the instrument in the time-domain.

2.3.3.2 Experimental

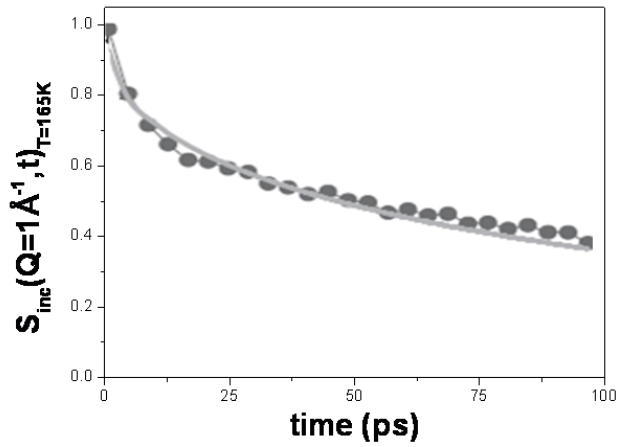
The measurements were performed using the IN10 spectrometer at the Institut Laue-Langevin (France) and the instrument OSIRIS of ISIS-RAL in Oxford.

IN10 is a backscattering spectrometer with inverse geometry in which the energy transfer is scanned by varying the incident energy whilst keeping the final energy fixed. The incident energy is changed by Doppler shifting the neutron wavelength. The energy resolution is less than μeV.

OSIRIS is a backscattering instrument. The energy resolution is 25 μeV and the energy range is $\pm$1 meV, which is equivalent to a time range of 18 ps to 90 ps.



(a)



(b)

Figure 2.7: Quasi-elastic intensity $I_{exp}(Q = 1Å^{-1}, \omega)_{T=165K}$ in the energy domain and the corresponding intermediate scattering function $S_{inc}(Q = 1Å^{-1}, t)_{T=165K}$ in the time domain obtained by Fourier transform for P3HT. Measurements by Antonio Urbina .

Section 2.4

Sample preparation

2.4.1 Materials

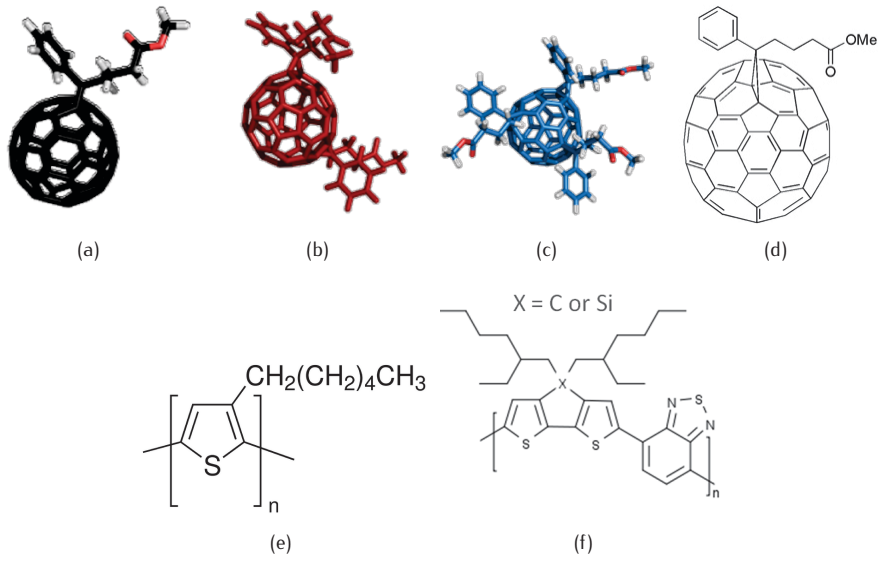


Figure 2.8: (a) $PC_{61}BM$, $PC_{61}BM$ (b) bis- and (c) tris-adducts, (d) $PC_{71}BM$, (e) P3HT and (f) C6- and Si-PCPDTBT.

$PC_{61}BM$, its bis- and tris-adducts and $PC_{71}BM$ were supplied by Solenne BV with molecular weights of 910.88, 1101.10, 1291.32 and 1031.0 g/mol, respectively. RR-P3HT was supplied by Merck Chemicals (RR=94.7%, M_n = 19.5 kg/mol, M_w = 34.1 kg/mol, PD=1.74). RRa-P3HT was supplied by Sigma-Aldrich (1:1 (head-to-head):(head-to-tail) linkages of regioisomers). C6-PCPDTBT and Si-PCPDTBT were supplied by Konarka Technologies. The molecular weight of RRa-P3HT, C6-PCPDTBT and Si-PCPDTBT were not furnished by the supplier.

2.4.2 Photophysical methods

Quartz substrates were cleaned in sequence with acetone (10 min) and isopropanol (10 min) using an ultrasonic bath.

For the RR-P3HT blended with the fullerene multi-adducts, thin films were fabricated by spin-coating (spinning speed of 2000 rpm during 120 s with an acceleration of 400 rpm/s) of material mixtures from chlorobenzene (10 mg/mL) onto quartz substrates. Approximately 30 μL of solution was deposited on the substrate before spinning resulting in film thicknesses of about 100 nm.

For the RRa-P3HT blended with the fullerene multi-adducts, thin films were fabricated by spin-coating (spinning speed of 1500 rpm during 30 s with an acceleration of 2250 rpm/s) of material mixtures from chlorobenzene (10 mg/mL) onto quartz substrates. Approximately 30 μL of solution was deposited on the substrate before spinning resulting in film thicknesses of about 100 nm.

When the samples were annealed, they were annealed at 150 °C for 30 min under nitrogen atmosphere.

2.4.3 Differential scanning calorimetry

Glass substrates were cleaned using acetone. Films were fabricated by drop-casting of material mixtures from chlorobenzene (10 mg/mL) onto glass substrates, followed by evaporation of the solvent at ambient temperature. Afterwards, the films were scratched and placed in aluminium pans to be analysed. The sample weight was about 5 mg.

2.4.4 Structural characterisation

2.4.4.1 Transmission electron microscopy

Glass substrates were cleaned in sequence with acetone (10 min) and isopropanol (10 min) using an ultrasonic bath.

A PEDOT:PSS layer was spin-coated (spinning speed of 4000 rpm during 1 min with an acceleration of 8000 rpm/s) on a glass substrate and then annealed at 120 °C for 30 min. Thin films were fabricated by spin-coating (spinning speed of 1500 rpm during 1 min with an acceleration of 2250 rpm/s) of material mixtures from chlorobenzene (10 mg/mL) on top of the PEDOT:PSS layer. Approximately 30 μL of solution was deposited on the substrate before spinning resulting in film thicknesses of about 100 nm. Then, the thin films were floated from the water-soluble PEDOT:PSS onto the surface of deionized water and caught on 300 mesh copper grids.

When the samples were annealed, they were annealed at 150 °C for 30 min under nitrogen atmosphere.

2.4.4.2 Grazing Incidence X-Ray Diffraction

1 mm thick silicon substrates (IDB Technologies) were cleaned in sequence with acetone (15 min) and isopropanol (15 min) using an ultrasonic bath, and then dried using a nitrogen gun. The films were then prepared by spin coating at a spinning speed of 1200 rpm, resulting in thicknesses of about 100 nm.

2.4.4.3 Quasi-elastic incoherent neutron scattering

Thin films were fabricated by spin-coating of material mixtures from toluene. Then, the thin films were floated onto the surface of deionized water and stacked on top of each other until reaching a micrometer thickness.

Section 2.5

Molecular Dynamics

Since the Gromacs package is used to perform Molecular Dynamics (MD), the algorithms and formalisms presented in the following are the ones used in Gromacs [109, 110, 111, 112]. The quantum chemical computations are realised in this work using the Gaussian quantum chemistry package [113].

2.5.1 Principle

In Molecular Dynamics (MD), the classical equations of motion (Equation 2.10) are solved for each particle of a N-body system that interacts through a given potential energy $V(\vec{r_1}, ..., \vec{r_N})$.

$$\begin{gathered} m_i \frac{\partial^2 \vec{r_i}}{\partial t^2} = \vec{F_i} \\ \text{with} \\ \vec{F_i} = -\vec{\nabla}_i V(\vec{r_1}, ..., \vec{r_N}) \end{gathered} \tag{2.10}$$

where m_i and $\vec{r_i}$ represent the mass and the coordinates of body i respectively, t represents the time, $\vec{F_i}$ represents the sum of the forces acting on body i and ∇_i is the derivative with respect to the coordinates of body i.

In order to integrate those N coupled equations of motion, the use of a finite difference method is required. The default integrator in Gromacs and the one we have been using is the leap-frog algorithm. The velocity v at $t + \frac{1}{2}\delta t$ is expressed as a function of the velocity at $t - \frac{1}{2}\delta t$ and the acceleration a at t (equation 2.11) while the position r at $t + \delta t$ can be expressed as a function of the position at t and the velocity at $t + \frac{1}{2}\delta t$ (equation 2.12).

$$v(t + \frac{1}{2}\delta t) = v(t - \frac{1}{2}\delta t) + a(t)\delta t \tag{2.11}$$

$$r(t+\delta t) = r(t) + v(t+\frac{1}{2}\delta t)\delta t \tag{2.12}$$

If needed, the velocity at t might be estimated by:

$$v(t) = \frac{v(t+\frac{1}{2}\delta t) + v(t-\frac{1}{2}\delta t)}{2} \tag{2.13}$$

As a consequence, the equations of motion are solved on a step-by-step basis (see Figure 2.9). Unless specifically stated, a time step of 1 fs and a maximum step size of 0.01 nm have been used.

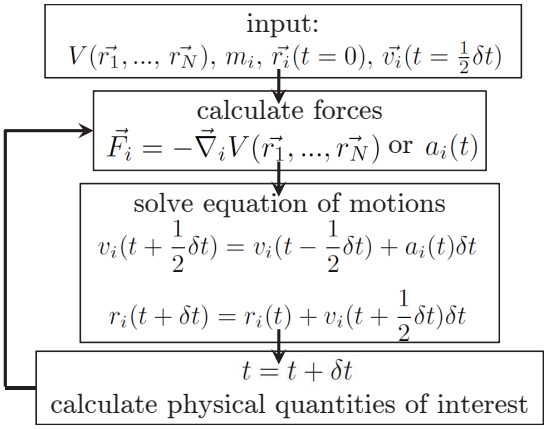


Figure 2.9: Flow chart of a Molecular Dynamics algorithm.

2.5.2 Force field

As discussed previously, in MD, the initial particle coordinates and velocities as well as the potential energy of the system are required as inputs of the simulation. We generate the initial set of nuclear coordinates of an approximate structure from tabulated inter-atomic distances and geometries considering atom hybridisation using Gaussview [114]. We generate velocities according to a Maxwell distribution at the required temperature. We use fully atomistic models to represent molecules. In atomistic models, molecules are represented as atoms connected by chemical bonds. We describe the interactions between atoms by both a set of equations (called the functional form) and the parameters that are used in this set of equations. These two

components constitute the force field of the studied system.

2.5.2.1 Functional form

According to OPLS-AA FF [115, 116, 117, 118, 119, 120], the following functional form has been adopted for the FF:

$$
\begin{aligned}
E = \sum_{\substack{i<j \\ \text{non-bonded} \\ \text{interactions}}} \left\{ 4\epsilon_{ij} \left[\left(\frac{\sigma_{ij}}{r_{ij}} \right)^{12} - \left(\frac{\sigma_{ij}}{r_{ij}} \right)^{6} \right] + \frac{1}{4\pi\epsilon_r\epsilon_0} \frac{q_i q_j}{r_{ij}} \right\} f_{ij} \\
+ \sum_{bonds} \frac{1}{2} K_b (b - b_0)^2 \\
+ \sum_{angles} \frac{1}{2} K_\theta (\theta - \theta_0)^2 \\
+ \sum_{\substack{\text{improper} \\ \text{dihedrals}}} \frac{1}{2} K_\xi (\xi - \xi_0)^2 \\
+ \sum_{\substack{n=0 \\ dihedrals}}^{5} C_n \cos^n(\phi - \phi_0)
\end{aligned}
\tag{2.14}
$$

The first term of Equation 2.14 corresponds to the energy due to the non-bonded or intermolecular interactions. It is described by the Lennard-Jones and Coulomb functional form with r_{ij} the distance between atom i and j, $\epsilon_{ij} = (\epsilon_{ii}\epsilon_{jj})^{\frac{1}{2}}$ the depth of the Lennard-Jones potential well, $\sigma_{ij} = (\sigma_{ii}\sigma_{jj})^{\frac{1}{2}}$ the finite distance at which the Lennard-Jones potential is equal to zero, q_i the effective charges and ϵ_0 and ϵ_r the vacuum permittivity and relative permittivity respectively. The 1-2 and 1-3 interactions are excluded from the Lennard-Jones interactions list ($f_{ij} = 0$) and the 1-4 Coulomb and Lennard-Jones interactions are reduced by a factor of 2 ($f_{ij} = 0.5$).

The four last terms of Equation 1 correspond to the part of the potential energy due to bonded or intramolecular interactions (see Figure 2.10). b_0, θ_0, ϕ_0 and ξ_0 are the equilibrium bond distance, angle, proper and improper dihedral angle respectively. b, θ, ϕ and ξ are the bond distance, angle, proper and improper dihedral angle respectively. K_b, K_θ and K_ξ are the bond, angle and improper dihedral force constants. C_n are the coefficients of the Fourier series describing proper dihedral potentials.

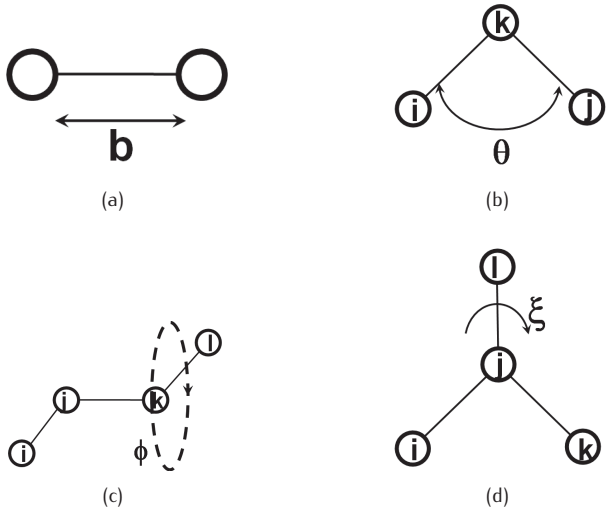


Figure 2.10: Representation of the different distances and angles in atomistic models: (a) bond distance b, (b) angle θ, (c) proper dihedral angle ϕ and (d) improper dihedral angle ξ.

2.5.2.2 Parametrisation

We took the Lennard-Jones potential parameter ϵ_{ii} and σ_{ii} values from OPLS-AA FF. We took these values for silicon atoms from [186].

We derive the equilibrium bond lengths b_0, bond angles θ_0 and torsional angles ϕ_0 from the quantum chemical energy-minimised structure of the studied system (we optimise the molecular geometry using a hybrid density functional theory method b3lyp/6-311**) and for alkyl side-chains, we took the values from OPLS-AA FF.

We took the values of the force constants from OPLS-AA FF. When missing, we calculate the bond force constants using a modified Badger rule [122] ($K_b = \frac{\alpha}{R^3}$ with $\alpha = 104.74 kJ.nm.mol^{-1}$ and the reduced bond length $R = b_0 - d$ where $d = d_i + d_j$ with $d_{i,j}$ being half the covalent radii) and the angle force constants a modified Halgren rule [123, 124] (for an angle a-b-c, $K_\theta = 48.76 Z_a C_b Z_c (R_{ab}+R_{bc})^{-1} \theta_0^{-2} \exp(-2D)$ with $Z = 2.49$ and 2.35, $C = 1.05$ and 0.95 for a Carbon and a Silicon atom respectively, R_{ij} being the reduced bond length and is calculated as mentioned above and with $D = \frac{(R_{ab}-R_{bc})^2}{(R_{ab}+R_{bc})^2}$. We calculate the missing torsional potential parameters using quantum chemical calculations and insert in the FF using the force matching approach as following:

1. We optimise the molecular geometry of the system with the relevant degree of freedom being constrained for each angular value using a hybrid-DFT method (B3LYP/6-311g(d,p))

2. For each optimised molecular conformation, we calculate the energy using a post-Hartree-Fock method Møller-Plesset 2 (MP2/cc-pVTZ) [125] (the geometry is not re-optimised in that step).

3. We evaluate the potential energy for each angular value using the incomplete force-field with the angle/dihedral in question switched off.

4. We fit the difference between the quantum chemical and force-field-based energies with a Fourier series as in Equation 2.14 and we include it in the FF.

OPLS provides crude values for partial charges in order to retain its transferable feature. In order to increase the accuracy of the method, we derive the charges in the following from a quantum chemical method of generating partial charges called CHELPG (CHarges from Electrostatic Potentials using a Grid). First of all, the studied molecule is placed at a centre of a cube. The distance between the molecule and the edge of the cube should be 28.0 pm in all three dimensions. The molecular electrostatic potential is then calculated from the basis functions and electron occupancy at grid points spaced 3.0 pm apart. The molecular electrostatic potential is not calculated if the grid points are falling inside the van der Waals radius of the molecule. After the molecular-electrostatic-potential evaluation at all valid grid points, the atomic charges are thus the sets of atomistic charges that fit optimally the molecular electrostatic potential.

The CHELPG method is less dependent on the underlying Hamiltonian and basis sets than other methods such as the Mulliken method but may be inaccurate in the treatment of large systems. This is due to the fact that in the case of large systems, atoms may be situated far away from the grid points where the molecular electrostatic potential is evaluated. The charges generated by the CHELPG method depend also on the molecule conformation. Therefore, if the molecule possess a degree of freedom, the possible conformations need to be studied and thus, the charges that derived from these possible conformations.

We take the Lennard-Jones parameters for Silicon atoms from the FF from Pereira *et al.* [186] and for the other atoms from the OPLS-AA FF.

2.5.3 Molecular dynamics parameters

The system was coupled to a bath using a velocity rescaling method similar to a Berendsen coupling with a stochastic term (the random seed is 1993) with a time constant of 0.1 ps. When working in the isothermal-isobaric ensemble (NPT) rather than in the canonical ensemble (NVT), the pressure was regulated by an isotropic Berendsen weak coupling at 1 bar with a time constant of 5 ps. The compressibility is set to 4.5 x 10^{-5} bar^{-1}. The leap-frog algorithm is used to integrate Newton equations of motion. The time step is set to 1 fs. A Brownian dynamics friction coefficient of 0.5 $amu.ps^{-1}$ is used. Velocities are generated according to a Maxwell distribution at the system temperature with the random seed 173529.

When using periodic boundary conditions, the centre of mass translation is removed. The neighbour list is updated every 5 steps using a grid search and the cut-off distance for the short-range neighbour list is set to 1 nm. For electrostatic and van der Waals interactions, a cut-off distance is set to 1 nm. The relative dielectric constant is set to 1. Long-range dispersion correction are applied for energy and pressure.

When periodic boundary conditions are not applied, the centre of mass translation and the rotation around the centre of mass are removed. No cut-off are used. The neighbour list is updated every step using a simple search (every atom of the box is checked). The relative dielectric constant is set to 1. Long-range dispersion correction are applied for energy and pressure. Particle decomposition is used instead of domain decomposition.

Prior to the MD simulations, an energy minimisation step is performed using a steepest descent integrator. The same parameters as the ones used for MD are used. The minimization is converged when the maximum force is smaller than 10 $kJ.mol^{-1}.nm^{-1}$.

Bibliography

[103] P. Parkinson, C. Muller, N. Stingelin, M. B. Johnston, and L. M. Herz. Role of ultrafast torsional relaxation in the emission from polythiophene aggregates. *The Journal of Physical Chemistry Letters*, 1(19):2788–2792, 2010.

[104] A. Bruno, A. De Girolamo Del Mauro, G. Nenna, S.A. Haque, and C. Minarini. Insights on photophysical proprieties of DCM dye in PVK host matrix. *Polymer Composites*, pages n/a–n/a, 2013.

[105] H. G. Tompkins and E. A. Irene. *Handbook of Ellipsometry*. William Andrew Publishing, 2005.

[106] Differential scanning calorimetry: first and second order transitions in polymers. http://www.colby.edu/chemistry/PChem/lab/DiffScanningCal.pdf.

[107] C. Schick. Differential scanning calorimetry (DSC) of semicrystalline polymers. *Analytical and Bioanalytical Chemistry*, 395(6):1589–1611, 2009.

[108] S. S. van Bavel, M. Barenklau, G. de With, H. Hoppe, and J. Loos. P3HT/PCBM bulk heterojunction solar cells: impact of blend composition and 3D morphology on device performance. *Advanced Functional Materials*, 20(9):1458–1463, 2010.

[109] H. J. C. Berendsen, D. van der Spoel, and R. van Drunen. Gromacs: A message-passing parallel molecular dynamics implementation. *Computer Physics Communications*, 91(1-3):43 – 56, 1995.

[110] E. Lindahl, B. Hess, and D. van der Spoel. Gromacs 3.0: a package for molecular simulation and trajectory analysis. *Molecular modeling annual*, 7:306–317, 2001.

[111] D. Van Der Spoel, E. Lindahl, B. Hess, G. Groenhof, A. E. Mark, and H. J. C. Berendsen. Gromacs: fast, flexible, and free. *Journal of Computational Chemistry*, 26(16):1701–1718, 2005.

[112] B. Hess, C. Kutzner, D. van der Spoel, and E. Lindahl. Gromacs 4: algorithms for highly efficient, load-balanced, and scalable molecular simulation. *Journal of Chemical Theory and Computation*, 4(3):435–447, 2008.

[113] M. J. Frisch, G. W. Trucks, H. B. Schlegel, G. E. Scuseria, M. A. Robb, J. R. Cheeseman, G. Scalmani, V. Barone, B. Mennucci, G. A. Petersson, H. Nakatsuji, M. Caricato, X. Li, H. P. Hratchian, A. F. Izmaylov, J. Bloino, G. Zheng, J. L. Sonnenberg, M. Hada, M. Ehara, K. Toyota, R. Fukuda, J. Hasegawa, M. Ishida, T. Nakajima, Y. Honda, O. Kitao, H. Nakai, T. Vreven, J. A. Montgomery, Jr., J. E.

Peralta, F. Ogliaro, M. Bearpark, J. J. Heyd, E. Brothers, K. N. Kudin, V. N. Staroverov, R. Kobayashi, J. Normand, K. Raghavachari, A. Rendell, J. C. Burant, S. S. Iyengar, J. Tomasi, M. Cossi, N. Rega, J. M. Millam, M. Klene, J. E. Knox, J. B. Cross, V. Bakken, C. Adamo, J. Jaramillo, R. Gomperts, R. E. Stratmann, O. Yazyev, A. J. Austin, R. Cammi, C. Pomelli, J. W. Ochterski, R. L. Martin, K. Morokuma, V. G. Zakrzewski, G. A. Voth, P. Salvador, J. J. Dannenberg, S. Dapprich, A. D. Daniels, Ö. Farkas, J. B. Foresman, J. V. Ortiz, J. Cioslowski, and D. J. Fox. Gaussian 09. Gaussian Inc. Wallingford CT 2009.

[114] R. Dennington, T. Keith, and J. Millam. Gaussview Version 5. Semichem Inc. Shawnee Mission KS 2009.

[115] W. L. Jorgensen, D. S. Maxwell, and J. Tirado-Rives. Development and testing of the OPLS all-atom force field on conformational energetics and properties of organic liquids. *Journal of the American Chemical Society*, 118(45):11225–11236, 1996.

[116] W. L. Jorgensen and N. A. McDonald. Development of an all-atom force field for heterocycles. Properties of liquid pyridine and diazenes. *Journal of Molecular Structure: THEOCHEM*, 424(1-2):145 – 155, 1998.

[117] N. A. McDonald and W. L. Jorgensen. Development of an all-atom force field for heterocycles. Properties of liquid pyrrole, furan, diazoles, and oxazoles. *The Journal of Physical Chemistry B*, 102(41):8049–8059, 1998.

[118] R. C. Rizzo and W. L. Jorgensen. OPLS all-atom model for amines: resolution of the amine hydration problem. *Journal of the American Chemical Society*, 121(20):4827–4836, 1999.

[119] M. L. P. Price, D. Ostrovsky, and W. L. Jorgensen. Gas-phase and liquid-state properties of esters, nitriles, and nitro compounds with the OPLS-AA force field. *Journal of Computational Chemistry*, 22(13):1340–1352, 2001.

[120] E. K. Watkins and W. L. Jorgensen. Perfluoroalkanes: conformational analysis and liquid-state properties from ab initio and monte carlo calculations. *The Journal of Physical Chemistry A*, 105(16):4118–4125, 2001.

[121] J. C. G. Pereira, C. R. A. Catlow, and G. D. Price. Molecular dynamics simulation of methanolic and ethanolic silica-based sol-gel solutions at ambient temperature and pressure. *The Journal of Physical Chemistry A*, 106(1):130–148, 2002.

[122] E. Kurita, H. Matsuura, and K. Ohno. Relationship between force constants and bond lengths for CX (X = C, Si, Ge, N, P, As, O, S, Se, F, Cl and Br) single and multiple bonds: formulation of badger's rule for universal use. *Spectrochimica Acta Part A: Molecular and Biomolecular Spectroscopy*, 60(13):3013 – 3023, 2004.

[123] T. A. Halgren. Maximally diagonal force constants in dependent angle-bending coordinates: Part I. Mathematical formulation. *Journal of Molecular Structure: THEOCHEM*, 163(0):431 – 446, 1988.

[124] T. A. Halgren. Maximally diagonal force constants in dependent angle-bending coordinates. II. Implications for the design of empirical force fields. *Journal of the American Chemical Society*, 112(12):4710–4723, 1990.

[125] P. M. Viruela and E. Viruela, R.and Orti. Difficulties of density functional theory in predicting the torsional potential of 2,2'-bithiophene. *International Journal of Quantum Chemistry*, 70(2):303–312, 1998.

CHAPTER 3

Probing the miscibility and phase behaviour of blends of poly(3-hexylthiophene) and fullerene multi-adducts using photoluminescence spectroscopy and differential scanning calorimetry

In this chapter, we focus on the P3HT:multi-adduct fullerene system in order to understand the effect of the fullerene chemical structure on the blend microstructure development. We firstly review the properties of P3HT:multi-adducts blends and solar cells (section 3.2). Secondly, we use a complementary set of techniques: transmission electron microscopy, grazing-incidence X-Ray diffraction, UV-vis absorption and steady-state and ultra-fast time-resolved photoluminescence spectroscopy to characterise the microstructure of P3HT:PCBM, P3HT:bis-PCBM, and P3HT:tris-PCBM blends (section 3.3). We consider the miscibility of the fullerenes with P3HT in the solid state and the extent of phase separation (section 3.4). We use differential scanning calorimetry to investigate the phase behaviour of blends of P3HT with PCBM and its higher adducts, so establishing temperature composition phase diagrams for the individual binary systems. We relate the phase behaviour of the P3HT:fullerene blends with the device performances reported previously [126, 127](section 3.5).

We propose two mechanisms of microstructure development within blends of P3HT with PCBM multi-adducts. The first originates from crystallization through thermal annealing and leads to high solar cell performances, while the second originates from the low solubility of fullerenes within the amorphous phase of the polymer and leads to poorer solar cell performances even after annealing procedures. This chapter highlights the importance of the solubility of the fullerenes in the amorphous part of the polymer as a factor to control the microstructure of polymer:fullerene blends. Moreover, this chapter points out that the ability of the fullerene to crystallise can help to overcome a too high solubility.

This work has been published in ACS nano [128].

Section 3.1

Motivations

The required LUMO offset between donor and acceptor to get efficient electron transfer is believed to lie in the range of 0.3 to 0.5 eV [129, 130]. However, in the case of P3HT:PCBM, this offset is around 1.1 eV. This high offset results in loss in electrochemical potential energy. From this perspective, modifying the energy levels (HOMO, LUMO) of the blend components to improve energy level alignment can lead to higher efficiencies [131, 130].

New low-bandgap polymer donors have resulted in efficiencies over 8% [132], partly as a result of a broader absorption profile leading to an increase in photocurrent and partly due to improved energy level alignment. However, if lots of newly-synthesised low bandgap polymers (polythiophene derivatives and push-pull copolymers: benzodiathiazole, pyrrolopyroledione and benzodiathiazole derivatives) have the bandgap in the desired range, it does not ensure good performances. A review of the latest conjugated low-bandgap polymers and their solar cell performances can be found in reference [133]. For example, the chemical substitution of the sulphur atom in the thiophene ring by a selenium atom leads to a reduction of the band gap from 1.9 eV (P3HT) to 1.6 eV (poly(3-hexylselenophene) P3HS) [134]. However, even though a more pronounced absorption in the red than in the case of P3HT have been observed, the performances of the optimised solar cell do not overcome the performances of P3HT:PCBM solar cells [135] .It has been explained by a lower crystallinity of P3HS than P3HT when blended with PCBM, leading to a larger amount of PCBM dissolve in the amorphous part of the polymer [136, 137]. Crystallization is known to drive phase separation processes, while the amorphous (or molecularly less ordered) regions of the donor polymers can accommodate a large fraction of solubilised acceptor molecules [138]. These observations are consistent with other studies which demonstrate that bulk heterojunction solar cells exhibit a strong dependence of the power conversion efficiency upon composition and processing conditions (such as thermal treatment), suggesting that the active layer microstructure indeed plays a critical role in the performance of devices [139, 140, 141, 142].

In contrast to the wide variety of p-type polymers under development, fullerenes remain the acceptors of choice in the best performing OPV devices. Recently, a number of new fullerene derivatives have been synthesized in order to enhance device

performances. The main strategy has been to raise the fullerene LUMO level through side group attachment in order to decrease the electrochemical loss when charges are transferred from polymer to fullerene and increase the open circuit voltage concomitantly [131, 130].

Multiple side group attachments hardly change the electronic structure of fullerenes. It only tunes their HOMO and LUMO positions. Consequently, fullerene multi-adducts are a system of choice to study the effects of multiple side chains and thus, disorder on the microstructure of blends and on device performances.

In this chapter, we focus on P3HT blended with PCBM and with the bis and tris adducts of PCBM. In this system, the rise in fullerene LUMO do not result in an improvement of the power conversion efficiency of the devices but even lead to very poor efficiencies in the case of the tris adducts of PCBM. We want to find out whether different performance of fullerenes as acceptors can be explained by differences in phase behaviour and microstructure development. First, we use transmission electron microscopy to investigate the microstructure explicitly and fluorescence spectrocopies to investigate the microstructure implicitly. Then, we use differential scanning calorimetry to study the phase behaviour of the three systems.

Section 3.2

Background: fullerene multi-adducts blended with P3HT - a decrease in electrochemical loss that does not translate into an improvement of power conversion efficiency

---

The bis adducts of PCBM (in the following, it will be referred to as bis-PCBM - see Figure 2.8) was first reported by Lenes *et al.* as potential acceptor for organic solar cells [126] with a LUMO level increased by about 100 meV relative to PCBM [143, 126, 144]. Even though previous studies using a mixture of higher fullerene adducts as acceptor failed to demonstrate good power-conversion efficiencies, using the separated bis-PCBM fraction led to efficiencies of 4.5% [126]. This underlines the significant influence of disorder. As a matter of fact, some disorder remains in bis-PCBM because bis-PCBM is still a mix of isomers [145]. In later work [127, 144], the tris adduct of PCBM (in the following, it will be referred to as tris-PCBM - see Figure 2.8) was also studied.

Upon replacing PCBM with bis-PCBM in blends with P3HT, a significant increase in open-circuit voltage (V_{oc}) has been indeed observed, albeit with a slight decrease in short-circuit current (J_{sc}) [126, 127, 144]. When bis-PCBM is replaced with tris-PCBM, a slight increase in V_{oc} is again observed but J_{sc} reduces drastically [126, 127, 144]. Since no significant decrease in charge generation has been found with higher adduct fullerenes [144], the decrease in J_{sc} for blends containing higher-adduct fullerenes and the relatively small effect of LUMO level rise on V_{oc} in the case of tris-PCBM have been attributed to the decrease in electron mobility of the higher-adduct fullerenes in comparison to PCBM [126, 127, 144].

The observed decrease in electron mobility was explained on the one hand by the increasing disorder in electronic states for higher adduct fullerenes [127, 145] which results in electronic traps and on the other hand by the fact that adding side chains prevent close packing of the fullerene derivatives [144, 146].

In addition, it has been argued that the three fullerenes feature different blend microstructures; thermal annealing leads to the appearance of micrometer-sized fullerene aggregates in the case of PCBM only, while blend films containing the higher-adduct fullerenes remain essentially featureless [144]. Even more pronounced differences in microstructure have been observed when the fullerene derivatives were used in combination with polymers such as poly(2-methoxy-5-(3'-7'-dimethyloctyloxy)-1,4-phenylenevinylene) (MDMO-PPV) and poly[(9,9-dioctylfluorenyl-2,7-diyl)-co-5,5-4',7'-di-2-thienyl-2',1',3'-benzothiadiazole] (APFO-3). In particular, bis-PCBM blended with the latter two polymers results in poor solar cell performances in comparison with PCBM based devices, in contrast to the case of P3HT-based blends. Since MDMO-PPV and APFO-3 are less crystalline than P3HT, the poorer device performances suggest that the relative effect of bis-PCBM on solar cell performance for different polymers may be related to the tendency of the polymers to crystallize [147].

Section 3.3

Characterisation of the microstructure of P3HT:fullerene multi-adduct blend films

3.3.1 Structural characterisation

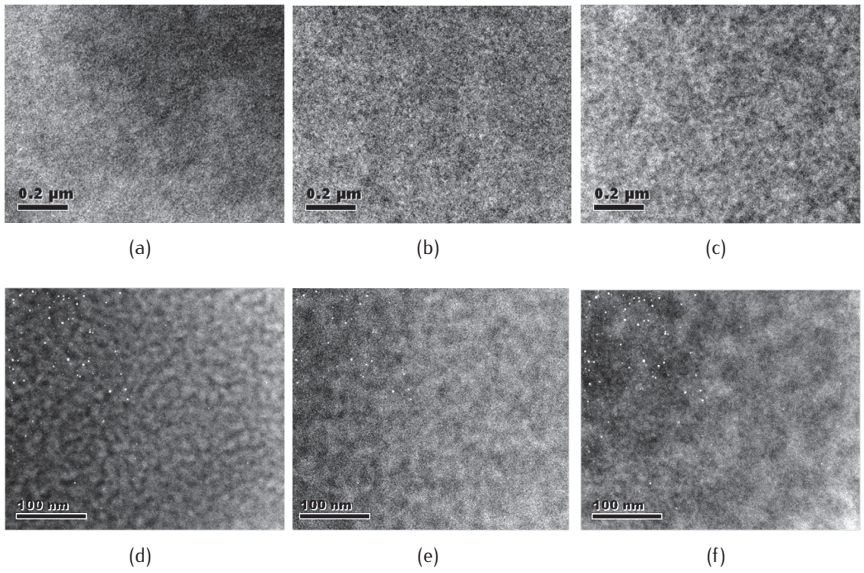


Figure 3.1: TEM micrographs of as-spun (a-c) and annealed (d-f) ~85 mol% P3HT blend films of P3HT:PCBM (a,d),P3HT:bis-PCBM (b,e), and P3HT:tris-PCBM (c,f). TEM measurements by Simon P. King and Andrew MacLachlan.

TEM micrographs of as-spun and annealed P3HT:fullerene films comprising 50 wt% P3HT (~85 mol% P3HT) [1] are displayed in Figure 3.1. The blends containing

[1] mol% P3HT will be used from here on for clarity and refers to the ratio of the number of moles of 3HT monomers to the total number of moles in the blend.

higher adduct fullerenes seem to feature a rougher phase separation compared to P3HT:PCBM binaries. Thermal treatment promotes phase separation for P3HT:PCBM, while no significant change is observed for blends containing higher-adduct fullerenes. However, no quantitative information on either the domain composition or the domain size can be deduced from the TEM data.

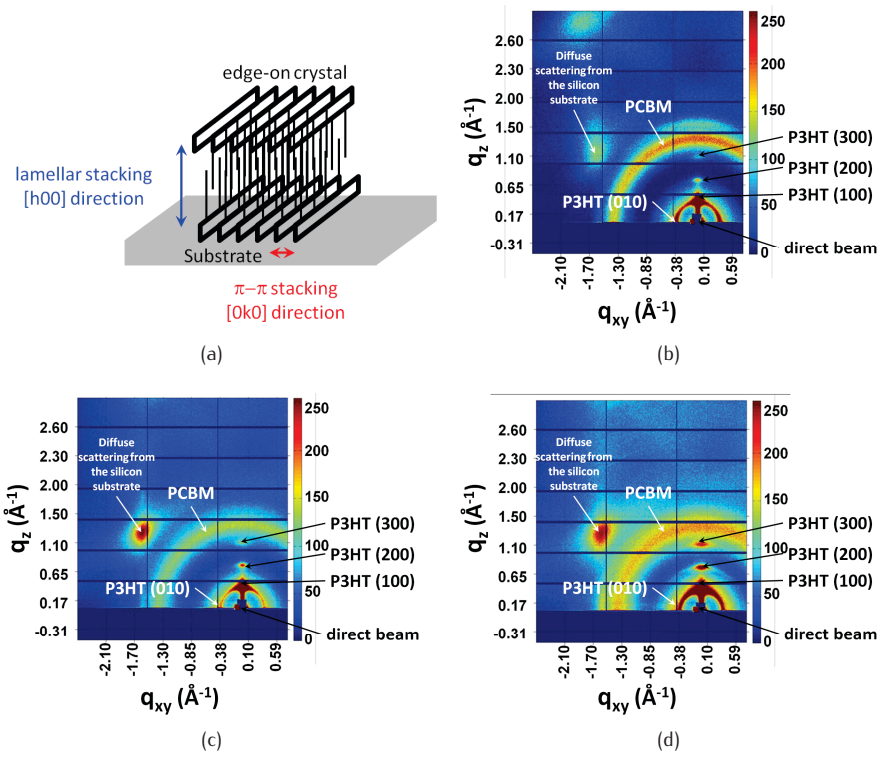


Figure 3.2: (a) Proposed monoclinic unit cell for P3HT. GIXRD patterns of as-spun films: (b) P3HT:PCBM, (c) P3HT:bis-PCBM, and (d) P3HT:tris-PCBM (1:1). The diffuse peak at $q_{xy} = 1.6\text{Å}^{-1}$, $q_z = 1.2\text{Å}^{-1}$ arises from thermal diffuse scattering from the silicon substrate. GIXRD measurements in collaboration with Tiziano Agostinelli, Ellis Pires and J. Emyr Macdonald.

The crystalline phases of the blends can be probed by GIXRD (see Figure 3.2). We propose a monoclinic crystal unit cell for P3HT. The crystal structure of P3HT is not disrupted by the presence of the fullerenes (see Figure 3.3 and Table 3.1). Thus, no fullerene intercalation within the P3HT crystalline structure or co-crystallisation occurs. Furthermore, P3HT crystalline domains of P3HT:fullerenes blends are on average of a similar size, of the order of 10 nm (see Table 3.1). However, no information can be deduced on the degree of phase separation in the blends from the GIXRD data.

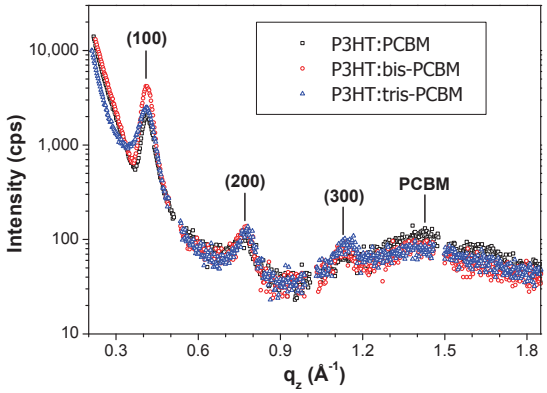


Figure 3.3: GIXRD out-of-plane profiles of as-spun films of P3HT:PCBM, P3HT:bis-PCBM and P3HT:tris-PCBM (1:1). (n00) peaks are P3HT peaks.

Table 3.1: Fit parameters of GIXRD line profiles and estimated P3HT domain sizes of as-spun P3HT:PCBM, P3HT:bis-PCBM and P3HT:tris-PCBM (1:1). P3HT diffraction peaks (i00) have been modelled by Gaussians $\left(I = A\exp\left\{-\left(\frac{q-q_0}{w}\right)^2\right\}\right)$. P3HT domain sizes have been estimated using the Scherrer equation $\left(\frac{0.9*2\pi}{FWHM*cos(\theta)}\right)$ where the full width at half maximum $FWHM = 2\sqrt{ln(2)}w$

	P3HT diff. peaks	PCBM	bis-PCBM	tris-PCBM
x_0(Å^{-1})	(100)	0.414	0.413	0.412
w(Å^{-1})	(100)	0.030	0.027	0.025
A (cps)	(100)	1837	4103	1438
domain size (nm)	(100)	11.3	12.6	13.6

3.3.2 Photophysical characterisation

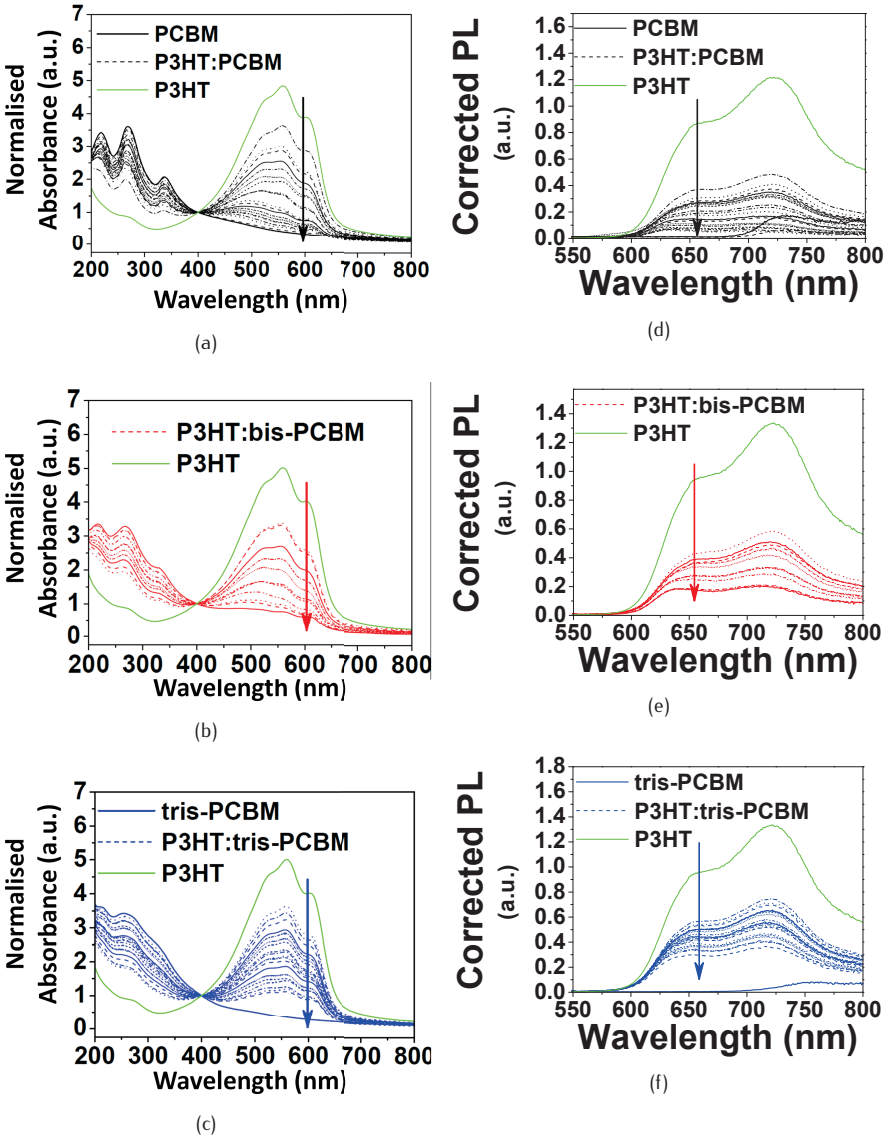


Figure 3.4: Absorption (a-c) and steady-state PL (d-f) profiles for as-spun P3HT:PCBM (a,d), P3HT:bis-PCBM (b,e), and P3HT:tris-PCBM (c,f) blends. The absorption traces are normalised at 400 nm for clarity. The excitation wavelength for PL is 510 nm. The arrows show increasing acceptor concentration from 0 to 100 mol% P3HT

Steady-state photoluminescence spectroscopy has previously been used to infer the degree of phase separation in blends [148]. In a similar manner, we have performed steady-state PL measurements of blend films of different polymer:fullerene ratios (see Figure 3.4). No variation in the shape of the polymer emission spectrum is observed upon adding fullerenes in the blend samples, implying that the emission between 640 and 696 nm is due solely to the polymer and not to any other species such as a charge transfer state. Therefore, any difference in quenching ability could be attributed to one or more of three effects: a difference in polaron generation yield, a difference in non-radiative decay pathways, or a difference in microstructure. Since steady-state PL provides us with the time-integrated PL signal, it cannot distinguish between the decay mechanisms responsible for P3HT emission quenching. Therefore, we have also performed ultrafast time-resolved PL spectroscopy measurements. Ultra-fast spectroscopy has the advantage of allowing the direct observation of the emissive decay dynamics of the initial excited-state species in the blend films.

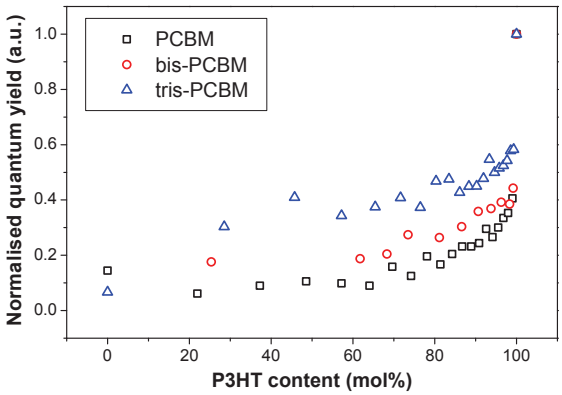


Figure 3.5: Normalised quantum yield of as-spun P3HT:fullerene films of different compositions. The excitation wavelength was 510 nm, and the fluorescent yield was calculated between 640 and 696 nm.

Table 3.2: Ratio of initial fluorescence intensity of as-spun P3HT:fullerene blends with respect to neat P3HT films from fluorescence up-conversion measurements. Data from Luke X. Reynolds and Annalisa Bruno.

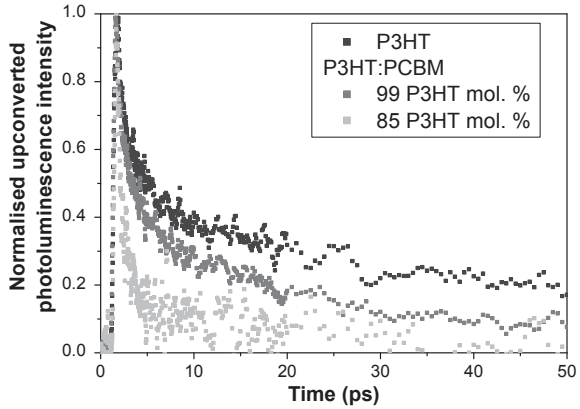
		P3HT:PCBM	P3HT:bis-PCBM	P3HT:tris-PCBM
as-spun	99 mol%	0.89	0.95	0.96
	85 mol%	0.27	0.35	0.36
annealed	85 mol%	0.33	0.35	0.35

In Figure 3.5, the normalized quantum yield is plotted for blends of P3HT and the three fullerenes as a function of the P3HT content. The quenching of the polymer emission in as-spun blends comprising all three fullerenes is seen to become more

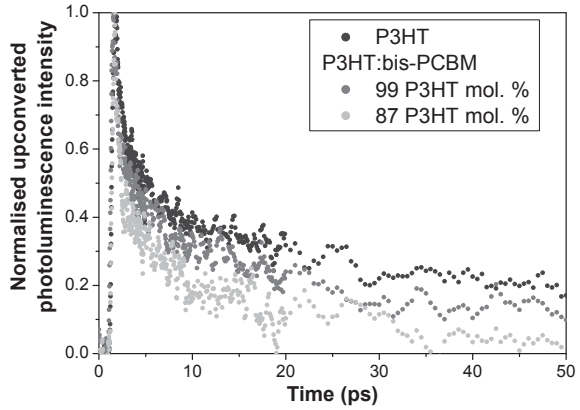
efficient upon increasing the acceptor content. However, for blends of the same acceptor content, it is evident from our data that PCBM consistently quenches the polymer emission more than bis-PCBM, which in turn quenches much more than tris-PCBM. The same trend is observed in the initial peak intensity of the ultra-fast PL (see Table 3.2) for the as-spun films. In contrast, for the annealed films, the intensity ratio is similar for all fullerenes (see Table 3.2).

The ultrafast time-resolved emission decay traces are plotted in Figure 3.6. Comparing the time decay curves, it can be observed that PCBM quenches the polymer emission more efficiently than bis-PCBM, which in turn quenches the polymer emission more efficiently than tris-PCBM. The time-resolved photoluminescence decays are not mono-exponential but can be well modelled with a sum of two exponentials suggesting phenomena on different time scales [149, 150, 151]. The fast ($<$3 ps) and slow ($>$3 ps) time decays are plotted as a function of the blend composition in Figure 3.7.

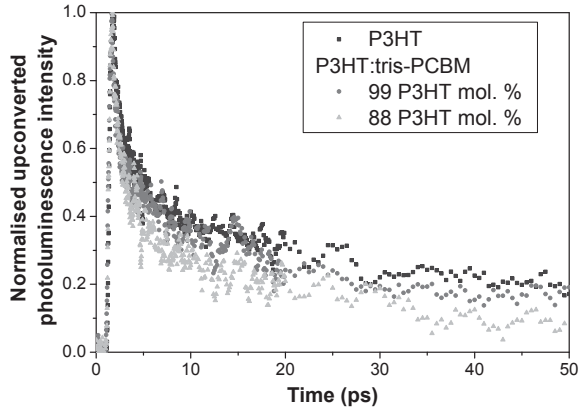
The fast-phase dynamics remain approximately constant over all blend compositions, whereas the slow-phase time decay decreases upon increasing the relative content of quencher. In addition, it is observed that even at low fullerene contents (99 mol % P3HT) the PL is quenched more slowly for blends comprising higher adduct fullerenes (as has been shown previously for PCBM and bis-PCBM) [152], and this difference in quenching efficiency increases when increasing the fullerene content. Upon annealing, decay times observed for P3HT:PCBM blends are lengthened, while the decay times observed for P3HT blended with higher adducts seem not to be significantly affected by the annealing procedure. As a result, after annealing, decay times for films containing high loadings of PCBM and bis-PCBM are similar while those for tris-PCBM remain longer.



(a)



(b)



(c)

Figure 3.6: Ultra-fast time-resolved emission decay traces of as-spun blends of (a) P3HT:PCBM, (b) P3HT:bis-PCBM, and (c) P3HT:tris-PCBM. The excitation wavelength was 400 nm, and the P3HT emission was detected at 650 nm. Fluorescence up-conversion measurements by Luke X. Reynolds and Annalisa Bruno.

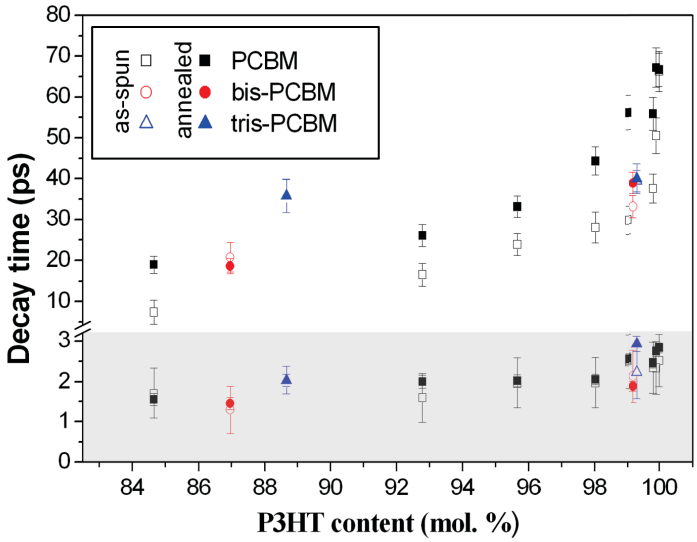


Figure 3.7: Time components of the bi-exponential decay fits to the ultrafast fluorescence up-conversion decays for as-spun (open shapes) and annealed (solid shapes) films showing the fast-phase decay rate (<3 ps) and the slow-phase decay rate (>3 ps). Data from Luke X. Reynolds and Annalisa Bruno.

Section 3.4

Discussion: different mechanisms of microstructure development

---

The observed difference in quenching ability of the fullerenes could, in principle, be attributed to the differing electron affinities of the fullerenes and hence different driving forces for electron transfer. However, even for P3HT:tris-PCBM, the LUMO energy difference is ~0.8 eV, which far exceeds the 0.3-0.5 eV thought to be needed for efficient charge separation [153]; indeed, similar polaron generation yields have been observed for blend films of P3HT with all three fullerenes [144].

We note that some differences in quenching ability could arise from variations in charge transfer rate due to variations in the donor-acceptor interface distances. However, in studies of similar polymer:fullerene systems, differences in quenching have been mainly attributed to microstructure, a conclusion further supported by the transient absorption data on P3HT: PCBM and bis- and tris-PCBM published by Faist *et al.*[144] and the temperature-dependent transient absorption data on P3HT blended with low concentration of fullerenes such as PCBM and bis-PCBM published by Busby *et al.* [154]. In the latter study, the authors found that the recombination rate is strongly dependent on the acceptor functionalisation at low temperature, which they attributed to a dielectric shielding effect of the functional group that leads to an increase in donor-acceptor distance and to a decrease in back-transfer from the neighbouring donor polymer chains. However, this recombination dependence is not as pronounced at room temperature [154]. Further insight is provided by the independence of the fast phase of the ultrafast PL decay data on the fullerene adduct. This fast phase has previously been related to the changes in conformation of P3HT polymer chains [149, 155]. The fact that the fast-phase decay remains constant over all blend compositions and with all three fullerene acceptors suggests that the non-radiative decay pathways are similar for all three fullerene acceptors and so are unlikely to be responsible for any difference in quenching ability between the three fullerenes. Therefore, the difference in quenching ability is more likely to be due to a difference in microstructure.

Since steady-state PL provides us with the time integrated PL signal, it is very sensitive to the initial (<150 fs) PL intensity and less to the decay, which explains why the trends, observed by steady-state PL and the amplitude of the initial peak intensity of

the ultrafast PL, are similar. This pre-150 fs time scale quenching is more likely to be due to the fraction of excitons that are formed within the quenching radius of fullerenes [156]. Thus, the less quenched polymer emission for as-spun blends comprising higher adducts suggests that the higher adducts are less well-dispersed within P3HT. Since there is no evidence of fullerene intercalation (or co-crystallization) with P3HT as deduced from GIXRD and since the crystalline domains of P3HT:PCBM derivative blends are on average of a similar size as deduced from GIXRD, it is likely to be the solubility of the fullerene derivatives in the amorphous phase of P3HT that differs. The similar PL intensity for all three fullerenes after thermal treatment suggests that after annealing all three fullerenes are dispersed to a comparable extent within P3HT.

The slow phase observed in ultrafast spectroscopy may be attributed to exciton hopping processes between segments of the same polymer chain or to segments of an adjacent chain and so reflects the diffusive movement of the exciton before it reaches a polymer:fullerene heterojunction [157, 158]. In as-spun films, the lengthening of the slow-phase decay by replacing PCBM with higher-adduct fullerenes points toward a longer average distance from the point of exciton generation to a heterojunction in higher-adduct blends than in P3HT:PCBM. After annealing, excitons in blends containing PCBM and bis-PCBM travel on average the same distance before being dissociated, and this distance remains shorter than the average distance that an exciton has to travel in P3HT:tris-PCBM blends to reach a heterojunction.

Thermal annealing is known to promote demixing in P3HT:PCBM system through crystallization-driven phase segregation [159]. This is consistent with our photophysical data. However, in as-spun films, rougher phase separation of blends containing higher-adduct fullerenes has been observed by TEM, while the size of P3HT crystal domains, as probed by GIXRD, is similar for blends containing all three fullerene derivatives. Therefore, demixing cannot solely be driven by crystallization. From our steady-state and ultrafast PL data, we propose a second demixing mechanism, namely, demixing within the amorphous phase of as-spun blends containing higher-adduct fullerenes. This demixing is due to less solubility of higher-adduct fullerenes within the amorphous phase of P3HT. In other words, it is likely that crystalline P3HT, a fullerene amorphous phase, a P3HT amorphous phase, and a "solid solution"of molecularly relatively unordered fullerenes and P3HT coexist in the blends containing higher-adduct fullerenes. Furthermore, thermal treatments do not seem to affect the microstructure of P3HT:tris-PCBM blends and only slightly affect P3HT:bis-PCBM blends. This is consistent with a phase segregation in blends containing higher-adduct fullerenes occurring in the amorphous phase and being almost independent of crystallization processes. Because steady-state PL but not ultrafast dynamics is slightly affected by thermal annealing in the case of bis-PCBM, it cannot be excluded that during annealing some bis-PCBM diffuses through P3HT amorphous

phase to form some small crystallites. This diffusion process, which is expected to be of small extent, should lead to slightly less bis-PCBM dissolved in the P3HT amorphous phase but should not modify the distance an exciton has, on average, to travel from the photoexcitation location to a heterojunction. Schematics depicting the microstructures of the various blends, as-spun and annealed, in agreement with our photophysical and TEM data are presented in Figure 3.8. The observed difference in microstructure reflected by our photophysical study can be explained in terms of increased repulsion between the polymer and higher-adduct fullerenes compared to those that exist between the polymer and lower adduct fullerenes. In the following section, we will use thermal analysis to study the polymer:fullerene interactions.

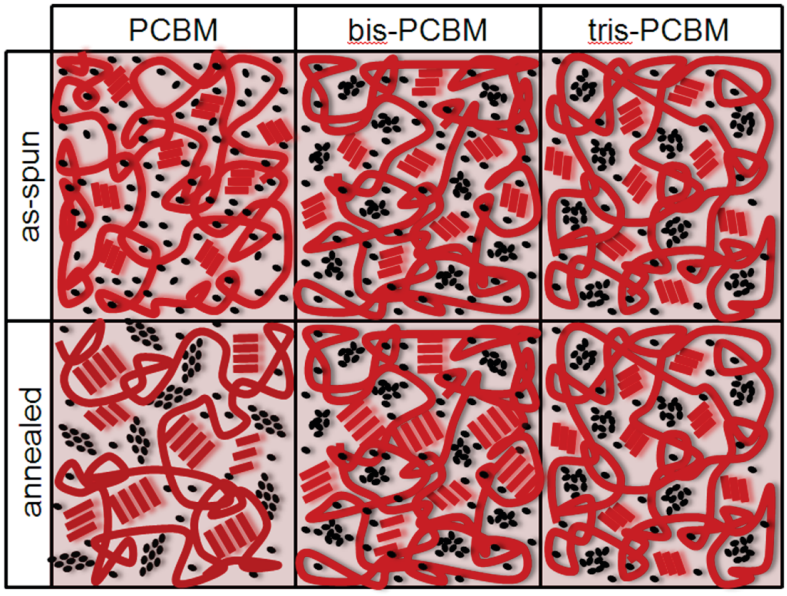


Figure 3.8: Schematics depicting the proposed microstructure of as-spun and annealed films of P3HT:PCBM, P3HT:bis-PCBM, and P3HT:tris-PCBM.

Section 3.5

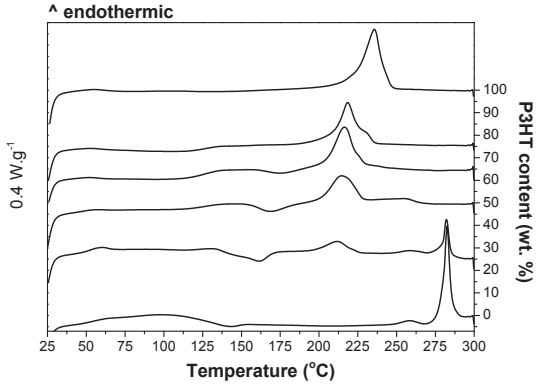
Characterisation of the phase behaviour of P3HT:fullerene blend films

---

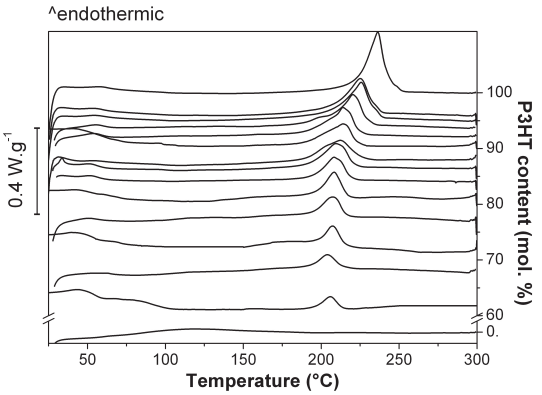
The photophysical study described above suggests that the fullerene-P3HT molecular interaction is altered by modifying the chemical structure of the fullerene. Further information can be obtained from thermal analysis, especially DSC. Müller *et al.* [160] found using DSC that the P3HT:PCBM system exhibits a eutectic phase behaviour with a eutectic composition at 91 mol % P3HT and a eutectic temperature around 200 °C. In this section, we characterise blends of P3HT with higher adduct fullerenes using identical procedures; the resulting DSC thermographs of P3HT:PCBM, P3HT:bis-PCBM and P3HT:tris-PCBM blends are plotted in Figure 3.9. In contrast to PCBM, no melting endotherm corresponding to either bis-PCBM or tris-PCBM is observed, illustrating the low tendency to crystallize of these two PCBM derivatives [144, 146]. However, for both systems, the addition of fullerenes results in a noticeable depression of the melting temperature of P3HT as previously observed adding PCBM to P3HT [160]. The effect is stronger for blends of P3HT and bis-PCBM than for P3HT:tris-PCBM and stronger still for P3HT:PCBM, indicating stronger interactions between the two components in P3HT:PCBM blends than in P3HT:bis-PCBM and P3HT:tris-PCBM binaries.

From our thermal analysis, we further conclude that, similar to the P3HT:PCBM system, bis- and tris-PCBM when blended with P3HT exhibit a eutectic phase behaviour. This is evident from the endotherms observed at approximately 210 and 220 °C for blends based on bis- and tris-PCBM, respectively (leading at higher polymer concentrations to an endothermic "shoulder"at the low-temperature regime of the P3HT melting endotherm) (see Figure 3.9). In order to better resolve the eutectic temperature, we performed additional DSC runs using a heating rate of 2 °C/min (see Figure 3.10). On the basis of this data set, the eutectic composition and temperature can be assigned to be 80 mol % P3HT and 220 °C for P3HT:bis-PCBM blends and lower than 65 mol % P3HT and < 220 °C for P3HT:tris-PCBM. For comparison, the eutectic composition for P3HT:PCBM is 91 mol % at a temperature of 225 °C (see Figure 3.11). The fact that the eutectic composition is shifted to higher fullerene

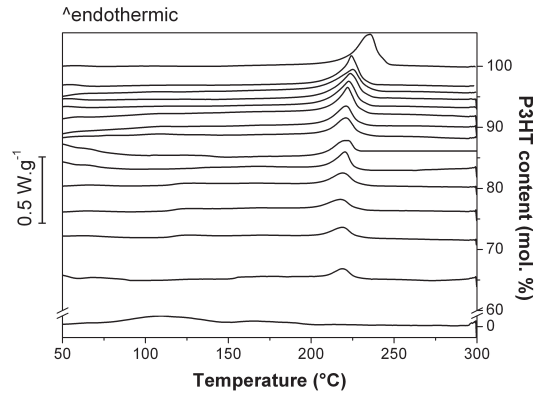
content and the eutectic temperature is lowered when increasing the number of side chains attached to the fullerene cage may result from both weaker interactions between fullerene and P3HT [144, 146] as well as lower fullerene melting temperature.



(a)



(b)



(c)

Figure 3.9: DSC scans of (a) P3HT:PCBM, (b) P3HT:bis-PCBM and (c) P3HT:tris-PCBM films of different compositions at a heating rate of 10 °C/min.

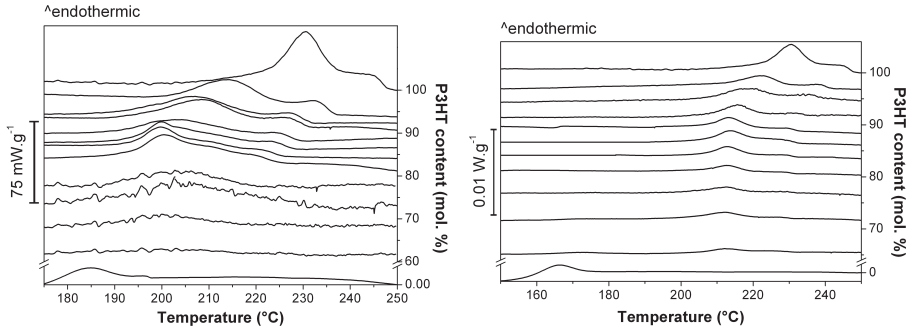


Figure 3.10: DSC scans of (a) P3HT:bis-PCBM and (b) P3HT:tris-PCBM films of different compositions at a heating rate of 2°C/min. The neat fullerene signal results from reseed experiments where the samples have been heated three times up to 160°C in order to allow recrystallisation around existing nuclei before running the 2°C/min scan.

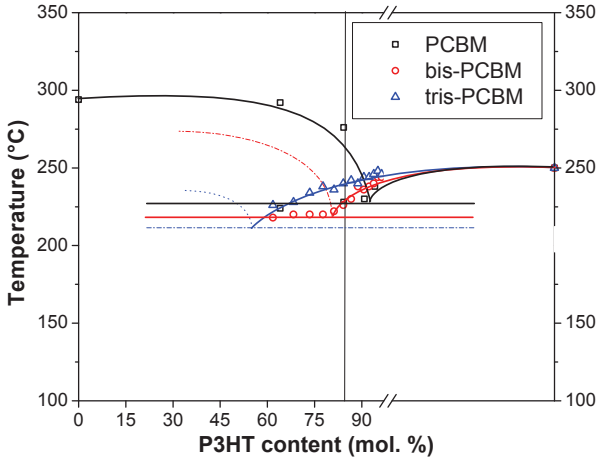


Figure 3.11: P3HT:PCBM, P3HT:bis- and tris-PCBM non-equilibrium phase diagrams. The points represent the melting temperatures extracted from the DSC scans. The dashed lines are extrapolated. The vertical line corresponds to a composition of 50 wt % P3HT.

Compositions of slightly lower polymer content than the eutectic composition are usually found to be attractive for high solar cell performance because at these particular compositions the finest phase separation of the crystalline parts of the two components can be expected, and this is combined with the presence of fullerene "primary crystals". The excess fullerene is expected to enhance the electron mobility due to interconnection of larger electron PCBM conducting domains [139], while hole percolation is still facilitated by the polymer component of the mixed phase [155].

While a P3HT content of 85 mol % (50 wt % P3HT) is in the hypo-eutectic regime for P3HT:PCBM blends, P3HT contents of 85 mol % are in the hyper-eutectic regime for blends comprising higher-adduct fullerenes. Therefore, the primary crystals of fullerene that appear to be critical for efficient electron transport are less likely to form and electron collection may therefore be limited. Indeed, device measurements show that annealed blends containing bis-PCBM require a higher fullerene content to maximize the photocurrent (see Figure 3.12). This may explain, at least partially, the small decrease in J_{sc} observed when replacing PCBM with bis-PCBM in blends of 50 wt % polymer and the larger decrease in J_{sc} when replacing bis-PCBM with tris-PCBM [144] and helps to explain the observed decrease in J_{sc} when replacing PCBM by either bis-PCBM or tris-PCBM [126, 127].

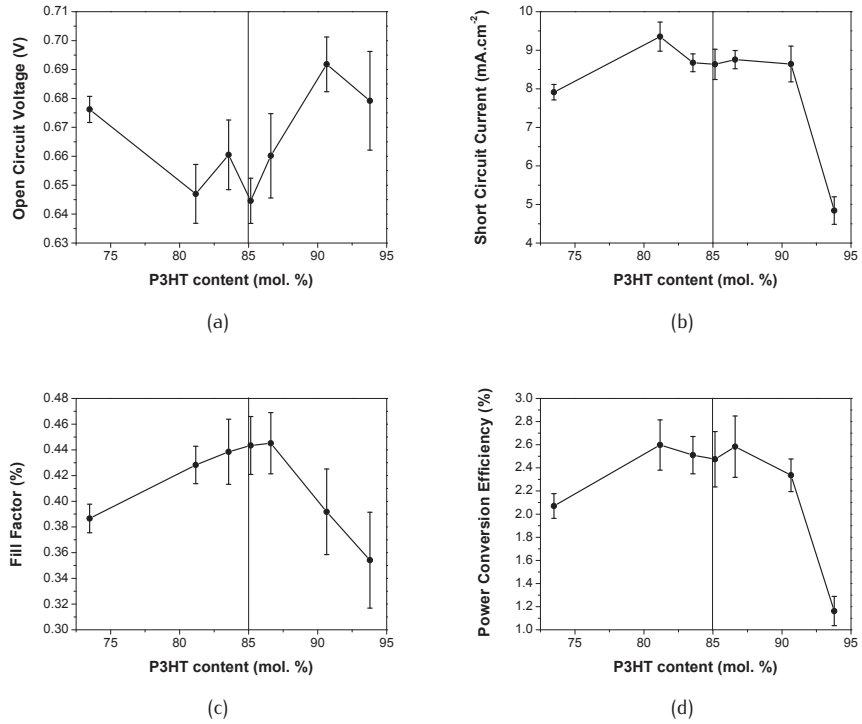


Figure 3.12: Open circuit voltage V_{oc} (a), short circuit current J_{sc} (b), fill factor FF (c) and power conversion efficiency PCE (d) as a function of P3HT content (mol %) averaged on five ITO/PEDOT:PSS/P3HT:bis-PCBM/Al devices under illumination of 900 W.m^2 (AM 1.5) for each concentration. The devices have been annealed at 150 °C for 30 minutes under nitrogen atmosphere. The grey lines represent the optimum composition for P3HT:PCBM which is known to be 50 wt% (~85 mol%). The devices based on tris-PCBM giving poor PCE, the variations of V_{oc}, J_{sc}, FF and PCE are within the experimental errors. Data from Mark A. Faist.

Section 3.6

Conclusion

We have used a complementary set of techniques to elucidate the microstructure development and the phase behaviour of blends of P3HT and fullerene derivatives. TEM reveals a rougher phase separation for the higher-adduct fullerenes for as-spun blends. We attribute this rougher phase separation to the lower solubility of higher-adduct fullerenes in the amorphous phase of P3HT. This can be deduced from the fact that higher-adduct fullerenes lead to less efficient PL quenching than observed for P3HT:PCBM, while no evidence of co-crystallisation was found in GIXRD, and the crystalline P3HT domain sizes are similar for all three systems. Thermal treatment promotes demixing of P3HT:PCBM as evidenced through the TEM micrographs, the decrease of PL quenching, and the lengthening of the PL decay times. In contrast, only small changes are observed for blends containing higher-adduct fullerenes during the annealing procedure (the PL quenching of bis-PCBM decreases slightly, while the PL quenching of tris-PCBM remains essentially identical to the one of as-spun films). Annealing procedures do not lead to further phase separation in the case of higher-adduct fullerene-based blends. This has been explained by the comparatively low solubility of bis- and tris-PCBM in P3HT, as well as their low tendency to crystallize. Therefore, we propose that the origins of phase separation are different in the three systems. In P3HT:PCBM blends, the two components phase segregate due to crystallization of both components as facilitated by thermal treatments. In contrast, for blends containing higher adducts, the phase separation originates from the low solubility of the fullerenes in the amorphous phase of P3HT, leading to partial demixing of the amorphous phases. Thermal treatment seems to lead to slightly larger demixing in the case of bis-PCBM but no significant differences have been observed between blends of P3HT:tris-PCBM before and after annealing. The low solubility of higher-adduct fullerenes in the amorphous polymer fractions has been related to weaker interactions between fullerenes and polymer (evidenced through the lower P3HT melting point depression). The weaker interactions of P3HT with the higher-adduct fullerenes are thought to at least partly explain the shift of the eutectic composition toward higher fullerene content as well as the lower eutectic temperature found for these binaries compared to P3HT:PCBM. This shift in eutectic composition toward higher fullerene content make less likely the formation of fullerene primary crystals for the higher adduct fullerenes for 1:1 blend compositions. This may explain the larger and larger decrease in J_{sc} when adding more and more side chains and

thus, the poor power conversion efficiencies.

To summarise, we have found two mechanisms of microstructure development within blends of P3HT with PCBM, bis-PCBM, and tris-PCBM. The first originates from crystallization through thermal annealing and leads to high solar cell performances, while the second originates from the low solubility of fullerenes within the amorphous phase of the polymer and leads to poorer solar cell performances even after annealing procedures. The solubility of the fullerenes in the amorphous part of the polymer seems to be an important factor to control the microstructure of polymer:fullerene blends. However, the ability of the fullerene to crystallise can help to overcome a too high solubility like in the case of P3HT:PCBM.

This conclusion is consistent with the work that has been done by Treat *et al.* [161] where they decrease the solubility of the fullerene derivatives in the amorphous part of P3HS by shortening the side chains of the fullerenes. It has been previously reported that P3HS:PCBM solar cells were giving equal performances to P3HT:PCBM even if the absorption in the red was improved by the selenium substitution [135]. It has been attributed to a larger amount of PCBM dissolve in the amorphous part of P3HS [136, 137] or in other words to a too high solubility of PCBM in the amorphous part of P3HS. Thus, by optimising the solubility, they have been able to increase significantly the power conversion efficiency. Furthermore, the fact that we found an optimal composition for P3HT:bis-PCBM solar cells at composition slightly lower than the eutectic composition (shifted to higher fullerene content) is consistent with the work from Müller *et al* [160] on poly(3-alkylthiophene):PCBM blends.

Bibliography

[126] M. Lenes, G.-J. A. H. Wetzelaer, F. B. Kooistra, S. C. Veenstra, J. C. Hummelen, and P. W. M. Blom. Fullerene bisadducts for enhanced open-circuit voltages and efficiencies in polymer solar cells. *Advanced Materials*, 20:2116–2119, 2008.

[127] M. Lenes, S. W. Shelton, A. B. Sieval, D. F. Kronholm, J. C. Hummelen, and P. W. M. Blom. Electron trapping in higher adduct fullerene-based solar cells. *Advanced Functional Materials*, 19:3002–3007, 2009.

[128] Anne A. Y. Guilbert, Luke X. Reynolds, Annalisa Bruno, Andrew MacLachlan, Simon P. King, Mark A. Faist, Ellis Pires, J. Emyr Macdonald, Natalie Stingelin, Saif A. Haque, and Jenny Nelson. Effect of multiple adduct fullerenes on microstructure and phase behavior of P3HT:fullerene blend films for organic solar cells. *ACS Nano*, 6(5):3868–3875, 2012.

[129] B. C. Thompson and J. M. J. Frechet. Polymer-fullerene composite solar cells. *Angewandte Chemie International Edition*, 47:58–77, 2008.

[130] M .C.. Scharber, D. Mallbacher, M. Koppe, P. Denk, C. Waldauf, A. J. Heeger, and C. J. Brabec. Design rules for donors in bulk-heterojunction solar cells - towards 10% energy-conversion efficiency. *Advanced Materials*, 18(6):789–794, 2006.

[131] L. J. A. Koster, V. D. Mihailetchi, and P. W. M. Blom. Ultimate efficiency of polymer/fullerene bulk heterojunction solar cells. *Applied Physics Letters*, 88:093511, 2006.

[132] Yongye Liang, Zheng Xu, Jiangbin Xia, Szu-Ting Tsai, Yue Wu, Gang Li, Claire Ray, and Luping Yu. For the bright future–bulk heterojunction polymer solar cells with power conversion efficiency of 7.4%. *Advanced Materials*, 22(20):E135–E138, 2010.

[133] Pierre-Luc T. Boudreault, Ahmed Najari, and Mario Leclerc. Processable low-bandgap polymers for photovoltaic applications. *Chemistry of Materials*, 23(3):456–469, 2011.

[134] Martin Heeney, Weimin Zhang, David J. Crouch, Michael L. Chabinyc, Sergey Gordeyev, Rick Hamilton, Simon J. Higgins, Iain McCulloch, Peter J. Skabara, David Sparrowe, and Steve Tierney. Regioregular poly(3-hexyl)selenophene: a low band gap organic hole transporting polymer. *Chem. Commun.*, 0:5061–5063, 2007.

[135] A. M. Ballantyne, L. Chen, J. Nelson, D. D. C. Bradley, Y. Astuti, A. Maurano,

C. G. Shuttle, J. R. Durrant, M. Heeney, W. Duffy, and I. McCulloch. Studies of highly regioregular poly(3-hexylselenophene) for photovoltaic applications. *Advanced Materials*, 19(24):4544–4547, 2007.

[136] Amy M. Ballantyne, Toby A. M. Ferenczi, Mariano Campoy-Quiles, Tracey M. Clarke, Andrea Maurano, Kien Hon Wong, Weimin Zhang, Natalie Stingelin-Stutzmann, Ji-Seon Kim, Donal D. C. Bradley, James R. Durrant, Iain McCulloch, Martin Heeney, Jenny Nelson, Steve Tierney, Warren Duffy, Christian Mueller, and Paul Smith. Understanding the influence of morphology on poly(3-hexylselenothiophene):PCBM solar cells. *Macromolecules*, 43(3):1169–1174, 2010.

[137] Wing C. Tsoi, David T. James, Ester Buchaca Domingo, Jong Soo Kim, Mohammed Al-Hashimi, Craig E. Murphy, Natalie Stingelin, Martin Heeney, and Ji-Seon Kim. Effects of a heavy atom on molecular order and morphology in conjugated polymer:fullerene photovoltaic blend thin films and devices. *ACS Nano*, 6(11):9646–9656, 2012.

[138] Brian A. Collins, Eliot Gann, Lewis Guignard, Xiaoxi He, Christopher R. McNeill, and Harald Ade. Molecular miscibility of polymer-fullerene blends. *The Journal of Physical Chemistry Letters*, 1(21):3160–3166, 2010.

[139] Y. Kim, S. Cook, S. M. Tuladhar, S. A. Choulis, J. Nelson, J. R. Durrant, D. D. C. Bradley, M. Giles, I. McCulloch, C.-S. Ha, and M. Ree. A strong regioregularity effect in self-organizing conjugated polymer films and high-efficiency polythiophene:fullerene solar cells. *Nature Materials*, 5(3):197–203, 2006.

[140] Sukhbinder Rait, Shipra Kashyap, P.K. Bhatnagar, P.C. Mathur, S.K. Sengupta, and J. Kumar. Improving power conversion efficiency in polythiophene/fullerene-based bulk heterojunction solar cells. *Solar Energy Materials and Solar Cells*, 91(9):757 – 763, 2007.

[141] Tracey M. Clarke, Amy M. Ballantyne, Jenny Nelson, Donal D. C. Bradley, and James R. Durrant. Free energy control of charge photogeneration in polythiophene/fullerene solar cells: the influence of thermal annealing on P3HT/PCBM blends. *Advanced Functional Materials*, 18(24):4029–4035, 2008.

[142] Panagiotis E. Keivanidis, Tracey M. Clarke, Samuele Lilliu, Tiziano Agostinelli, J. Emyr Macdonald, James R. Durrant, Donal D. C. Bradley, and Jenny Nelson. Dependence of charge separation efficiency on film microstructure in poly(3-hexylthiophene-2,5-diyl):[6,6]-phenyl-C61 butyric acid methyl ester blend films. *The Journal of Physical Chemistry Letters*, 1(4):734–738, 2010.

[143] F. Diederich and R. Kessinger. Templated regioselective and stereoselective

synthesis in fullerene chemistry. *Accounts of Chemical Research*, 32:537–545, 1999.

[144] M. A. Faist, P. E. Keivanidis, S. Foster, P. H. Woebkenberg, T. D. Anthopoulos, D.D. C. Bradley, J. R. Durrant, and J. Nelson. Effect of multiple adduct fullerenes on charge generation and transport in photovoltaic blends with poly(3-hexylthiophene-2,5-diyl). *Journal of Polymer Science: part B*, 49(1):45–51, 2010.

[145] Jarvist Moore Frost, Mark Anton Faist, and Jenny Nelson. Energetic disorder in higher fullerene adducts: a quantum chemical and voltammetric study. *Advanced Materials*, 22(43):4881–4884, 2010.

[146] R. C. I. MacKenzie, J. M. Frost, and J. Nelson. A numerical study of mobility in thin films of fullerene derivatives. *Journal of Chemical Physics*, 132:064904, 2010.

[147] Mark A. Faist, Thomas Kirchartz, Wei Gong, Raja Shahid Ashraf, Iain McCulloch, John C. de Mello, Nicholas J. Ekins-Daukes, Donal D. C. Bradley, and Jenny Nelson. Competition between the charge transfer state and the singlet states of donor or acceptor limiting the efficiency in polymer:fullerene solar cells. *Journal of the American Chemical Society*, 134(1):685–692, 2012.

[148] Svetlana S. van Bavel, Maik Barenklau, Gijsbertus de With, Harald Hoppe, and Joachim Loos. P3HT/PCBM bulk heterojunction solar cells: impact of blend composition and 3d morphology on device performance. *Advanced Functional Materials*, 20(9):1458–1463, 2010.

[149] Patrick Parkinson, Christian Muller, Natalie Stingelin, Michael B. Johnston, and Laura M. Herz. Role of ultrafast torsional relaxation in the emission from polythiophene aggregates. *The Journal of Physical Chemistry Letters*, 1(19):2788–2792, 2010.

[150] Yu Xie, Yong Li, Lixin Xiao, Qiquan Qiao, Rabin Dhakal, Zhiling Zhang, Qihuang Gong, David Galipeau, and Xingzhong Yan. Femtosecond time-resolved fluorescence study of P3HT/PCBM blend films. *The Journal of Physical Chemistry C*, 114(34):14590–14600, 2010.

[151] Natalie Banerji, Sarah Cowan, Eric Vauthey, and Alan J. Heeger. Ultrafast relaxation of the poly(3-hexylthiophene) emission spectrum. *The Journal of Physical Chemistry C*, 115(19):9726–9739, 2011.

[152] Dorota Jarzab, Fabrizio Cordella, Martijn Lenes, Floris B. Kooistra, Paul W. M. Blom, Jan C. Hummelen, and Maria A. Loi. Charge transfer dynamics in polymer-fullerene blends for efficient solar cells. *The Journal of Physical Chemistry B*, 113(52):16513–16517, 2009.

[153] J. J. M. Halls, J. Cornil, D. A. dos Santos, R. Silbey, D.-H. Hwang, A. B. Holmes, J. L. Brédas, and R. H. Friend. Charge- and energy-transfer processes at polymer/polymer interfaces: A joint experimental and theoretical study. *Phys. Rev. B*, 60:5721–5727, Aug 1999.

[154] Erik Busby, Christopher W. Rochester, Adam J. Moule, and Delmar S. Larsen. Acceptor dependent polaron recombination dynamics in poly 3-hexyl thiophene: fullerene composite films. *Chemical Physics Letters*, 513(1-3):77 – 83, 2011.

[155] Tieneke E. Dykstra, Emmanuelle Hennebicq, David Beljonne, Johannes Gierschner, Gil Claudio, Eric R. Bittner, Jasper Knoester, and Gregory D. Scholes. Conformational disorder and ultrafast exciton relaxation in ppv-family conjugated polymers. *The Journal of Physical Chemistry B*, 113(3):656–667, 2009.

[156] Stefan Trotzky, Theo Hoyer, Wilfried Tuszynski, Christoph Lienau, and Jurgen Parisi. Femtosecond up-conversion technique for probing the charge transfer in a P3HT:PCBM blend via photoluminescence quenching. *Journal of Physics D: Applied Physics*, 42(5):055105, 2009.

[157] Nathan P. Wells, Bryan W. Boudouris, Marc A. Hillmyer, and David A. Blank. Intramolecular exciton relaxation and migration dynamics in poly(3-hexylthiophene). *The Journal of Physical Chemistry C*, 111(42):15404–15414, 2007.

[158] Arvydas Ruseckas, Paul E. Shaw, and Ifor D. W. Samuel. Probing the nanoscale phase separation in binary photovoltaic blends of poly(3-hexylthiophene) and methanofullerene by energy transfer. *Dalton Trans.*, 0:10040–10043, 2009.

[159] F. Padinger, R. S. Rittberger, and N. S. Sariciftci. Effects of postproduction treatment on plastic solar cells. *Advanced Functional Materials*, 13:85–88, 2003.

[160] C. Muller, T. A. M. Ferenczi, M. Campoy-Quiles, J. M. Frost, D. D. C. Bradley, P. Smith, N. Stingelin-Stutzmann, and J. Nelson. Binary organic photovoltaic blends: a simple rationale for optimum compositions. *Advanced Materials*, 20:3510–3515, 2008.

[161] Neil D. Treat, Alessandro Varotto, Christopher J. Takacs, Nicolas Batara, Mohammed Al-Hashimi, Martin J. Heeney, Alan J. Heeger, Fred Wudl, Craig J. Hawker, and Michael L. Chabinyc. Polymer-fullerene miscibility: a metric for screening new materials for high-performance organic solar cells. *Journal of the American Chemical Society*, 134(38):15869–15879, 2012.

CHAPTER 4

Probing the PCBM multi-adduct solubility in regiorandom poly(3-hexylthiophene)

In the previous chapter, we emphasise the importance of both the solubility of the fullerenes in the amorphous part of the polymer and the ability of the fullerenes to crystallise. In fact, we showed that in the case of the amorphous fullerenes, phase separation occurs within the amorphous part of the system and annealing has almost no effect. However, for the crystalline fullerene, crystallisation induced by annealing was the mechanism promoting demixing.

In this chapter, we use ultra-fast photoluminescence as a simple optical technique to probe the onset of aggregation of fullerenes in an amorphous polymer. We also study the relationship between blend film microstructure and the electronic energy landscape of the system, especially how the charge transfer state is influenced by the microstructure.

Section 4.1

Motivation

In the previous chapter, we showed that the microstructure of polymer:fullerene blends is complex and involves multiple types of phase. We found that demixing can be controlled by both solubility of the fullerenes in the amorphous part of the polymer and crystallisation. However, direct techniques such as transmission electron microscopy do not allow to probe the onset of aggregation of the fullerenes, or in other words the solubility of fullerenes in polymer. Thus, it would be helpful to have a rapid, non-destructive implicit technique to probe the onset of aggregation of fullerenes in polymer and its dependence on various processing temperatures such as solvent and temperatures. In this chapter, we use ultra-fast photoluminescence spectroscopy to probe the onset of aggregation of the fullerenes in polymer.

Since we want to focus on the interactions between fullerenes versus fullerene-polymer interactions, we select an amorphous polymer. We take regiorandom poly(3-hexylthiophene-2,5-diyl) (RRa-P3HT) because it should have similar fullerene- polymer interactions as the amorphous part of regioregular poly(3-hexylthiophene-2,5-diyl) (RR-P3HT). To vary the fullerene interactions, we select two different types of fullerenes: a crystalline fullerene (PCBM) and an amorphous fullerene (bis-PCBM).

Section 4.2

Probing the onset of fullerene aggregation

As shown in the previous chapter, combining steady-state and ultra-fast time-resolved photoluminescence spectroscopy is a relevant method to probe the microstructure of conjugated-polymer:fullerene blends. In this chapter, we use PL spectroscopy to probe the onset of PCBM and bis-PCBM aggregation in RRa-P3HT. The onset of aggregation can be related to the solubility limit of PCBM and bis-PCBM in amorphous RRa-P3HT.

4.2.1 Photophysical characterisation

Steady-state PL spectra of blends of RRa-P3HT:PCBM and RRa-P3HT:bis-PCBM of different polymer:fullerene ratios are plotted in Figure 4.1. The peak around 620 nm (2 eV) is the emission peak of neat RRa-P3HT. Upon addition of fullerenes, the emission peak of RRa-P3HT is more efficiently quenched and is blue-shifted. A peak at higher wavelength than 850 nm ($>$ 1.45 eV) arises for fullerene content of over 5 wt% and a peak at about 730 nm (1.7 eV) arises for content of 50 wt% of PCBM and about 10 wt% of bis-PCBM. The emission at higher wavelength than 850 nm is assigned to the charge-transfer state. The 730 nm emitting peak arises from the neat fullerene contribution.

The fluorescence yield of RRa-P3HT calculated between 500 and 650 nm follows a similar trend for blends of RRa-P3HT:PCBM and RRa-P3HT:bis-PCBM (see Figure 4.2). Most of the polymer emission is quenched for fullerene content of 10 wt%. However, the polymer emission seems to be less efficiently quenched by bis-PCBM than by PCBM between 1 and 10 wt% (not that in this chapter we use wt% and not mol%).

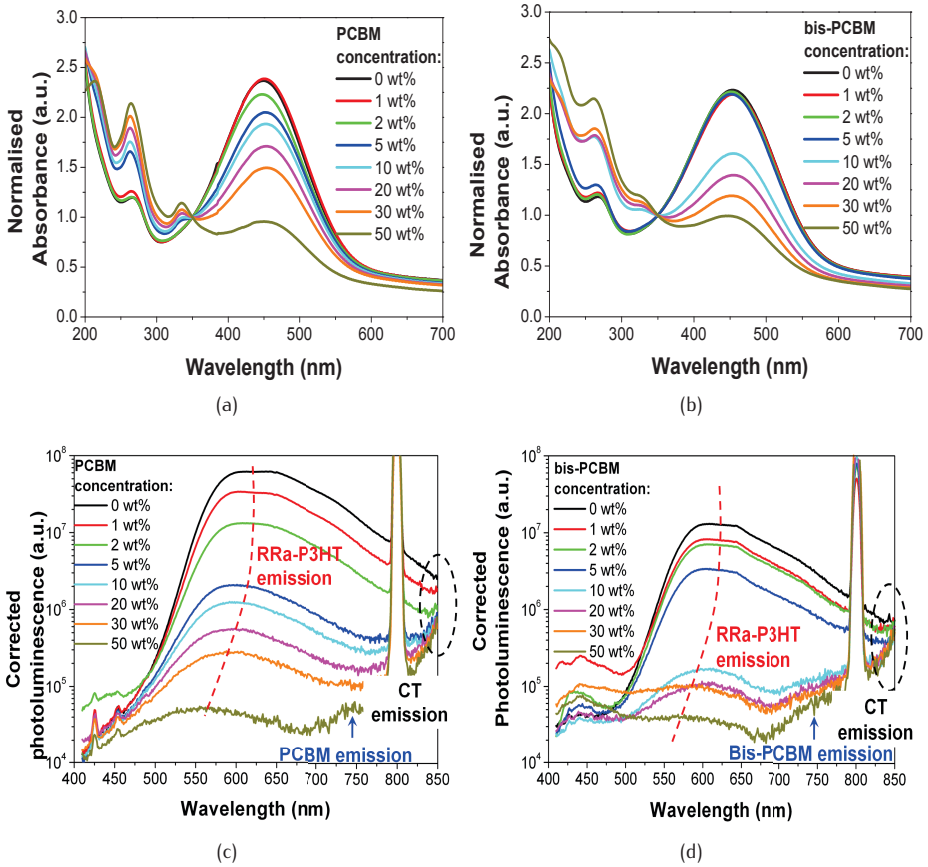


Figure 4.1: Absorption (a,b) and steady-state PL (c,d) profiles for as-spun blends of RRa-P3HT:PCBM (a,c), and RRa-P3HT:bis-PCBM (b,d). (e) Normalised quantum yield of as-spun RRa-P3HT:fullerene films of different compositions. The absorption traces are normalised at 350 nm for clarity. Note that the trend in absorption seems to be different for PCBM and bis-PCBM at very low concentrations. This is due to the absorption of bis-PCBM and RRa-P3HT overlapping and is thus an artefact of the normalisation. The excitation wavelength for PL is 450 nm.

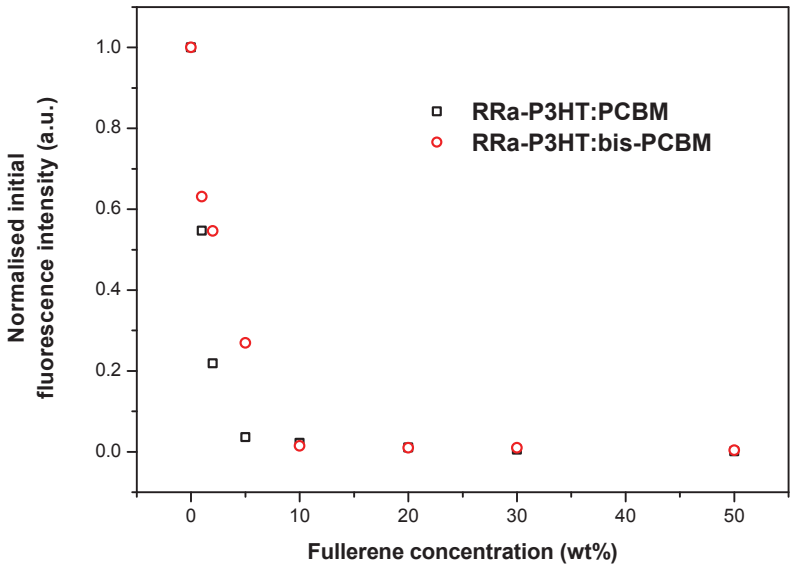


Figure 4.2: Normalised quantum yield of as-spun RRa-P3HT:fullerene films of different compositions. The fluorescent yield was calculated between 500 and 650 nm.

The ultrafast time-resolved emission decay traces are plotted in Figure 4.3. The initial fluorescence intensity follows the same trend as the fluorescence quantum yield plotted in Figure 4.1, except that the polymer emission is more sharply quenched and seems more efficiently quenched by bis-PCBM than PCBM at low fullerene content. These differences between the quantum yield extracted and steady-state PL spectroscopy are a result of a different response time of the set-up.

The amorphous polymer RRa-P3HT exhibits higher photoluminescence quantum efficiency than the semi-crystalline RR-P3HT. Moreover, RRa-P3HT shows mono-exponential emission kinetics while RR-P3HT shows bi-exponential emission kinetics (see Figure 4.4). This is probably due to less available second-order non-radiative processes.

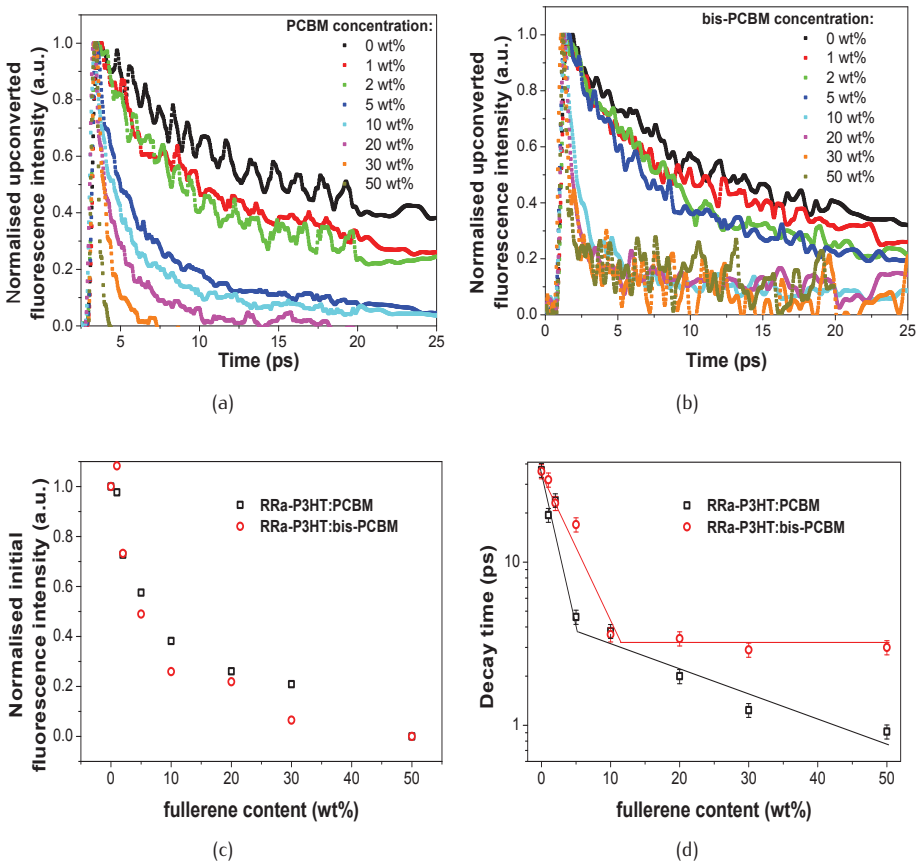


Figure 4.3: Normalised ultrafast time-resolved emission decay traces of as-spun blends of (a) RRa-P3HT:PCBM, and (b) RRa-P3HT:bis-PCBM. The excitation wavelength was 400 nm, and the P3HT emission was detected at 620 nm. (c) Normalised initial fluorescence intensity of as-spun blends of RRa-P3HT:PCBM and RRa-P3HT:bis-PCBM. (d) Time components of the mono-exponential decay fits to the ultrafast fluorescence up-conversion decays for as-spun blends of RRa-P3HT:PCBM and RRa-P3HT:bis-PCBM. Data in collaboration with Annalisa Bruno.

The time decays for RRa-P3HT:PCBM and RRA-P3HT:bis-PCBM blends are plotted as a function of the blend composition in Figure 4.3 (d). The quenching of the polymer emission in as-spun blends containing PCBM is seen to become more efficient upon increasing the acceptor content. Similarly, the polymer emission is continuously quenched for bis-PCBM contents lower than 10 wt%. However, at higher bis-PCBM contents, the polymer emission saturates at a longer decay time than for PCBM. Interestingly, in both cases a significant deceleration of the polymer emission quenching is observed. This deceleration occurs between 2 and 5 wt% of PCBM and between 5 and 10 wt% of bis-PCBM. PCBM quenches more efficiently RRa-P3HT emission for all fullerene contents.

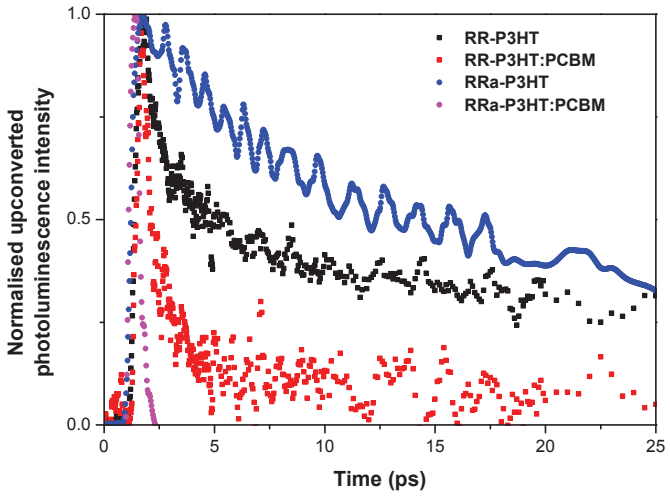


Figure 4.4: Normalised ultrafast time-resolved emission decay traces of regio-regular (RR) P3HT, regio-random (RRa) P3HT and blends of RR-P3HT:PCBM and RRa-P3HT:PCBM (1:1 ratio in weight). The excitation wavelength was 400 nm, and the RR-P3HT and RRa-P3HT emissions were detected at 650 nm and 620 nm respectively. Up-conversion fluorescence measurements in collaboration with Luke X. Reynolds and Annalisa Bruno.

4.2.2 Discussion: solubility limit

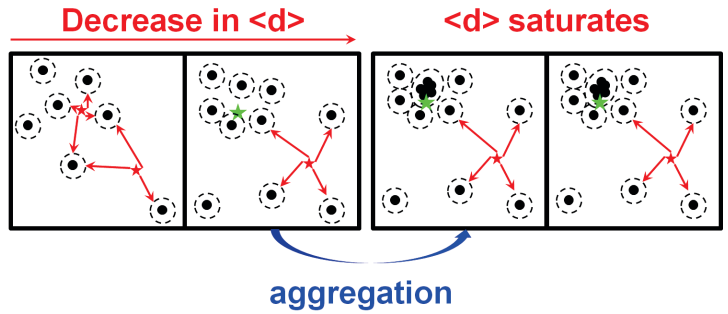
The fluorescence quantum yield and the initial fluorescence intensity are both a measure of the fraction of excitons that are created near to a fullerene quenching site. Thus, the similar trends observed for RRa-P3HT:PCBM and RRa-P3HT:bis-PCBM are consistent with a similar microstructure. Although the fluorescence quantum yield points toward slightly different behaviours of PCBM and bis-PCBM at low fullerene content (the difference of quantum yield at the same molar composition should be reduced in comparison with the difference of quantum yield at the same weight composition). As mentioned in the previous section, the less efficient quenching of the polymer emission by bis-PCBM at low fullerene content can be explained by a difference in exciton dissociation efficiency, a difference in non-radiative decay pathways, or a difference in microstructure. Following the discussion of the previous section, the weaker PL quenching by bis-PCBM for fullerene content lower than 10 wt% is likely to be due to less homogeneously dispersed bis-PCBM in RRa-P3HT.

The saturation of the ultra-fast polymer emission has been previously reported by Bruno *et al.* and have been assigned to fullerene aggregation [162]. This is supported by the appearance of a bis-PCBM contribution in the steady-state PL spectra at about 10 bis-PCBM wt% that can be assigned to aggregation of bis-PCBM. Interestingly, no saturation is observed for PCBM. However, the appearance of PCBM contribution in the steady-state PL at 50 wt% PCBM points towards the presence of PCBM clusters in the blend of sizes larger than the exciton diffusion length in PCBM. Thus, the deceleration in quenching for both PCBM and bis-PCBM is attributed to the onset of fullerene aggregation.

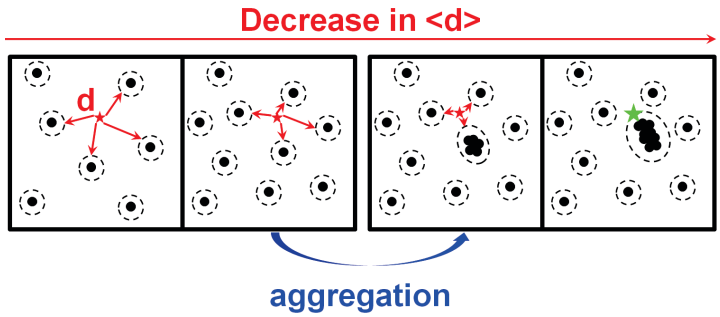
This continuous quenching of RRa-P3HT emission when increasing the amount of PCBM above 10 wt% may have different explanations.

On the one hand, the saturation of the ultra-fast decay time can be explained by bis-PCBM being less homogeneously dispersed than PCBM in RRa-P3HT. In fact, a less homogeneous dispersion of bis-PCBM in RRa-P3HT may lead to the formation of poor-fullerene phases where the photoluminescence is weakly quenched and of rich-fullerene phases where all generated excitons are within the quenching radius of the fullerenes. Thus, when aggregation occurs, it will occur likely in the rich-fullerene phases. Since all excitons generated within the fullerene rich phase are already within the quenching radius of the fullerenes, aggregation will not affect the ultra-fast decays. As a result, when the onset of aggregation is reached, the ultra-fast decays saturate (see Figure 4.5 (a)). However, in an homogeneous dispersed PCBM

phase, all generated excitons are not within the quenching radius of the fullerenes but needs to travel towards an heterojunction. Thus, when the aggregation onset is reached, the increase in cluster sizes will lower the distance from the exciton generation site to the heterojunction, leading to extra quenching by PCBM. Since the surface created by the adsorption of a molecule into a cluster is smaller than the total surface of the molecule, in average the amount of excitons that will be additionally quenched when aggregation happens will be lower than when the fullerenes are fully dispersed in the polymer (see Figure 4.5 (b)). That would explain the decrease in slope that is observed for the decay times in Figure 4.3.



(a)



(b)

Figure 4.5: Schemes representing the average distance from an exciton generation site to a quenching site $< d >$ for (a) a non-homogeneously and (b) a homogeneously dispersed system. The black spots represent the fullerenes. The dashed circles represent the quenching radius of each fullerene. The stars represent the excitons.

On the other hand, PCBM may crystallise and the crystallisation of PCBM is expected to further stabilise the LUMO level of PCBM. Such stabilisation may lead to an enhancement of the charge transfer at the heterojunction, thus leading to more efficient quenching. Since this process is likely to be less efficient than creating more available surfaces for exciton quenching, this would be also consistent with a reduction in slope that is observed for the decay times (see Figure 4.3).

4.2.3 Evidence of PCBM crystallisation

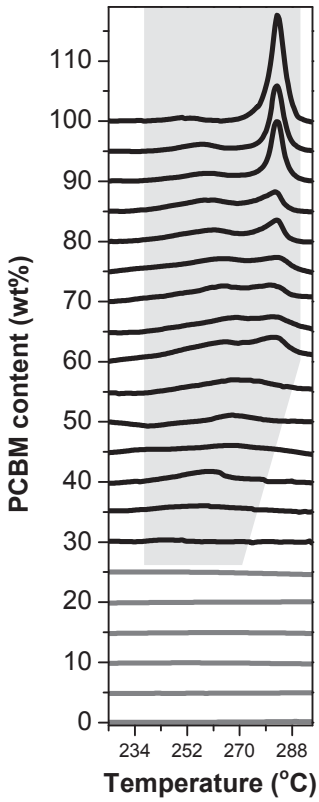


Figure 4.6: DSC scans of RRa-P3HT:PCBM blends of different compositions at a heating rate of 20 °C/min.

In order to probe the onset of PCBM crystallisation in RRa-P3HT, we performed DSC measurements for different PCBM content (see Figure 4.6). Since RRa-P3HT is amorphous, no features are visible in the neat RRa-P3HT DSC scans. Crystallites of PCBM can be detected at content as low as 30 wt% of PCBM. This value provides an upper limit for the onset of PCBM crystallisation. In fact, it is possible that some crystallites are formed for lower PCBM content but are not detectable by DSC. Moreover, stress in thin films lead usually to crystallisation at lower concentration than in bulk samples as studied by DSC.

As mentioned in the previous chapter, in contrast to PCBM, no melting endotherm corresponding to bis-PCBM is observed using DSC.

By combining steady-state and ultrafast photoluminescence, we have identified the onset of aggregation of both fullerenes into RRa-P3HT to occur between 2 and 5 wt% for PCBM and between 5 and 10 wt% for bis-PCBM. Before aggregation, bis-PCBM seems to be less homogeneously dispersed in RRa-P3HT than PCBM. PCBM crystallisation occurs from about 30 wt%.

To summarise, PCBM disperses in RRa-P3HT up to 2-5 wt%, then begins to aggregate and finally crystallise. Bis-PCBM disperses up to 5-10 wt% but less homogeneously and then aggregates.

After the aggregation onset, adding PCBM continues to further quench the polymer emission while it is saturated in the case of bis-PCBM. That can result from either less homogeneous films when RRa-P3HT is blended with bis-PCBM or/and an enhancement of charge transfer rate due to the stabilisation of PCBM LUMO through crystallisation.

To summarise, the different behaviours in exciton lifetime that are observed for RRa-P3HT:PCBM and RRa-P3HT:bis-PCBM can result from a difference in microstructure or in energetics.

To further probe possible change in energetics, we will first use spectroscopic ellipsometry to infer that a change in electronic structure does occur when increasing PCBM content in RRa-P3HT. Secondly, in both blends, charge transfer (CT) state emission is observed (see Figure 4.3 (c) and (d)). Thus, we can study the effect of composition on the intensity and energy of emission from the CT state. The CT emission energy should reflect energetic difference between the acceptor LUMO and the donor HOMO, and so be affected by fullerene crystallisation. The relative CT emission intensity should reflect the balance between the charge transfer yield, the CT recombination yield and the CT dissociation yield. Since all these processes are affected by crystallisation, the relative CT emission should be different for RRa-P3HT:PCBM and RRa-P3HT:bis-PCBM blends. In the next section, we will study the CT emission of RRa-P3HT:PCBM blends as a function of fullerene content using photoluminescence spectroscopy.

Section 4.3

Energetics

4.3.1 Probing changes in electronic structure by spectroscopic ellipsometry

By fitting the extinction coefficient measured by variable angle spectroscopic ellipsometry (the fitting procedure is explained in the paragraph 2.1.5.2), it is possible to extract the absorption coefficient of PCBM in RRa-P3HT:PCBM blends of different compositions. The absorption coefficients of PCBM into RRa-P3HT for different PCBM content are plotted in Figure 4.7.

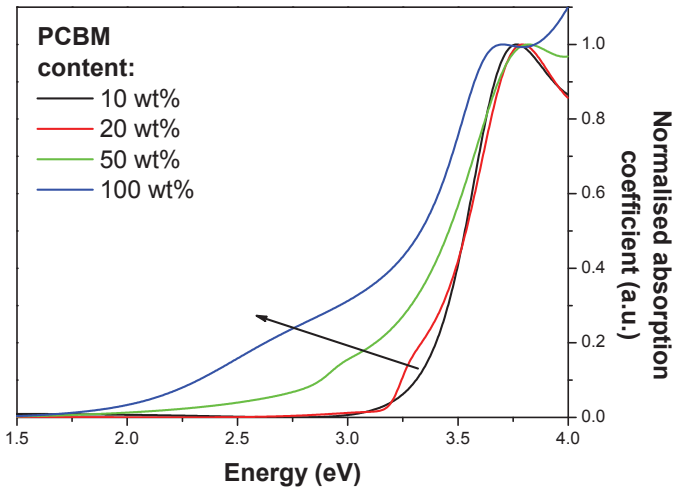


Figure 4.7: Absorption coefficients of PCBM into RRa-P3HT extracted from VASE measurements for different PCBM content. The arrow shows the broadening of the spectra and the resulting shift toward lower energies of the absorption edge. Analysis and measurements from Mariano Campoy-Quiles.

In Figure 4.7, for all the blends the high energy peak remain unshifted around the energy found for dilute solution of PCBM. For pure PCBM, this peak is shifted by 100

meV to lower energies. At higher PCBM content, a shoulder at low energy appears. When increasing the PCBM content, this shoulder broadens and shifts towards lower energies. This shoulder is attributed to aggregation. The shift to lower energies is attributed to a stabilisation of the energy levels of the aggregates as a result of a greater delocalisation of the wavefunctions. Such delocalisation can be explained by crystallisation. The shift of about 100 meV to lower energies of the high energy peak for the pure PCBM is probably an indication of the presence of PCBM crystallites of critical sizes.

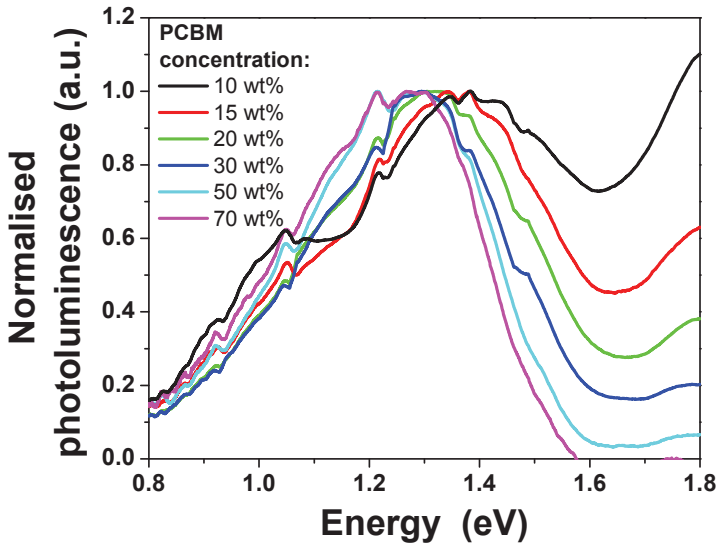
To summarise, ellipsometry shows a change in electronic structure when increasing PCBM content in the blends. This change in electronic structure can results from crystallisation.

4.3.2 CT emission

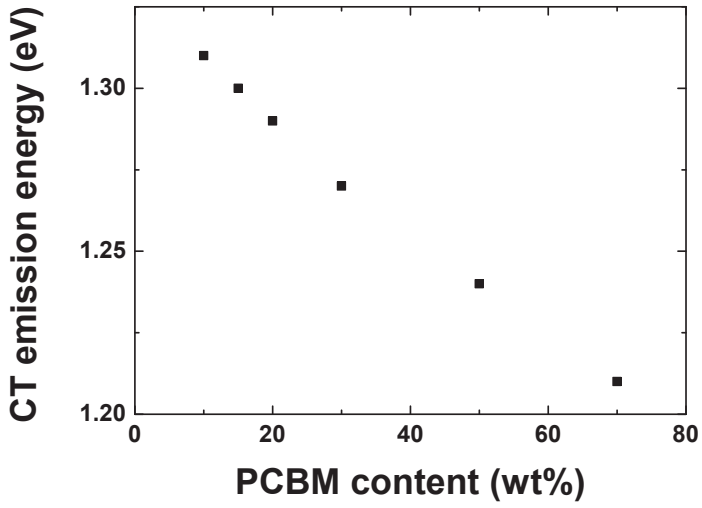
The CT state energy is linked with the LUMOs of the polymer and the fullerene. Thus, studying its energy level should give an insight about the fullerene possible LUMO stabilisation.

PL spectra of RRa-P3HT:PCBM blends of different concentrations are plotted in Figure 4.8. A clear red-shift of the CT energy is observed with increasing PCBM content. The change of dielectric constant of the medium with increasing the fullerene content has been previously reported to lower the CT energy [163] and cannot be fully ignored. However, the total shift of about 100 meV can be in principle assigned to the stabilisation of the LUMO of the fullerene due to crystallisation. This is further supported by the shift towards lower energies of the PCBM absorption edge as can be seen in Figures 4.7.

To conclude, the CT level is red-shifted due to a stabilisation of the LUMO level of PCBM. This stabilisation of the LUMO level of PCBM is attributed to the electron delocalisation that results from crystallisation.



(a)



(b)

Figure 4.8: (a) Normalised PL spectra of RRa-P3HT:PCBM blends at different concentrations. (b) CT emission energy of RRa-P3HT:PCBM blends as a function of PCBM content. The excitation wavelength is 448 nm. Data from Jizhong Yao and Thomas Kirchartz.

Section 4.4

Conclusion

By combining steady-state and ultrafast photoluminescence, we have identified the onset of aggregation of both fullerenes into RRa-P3HT to occur between 2 and 5 wt% for PCBM and between 5 and 10 wt% for bis-PCBM. Before aggregation, bis-PCBM seems to be less homogeneously dispersed in RRa-P3HT than PCBM. PCBM crystallisation occurs from about 30 wt%. To summarise, PCBM disperses in RRa-P3HT up to 2-5 wt%, then begins to aggregate and finally crystallise. Bis-PCBM disperses up to 5-10 wt% but less homogeneously and then aggregates.

After the aggregation onset, adding PCBM continues to further quench the polymer emission while it is saturated in the case of bis-PCBM. That can result from either less homogeneous films when RRa-P3HT is blended with bis-PCBM or/and an enhancement of charge transfer rate due to the stabilisation of PCBM LUMO through crystallisation. To summarise, the different behaviours in exciton lifetime that are observed for RRa-P3HT:PCBM and RRa-P3HT:bis-PCBM can result from a difference in microstructure or in energetics.

We showed using spectroscopic ellipsometry and by the looking the CT emission energy that a change in energetics occur when increasing PCBM content. This change in energetics is attributed to the crystallisation of PCBM.

From this study, it seems clear that ultra-fast photoluminescence can be used to probe the onset of aggregation of fullerenes into an amorphous polymer. Moreover, crystallisation is also detected due to a clear change of energetics as probed by the shift in CT energy. However, it is not possible to clearly assign a further change in PL quenching after the aggregation onset to either a difference in microstructure or in energetics.

Bibliography

[162] A. Bruno, L. X. Reynolds, C. Dyer-Smith, J. Nelson, and S. A. Haque. Determining the exciton diffusion length in a polyfluorene from ultrafast fluorescence measurements of polymer:fullerene blend films. submitted.

[163] Dirk Veldman, Ozlem Ipek, Stefan C. J. Meskers, Joergen Sweelssen, Marc M. Koetse, Sjoerd C. Veenstra, Jan M. Kroon, Svetlana S. van Bavel, Joachim Loos, and Rene A. J. Janssen. Compositional and electric field dependence of the dissociation of charge transfer excitons in alternating polyfluorene copolymer/fullerene blends. *Journal of the American Chemical Society*, 130(24):7721–7735, 2008.

CHAPTER 5

Influence of bridging atom type and side chains on the crystallisation of cyclopentadithiophene-benzothiadiazole polymer derivatives

So far, we have been studying the polymer-fullerene and fullerene interactions. As emphasised earlier, crystallisation of the polymer plays an important role in the microstructure development and has huge impact on processes such as absorption, charge transport and charge separation (subsection 1.4.4), thus on solar cell performances.

In this chapter, we study the influence of the chemical structure of the polymer on the interactions between polymer chains and on the crystallisation of the polymer. We select a system, the bridged cyclopentadithiophene-benzothiadiazole polymer derivatives, where the carbon atom bridging the side chains to the backbones can be replaced by a silicon atom, with a huge impact on the crystallisation (section 5.2). First, we characterise the packing by GIXRD (section 5.3). Then, we use modelling techniques: quantum chemical methods (section 5.4) and molecular dynamics (section 5.5) to rationalise the observed structures. We extend the study to a similar pair of copolymers where thiophene units have been added to increase the separation between side chains. Finally, we consider a set of copolymers with the same backbone structure but different side chains (section 5.6).

Section 5.1

Motivation

The chemical structure of polymers influences the microstructure of polymer:fullerene blends that influences the optoelectronic processes and thus, the device performances. In particular, the nature of the side chains and side chain attachment can influence polymer packing with little or no effect on the π system of the polymer.

In this chapter, we want to find out the extent to which modelling techniques can explain observed differences in packing of conjugated polymers and solar cell performances. We select a material system where a small change in chemical structure influencing side chain attachment is known to have a strong effect on polymer crystallisation: poly[2,1,3-benzothiadiazole-4,7-diyl[4,4-bis(2-ethylhexyl)-4H-cyclopenta[2,1-b:3,4-b']dithiophene-2,6-diyl]] (PCPDTBT) and poly(4,4-dioctyldithieno(3,2-b:2',3'-d) silole-2,6-diyl-alt-(2,1,3-benzothiadiazole)-4,7-diyl) (PSBTBT).

Section 5.2

Background: improvement of the power conversion efficiency by substituting the sp3 carbon bridging atom in cyclopentadithiophene-benzothiadiazole polymer derivatives

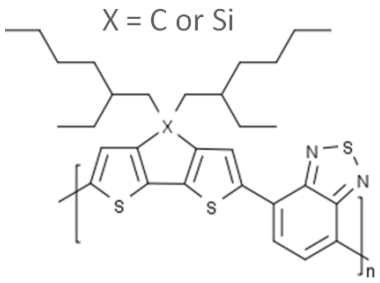


Figure 5.1: Chemical structure of PCPDTBT.

Because poly[2,1,3-benzothiadiazole-4,7-diyl[4,4-bis(2-ethylhexyl)-4H-cyclopenta[2,1-b:3,4-b']dithiophene-2,6-diyl]] (PCPDTBT) (see Figure 5.1) is a low-bandgap polymer (the LUMO of PCPDTBT is believed to lie 0.5 eV below the LUMO of P3HT), the broadening of the spectral range of absorbed photons was expected to lead to an increase in photocurrent relative to the photocurrent of P3HT-based solar cells and thus, an enhancement in power conversion efficiency. However, while the absorption range is indeed improved relative to P3HT, the short circuit current is rather low in comparison with P3HT-based devices (see Table 5.1). Furthermore, no improvements were observed after annealing.

The low performance of PCPDTBT:PC71BM-based devices have been explained by Peet *et al.* in term of microstructure. They found that adding a small amount of 1,8-octanedithiol (ODT) in the solvent results in a significant increase in short circuit

Table 5.1: Characteristics of solar cells based on C- and Si-PCPDTBT.

	polymer:fullerene ratio	V_{oc} mV	J_{sc} mA.cm^{-2}	FF %	η %
C-PCPDTBT [164]	1:3.4	660	9.2	50	3
C-PCPDTBT +ODT [176]	1:2.7	620	16.2	55	5.5
Si-PCPDTBT [166]	1:1.5	576	14.92	61	5.24

current and leads to power conversion efficiencies around 5% [176]. They correlated those improvements with the fact that the phases tend to separate with the addition of ODT while without ODT, the blend remains finely mixed.

Following the work on poly[2,7-(9,9-dihexylfluorene)-alt-2,3-di-methyl-5,7-dithien-2-yl-2,1,3-benzothiadiazole] PFDTBT [167] and on poly[(2,7-di-octylsilafluorene)-2,7-diyl-alt-(4,7-bis(2-thienyl)-2,1,3-benzothiadiazole)-5,50-diyl] PSiFDTBT [168], Hou *et al.* synthesised poly(4,4-dioctyldithieno(3,2-b:2',3'-d)silole-2,6-diyl-alt-(2,1,3-benzothiadiazole)-4,7-diyl) PSBTBT [169] by chemically substituting the sp3 carbon atom to which are attached the side chains by a silicon atom (see Figure 5.1). Konarka had already synthesised PSBTBT by 2007. In the following, PCPDTBT and PSBTBT will be refer as to C-PCPDTBT and Si-PCPDTBT respectively.

The substitution of the carbon bridging atom in PCPDTBT by silicon led to a twofold increase in power conversion efficiency for polymer:fullerene devices without additives as a result of a significant improvement in short circuit current (see Table 5.1). This short circuit current enhancement has been mainly explained by the higher tendency of the polymer to crystallise [170, 171] and of the blends to phase separate, which results in a concomitant increase in both hole and electron mobilities [166].

The more efficient packing in Si-PCPDTBT has been reported to result from a decrease in steric hindrance between the alkyl groups and the thiophene rings because the carbon-silicon bonds are longer than the carbon-carbon bonds [171].

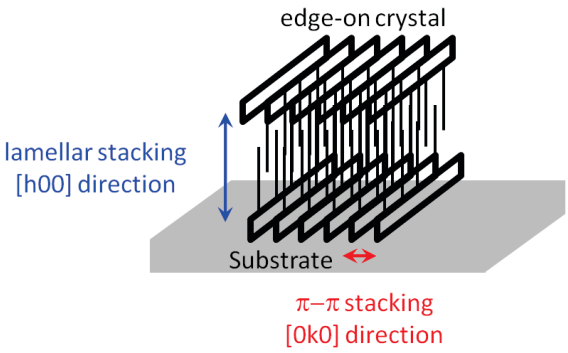
The donor-acceptor phase separation is more defined in the case of Si-PCPDTBT than C-PCPDTBT with a characteristic domain size of about 10-20 nm. The more defined phase separation in Si-PCPDTBT blends is correlated with the lower solubility of Si-PCPDTBT in chlorobenzene and also the stronger tendency of Si-PCPDTBT to crystallise [170]. This more defined acceptor-donor separation was observed to quench the charge transfer complexes which are involved in radiative exciton recombinations. The same quenching effect was observed in C-PCPDTBT processed with ODT but was in this case strongly dependent on the fullerene concentration [170].

Post-production annealing was found to further enhance the Si-PCPDTBT crystallinity and lead to more ordered PCBM domains (appearance of additional PCBM peaks in GIXRD patterns). Furthermore, structural studies using GIXRD revealed that the edge-on orientation of Si-PCPDTBT is enhanced by annealing due to the presence of PCBM (the $\frac{I_{(100)}}{I_{(010)}}$ ratio is increased in GIXRD patterns) [172, 171]. In addition, some portion of the PCBM molecules are believed to diffuse during annealing into the space between the side-chain groups in the $\pi - \pi$ conjugated planes (the distance $d_{(100)}$ in GIXRD patterns increases during annealing) [171].

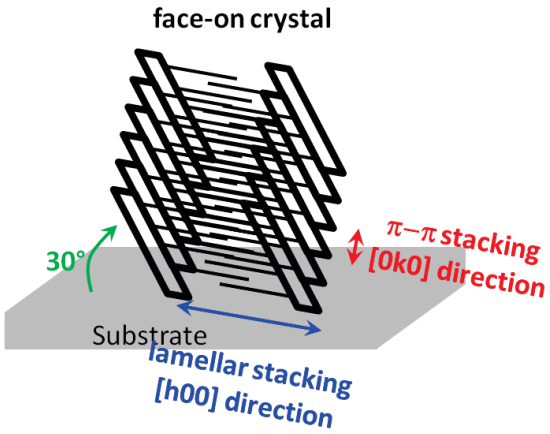
To understand better this crystallisation enhancement by chemically substituting the sp3 bridging carbon atom by a silicon atom in C-PCPDTBT, more detailed structural studies are needed. Thus, we carried out GIXRD of both neat C-PCPDTBT and Si-PCPDTBT and blends with $PC_{70}BM$. The results are presented in the next section.

Section 5.3

Characterisation of polymer packing using GIXRD



(a)



(b)

Figure 5.2: Proposed monoclinic crystal structure for (a) C-PCPDTBT and (b) Si-PCPDTBT. The [100] and [010] directions have been chosen to be the lamellar stacking direction and the $\pi - \pi$ stacking direction respectively. The crystal is fully edge on when the backbones or the [100] direction are perpendicular to the substrate. Alternatively, the crystal is fully face on when the backbones or the [100] direction are parallel to the substrate.

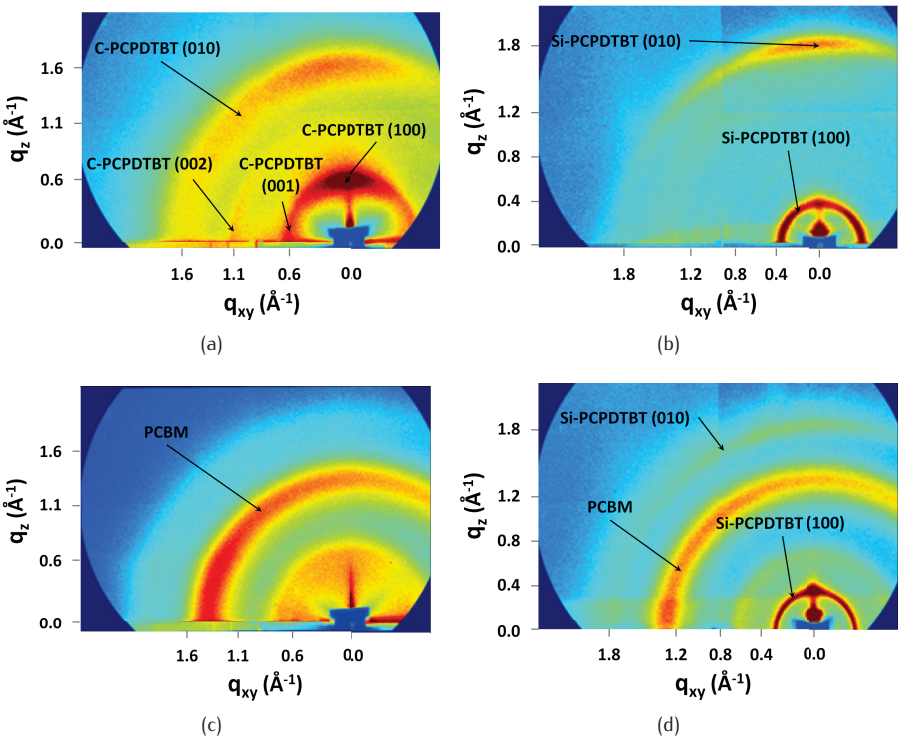


Figure 5.3: GIXRD patterns of (a) C-PCPDTBT, (b) Si-PCPDTBT, (c) C-PCPDTBT:$PC_{70}BM$ and (d) Si-PCPDTBT:$PC_{70}BM$. Data from Tiziano Agostinelli, Ellis Pires, Samuele Liliu and J. Emyr Macdonald.

In Figure 5.4, the out-of-plane (OOP) and the in-plane (IP) GIXRD profiles of C-PCPDTBT and Si-PCPDTBT, neat and blended with $PC_{70}BM$ are plotted. The corresponding diffraction patterns are displayed in Figure 5.3. Tables 5.2 and 5.3 summarise the position and full width half maximum (FWHM) of the diffraction peaks as well as the corresponding spacing distances and coherence lengths.

First of all, the intensity of the (100) peak is stronger in-plane for C-PCPDTBT and out-of-plane for Si-PCPDTBT. This suggests that Si-PCPDTBT chains are more face-on oriented than C-PCPDTBT chains. This is confirmed by a closer inspection of the radial profiles (see Figure 5.5). In fact, it is revealed that while the maximum (100) peak intensity is observed at 90° with respect to the substrate surface for C-PCPDTBT, two symmetric maxima are observed at 30° and 150° for Si-PCPDTBT. This means that while C-PCPDTBT chains are fully edge-on, Si-PCPDTBT chains are almost face-on, tilted by 30° with respect to the substrate surface. This explains that (00l) peaks are not observed either in the out-of-plane or in-plane profiles for Si-PCPDTBT.

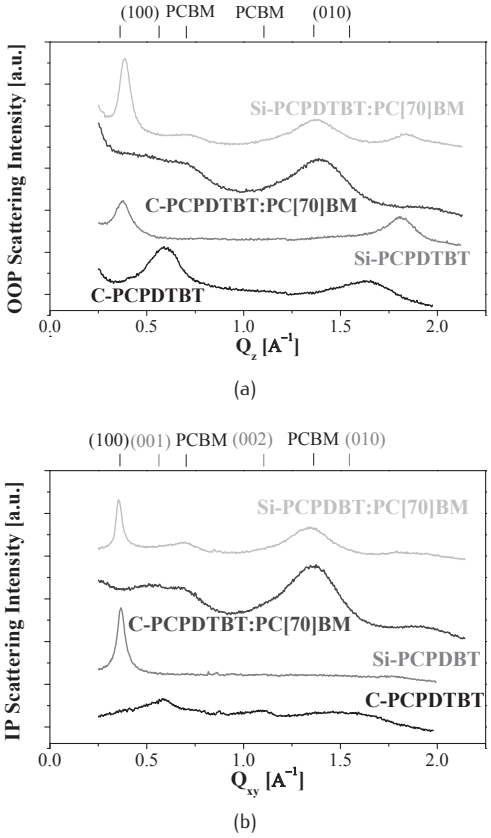


Figure 5.4: GIXRD (a) out-of-plane and (b) in-plane profiles of C-PCPDTBT, Si-PCPDTBT, C-PCPDTBT:$PC_{70}BM$ and Si-PCPDTBT:$PC_{70}BM$ films. Data from Tiziano Agostinelli, Ellis Pires, Samuele Liliu and J. Emyr Macdonald.

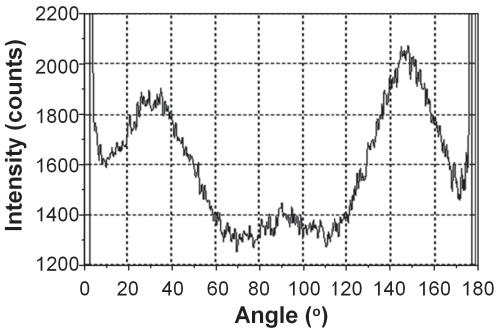


Figure 5.5: Azimuthal scan profile obtained at $q_{(100)}$ peak positions for Si-PCPDTBT film. Data from Tiziano Agostinelli, Ellis Pires, Samuele Liliu and J. Emyr Macdonald.

Table 5.2: Indexes, positions q, corresponding spacing distances d, $FWHM$, and coherence length ξ of the OOP GIXRD peaks of C-PCPDTBT, Si-PCPDTBT, C-PCPDTBT:$PC_{70}BM$ and Si-PCPDTBT:$PC_{70}BM$. The (100) and (010) peaks refer to spacing distances d along the lamellar stacking and the π-stacking directions respectively. ξ is calculated assuming the validity of the Scherrer equation. Data from Tiziano Agostinelli, Ellis Pires, Samuele Liliu and J. Emyr Macdonald.

OOP	index	q(Å^{-1})	d(Å)	$FWHM$(Å^{-1})	ξ(Å)
C-PCPDTBT	100	0.59	10.65	0.17	34.6
	010	1.62	3.88	0.24	23.3
Si-PCPDTBT	100	0.38	16.70	0.07	84.1
	010	1.81	3.47	0.13	42.5
C-PCPDTBT:$PC_{70}BM$	N.A.	N.A.	N.A.	N.A.	N.A.
Si-PCPDTBT:$PC_{70}BM$	100	0.39	16.23	0.05	105.0
	010	1.84	3.41	0.12	46.0

Table 5.3: Indexes, positions q, corresponding spacing distances d, $FWHM$, and coherence length ξ of the IP GIXRD peaks of C-PCPDTBT, Si-PCPDTBT, C-PCPDTBT:$PC_{70}BM$ and Si-PCPDTBT:$PC_{70}BM$. The (00l) peaks refer to spacing distances d along the polymer backbone directions. Data from Tiziano Agostinelli, Ellis Pires, Samuele Liliu and J. Emyr Macdonald.

IP	index	q(Å^{-1})	d(Å)	$FWHM$(Å^{-1})	ξ(Å)
C-PCPDTBT	001	0.58	10.80	0.17	33.3
	002	1.08	5.79	0.11	51.2
	010	1.59	3.94	0.22	25.9
Si-PCPDTBT	100	0.37	17.12	0.05	124.5
C-PCPDTBT:$PC_{70}BM$	N.A.	N.A.	N.A.	N.A.	N.A.
Si-PCPDTBT:$PC_{70}BM$	100	0.35	17.75	0.04	161.6
	010	1.80	3.50	N.A.	N.A.

Secondly, substituting the carbon bridging atom by a silicon atom leads to a lengthening of the spacing distance along the lamellar stacking distance d_{100} and a shortening of the π stacking distance d_{010} (see Tables 5.2 and 5.3). This suggests that the silicon bridge substitution allows the backbones to move closer in the π direction, at the cost of pushing them further apart in the lamellar stacking direction.

Importantly, the coherence lengths, calculated by assuming the validity of the Scherrer equation, increase drastically for Si-PCPDTBT (see Tables 5.2 and 5.3), especially in the lamellar direction, implying a larger size of ordered domains.

When Si-PCPDTBT is blended with $PC_{70}BM$, it remains crystalline while C-PCPDTBT blended with $PC_{70}BM$ do not exhibit any significant crystallinity, with a GIXRD pattern close to that of the neat $PC_{70}BM$ (see Figure 5.6). The distances between the

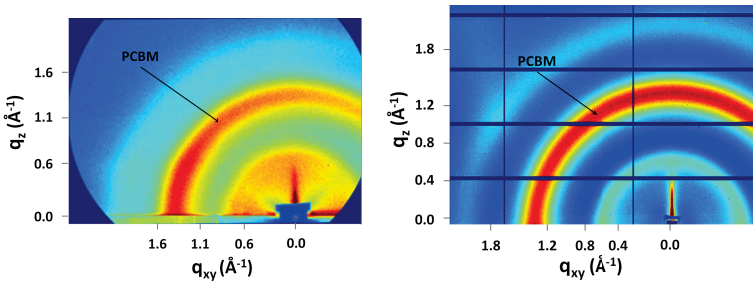


Figure 5.6: GIXRD patterns of (a) C-PCPDTBT:$PC_{70}BM$ and (b) $PC_{70}BM$. Data from Tiziano Agostinelli, Ellis Pires, Samuele Lilliu and J. Emyr Macdonald.

Si-PCPDTBT backbones in blend remain similar to the ones in the neat films, except that in the in-plane profile the (100) diffraction peak is located at a higher q value than in the out-of-plane profile. This suggests that the Si-PCPDTBT crystals is under stress when Si-PCPDTBT is blended with $PC_{70}BM$. Interestingly, the coherence lengths of the Si-PCPDTBT crystals is lengthened in all directions when blended with $PC_{70}BM$.

To summarise, C-PCPDTBT chains are edge-on oriented while Si-PCPDTBT chains are almost face-on oriented (tilt of about 30 ° with respect to the substrate surface). When the carbon bridging atom is substituting by a silicon atom, the $\pi - \pi$ stacking distance is decreased at the cost of increasing the lamellar stacking distance and the coherence lengths are increased. When blended with $PC_{70}BM$, Si-PCPDTBT remains crystalline and the coherence lengths are further increased.

Section 5.4

Force field development

In order to understand how the observed differences in crystal structure relate to the chemical structure of the polymer, molecular modelling techniques are used to investigate the potential energy surfaces and molecular dynamics.

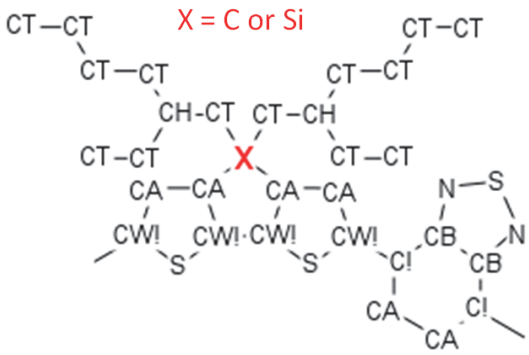


Figure 5.7: Atom class definitions for C-PCPDTBT and Si-PCPDTBT.

To define the intermolecular and intramolecular interactions, we define different classes of atoms (see Figure 5.7): aromatic carbons (CA), hydrogens bonded to aromatic carbons (HA), biphenyl-like aromatic carbons either bonded to aromatic carbons (C!) or to sulfur (CW!), purine-like aromatic carbons (CB), sulfurs (S), nitorgens (N), sp3 carbon bridging atom (Csp3), silicon bridging atom (Si), alkyl carbons either CH2 and methyl end group (CT) or CH (CH) and alkyl hydrogens (HC).

In the first instance, in order to parametrise the CA-CW!-C!-CA torsion between the cyclopentadithiophene and benzothiadiazole units and calculate the partial charges, we replace the ethylhexyl side chains by methyl groups and we consider hydrogen-end-capped monomers. The dihedral angle is constrained from 0 to 180° every 20° (the cis conformer is defined as $\phi = 0°$). The molecular geometry of the monomer with the constrained dihedral is optimised for each angular value using B3LYP/6-311g(d,p). Then, for each optimised monomer conformation, the energy is calculated using MP2/cc-pVTZ and a CHELPG method is used to reproduce the electrostatic potential from the MP2 quantum chemical calculation. No significant differences are observed between C-PCPDTBT and Si-PCPDTBT. The potential energy calculated using first principle methods as well as the intrinsic potential energy (calculated from

the difference between the first principle and force-field based energies as mentioned in the subsection 2.5.2.1) are plotted in Figure 5.8 as a function of the dihedral angle for C-PCPDTBT. The partial charges are averaged over the different conformations and weighted by the dihedral angular distribution (inverse of the normalised potential energy plotted un Figure 5.8) to account for the likeliness of the conformation. The partial charges are summarised in Figure 5.9. The partial charges of hydrogens bonded to aromatic carbons are +0.105 and +0.139 on the cyclopentadithiophene unit and +0.136 and +0.137 on the benzothiazole unit for C-PCPDTBT and Si-PCPDTBT respectively. The partial charges assigned to the side chains are assigned according to OPLS-AA FF. The partial charges assigned to the aliphatic hydrogens are +0.060 for both C-PCPDTBT and Si-PCPDTBT according to OPLS-AA FF.

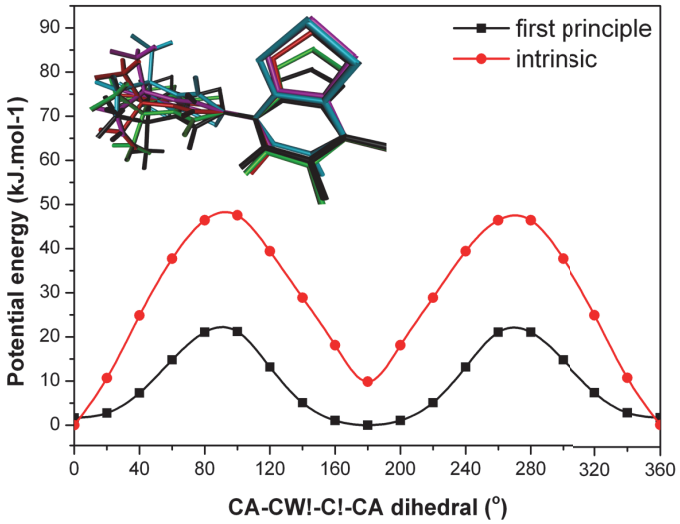


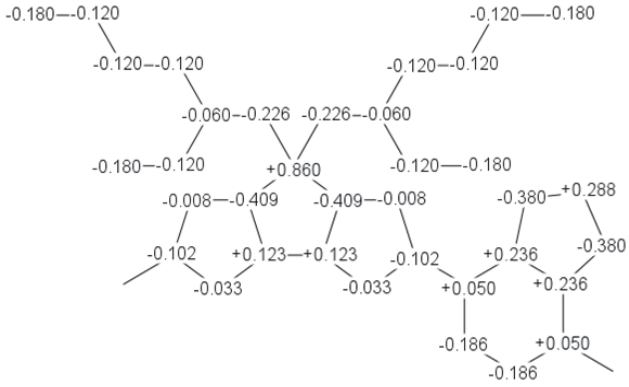
Figure 5.8: Energies calculated using first principle methods and potential that we include in the force field (denoted as "intrinsic") for the CA-CW!-C!-CA dihedral of C-PCPDTBT. The scanned dihedral is depicted in the inset.

The angle CT-X-CT between the side chains as well as the isopentane-like dihedrals CA-X-CT-CH, X-CT-CH-CT and CT-CT-CH-CT (see Figures 5.10) for both C-PCPDTBT and Si-PCPDTBT are scanned in a similar way (the doubly gauche conformer is defined as $\phi = 0$ °). The results are plotted in Figure 5.11.

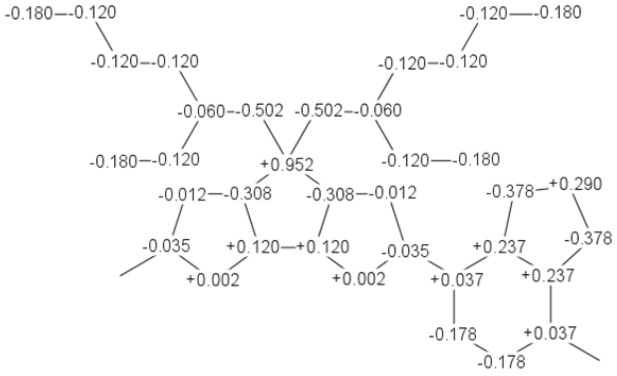
It can be noticed that the energy barrier for all of the studied side chain torsions are systematically decreased for Si-PCPDTBT compared to C-PCPDTBT. This implies more flexibility of the side chains of Si-PCPDTBT than C-PCPDTBT. We perform a MD simulations of 10 ns on a monomer of C- and Si-PCPDTBT in a box of chloroform

and look at the spatial distribution function of the side chains (see Figure 5.12). It can be seen that more conformations are allowed in the case of the silicon bridging atom. This may have a huge impact on the kinetics of the polymer crystallisation, leading to greater ease for Si-PCPDTBT to crystallise as well as lower perturbation of the crystallisation when blended with fullerenes.

All these newly calculated parameters are integrated in the empirical force field built from OPLS-AA parameters using the method described in 2.5.2.2. The complete new force field for C-PCPDTBT and Si-PCPDTBT can be found in Appendix B.



(a)



(b)

Figure 5.9: Partial charges for (a) C-PCPDTBT and (b) Si-PCPDTBT derived from quantum chemical calculations.

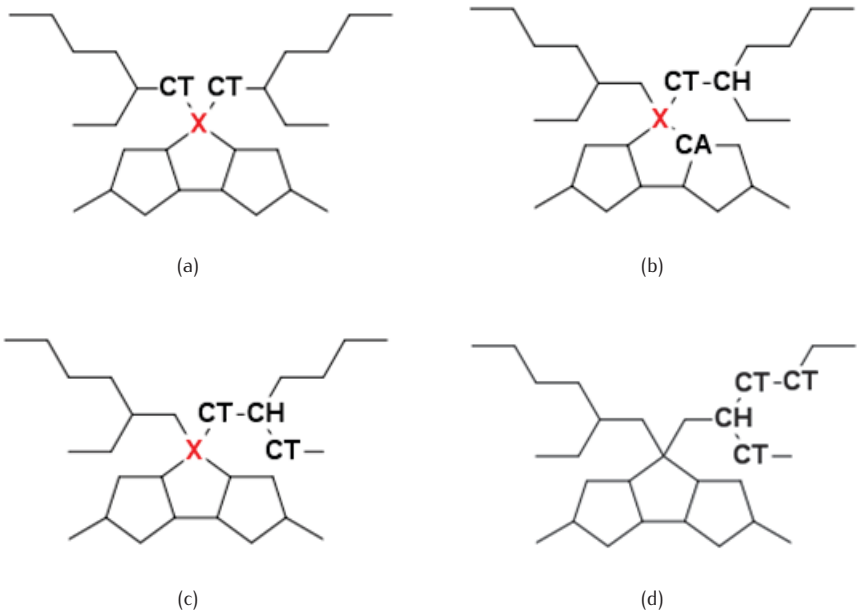


Figure 5.10: (a) CT-X-CT angle, (b) CA-X-CT-CH, (c) X-CT-CH-CT and (d) CT-CT-CH-CT dihedrals.

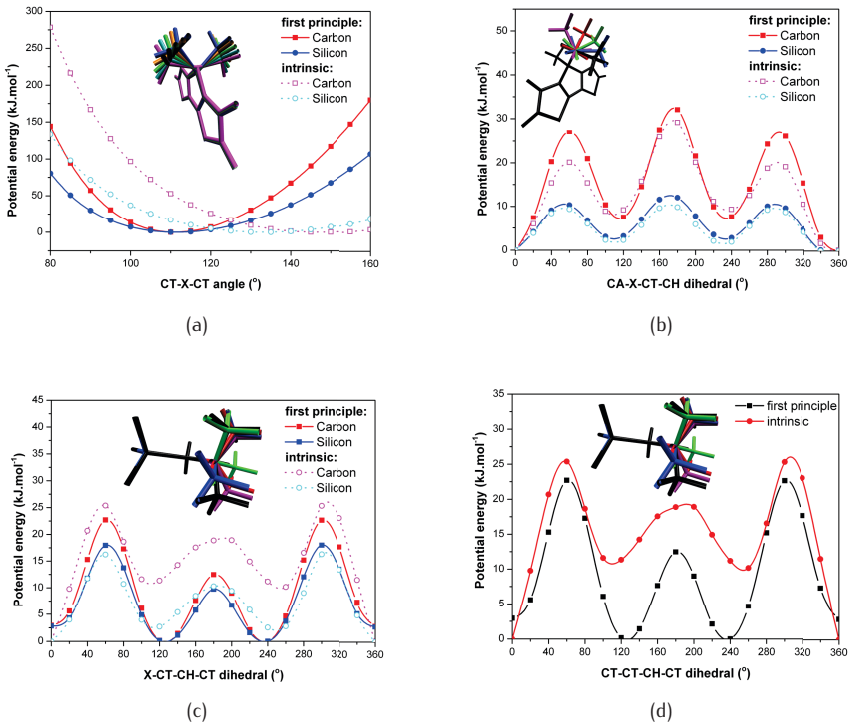
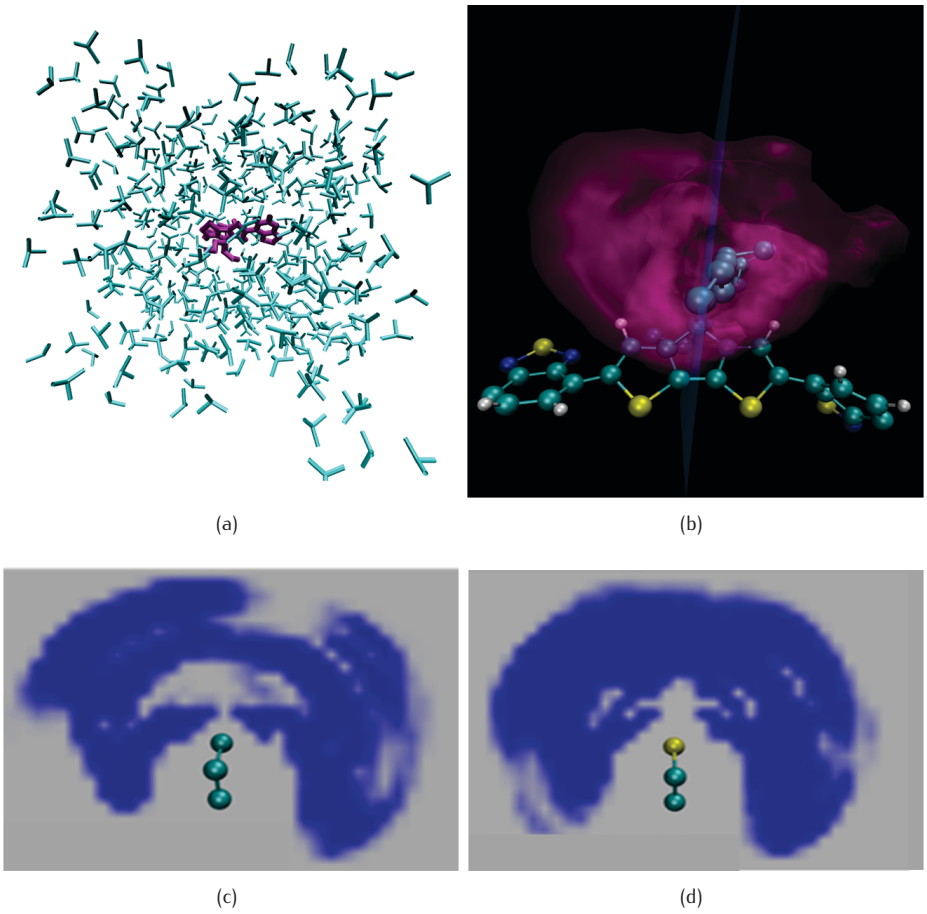


Figure 5.11: Energies calculated using first principles methods and potential that we include in the force field (denoted as "intrinsic") for (a) the angle CT-X-CT, the dihedrals (b) CA-X-CT-CH, (c) X-CT-CH-CT for both C-PCPDTBT and Si-PCPDTBT and (d) CT-CT-CH-CT (there are no difference between C-PCPDTBT and Si-PCPDTBT for this dihedral). A range of positions of the concerned angle is depicted in the insets.



(a) (b)

(c) (d)

Figure 5.12: (a) Isolated monomer in a box of chloroform. (b) 3D spatial distribution function of side chains. (c,d) 2D slices perpendicular to the backbone of the spatial distribution of side chains of isolated (c) C-PCPDTBT and (d)Si-PCPDTBT monomers solvated in chloroform obtained by MD simulations

In the last section, we have derived the force field parameters for relevant degrees of freedom for C-PCPDTBT and Si-PCPDTBT. We have shown that the torsional potential for the backbones is almost identical for both polymers, the potentials for the side chain motion are different with side chains more flexible for Si-PCPDTBT than C-PCPDTBT.

These difference in potentials are likely to lead to differences in the potential energy of similar crystal structures. In the next section, we implement the calculated potentials in the force fields in order to calculate the potential energy surfaces of tetramers arranged in a structure representative of a crystal. We study the intermolecular interactions between the backbones and the side chains.

We find that the different shape of the backbones and the different side chain potentials are able to explain the observed differences in crystal structure for the two pristine polymers.

Section 5.5

Crystal structure, Gibbs free energy and potential energy surface

In NPT ensemble, the Gibbs free energy G is given by $G = U + PV - TS$ (U is the internal energy, P the pressure, V the volume , T the temperature and S the entropy) and is minimised at equilibrium. For calculation purpose, we assume that the Gibbs free energy of a crystal can be approximated by its potential energy E_{pot} ($U = E_{pot} + E_{kin}$ where E_{kin} is the kinetic energy) and thus, the global minimum of the potential energy is the most favourable crystal.

As seen in the previous section (see Figure 5.8), the cyclopentadithiophene and the benzothiadiazole units prefer to have a dihedral angle of $\phi = \pi$, though the second minimum of $\phi = 0$ is only 0.017 eV ($\sim 0.7 k_B T_{RT}$) higher. Thus, it can be concluded that there is practically almost no preference for the backbones to be in trans or cis conformations between the repeat units.

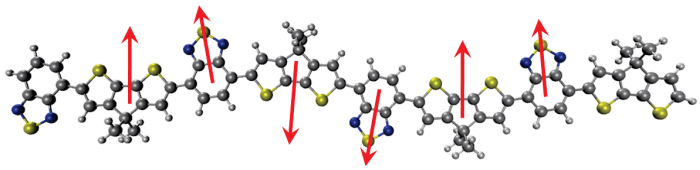
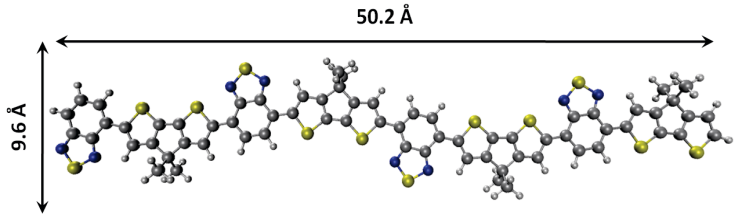


Figure 5.13: Alternating cyclopentadithiophene and benzothiadiazole units pointing in the opposite directions

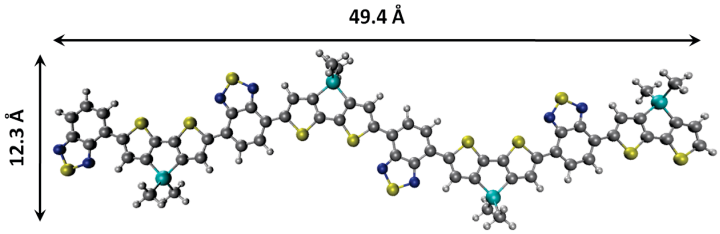
In the following, we consider linear polymer chains with alternating cyclopentadithiophene and benzothiadiazole units pointing in the opposite directions (see Figure 5.13) since they are more likely to organise into ordered domains.

5.5.1 Effect of the backbones on the intermolecular potential energy

In order to study the effect of the backbone structure on intermolecular potential energy, we replace the ethylhexyl side chains by methyl groups. We optimised using B3LYP/6-311g(d,p) the geometry of C-PCPDTBT tetramers. We find that the monomer has a length of about 9.7 Å which is compatible with the distance along the backbones d_{001} extracted from GIXRD (see Table 5.3). The geometry of a tetramer of Si-PCPDTBT is optimised the same way and both are plotted in Figure 5.14. It can be seen that the backbones of Si-PCPDTBT are slightly more bent than the C-PCPDTBT due to the steric hindrance caused by the longer C-Si bond. This optimised structures are used as an input for the following energy minimisation and molecular dynamics simulations.



(a)



(b)

Figure 5.14: Backbones of C-PCPDTBT and Si-PCPDTBT quantum chemically relaxed using B3LYP/6-311g(d,p).

We study the equilibrium separation of tetramers in an arrangement representative of a crystal. Three tetramers are packed on top of each other in the z-direction, alternatively tilted by 180° around the x-axis. This stack is then repeated three times in the y-direction (see geometry in Figure 5.15). We scan the $\pi - \pi$ stacking distance and the lamellar stacking distance.

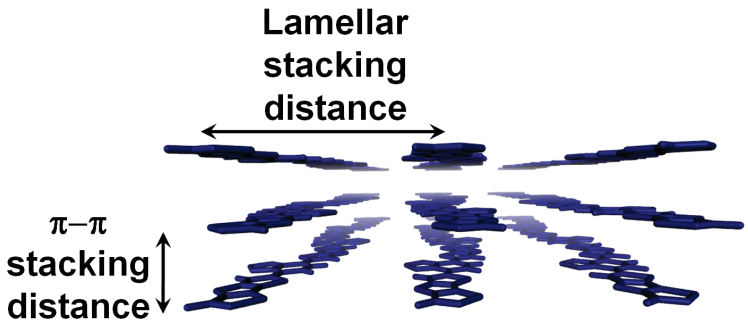


Figure 5.15: Geometry of the initial structure representative of a crystal.

We generate a set of initial structures with fixed $\pi-\pi$ and lamellar stacking distances using Packmol [181]. For each pair of $\pi-\pi$ and lamellar stacking distances, we run an energy minimisation without periodic boundary conditions using the developed force field in order to generate the potential energy surface. The position of the atoms are restrained around their initial positions in all three directions using the following potential:

$$V_{PR}(\vec{r_i}) = \frac{1}{2}[k^x_{PR}(x_i - X_i)^2\vec{x} + k^y_{PR}(y_i - Y_i)^2\vec{y} + k^z_{PR}(z_i - Z_i)^2\vec{z}] \tag{5.1}$$

where X_i, Y_i, Z_i are the Cartesian coordinates of the fixed reference positions of the atoms, $k^x_{PR}, k^y_{PR}, k^z_{PR}$ are the components of the force constant and $\vec{r_i}$ or x_i, y_i, z_i are the positions of the atoms during the simulation. Restraining the position of the atoms instead of freezing the atoms allows the tetramers to relax according to the force field without significantly changing the $\pi-\pi$ and lamellar stacking distances. Different values have been tried for $k^x_{PR}, k^y_{PR}, k^z_{PR}$. We found that 100 000 kJ.mol^{-1} allows to keep the $\pi-\pi$ and lamellar stacking distance unchanged. The force constant in the remaining direction is set to 10 000 kJ.mol^{-1}. The cut-off radii for the Coulomb and van der Waals interactions are taken to be much larger than the size of the "crystals" to prevent any artefacts.

The energy minimisation is used to find the nearest local minimum for each configuration. We perform the energy minimisation using the steepest descent method. According to the steepest descent method, the positions of each atom (r_k) are updated at each step following the direction of the negative gradient $\vec{\nabla}E_{pot}(r_k)$ (calculated with respect to all coordinates) using the following equation:

$$\vec{r_{k+1}} = \vec{r_k} - \lambda_k \vec{\nabla} E_{pot}(r_k) \tag{5.2}$$

where λ_k is the maximum displacement.

The potential energy surfaces for C- and Si-PCPDTBT are plotted in Figure 5.16. A potential energy minimum is found for both C- and Si-PCPDTBT at a $\pi - \pi$ stacking distance of 3.5 Å. In the lamellar stacking direction, the potential energy is minimised at a separation of 8.6 Å for C-PCPDTBT and 9.1 Å for Si-PCPDTBT. This small difference can be mainly explained by the difference in shape of the tetramers (see Figure 5.14).

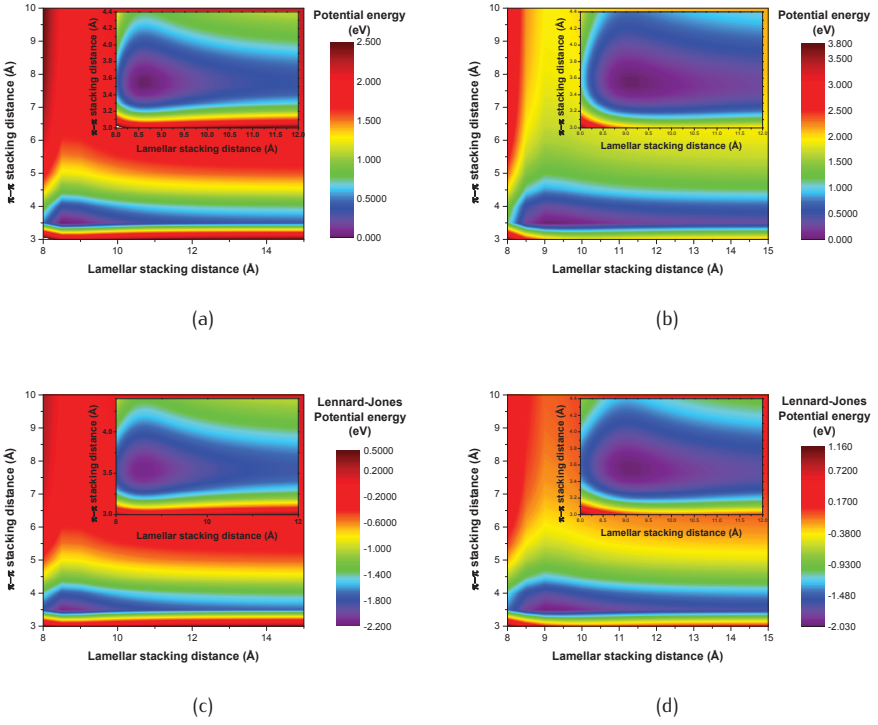


Figure 5.16: (a,b) Potential energy surfaces and (c,d) Lennard-Jones potential energy surfaces for (a,c) C-PCPDTBT and (b,d) Si-PCPDTBT. The insets display finer scans around the minima. The potential energy surfaces are generated on systems of nine tetramers of C- and Si-PCPDTBT. The side chains have been replaced by methyl group.

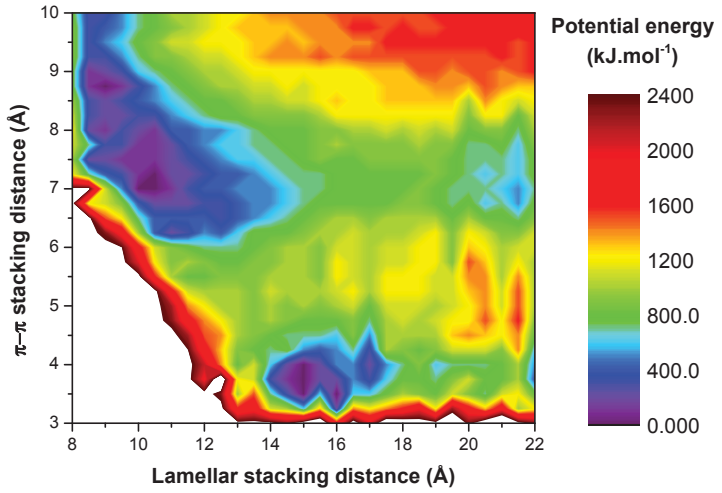
For each energy minimisation, the different contributions to the potential energy are also calculated. The largest contribution is the energy contribution due to the Lennard-Jones potential that is used to approximate the repulsive component resulting from the Pauli exclusion principle and the and the attractive component at long ranges (dispersion) of the intermolecular or van der Waals interactions. In Figure 5.16, the Lennard-Jones potential energy surfaces for C- and Si-PCPDTBT are plotted. It can be noticed that the difference in both potential energy and Lennard-Jones

potential energy are very large in the $\pi-\pi$ stacking direction in comparison with the difference in potential energy in the lamellar stacking direction. This points towards a stabilisation of the $\pi-\pi$ stacking due to the van der Waals interactions between the backbones.

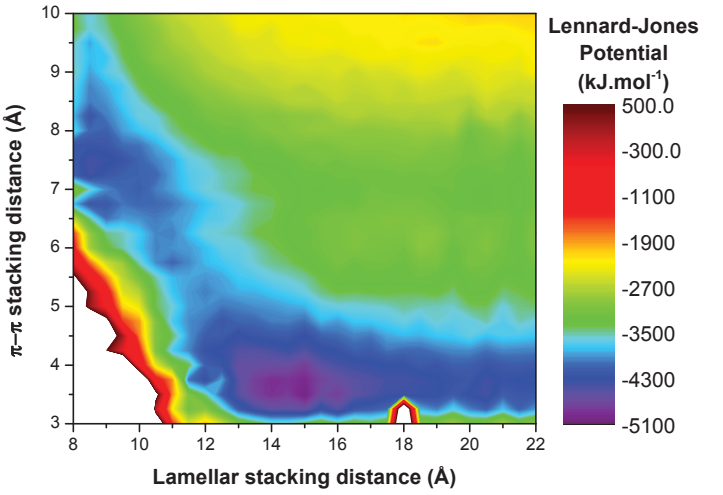
The optimum value of the $\pi-\pi$ stacking distance is in good agreement with the $\pi-\pi$ stacking distance extracted from GIXRD for Si-PCPDTBT (see Table 5.2 and Table 5.3). However, the simulation does not reflect the difference in $\pi-\pi$ stacking between C- and Si-PCPDTBT. The simulation underestimates the lamellar stacking distance, especially for Si-PCPDTBT (see Table 5.2 and Table 5.3). This disagreement between the simulation and the experiment is probably due to the fact that so far, we are considering only the backbones of the polymer. The $\pi-\pi$ stacking is stabilised by the van der Waals interactions between the backbones as showed by the large difference in potential energy in the $\pi-\pi$ stacking direction. The side chains are expected to increase the coherence in the lamellar stacking distance. Concomitantly, the side chains may disturb the $\pi-\pi$ stacking because of steric hindrance.

5.5.2 Effect of the side chains on the intermolecular potential energy

We study the equilibrium separation of tetramers of C- and Si-PCPDTBT with side chains in an arrangement representative of a crystal. We generate a set of initial structures with fixed $\pi-\pi$ and lamellar stacking distances. During all the following steps to generate the potential energy surface, the position of the atoms belonging to the backbones of the tetramers are restrained. The atoms belonging to the side chains are unrestrained and unfrozen. The first step consists of an energy minimisation as in the following section. This is followed by a molecular dynamics run at 300 K for 50 ps (50000 steps) in order to allow the side chains to relax and the potential energy to stabilise. The temperature is then slowly quenched to 0 K (-15 $K.ps^{-1}$). A final molecular dynamics run is performed at 0 K for 1 ps (1000 steps). The potential energies reported in Figure 5.17 are an average of the potential energy over 1000 steps at 0 K. Since there is no noticeable difference in potential energies for C- and Si-PCPDTBT, only the potential energy surface of C-PCPDTBT is plotted in Figure 5.17.

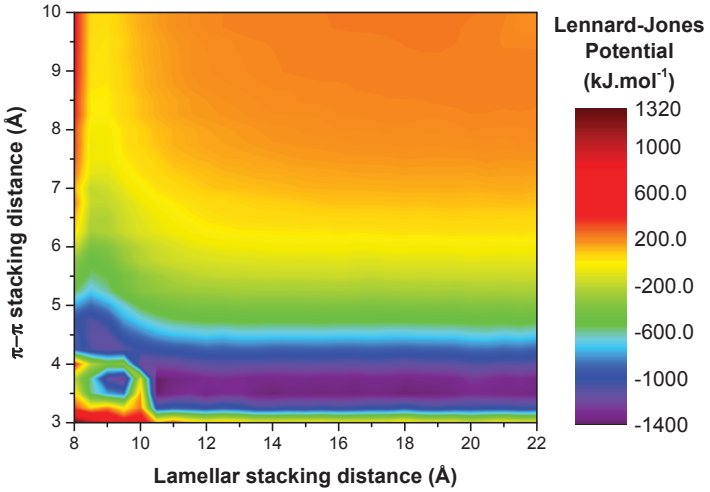


(a)

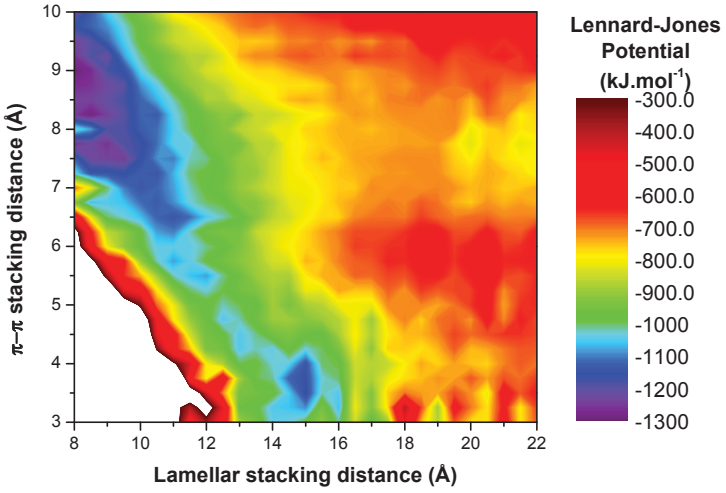


(b)

Figure 5.17: (a) Potential energy surface and (b) Lennard-Jones potential energy surface for C-PCPDTBT. The potential energy surfaces are generated on systems of nine tetramers of C-PCPDTBT with side chains.



(a)



(b)

Figure 5.18: Contributions of the (a) backbones-backbones and (b) side chains-side chains interactions to the Lennard-Jones potential energy surface for C-PCPDTBT. The potential energy surfaces are generated on systems of nine tetramers of C-PCPDTBT with side chains.

By introducing the side chains, the potential energy varies significantly in the lamellar stacking direction in comparison with the potential energy surface generated on systems without side chains (see Figure 5.16). A clear potential energy minimum is found at a $\pi - \pi$ stacking separation of 3.5Å $\pm$ 0.25Å and a lamellar stacking separation of 15Å $\pm$ 0.5Å. The optimum lamellar stacking separation is drastically increased in comparison with the optimum lamellar stacking separation found for tetramers without side chains. Furthermore, a second minimum in potential energy is found for a $\pi - \pi$ stacking separation of 7.5Å $\pm$ 0.25Å and a lamellar stacking separation of 10Å $\pm$ 0.5Å. As in the previous section, the largest contribution to the energy potential is found to come from the potential energy due to the Lennard-Jones potential. In this case, the potential energy due to Lennard-Jones potential has two main contributions, the potential energy due to Lennard-Jones potential between the backbones on the one hand and between the side chains on the other hand. Both contributions are plotted in Figure 5.18.

The contribution to the Lennard-Jones potential energy surface due to the backbones-backbones interactions is very similar to that simulated in the previous subsection (see Figure 5.16). The contribution due to the side chains-side chains interactions introduces a difference in potential energy in the lamellar stacking direction.

5.5.3 Discussion

The optimum values of 3.5Å and 15Å for the $\pi-\pi$ and the lamellar stacking distances agree reasonably well with the distances extracted from GIXRD for Si-PCPDTBT (see Table 5.2 and Table 5.3). The optimum lamellar stacking distance of 10Å agrees well with the one extracted from GIXRD for C-PCPDTBT (see Table 5.2 and Table 5.3). However, the corresponding $\pi-\pi$ stacking distance is for that minimum overestimated.

The overestimation of the $\pi - \pi$ stacking distance can be explained by the limitation of the method used in this section. In fact, the restraint of the backbone positions can limit, especially at small distance, the rearrangement of the side chains leading to high potential energies. Moreover, the strong repulsive term of the Lennard-Jones potential may create artefact at small distances and a more elaborate potential to approximate the van der Waals interactions should be used.

The $\pi - \pi$ stacking is stabilised by the van der Waals interactions between the backbones as shown by the strong variation in potential energy in the $\pi-\pi$ stacking

direction when considering only the backbones, resulting mainly from the strong variation in Lennard-Jones potential energy. The side chains affect mainly the potential energy in the stacking direction, assuring the coherence of the crystal in that direction.

Interestingly, those two potential energy minima are found for both C-PCPDTBT and Si-PCPDTBT. Firstly, the simulation suggests that it is possible to crystallise C-PCPDTBT in the same crystal structure as Si-PCPDTBT varying the kinetics of crystallisation. Secondly, the simulation suggests that the difference in side chain flexibility as found by quantum chemical calculations is changing the crystallisation kinetics and is probably also responsible for the ease of crystallisation of Si-PCPDTBT.

In the next section, we study the influence of the chemical structure on the crystallisation of the polymer using the same method as developed here. First, we keep the same side chains but introduce backbones with more units leading to an increased distance between the side chain anchoring points. Secondly, we keep the C-PCPDTBT backbones but vary the bulkiness and the length of the side chains. We compare our results to available data.

Section 5.6

Influence of the chemical structure on the crystalline order

5.6.1 Influence of the chemical structure of the backbones on the intermolecular potentials

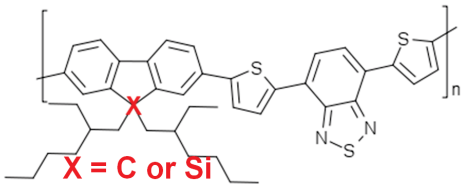
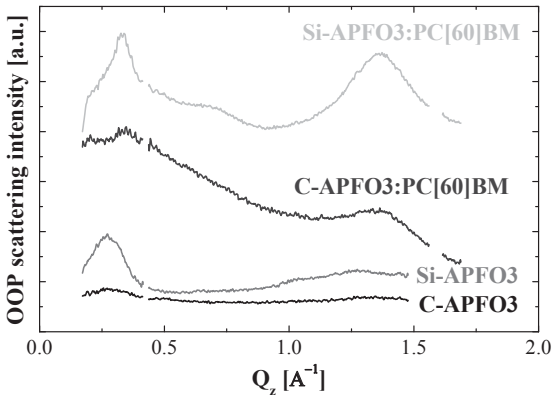


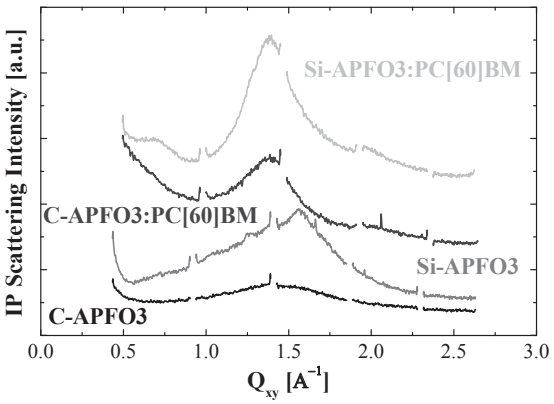
Figure 5.19: Chemical structures of pFTBTT and pSiF-DBT

In this section, we introduce an alternating polyfluorene (APFO) copolymer poly[(9,9-ethylhexylfluorenyl-2,7-diyl)-alt-5,5-(40,70-di-2-thienyl-20,10,30-benzothiadiazole) (pFTBTT). The sp3 carbon atom to which the side chains are attached has also been successfully chemically substituted by a silicon atom [168]. The chemical structures of these copolymers are shown in Figure 5.19. In the following, pFTBTT and pSiF-DBT will be refer as to C-APFO3 and Si-APFO3 respectively.

By substituting the carbon bridging atom with a silicon atom in the case of C-APFO3, an increase in power conversion efficiency has bee observed [168]. However, in this case, this is due to an increase in open circuit voltage and no difference in short circuit current is observed. This increase in open circuit voltage is easily explained by the lowering of the HOMO energy of the conjugated polymer when the substitution is realised [168].



(a)

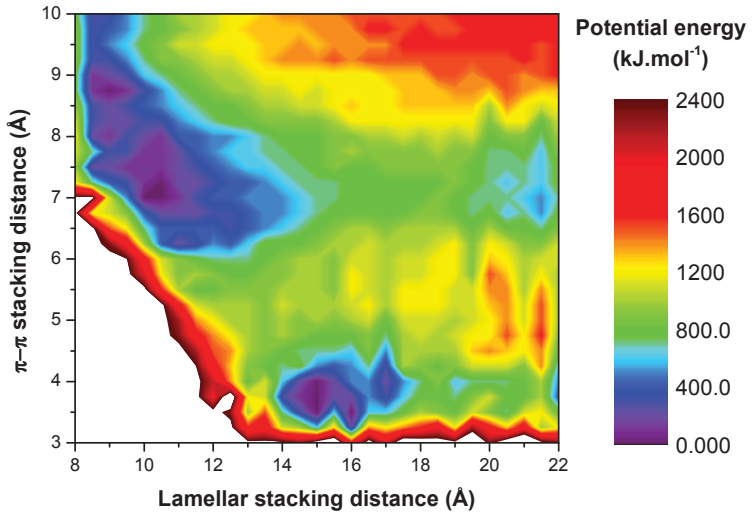


(b)

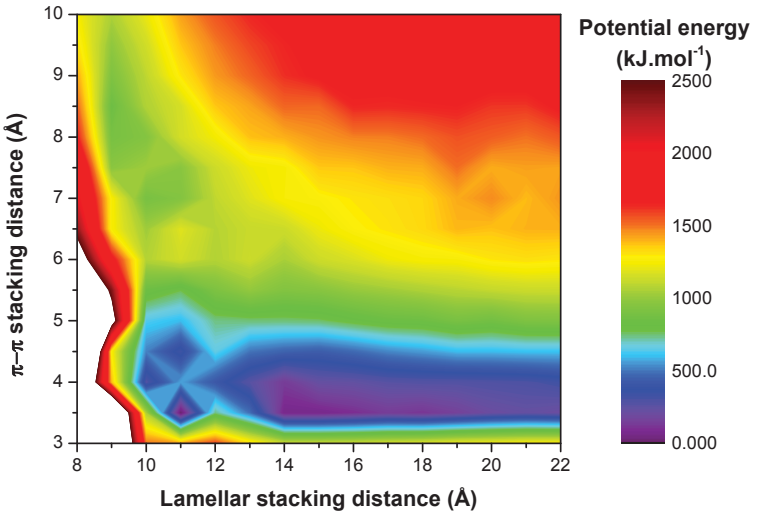
Figure 5.20: GIXRD (a) out-of-plane and (b) in-plane profiles of C-APFO3, Si-APFO3, C-APFO3:$PC_{60}BM$ and Si-APFO3:$PC_{60}BM$. Data from Tiziano Agostinelli, Ellis Pires, Samuele Liliu and J. Emyr Macdonald.

We performed GIXRD on C- and Si-APFO3 and blends of C-APFO3:$PC_{60}BM$ and Si-APFO3:$PC_{60}BM$ [1]. The out-of-plane and in-plane profiles are plotted in Figure 5.20. No significant difference in either crystal orientation or crystal structure can be observed (the diffraction peaks and the relative intensity of the peaks in-plane and out-of-plane are similar fr both polymers).

[1] The polymers were synthesised by Weimin Zhang and Iain McCulloch at Imperial College.



(a)



(b)

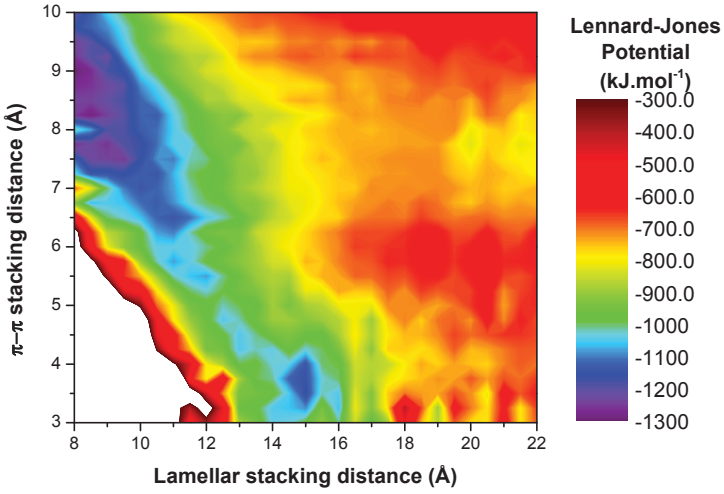
Figure 5.21: Potential energy surfaces of (a) C-PCPDTBT and (b) C-APFO3. The potential energy surfaces are generated on systems of nine tetramers of C-PCPDTBT and of nine dimers of C-APFO3 with side chains.

In the same way as for C- and Si-PCPDTBT, we developed a force field (see appendix C). It should be noticed that the fluorene and the thiophene units prefer to have a dihedral angle of $\phi = \pi$ and the benzothiadiazole and the thiophene units prefer to have a dihedral angle of $\phi = \frac{\pi}{9}$. We study the equilibrium separation of dimers in an arrangement representative of a crystal using the force fields. Since there is no noticeable difference in potential energies for C- and Si-APFO3, only the potential energy surface of C-APFO3 is plotted in Figure 5.21 in comparison with the corresponding potential energy surface for C-PCPDTBT (from Figure 5.17).

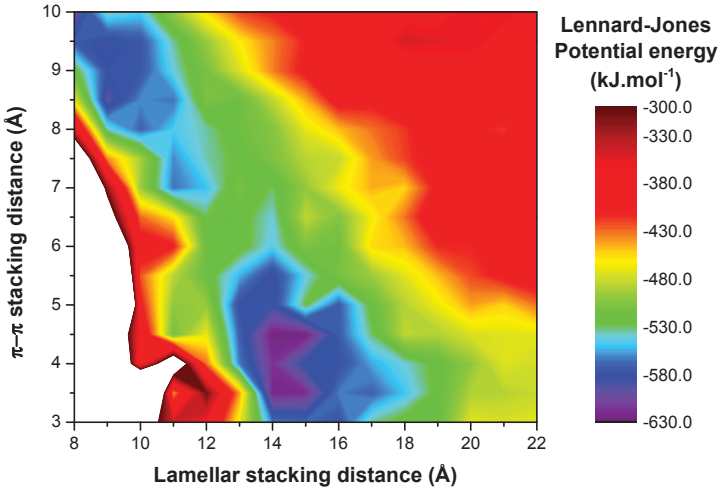
A minimum in potential energy is found at a $\pi - \pi$ stacking separation of 3.5 Å and at a lamellar stacking separation of 11 Å. No second minimum is found. The potential energy variation in the lamellar stacking direction is decreased in comparison with C-PCPDTBT. This can be easily explained by the decrease in density of side chains along the backbones.

In Figure 5.22, the contributions to the Lennard-Jones potential energy surface due to the side chain-side chain interactions is plotted. For both C-PCPDTBT and C-APFO3, two minima can be observed. However, in the case of C-PCPDTBT, the deepest minimum occurs at short lamellar stacking separation and long $\pi - \pi$ stacking separation while for C-APFO3, the deepest minimum occurs at long lamellar stacking separation and short $\pi - \pi$ stacking separation. This explains the appearance of only one minimum at long lamellar stacking separation and short $\pi - \pi$ stacking separation for C-APFO3 since the backbones-backbones interactions will stabilise further the $\pi - \pi$ stacking distance to values around 3.5 Å.

To conclude, no difference in crystal structure arises from the substitution of the carbon bridging atom of C-APFO3 by a silicon atom. The increased separation between the side chains, due to the addition of thiophene units, leads to only one minimum in potential energy at long lamellar stacking separation and short $\pi - \pi$ stacking separation. Thus, C- and Si-APFO3 crystallise in the same crystal structure. This could help to explain why charge transport is not affected by the substitution, leading to the same short-circuit current.



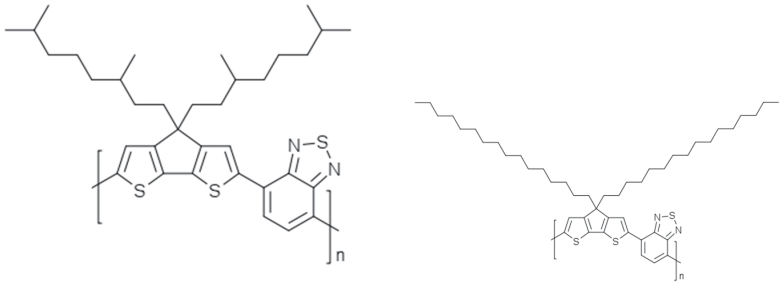
(a)



(b)

Figure 5.22: Contributions of the side chain-side chain interactions to the Lennard-Jones potential energy surface for (a) C-PCPDTBT and (b) C-APFO3. The potential energy surfaces are generated on systems of nine tetramers of C-PCPDTBT and of nine dimers of C-APFO3 with side chains.

5.6.2 Influence of the chemical structure of the side chains on the intermolecular potentials



(a) (b)

Figure 5.23: Chemical structure of (a) C8-PCPDTBT and (b) C16-PCPDTBT.

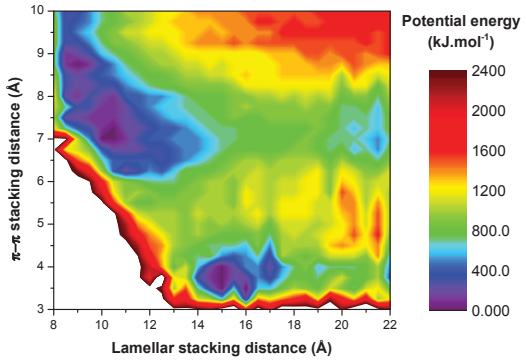
In this section, we study two copolymers reported by Tsao *et al.* [174] ; the backbone structures are identical to C-PCPDTBT but the side chains are replaced by 3,7-dimethyloctyl ($C_{8,2}$) in one case and hexadecyl (C_{16}) in the other case [175, 174]. GIXRD measurements are reported in [174] and high hole mobilities up to 2.62 $cm^2.(Vs)^{-1}$ [174] are reported. For comparison, hole mobilities of 1.10^{-3} and 1.10^{-2} $cm^2.(Vs)^{-1}$ have been reported for C-PCPDTBT [170] and Si-PCPDTBT [170] respectively. In the following, the polymers with $C_{8,2}$ and C_{16} side chains will be referred as to C8-PCPDTBT and C16-PCPDTBT respectively (see Figure 5.23) and C-PCPDTBT will be referred as to C6-PCPDTBT

We used the force field developed for C-PCPDTBT (the atom classes and the FF parameters are the same). We study using the force field the equilibrium separation of tetramers in an arrangement representative of a crystal. The potential energy surfaces for C8- and C16-PCPDTBT are plotted in Figure 5.24 in comparison with that for C6-PCPDTBT.

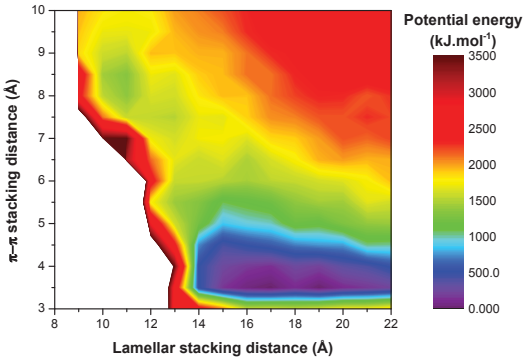
It can be observed that the less bulky and longer side chains suppress the existence of the second minimum at short lamellar stacking separation and long $\pi - \pi$ stacking separation. The potential energy variation in the lamellar stacking direction is also decreased in comparison with C6-PCPDTBT. The minimum in potential energy is found at a $\pi - \pi$ stacking distance of 3.5 Å $\pm$ 0.5Å and at a lamellar stacking distance of 17 Å for C8-PCPDTBT and 21 Å for C16-PCPDTBT. These values are compatible with the $\pi - \pi$ stacking distance of 3.7-3.8 Å and the lamellar stacking

distance of $\simeq$ 21Å for C8-PCPDTBT and 25.6-27.8 Å for C16-PCPDTBT reported from GIXRD [174]. The lamellar stacking separation is however underestimated. This can be the consequence of the Lennard-Jones potential being less accurate at long distances. In Figure 5.25, the contributions to the Lennard-Jones potential energy surface due to the side chains-side chains interactions is plotted. Only one minimum is seen at long lamellar stacking separation and short $\pi - \pi$ stacking separation for C8- and C16-PCPDTBT.

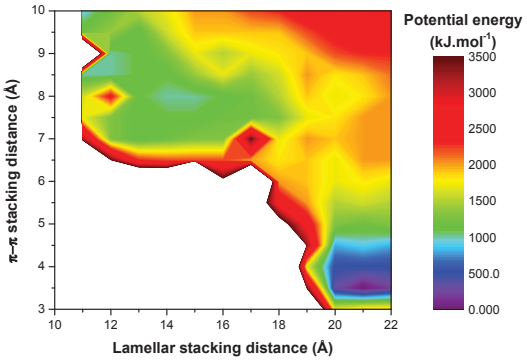
To conclude, the longer/unbranched side chains suppress the existence of a second energy potential minimum at long $\pi - \pi$ stacking distance and short lamellar stacking distance. Thus, the longer/unbranched side chains stabilise the packing in the $\pi - \pi$ stacking direction and so increase the mobility.



(a)

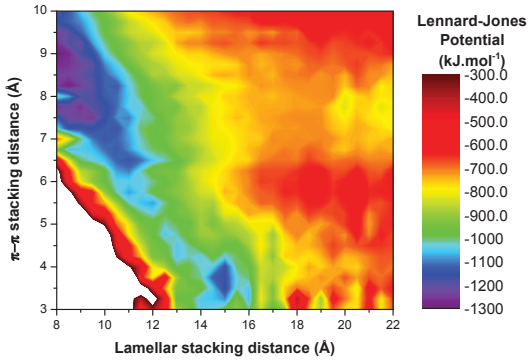


(b)

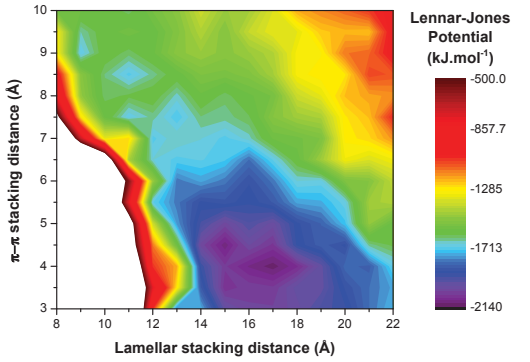


(c)

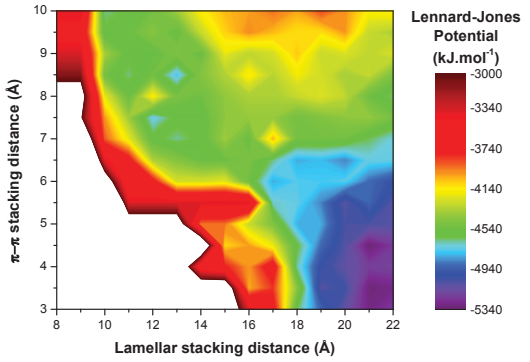
Figure 5.24: Potential energy surfaces of (a) C6-PCPDTBT, (b) C8-PCPDTBT and (c) C16-PCPDTBT. The potential energy surfaces are generated on systems of nine tetramers with side chains.



(a)



(b)



(c)

Figure 5.25: Contributions of the side chains-side chains interactions to the Lennard-Jones potential energy surfaces of (a) C6-PCPDTBT, (b) C8-PCPDTBT and (c) C16-PCPDTBT. The potential energy surfaces are generated on systems of nine tetramers with side chains.

Section 5.7

Conclusion

In this chapter, we have combined the use of GIXRD and modelling techniques to understand the difference in crystallisation between C-PCPDTBT and Si-PCPDTBT that is translated to a difference in hole mobilities leading to differences in short-circuit current and thus, in power conversion efficiency.

We have developed a new force field for these materials. From the quantum chemical calculations, we have concluded that Si-PCPDTBT side chains are more flexible than C-PCPDTBT side chains. This is likely to influence the kinetics of crystallisation and probably leads to greater ease of crystallisation for Si-PCPDTBT than for C-PCPDTBT.

We have studied the equilibrium separation of C-PCPDTBT and Si-PCPDTBT in arrangements representative of crystals using these new force fields. From this study, we found no significant differences between the potential energy surfaces of C- and Si-PCPDTBT. For each material, we found two minima: one agreeing reasonably well with the GIXRD data on Si-PCPDTBT and the other agreeing with the lamellar stacking separation for C-PCPDTBT but overestimating the $\pi - \pi$ stacking separation for C-PCPDTBT. This overestimation is probably linked with the restraint of the backbones during the simulation and the strong repulsive component of the Lennard-Jones potential at small distances. The simulation suggests that it is possible to crystallise C-PCPDTBT in the same crystal structure as Si-PCPDTBT by varying the kinetics of crystallisation.

We found that the major contribution to the potential energy is the energy due to the Lennard-Jones potential. Looking at both the Lennard-Jones potential energy between backbones and between side chains, we found that the backbones stabilise the $\pi - \pi$ stacking separation to a value around 3.5 Å and have almost no variation in the lamellar stacking distance. The side chains introduce a component in the lamellar stacking distance and disturb the $\pi - \pi$ stacking, probably due to steric hindrance.

We have extended the study to three other copolymers. Firstly, we have studied C- and Si-APFO3, the difference between those copolymers and C- and Si-PCPDTBT resides in a larger separation between the side chains. No difference in crystal

structure arises from the substitution of the carbon bridging atom of C-APFO3. The increased separation between the side chains, due to the addition of thiophene units, leads to only one minimum in potential energy at long lamellar stacking separation and short $\pi - \pi$ stacking separation. Thus, C- and Si-APFO3 crystallise in the same crystal structure. This explains that the charge transport is not affected by the substitution, leading to the same short-circuit current.

Secondly, we have introduced C8- and C16-PCPDTBT to study the influence of the chemical structure of the side chains on the polymer crystallisation. Those polymers are of interest since they achieved much higher hole mobilities [174] than C-PCPDTBT. We found only one minimum in potential energy for C8- and C16-PCPDTBT at a short $\pi - \pi$ stacking distance of 3.5 Å and a long lamellar stacking distance of 17 Å for C8-PCPDTBT and 21 Å for C16-PCPDTBT, suggesting that those materials crystallise in the same crystal structure as Si-PCPDTBT, explaining the enhanced mobility. Moreover, the less bulkier and longer side chains would probably affect significantly the kinetics of crystallisation leading to greater ease of crystallisation.

Bibliography

[164] J. Y. Kim, K. Lee, N. E. Coates, D. Moses, T.-Q. Nguyen, M. Dante, and A. J. Heeger. Efficient tandem polymer solar cells fabricated by all-solution processing. *Science*, 317:222–225, 2007.

[165] J. Peet, J. Y. Kim, N. E. Coates, W. L. Ma, D. Moses, A. J. Heeger, and G. C. Bazan. Efficiency enhancement in low-bandgap polymer solar cells by processing with alkane dithiols. *Nature Materials*, 6:497–500, 2007.

[166] M. C. Scharber, M. Koppe, J. Gao, F. Cordella, M. A. Loi, P. Denk, M. Morana, H.-J. Egelhaaf, K. Forberich, G. Dennler, R. Gaudiana, D. Waller, Z. Zhu, X. Shi, and C. J. Brabec. Influence of the bridging atom on the performance of a low-bandgap bulk heterojunction solar cell. *Advanced Materials*, 22:367–370, 2010.

[167] M. Svensson, F. Zhang, S. C. Veenstra, W. J. H. Verhees, J. C. Hummelen, J. M. Kroon, O. Inganäs, and M. R. Andersson. High-performance polymer solar cells of an alternating polyfluorene copolymer and a fullerene derivative. *Advanced Materials*, 15:988–991, 2003.

[168] E. Wang, L. Wang, L. Lan, C. Luo, W. Zhuang, J. Peng, and Y. Cao. High-performance polymer heterojunction solar cells of a polysilafluorene derivative. *Applied Physics Letters*, 92:033307, 2008.

[169] J. Hou, H.-Y. Chen, S. Zhang, G. Li, and Y. Yang. Synthesis, characterization, and photovoltaic properties of a low band gap polymer based on silole-containing polythiophenes and 2,1,3-benzothiadiazole. *Journal of the American Chemical Society*, 130:16144–16145, 2008.

[170] M. Morana, H. Azimi, G. Dennler, H.-J. Egelhaaf, M. Scharber, K. Forberich, J. Hauch, R. Gaudiana, D. Waller, Z. Zhu, K. Hingerl, S. S. van Bavel, J. Loos, and C. J. Brabec. Nanomorphology and charge generation in bulk heterojunctions based on low-bandgap dithiophene polymers with different bridging atoms. *Advanced Functional Materials*, 20:1180–1188, 2010.

[171] H.-Y. Chen, J. Hou, A. E. Hayden, H. Yang, K. A. Houk, and Y. Yang. Silicon atom substitution enhances interchain packing in a thiophene-based polymer system. *Advanced Materials*, 22:371–375, 2010.

[172] H. Sirringhaus, P. J. Brown, R. H. Friend, M. M. Nielsen, K. Bechgaard, B. M. W. Langeveld-Voss, R. A. J. Spiering, A. J. H. amd Janssen, E. W. Meijer, P. Herwig, and D. M. de Leeuw. Two-dimensional charge transport in self-organized, high-mobility conjugated polymers. *Nature*, 401:685, 1999.

[173] L. Martinez, R. Andrade, E. G. Birgin, and J. M. Martinez. Packmol: A package for building initial configurations for molecular dynamics simulations. *Journal of Computational Chemistry*, 30(13):2157–2164, 2009.

[174] Hoi Nok Tsao, Don M. Cho, Insun Park, Michael Ryan Hansen, Alexey Mavrinskiy, Do Y. Yoon, Robert Graf, Wojciech Pisula, Hans Wolfgang Spiess, and Klaus Mullen. Ultrahigh mobility in polymer field-effect transistors by design. *Journal of the American Chemical Society*, 133(8):2605–2612, 2011.

[175] Hoi Nok Tsao, Don Cho, Jens Wenzel Andreasen, Ali Rouhanipour, Dag W. Breiby, Wojciech Pisula, and Klaus Mullen. The influence of morphology on high-performance polymer field-effect transistors. *Advanced Materials*, 21(2):209–212, 2009.

CHAPTER 6

Quasi-Elastic Incoherent Neutron Scattering and Molecular Dynamics Study on the Dynamics of Poly-alkyl-thiophenes

In the previous chapter, we have emphasised the importance of kinetics in polymer crystallisation. In this part, we study the influence of the side chain lengths on the dynamics of polymers by quasi-elastic neutron scattering and molecular dynamics. We select two polymers from the poly-alkyl-thiophene families with different side chain lengths, poly-3-hexylthiophene and poly-3-octylthiophene.

First, we review the motivation of the study (section 6.1). Then, we present and discuss data on the dynamics of these poly-alkyl-thiophenes as a function of time and temperature obtained using quasi-elastic neutron scattering (section 6.2). Then, we use molecular dynamics to rationalise the observed dynamics (section 6.3).

Section 6.1

Motivation

In the previous chapter, we found no difference in the potential energy surfaces at 0K for C- and Si-PCPDTBT. However, we showed that the side chains of Si-PCPDTBT are more flexible than the side chains of C-PCPDTBT. This can help to explain the difference in crystal structure because different growth and nucleation kinetics may result in different thermodynamically stable structures being adopted. Moreover, it can explain the ease of crystallisation of Si-PCPDTBT in comparison with C-PCPDTBT. In fact, it has already been proved that by changing the solvent (adding ODT) and thus, by changing the kinetics of the system, it is possible to induce more easily crystallisation of C-PCPDTBT [176].

Polymer dynamics are very important since the typical morphologies of organic solar cell blends are non-equilibrium morphologies and thus, will continue to evolve in time leading to unreliability in solar cell efficiencies in time and short lifetimes. Especially, the glass transition is of great interest since the temperature range of operation of solar cells is quite large, well below room temperature (below freezing at night) to about 80 °C. If the glass transition is in that range of temperatures or close to, it can lead to detrimental changes in the blend microstructure.

To study the influence of the side chains on the dynamics of conjugated polymers, we have selected two polymers from the poly-alkyl-thiophene family, the well studied poly-hexyl-thiophene (P3HT) and poly-octyl-thiophene (P3OT). P3HT and P3OT have the same chemical structure, except they differ in side chain lengths. Both polymers are semi-crystalline. Annealing is reported to enhance the crystallinity of both polymers. P3HT gives better power conversion efficiencies when blended with PCBM than P3OT [177].

In this chapter, we study the dynamics of those polymers by combining quasi-elastic neutron scattering (QENS) and molecular dynamics. The accessible time range of QENS depends on the instrument but is on the order of magnitude of thousands of picoseconds which is compatible with the time ranges accessible with fully atomistic models used in molecular dynamics. In the next section, we will present the analysis of the QENS data.

Section 6.2

Quasi-Elastic Incoherent Neutron Scattering Study on the Dynamics of Poly-alkyl-thiophenes

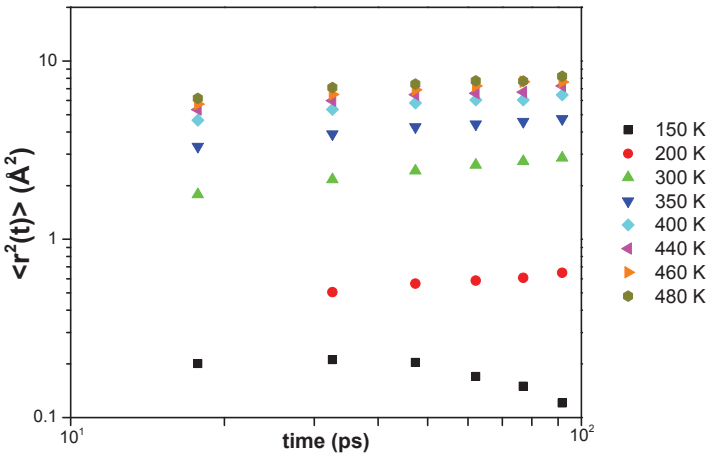
P3HT and P3OT films were studied using the IN10 spectrometer at the Institut Laue-Langevin (France) and the instrument OSIRIS of ISIS-RAL in Oxford at temperatures between 4 and 500 K. The data were collected and analysed by Antonio Urbina.

The incoherent scattering functions $(S_{inc}(Q,t))_T$ have been extracted in the time domain for the different explored transfer momenta Q and temperatures using the method described in the subsection 2.3.3. $(S_{inc}(Q,t))_T$ was fitted using the following equation:

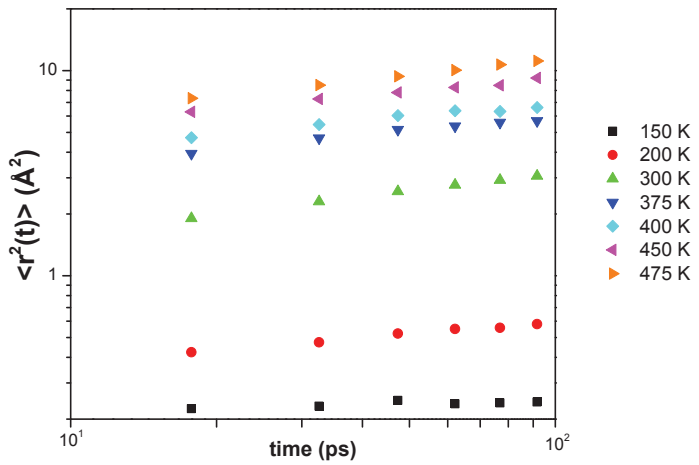
$$(S_{inc}(Q,t))_T = A\exp\left[-\frac{(<r^2(t)>)_T}{6}Q^2 + \frac{(\alpha_2(t))_T(<r^2(t)>)_T^2}{72}Q^4\right] \qquad (6.1)$$

where $(<r^2(t)>)_T$ is the mean square displacement of the hydrogens, $(\alpha_2(t))_T$ the second-order non-Gaussian parameter and A a pre-factor to account for slight deficiencies in the normalisation procedure and multiple scattering effects. During the fitting procedure, A, $(<r^2(t)>)_T$ and $(\alpha_2(t))_T$ are free parameters [178].

The mean square displacements for P3HT and P3OT are plotted as a function of time for different temperatures in Figure 6.1. The mean square displacement increases with both time and temperature, although the increase with temperature is more significant. The logarithm of the mean square seems to increase linearly with the logarithm of time. No significant difference can be observed between P3HT and P3OT mean square displacement in that time window except at the lowest studied temperature 150 K.



(a)



(b)

Figure 6.1: Mean square displacement as a function of time for different temperatures for (a) P3HT and (b) P3OT. The mean square displacement has been extracted by fitting the quasi-elastic neutron scattering measurements performed with OSIRIS using equation 6.1 after having corrected the data with the instrumental resolution using equation 2.9. Data from Antonio Urbina.

Three distinct time ranges are usually used to describe a glass. The microscopic regime corresponds to very short times ($\leq$ picoseconds), where the thermal vibrations dominate. At long times, long range motions such as backbone reptation take place. This time range is called as α-relaxation. At intermediate times before reptation takes place, the so-called β-relaxation governs the glass dynamics. β-relaxation is identified as a local jiggling of the molecules in a cage formed by their neighbours. This cage effect confines the molecules to a limited region in space. The glass transition takes place when the structural α-relaxation and the localised β-relaxation begin to decouple [179]. The different regime occurs at more or less short times depending on the temperatures.

Well below T_g, viscous transport is expected to be frozen and so the α-relaxation regime is expected to occur at very long times. Well above T_g, where polymers behave similarly to fluids, a more or less direct crossover from the microscopic dynamics to the α-relaxation regime is expected. At intermediate temperatures, all regimes are expected to be observed.

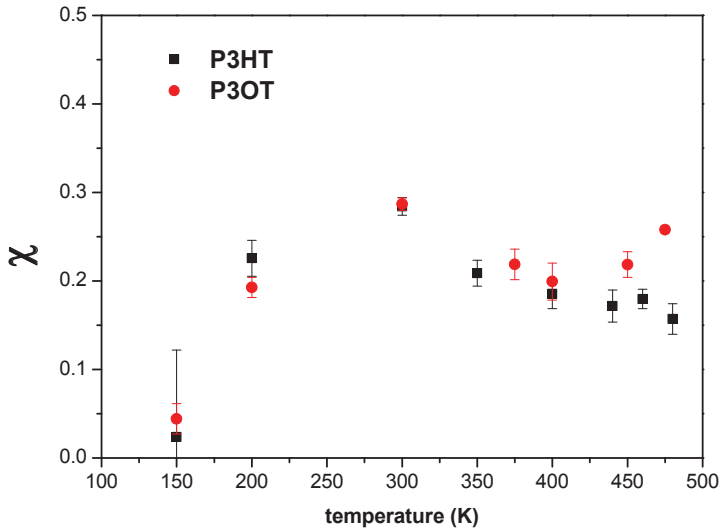


Figure 6.2: Temperature dependence of the exponent χ determining the sublinear dependence of the mean square displacement for P3HT and P3OT from the experiments performed with OSIRIS (18-90 ps). Data from Antonio Urbina.

The time dependence of the mean square displacement can be fitted using a power law $(< r^2(t) >) \propto t^{\chi}$ with $\chi < 1$, indicative of sublinear diffusion. The exponents χ can be in theory related to the different regimes: microscopic, α- and β relaxations. A χ exponent of 0.5 can be in theory assigned to the α-relaxation regime.

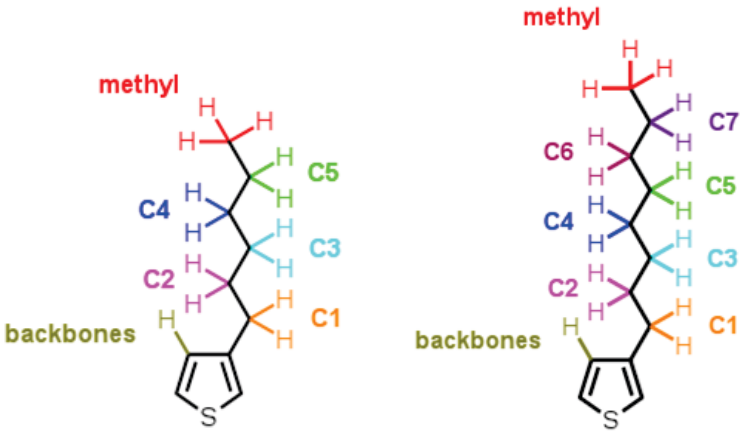
As mentioned above, this is expected to happen at long times or high temperatures. At intermediate times and intermediate temperatures, the χ exponent is expected to display a plateau at values lower than 0.5 indicative of the cage effect [178]. The exponents χ are plotted for both polymers as a function of the temperature in Figure 6.2.

No significant differences are observed between the polymers. The exponents χ are constant at a value of about 0.25 over the range of temperatures studied. This is indicative of the cage effect. No transition to the α-relaxation regime is observed even at high temperatures close to the melting temperature of the polymer (P3HT crystals are known to melt at about 510 K). This is probably due to the fact that the measurements are done at very short times ($\leq$ 90 ps).

Section 6.3

Molecular Dynamics on the Dynamics of Poly-alkyl-thiophenes

In order to understand how the observed behaviour is related to the different motions that can take place in these poly-alkyl-thiophenes, we use molecular dynamics (MD). We define different group of hydrogens: C1-C7, methyl and backbones in P3HT and P3OT (see Figure 6.3).



(a) (b)

Figure 6.3: Definition of the different hydrogen groups C1-C7, methyl and backbones for (a) P3HT and (b) P3OT.

6.3.1 Force Field and Molecular Dynamics Parameters

We use the P3HT force field developed by Moreno *et al.* [180]. For P3OT, we have modified the P3HT force field; two carbon atoms and four hydrogens have been added to the side chains with the same parameters as CT/R2CH2 and HC/alkyl thiophene

in Moreno *et al.* paper [180].

We generate a system comprising 16 chains of 16 monomers of either P3HT or P3OT using the Packmol package [181]. To prepare the morphologies, we anneal our systems at 1500 K in the canonical ensemble (N,V,T) with the density fixed at 1.0 g.cm^{-3} for 10 ns. The last frame is taken as input for the simulations.

We perform an energy minimization step after the annealing step in order to relax the system. For the energy minimization step, the steepest descent method is used with a tolerance of 10 kJ.mol^{-1}.nm^{-1}.

We perform the simulations in the isothermal-isobaric ensemble (N,P,T). Periodic boundary conditions are applied in all three directions. The temperature coupling is realised using a velocity rescaling with a stochastic term. The time constant for temperature coupling is set at 0.1 ps. The time step for the simulations is chosen to be 1 fs. The initial velocities are generated according to a Maxwell distribution at the requested temperature. The Coulomb and van der Waals forces are cut off at 1 nm. A relative dielectric constant of 1 is used. Long range dispersion corrections are applied for energy. Thus, we perform molecular dynamics simulations of 10 ns using a leap-frog algorithm for integrating Newton's equations of motion.

We calculate the average mean square displacement over all the hydrogens of the system or over all the hydrogens of specific groups (see Figure 6.3) from the obtained trajectories for each temperature. The first 100 ps of the trajectory are removed for the calculations. A moving average over multiple time origins separated by 100 ps is done to improve statistics.

6.3.2 Molecular dynamics results

The calculated mean square displacements of all the hydrogens of P3HT and P3OT are plotted as a function of time for different temperatures in Figure 6.4.

$(< r^2(t) >)_T$ of the hydrogens displays a relatively steep increase (approximately linear) with time below 1 ps. This is due to vibrations and various fast processes of the microscopic regime. At longer times, the cage effect induced by the presence of neighbouring atoms takes place. Finally, the α-relaxation is reached at times longer than 1000 ps. $(< r^2(t = 1ps) >)_T$ can be considered as a good measure of the extent

of the atomistic displacements in the microscopic regime.

$(< r^2(t = 1ps) >)_T$ is plotted as a function of the temperature for different groups of hydrogens in Figure 6.5 and compared with experimental data. The experimental data follow the simulations up to 300 K for all the hydrogens. Above 300 K, other processes than vibrational processes may be activated (the simulations integrate only vibrational processes) or MD simulations overestimate the thermal expansion (see Figure 6.6).

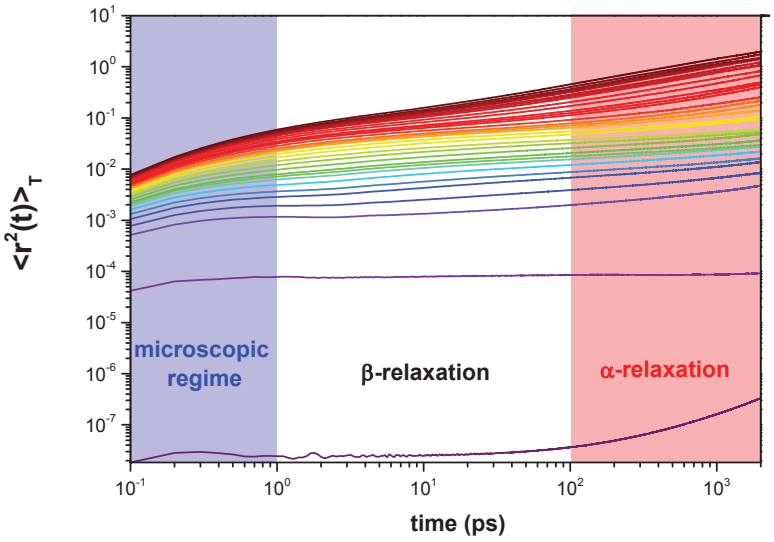
To investigate the thermal expansion, we fix in the simulation the density of P3HT to 1 g.cm^{-3} and redo the simulations in a NVT ensemble. The $(< r^2(t = 1ps) >)_T$ as calculated in both NPT and NVT ensembles for P3HT is plotted as a function of the temperature for all the hydrogens in Figure 6.7. It can be seen that the volume confinement has a huge impact on the temperature dependence especially at high temperatures and is a plausible explanation for the discrepancies observed between experiment and simulations in Figure 6.5.

In order to compare the mean square displacements extracted from the simulations with the experimental data, we extract the χ values for the same time windows. The χ values are plotted in Figure 6.8 as a function of temperatures for different group of hydrogens for time windows corresponding to the time window of OSIRIS.

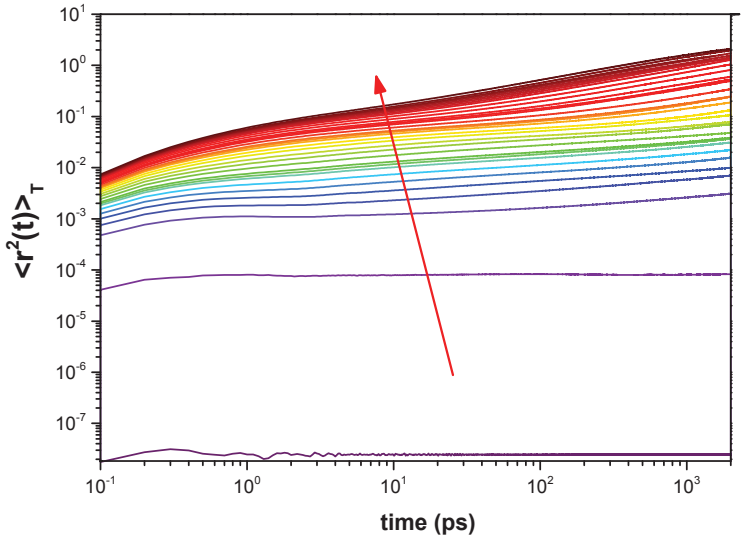
The χ values first increase to values up to 0.3-0.4 for temperatures between 50 and 150 K depending on the time windows. Then, the χ values decrease and a final drastic increase up to values around 0.5 occurs.

These values around 0.5 are compatible with what is expected at temperatures above the glass transition due to α-relaxations. Below the glass transition, χ are expecting to display a plateau regime indicative for the cage effect that extends until the decaging occurs. However, we observe a bump that shifts to higher temperatures when considering successively the hydrogens of the methyl end group, the hydrogens along the side chains (C7-C1) and the hydrogens present on the backbones of the polymers. Thus, this bump is probably associated with the activation of motions involving these group of hydrogens. Finally, the temperature range between 200 and 250 K can be associated with the glass transition. This is confirmed by the density drop in that specific temperature range (see Figure 6.6).

The experimental χ values seem to follow the same trend as the χ values extracted from molecular dynamics simulations, except that there is a shift in temperature. However, this might be due to a mismatch of time windows or due to a volume confinement effect.

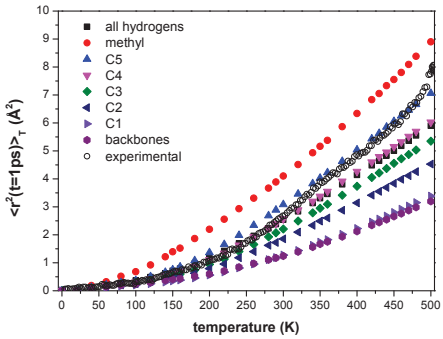


(a)

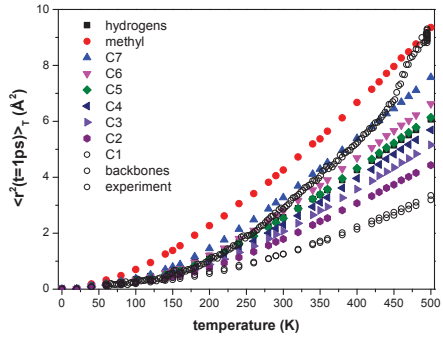


(b)

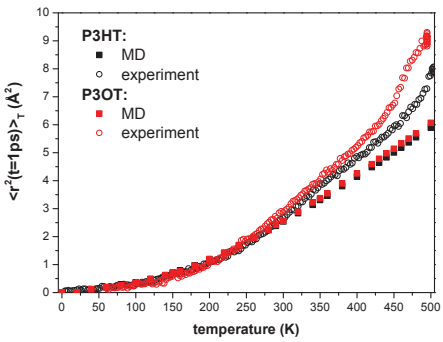
Figure 6.4: Mean-square displacement as a function of time for different temperatures between 0 K and 500 K (every 20 K) for (a) P3HT and (b) P3OT. The arrow shows the increase in temperature.



(a)



(b)



(c)

Figure 6.5: Temperature dependence of the mean square displacement at 1 ps for (a) P3HT and (b) P3OT for different group of hydrogens. It is compared with the mean square displacement extracted from measurements performed at IN10 (ILL) where the measured intensity corresponds to the pure elastic contributions. (c) Comparison between P3HT and P3OT mean square displacement obtained by MD simulations on all the hydrogens of the system and the mean square displacement extracted from measurements. Data from Antonio Urbina.

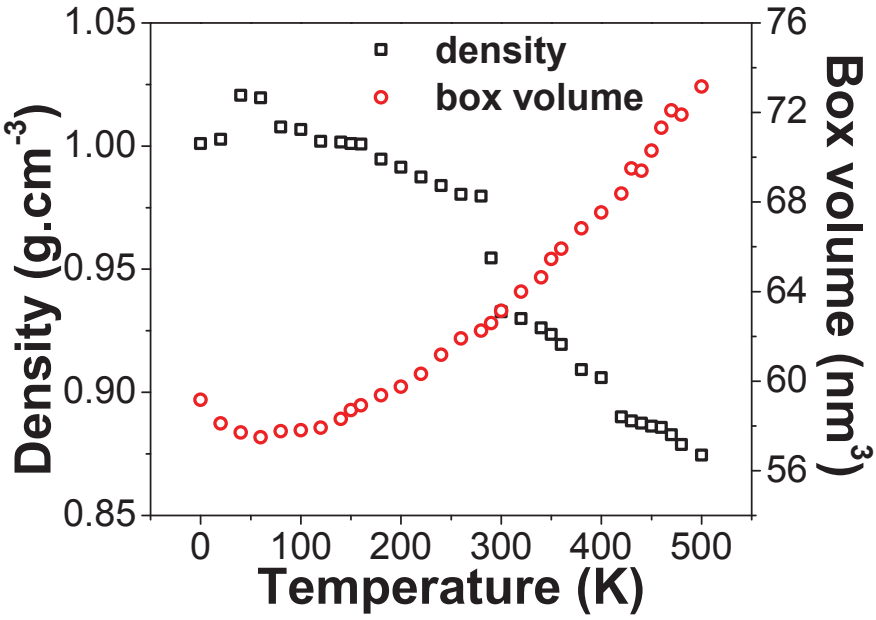


Figure 6.6: Density of P3HT calculating from simulations as a function of the temperature.

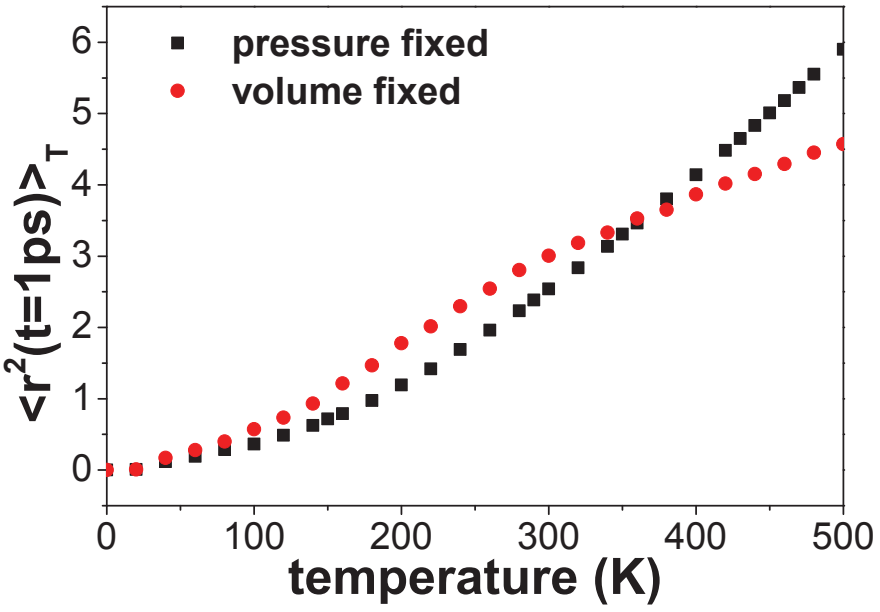
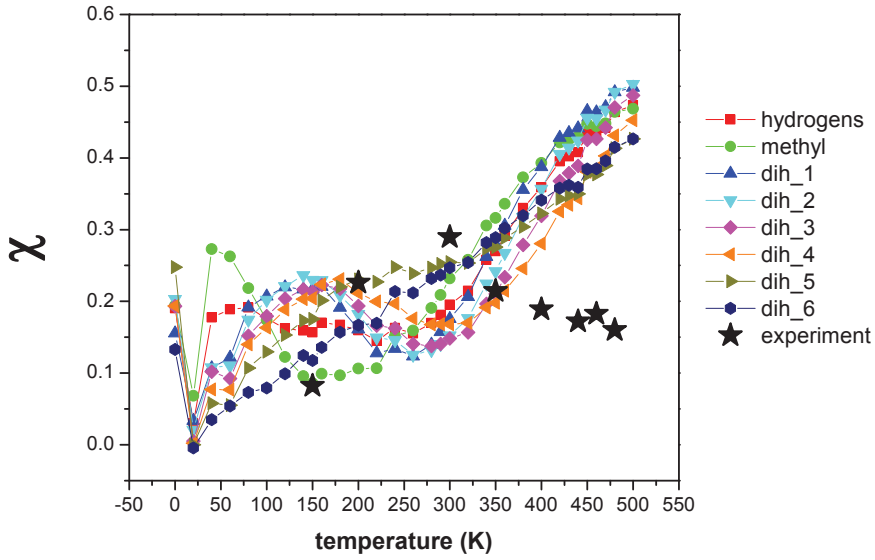
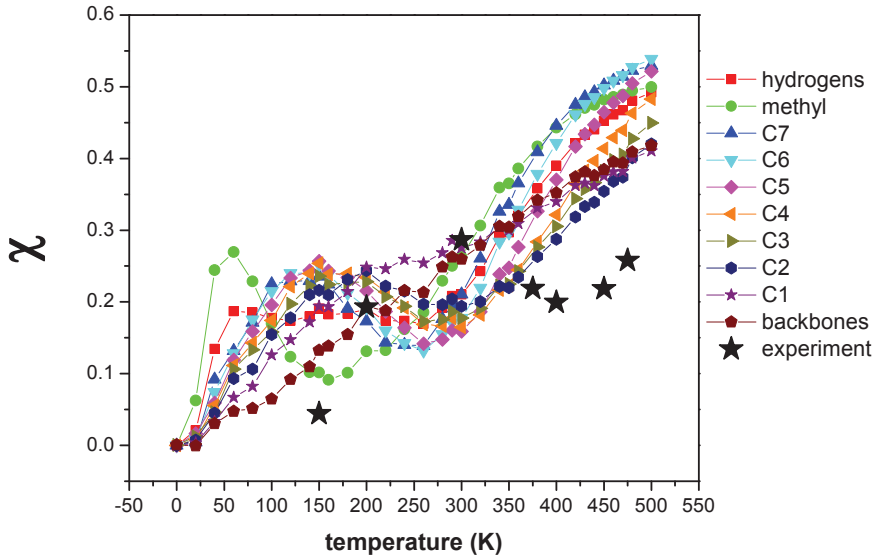


Figure 6.7: Temperature dependence of the mean square displacement at 1 ps for P3HT as calculated in NPT and NVT ensembles.



(a)

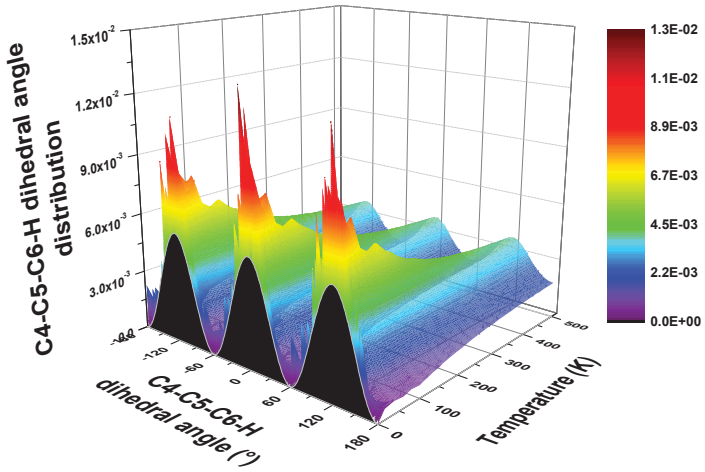


(b)

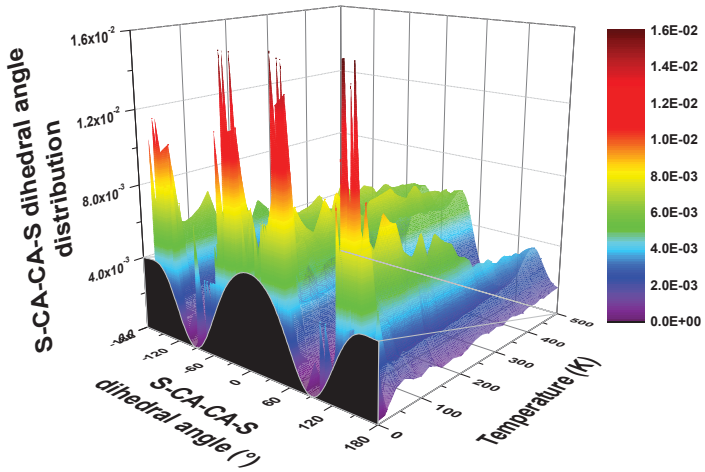
Figure 6.8: Temperature dependence of the exponent χ determining the sublinear dependence of the mean square displacement for (a) P3HT and (b) P3OT from molecular dynamics in time windows corresponding to the time window of OSIRIS (18-90 ps).

6.3.3 Activation energies of motions

From the trajectories simulated using molecular dynamics, we extract the dihedral angle distributions of hydrogens along the side chains and of the dihedral describing the torsion of the backbones (see Figure 6.9).



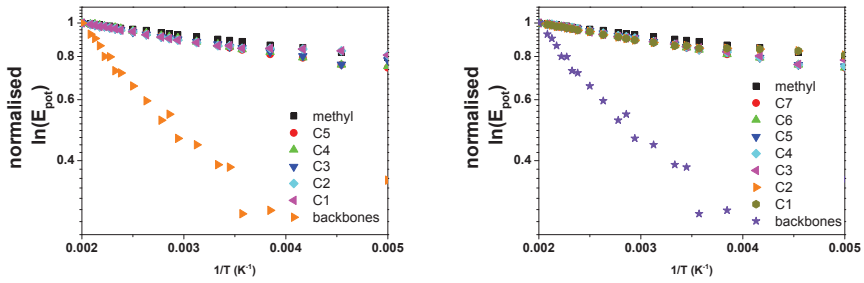
(a)



(b)

Figure 6.9: Dihedral angular distribution of (a) the methyl end group and (b) the dihedral describing the torsion of the backbones as a function of the temperature. The black distribution is the distribution calculated directly from the force field.

The potential energy has been calculated for each dihedral angles using the formalism of the force field and an average over all angles have been calculated weighted by the angle distribution. The natural logarithm of those potential energies is plotted as a function of the inverse of the temperature (see Figure 6.10). Since they follow an Arhenius law for a large range of temperature, by fitting those plots with a linear trend we can extract the activation energies of the different motions. This is summarised in the table 6.1. According to the simulations, β-relaxations are activated at 35 K and α-relaxations are activated at 295 K.



(a) (b)

Figure 6.10: Potential energy for each dihedral angles as a function of the inverse of the temperature for (a) P3HT and (b) P3OT.

Table 6.1: Temperature of activation for the different motions in (a) P3HT and (b) P3OT.

(a)

dihedral angle	temperature of activation
methyl	35 K
C5	49 K
C4	48 K
C3	47 K
C2	48 K
C1	48 K
backbones	295 K

(b)

dihedral angle	temperature of activation
methyl	35 K
C7	47 K
C6	48 K
C5	46 K
C4	48 K
C3	47 K
C2	48 K
C1	48 K
backbones	295 K

Section 6.4

Conclusion

In this chapter, we have combined the use of quasi-elastic neutron scattering with molecular dynamics simulations to understand the influence of side chain lengths on the dynamics of poly-alkyl-thiophene polymers. We focused on P3HT and P3OT.

The experimental data obtained in a time range of 18-90 ps showed no major differences between P3HT and P3OT. The χ exponent displays a plateau at about 0.25 for both polymers, indicative of the cage effect in the β-relaxation windows. An initial bump is though observed.

Molecular Dynamics have the advantage of exploring larger time scales (up to thousands of picoseconds). The mean square displacements of the hydrogens can be easily extracted from the trajectories and thus compared with the experimental data. The three regimes: microscopic, β- and α-relaxations are clearly observed.

The mean square displacement at 1 ps, representative of the Debye-Waller factor follow the experimental data up to 300 K. At higher temperatures, the simulation clearly underestimates the data. That was attributed to a volume confinement effect.

The χ values extracted from the simulations follow the same trend as the experimental data but are shifted and temperatures. Thus, in simulations, at high temperatures, the χ values reach 0.5 indicative of the α-relaxation regime. The glass transition is thus identified around 300 K which is in good agreement with the literature. In fact, P3HT glass transition has been measured by calorimetry at 12.1 [182, 183]. This mismatch between experiment and simulations can be explained by a mismatch of time windows or by a volume confinement effect. The simulations allow us to propose that the initial bump observed is linked with the activation of the β-relaxation.

The simulations suggest that a larger time window should be explored to see difference in dynamics of P3HT and P3OT. Moreover, the volume confinement effect should be studied in more details.

Bibliography

[176] J. Peet, J. Y. Kim, N. E. Coates, W. L. Ma, D. Moses, A. J. Heeger, and G. C. Bazan. Efficiency enhancement in low-bandgap polymer solar cells by processing with alkane dithiols. *Nature Materials*, 6:497–500, 2007.

[177] D. Gebeyehu, C.J. Brabec, F. Padinger, T. Fromherz, J.C. Hummelen, D. Badt, H. Schindler, and N.S. Sariciftci. The interplay of efficiency and morphology in photovoltaic devices based on interpenetrating networks of conjugated polymers with fullerenes. *Synthetic Metals*, 118(1-3):1 – 9, 2001.

[178] C. Gerstl, G. J. Schneider, A. Fuxman, M. Zamponi, B. Frick, T. Seydel, M. Koza, A.-C. Genix, J. Allgaier, D. Richter, J. Colmenero, and A. Arbe. Quasielastic neutron scattering study on the dynamics of poly(alkylene oxide)s. *Macromolecules*, 45(10):4394–4405, 2012.

[179] H. Franz, W. Petry, and A.Q.R. Baron. Quasielastic scattering: slow dynamics of glasses. *Hyperfine Interactions*, 123-124(1-4):865–879, 1999.

[180] Margherita Moreno, Mose Casalegno, Guido Raos, Stefano V. Meille, and Riccardo Po. Molecular modeling of crystalline alkylthiophene oligomers and polymers. *The Journal of Physical Chemistry B*, 114(4):1591–1602, 2010.

[181] L. Martinez, R. Andrade, E. G. Birgin, and J. M. Martinez. Packmol: a package for building initial configurations for molecular dynamics simulations. *Journal of Computational Chemistry*, 30(13):2157–2164, 2009.

[182] Yue Zhao, Guoxiong Yuan, Philippe Roche, and Mario Leclerc. A calorimetric study of the phase transitions in poly(3-hexylthiophene). *Polymer*, 36(11):2211 – 2214, 1995.

[183] Jun Zhao, Ann Swinnen, Guy Van Assche, Jean Manca, Dirk Vanderzande, and Bruno Van Mele. Phase diagram of P3HT/PCBM blends and its implication for the stability of morphology. *The Journal of Physical Chemistry B*, 113(6):1587–1591, 2009.

CHAPTER 7

Conclusion

In this thesis, we have studied the influence of chemical structure on the intermolecular interactions between polymer and fullerene governing the microstructure of organic photovoltaic blends.

7.0.1 Influence of the chemical structure of the fullerene

7.0.1.1 Importance of solubility of fullerenes in the amorphous part of the polymer: balance of polymer-fullerene and fullerene-fullerene interactions

We have found two mechanisms of microstructure development within blends of P3HT with PCBM, bis-PCBM, and tris-PCBM (chapter 3). The first originates from crystallization through thermal annealing and leads to high solar cell performances, while the second originates from the low solubility of fullerenes within the amorphous phase of the polymer and leads to poorer solar cell performances even after annealing procedures. The solubility of the fullerenes in the amorphous part of the polymer seems to be an important factor to control the microstructure of polymer:fullerene blends. However, the ability of the fullerene to crystallise can help to overcome a too high solubility like in the case of P3HT:PCBM.

Direct techniques used in this work do not allow to probe the onset of aggregation of the fullerenes, or in other words the solubility of fullerenes in polymer. We have demonstrated that ultra-fast photoluminescence spectroscopy can be used as an indirect technique to probe the onset of aggregation in the RRa-P3HT:PCBM and bis-PCBM systems. By probing the emission from the component materials and from interfacial (charge transfer) states, ultra-fast photoluminescence spectroscopy provides informations on the microstructure of the blend (crystallisation and mixing) and also on the interfacial energy levels (chapter 4).

7.0.1.2 Further work

It would be interesting to use this work to engineer polymer-fullerene blends with different phase separation length-scale and different fullerene amount dissolved in the amorphous part of the polymer to define what phase of the microstructure and what energetic landscape is relevant or favours one specific process involved in the conversion of light to electricity.

7.0.2 Influence of the chemical structure of the polymer

7.0.2.1 Importance of polymer side chain dynamics on polymer-polymer interactions

Crystallisation of the polymer and thus polymer-polymer interactions are known to play an important role in the microstructure development and to have a huge impact on processes such as absorption, charge transport and charge separation. We demonstrate that modelling techniques can help to explain observations done by grazing incidence X-ray diffraction. We found that the interactions between the backbones tend to stabilise the π-π stacking of the polymer crystal while the side chains introduce coherence in the lamellar direction (chapter 5). The side chain flexibility and dynamics have a huge impact on the kinetics of crystallisation and thus can favour one or other of the thermodynamically stable polymer crystal structure like in the case of C- and Si-PCPDTBT. Moreover, side chain dynamics may have a huge impact on the ease of polymer crystallisation, especially when blended with fullerenes. That explains as well that changing the side chain density along the backbones or structure lead to observed differences in polymer microstructure and charge mobilities.

We demonstrate the molecular dynamics in combination with quasi-elastic neutron scattering can give a valuable insight in the polymer dynamics providing that sufficiently large time windows are explored. In particular, it seems to be a very good tool to predict second-order transitions such as the glass transition that are relevant for the lifetime of organic photovoltaic devices (chapter 6).

7.0.2.2 Further work

It would be interesting to incorporate our treatment of side chain flexibility and crystallisation into modelling techniques suitable for larger system size such as Monte-Carlo or phase field simulations to be able to study the direct influence of microstructure on electrical properties such as charge transport studies in organic semiconducting materials.

Appendix A

Quantum Chemistry

In quantum chemical methods, the Schrödinger equation is solved in the Born-Oppenheimer approximation. The relavistic effects are generally neglected. The molecular orbital solutions of the Schrödinger equation are assumed to be a linear combination of a finite number of basis functions, usually chosen to be orthogonal.

A.1 Hartree-Fock method

In the Hartree-Fock method (HF) (Figure A.1), the set of nuclear coordinates given as input is used to guess an initial set of orbitals. In Gaussian, this realised by default by diagonalising the Harris functional [184]. Afterwards, this guessed wavefunction as well as the set of nuclear coordinates are used to create a Hartree-Fock operator F. In fact, the electronic molecular total energy is equal to the sum of the kinetic energy, the potential energy, the Hartree-Fock energy and the exchange energy (equation A.1). The Hartree-Fock energy is equivalent to the Coulomb interaction energy of an electron charge density with itself.

$$E_{tot} = E_{kinetic} + E_{potential} + E_{HF} + E_{exchange} \tag{A.1}$$

Finding the wave functions is now equivalent to solving the eigenfunction equation:

$$F\phi_i = \epsilon_i\phi_i \tag{A.2}$$

The eigenfunctions of the equation A.2 are new orbitals also called *Hartree-Fock Molecular Orbitals*.These Hartree-Fock Molecular Orbitals can be used as new inputs to construct a new Hartree-Fock operator. Here, the problem of self-consistency is posed. In fact, the orbitals that are used to calculate the energy should be the same as the orbitals that emerge from $F\phi_i = \epsilon_i\phi_i$. Consequently, the Hartree-Fock orbitals are optimised until the total energy has converged. When the convergence or the self-consistency is reached, the optimised Hartree-Fock molecular orbitals can be used to calculate any desired properties.

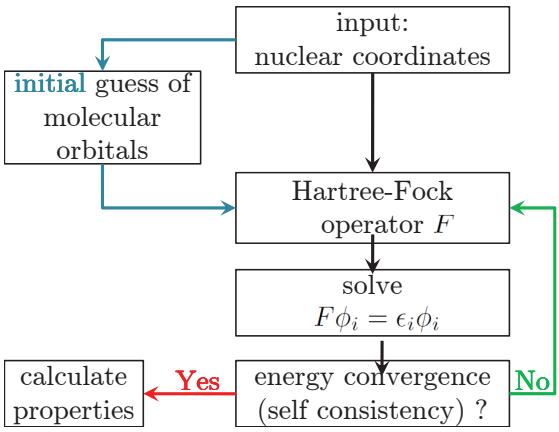


Figure A.1: Flow chart of the Hartree-Fock algorithm

However, the Hartree-Fock method suffers from limitations because especially, it does not take into account the electron correlation for electrons of opposite spins.

A.2 Møller-Plesset method

The Møller-Plesset methods (MPn) request a Hartree-Fock calculation followed by a Møller-Plesset correlation energy correction [185]. The correlation energy corrections is calculated by applying the Rayleigh-Schrödinger perturbation theory with the perturbation V defined as:

$$V \equiv H - F - < \phi_i^{(0)} | H - F | \phi_i^{(0)} > \tag{A.3}$$

where H is the perturbed Hamiltonian, F is the Hartree-Fock operator and $< \phi_i^{(0)} | H - F | \phi_i^{(0)} >$ is non-null in Hartree-Fock theory, $^{(0)}$ denotes that these quantities are associated with the unperturbed system. Then, the perturbed Hamiltonian H is defined by:

$$H \equiv H^{(0)} + \lambda V \tag{A.4}$$

with the non-perturbed Hamiltonian $H^{(0)}$ defined by:

$$H^{(0)} \equiv F + < \phi_i^{(0)} | H - F | \phi_i^{(0)} > \tag{A.5}$$

λ is a dimensionless parameter that can take any values between 0 (no perturbation) and 1 (the system is fully perturbed).

The energy levels of the perturbed system are given by the following Schrödinger equation:

$$(H^{(0)} + \lambda V)\phi_i = E_i\phi_i \tag{A.6}$$

where

$$E_i = E_i^{(0)} + \lambda E_i^{(1)} + \lambda^2 E_i^{(2)} + \ldots \quad with \quad E_i^{(k)} = \frac{1}{k!}\frac{d^k E_i}{d\lambda^k} \tag{A.7}$$

$$\phi_i = \phi_i^{(0)} + \lambda \phi_i^{(1)} + \lambda^2 \phi_i^{(2)} + \ldots \quad with \quad \phi_i^{(k)} = \frac{1}{k!}\frac{d^k \phi_i}{d\lambda^k} \tag{A.8}$$

By expanding the equation A.6 and equating the coefficients of each power of λ, different order energies can be calculated. Thereby, $E_i^{(0)}$is nothing else than the electronic energy calculated from the Hartree-Fock model. The first-order MP energy is zero. Therefore, the lowest order for which a correlation energy appears is the second order. The corrected energy is then given by:

$$E_{tot} \simeq E_{tot}^{HF} + E_{MP_n} \quad with \quad n \geq 2 \tag{A.9}$$

A.3 Density Functional Theory

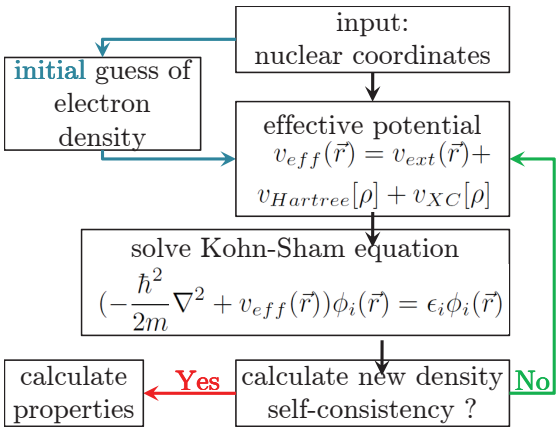


Figure A.2: Flow chart of Kohn-Sham algorithm

Alternatively, Density Functional Theory (DFT) can be used. As mentioned in the previous subsection, the total electronic energy is now devided into five terms, the kinetic energy $E_{kinetic}$, the potential energy $E_{potential}$, the Hartree-Fock energy E_{HF},

the exchange energy E_X and the correlation energy E_C.

$$E_{tot} = E_{kinetic} + E_{potential} + E_{HF} + E_X + E_C \tag{A.10}$$

The idea behind DFT is that the ground-state energy E_{tot} is uniquely determined by the electron density ρ (first Hohenberg and Kohn theorem). All the energy contributions should be then functionals of the electron density distribution ρ. Kohn and Sham rewrote then the equation A.10 as following:

$$E_{tot}[\rho] = E_{kinetic}[\rho] + E_{potential}[\rho] + E_{HF}[\rho] + E_{XC}[\rho] \tag{A.11}$$

with

$$E_{kinetic}[\rho] = \sum_{i=1}^{N} \int d\vec{r}\phi_i^*(\vec{r})(-\frac{\hbar^2}{2m}\nabla^2)\phi_i(\vec{r}) \tag{A.12}$$

$$E_{potential}[\rho] = \int d\vec{r}v_{ext}(\vec{r})\rho(\vec{r}) \tag{A.13}$$

$$E_{HF}[\rho] = \frac{e^2}{2}\int d\vec{r}\int d\vec{r'}\frac{\rho(\vec{r})\rho(\vec{r'})}{|\vec{r}-\vec{r'}|} \tag{A.14}$$

Nowadays, numerous exchange-correlation functional are available. In this work, the hybrid B3LYP (Becke, 3-parameter, Lee-Yang-Paar) is used. B3LYP is a mixture of an exact exchange functional from the Hartree-Fock theory and exchange-correlation functional issued from the General Gradient Approximations (GGA) and the Local Density Approximation (LDA).

$$E_{XC}^{B3LYP}[\rho] = E_{XC}^{LDA} + a_0(E_X^{HF} - (E_X^{LDA}) + a_X(E_X^{GGA} - (E_X^{LDA}) + a_C(E_C^{GGA} - (E_C^{LDA}) \tag{A.15}$$

where a_0, a_X and a_C are empirical parameters ($a_0 = 0.20$, $a_X = 0.72$ and $a_C = 0.81$). The LDA functionals are derived from the case of homogeneous gas. If the exchange functional is well known, the correlation functional is only known for the high- and low-density limits. For intermediate densities, quantum Monte-Carlo simulations able to reproduce both upper and lower limits have been used. However, GGA functionals are functionals of the magnitude of the gradient of the density $|\nabla\rho|$.

In order to simplify the problem, Kohn and Sham introduce an efficient potential $v_{eff}(r)$ defined as:

$$v_{eff}(\vec{r}) = v_{ext}(\vec{r}) + e^2\int\frac{\rho(\vec{r'})}{|\vec{r}-\vec{r'}|}d\vec{r'} + \frac{\delta E_{XC}[\rho]}{\delta\rho(\vec{r})} \tag{A.16}$$

leading to a Schrödinger equation for non-interacting particles called the Kohn-Sham

equation:

$$(-\frac{\hbar^2}{2m}\nabla^2 + v_{eff}(\vec{r}))\phi_i(\vec{r}) = \epsilon_i\phi_i(\vec{r}) \tag{A.17}$$

Consequently, in DFT (Figure A.2), the set of nuclear coordinates is used to guess an initial electron density. Afterwards, thiis initial electron density and the set of coordinates is used to calculate the effective potential. Then, the Kohn-Sham equation can be solved. The Kohn-Sham eigenfunctions are used to calculate the new electronic density. If self-consistency in electron density is reached, the required properties are calculated from the new density otherwise the new density is used as input of the algorithm.

A.4 Basis sets

For all the model chemistries presented above, a basis set of functions needs to be specified. In fact, this set of functions are used to create the molecular orbitals. The molecular orbitals are expanded as a linear combination of these functions with coefficients to be determined: $\Psi = \sum_{i=1}^{n} c_i\phi_i$ where $\{\phi_i\}$ is the basis set. In this work, the 6-311G(d,p) and the correlation-consistent basis sets cc-pVDZ, cc-pVTZ and cc-pVQZ are used.

Appendix B

C-PCPDTBT and Si-PCPDTBT force fields

Table B.1: Mass and Lennard-Jones parameters taken from the OPLS-AA force field except for the Silicon atom. Atom types correspond to those in Figure 5.7.

Atom	Mass (a.u.)	ϵ_{ii} (kJ.mol^{-1})	σ_{ii} (nm)
CA, C!, CW!, CB, Csp3	12.01100	0.293	0.3550
HA	1.00800	0.126	0.2420
S	32.06000	1.046	0.3550
N	14.00670	0.713	0.3250
Si	28.0800	0.398 [186]	0.4435 [186]
CT, CH	12.01100	0.347	0.3500
HC	1.00800	0.126	0.250

Table B.2: Equilibrium bond lengths and bond force constants.

Bond	b_0 (nm)	K_b (kJ.mol^{-1}.nm^{-2})
From OPLS-AA		
CA-CA	0.14000	392459.2
CA-HA	0.10800	307105.6
CA-CW!	0.13670	456892.8
S-CW!	0.17400	209200.0
CW!-CW!	0.14600	322168.0
CT-CH	0.15290	224262.4
CT-CT	0.15290	224262.4
CT-HC	0.10900	284512.0
CH-HC	0.10900	284512.0
CB-N	0.13910	346435.2
CA-C!	0.14000	392459.2
C!-CB	0.14040	392459.2
CB-CB	0.13700	435136.0
CW!-C!	0.14600	322168.0
Calculating using a modified Badger rule		
Csp3-CA	0.15300	230438.3
Si-CA	0.18928	119202.5
Csp3-CT	0.15431	218094.5
Si-CT	0.18600	132333.9
N-S	0.16384	300933.0

Table B.3: Equilibrium angles and angle force constants.

Angle	θ_0 (°)	K_θ (kJ.mol^{-1}.rad^{-2})
From OPLS-AA		
CA-CA-CW!	120.000	527.184
CA-CW!-S	110.000	585.760
CW!-S-CW!	90.000	619.232
CA-CA-HA	120.000	292.880
CW!-CA-HA	120.000	292.880
CW!-CW!-S	111.000	585.760
CW!-CW!-CA	120.000	527.184
CW!-CA-Csp3	120.000	527.184
CA-CA-Csp3	120.000	527.184
CA-Csp3-CA	120.000	527.184
CA-Csp3-CT	120.000	587.760
Csp3-CT-CH	114.000	527.184
Csp3-CT-HC	109.500	292.880
Si-CT-CH	114.000	527.184
Si-CT-HC	109.500	292.880
CT-CH-CT	112.700	488.273
CH-CT-CT	112.700	488.273
CT-CT-CT	112.700	488.273
CT-CH-HC	110.700	313.800
CH-CT-HC	110.700	313.800
CT-CT-HC	110.700	313.800
HC-CT-HC	107.800	276.144
CA-CA-C!	120.000	527.184
CA-C!-CB	120.000	527.184
C!-CB-CB	117.300	711.280
C!-CA-HA	120.000	292.880
CB-CB-N	110.400	585.760
C!-CB-N	132.400	585.760
CA-CW!-C!	120.000	527.174
S-CW!-C!	111.000	585.760
CA-C!-CW!	120.000	527.184
CB-C!-CW!	120.000	527.184
Calculating using a modified Halgren rule		
CW!-CA-Si	107.850	689.000
CA-CA-Si	140.750	689.000
CA-Si-CA	90.970	596.510
CA-Si-CT	113.510	385.126
CB-N-S	107.470	788.870
N-S-N	99.160	931.520
From force-matching		
CT-Csp3-CT	140.355	451.112
CT-Si-CT	134.059	261.217

Table B.4: Equilibrium dihedral angles and dihedral angle force constants.

Angle	ϕ_0 (°)	c_0 (kJ.mol^{-1})	c_1 (kJ.mol^{-1})	c_2 (kJ.mol^{-1})	c_3 (kJ.mol^{-1})	c_4 (kJ.mol^{-1})	c_5 (kJ.mol^{-1})
From OPLS-AA							
X-CA-X-X	180	30.334	0.000	-30.334	0.000	0.000	0.000
X-CW!-S-X	180	30.334	0.000	-30.334	0.000	0.000	0.000
X-CW!-CW!-X	180	30.334	0.000	-30.334	0.000	0.000	0.000
X-C!-CB-X	180	30.334	0.000	-30.334	0.000	0.000	0.000
X-CB-CB-X	180	30.334	0.000	-30.334	0.000	0.000	0.000
X-CB-N-X	180	30.334	0.000	-30.334	0.000	0.000	0.000
X-N-S-X	180	30.334	0.000	-30.334	0.000	0.000	0.000
X-C!-CW!-X	180	0.000	0.000	0.000	0.000	0.000	0.000
X-Csp3-CT-X	180	0.000	0.000	0.000	0.000	0.000	0.000
X-Si-CT-X	180	0.000	0.000	0.000	0.000	0.000	0.000
X-CT-H-X	180	0.000	0.000	0.000	0.000	0.000	0.000
CH-CT-CT-CT	180	2.929	-1.464	0.209	-1.674	0.000	0.000
CT-CT-CT-CT	180	2.929	-1.464	0.209	-1.674	0.000	0.000
CH-CT-CT-HC	180	0.628	1.883	0.000	-2.510	0.000	0.000
CT-CT-CT-HC	180	0.628	1.883	0.000	-2.510	0.000	0.000
HC-CT-CT-HC	180	0.628	1.883	0.000	-2.510	0.000	0.000
From force-matching							
CA-CW!-C!-CA	180	47.187	2.768	-26.664	-5.234	-13.883	7.785
CA-Csp3-CT-CH	60	14.288	-18.353	-2.839	30.817	2.587	1.813
CA-Si-CT-CH	60	5.797	-11.065	-1.500	16.635	0.536	-0.692
Csp3-CT-CH-CT	60	7.814	-13.474	9.628	17.388	-6.100	7.486
Si-CT-CH-CT	60	2.253	-9.593	8.157	17.070	-5.472	-3.158
CT-CC-CH-CT	60	13.459	-18.868	26.378	16.559	-29.772	11.472

Table B.5: Improper dihedral force constants.

Improper dihedral	K_ξ (kJ.mol^{-1}.nm^{-2})
CA-S-CW!-CW!	62.760
CA-S-CW!-C!	62.760
CA-CW!-CA-Csp3	62.760
CA-CW!-CA-Si	62.760
CW!-CA-CA-HA	43.932
C!-CA-CA-HA	43.932
C!-CB-CB-N	62.760
CA-CB-C!-CW!	62.760

Appendix C

C-APFO3 and Si-APFO3 force fields

The C-APFO3 and Si-APFO3 force fields are very similar to the C-PCPDTBT and Si-PCPDTBT force fields. Thus, they are not described entirely in this appendix but only the major differences are described.

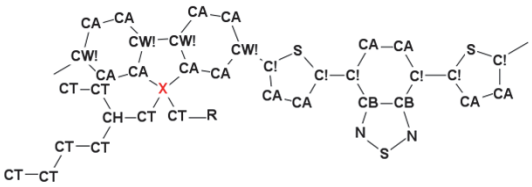


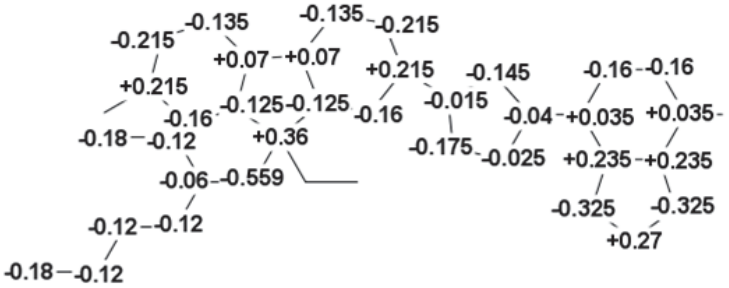
Figure C.1: Atom class definitions for C-APFO3 and Si-APFO3.

Table C.1: Equilibrium bond lengths and bond force constants.

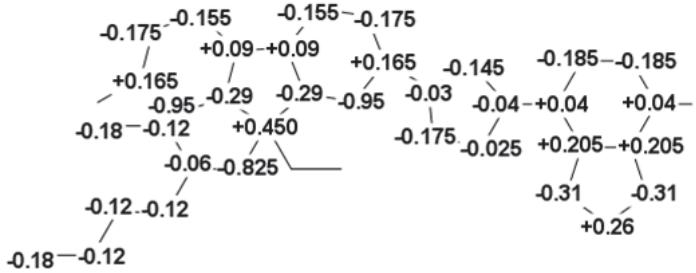
Bond	b_0 (nm)	K_b (kJ.mol^{-1}.nm^{-2})
From OPLS-AA		
S-C!	0.17400	209200.0

Table C.2: Equilibrium angles and angle force constants.

Angle	θ_0 (°)	K_θ (kJ.mol^{-1}.rad^{-2})
From OPLS-AA		
CA-C!-S	110.000	585.760
C!-S-C!	90.000	619.232
C!-CA-HA	120.000	292.880
CW!-CA-HA	120.000	292.880
S!-C!-C!	111.000	585.760
CA-C!-C!	120.000	527.184
S-C!-CW!	111.000	585.760
CA-C!-CW!	120.000	527.184
CA-CW!-C!	120.000	527.184
CA-C!-C!	120.000	527.184
CB-C!-C!	120.000	527.184



(a)



(b)

Figure C.2: Partial charges for (a) C-APFO3 and (b) Si-APFO3 derived from quantum chemical calculations.

Table C.3: Equilibrium dihedral angles and dihedral angle force constants.

Angle	ϕ_0 (°)	c_0 (kJ.mol^{-1})	c_1 (kJ.mol^{-1})	c_2 (kJ.mol^{-1})	c_3 (kJ.mol^{-1})	c_4 (kJ.mol^{-1})	c_5 (kJ.mol^{-1})
From OPLS-AA							
X-C!-S-X	180	30.334	0.000	-30.334	0.000	0.000	0.000
CA-CW!-C!-CA	180	18.36	2.68	-28.46	3.64	14.04	-2.38
CA-C!-C!-CA	180	29.3	5.35	-32.97	-5.83	10.07	6.86

Table C.4: Improper dihedral force constants.

Improper dihedral	K_ξ (kJ.mol^{-1}.nm^{-2})
CA-CA-CW!-CW!	62.760
CA-CW!-CA-Csp3	62.760
CA-CW!-CA-Si	62.760
CA-CA-CW!-C!	62.760
CA-CB-C!-C!	62.760
CA-S-C!-CW!	62.760

Bibliography

[184] J. Harris. Simplified method for calculating the energy of weakly interacting fragments. *Phys. Rev. B*, 31:1770–1779, Feb 1985.

[185] Chr. Møller and M. S. Plesset. Note on an approximation treatment for many-electron systems. *Phys. Rev.*, 46:618–622, Oct 1934.

[186] J. C. G. Pereira, C. R. A. Catlow, and G. D. Price. Molecular dynamics simulation of methanolic and ethanolic silica-based solâĹŠgel solutions at ambient temperature and pressure. *The Journal of Physical Chemistry A*, 106(1):130–148, 2002.